Modelling the Induced Magnetic Signature of Naval Vessels

Thesis submitted to the University of Glasgow

for the degree

of Doctor of Philosophy

Gordon J C Aird

Department of Physics and Astronomy

University of Glasgow

September 2000

Abstract

In the construction of naval vessels stealth is an important design feature. With recent advances in electromagnetic sensor technology the war time threat to shipping posed by electromagnetically triggered mines is becoming more significant and consequently the need to understand, predict and reduce the electromagnetic signature of ships is growing.

There are a number of components to the electromagnetic field surrounding a ship, with each component originating from different physical processes. The work presented in this study is concerned with the magnetic signature resulting from the magnetisation of the ferromagnetic material of the ship, under the influence of the earth's magnetic field. The detection threat arising from this induced magnetic signature has been known for many years, and consequently, warships are generally fitted with degaussing coils which aim to generate a masking field to counteract this signature. In this work computational models are developed to enable the induced magnetic signature and the effects of degaussing coils to be studied. The models are intended to provide a tool set, to aid the electromagnetic signature analyst in ensuring that pre-production designs of a vessel lie within specified induced magnetic signature targets. Techniques presented here also allow the rapid calculation of currents in degaussing coils. This is necessary because the induced magnetisation of a vessel changes with orientation. Three models are presented within this work.

The first model represents a ship as a simple geometric shape, a prolate spheroidal shell, of a given relative permeability. Analytical expressions are derived which characterise the magnetic perturbation to a previously uniform magnetic field, the earth's magnetic field, when the spheroid is placed within its in-

fluence. These results provide a quantitative insight into the shielding of large internal magnetic sources by the hull. This model is intended for use in preliminary design studies.

A second model is described which is based on the finite element method. This is a numerical model which has the capability of accurately reproducing the relatively complex geometry of a ship and of including the effects of degaussing coils. For these reasons this model is intended for detailed quantitative studies of the induced magnetic signature. A method is described to calculate the optimal set of degaussing coil currents required to minimise the induced magnetic signature. The induced signature without and with degaussing is presented. For the successful application of the finite element method the generation of a mesh is of extreme importance. In this work a mesh generation procedure is described which permits meshes to be generated around a collection of planar surfaces. The relative complex geometry of a ship can be easily specified as a number of planar surfaces and from this, the finite element mesh can be automatically generated. The automatic mesh generation detailed in this work eliminates an otherwise labour intensive step in the analysis procedure. These techniques are sufficiently powerful to allow meaningful calculations for real ships to be performed on desktop computers of modest power. An example is presented which highlights the application of this model to a hypothetical ship structure.

The third model detailed is specifically designed to study the induced magnetic signature of mine countermeasures vessels. Here the induced magnetic signature is no longer dominated by the gross structure of the ship, which is constructed from non-magnetic materials, but arises from the combined effect of the individual items of machinery onboard the craft. Each item is modelled individually and the interactions between them are taken into account. As in the finite element model the effects of degaussing coils are considered, and a method of calculating the

optimal set of coil currents is described. Results are presented for a hypothetical minesweeper.

Declaration

Except where specific references are given, the work in this thesis has been performed by myself, with guidance from my supervisor Dr. A. Watt.

Acknowledgements

I would like to thank sincerely my supervisor Dr. A. Watt of the Department of Physics and Astronomy, University of Glasgow, for his help and continuous support throughout the duration of this work. My thanks are also due to Professor M. Purshouse and Dr. A. Jennings of British Aerospace Systems, Glasgow, for their invaluable advice on the work presented in this thesis.

I am also grateful to Mr. D. Rothwell and Dr. I. Barbour for their input at the beginning of this work. Gratitude is also due to Professor C. Davies, Department of Physics and Astronomy, University of Glasgow for her encouragement throughout the preparation of this thesis.

Thanks is also due to friends and family for their unfailing support over the last few years.

Finally I wish to acknowledge that this work was funded by a CASE Research Studentship from the Engineering and Physical Sciences Research Council (EPSRC), sponsored by British Aerospace Systems.

Contents

List of Tables

List of Figures

Chapter 1

Naval Electromagnetics

1.1 Introduction

Since the use of the magnetic compass for navigation, electromagnetic fields have played an important role in naval history. It was not until the Second World War, however, that interest in DC and low frequency electromagnetic field signatures became important. During the First World War the Royal Navy had developed magnetically triggered mines but it was the German Navy which continued their development, and by the start of the Second World War a very effective and secret weapon against shipping had been deployed. It was only when the British forces finally captured a mine that its detonation mechanism could be revealed and countermeasures devised. The only effective defence against this type of mine was to reduce the magnetic signature of shipping by magnetic treatment and by degaussing [1] [2].

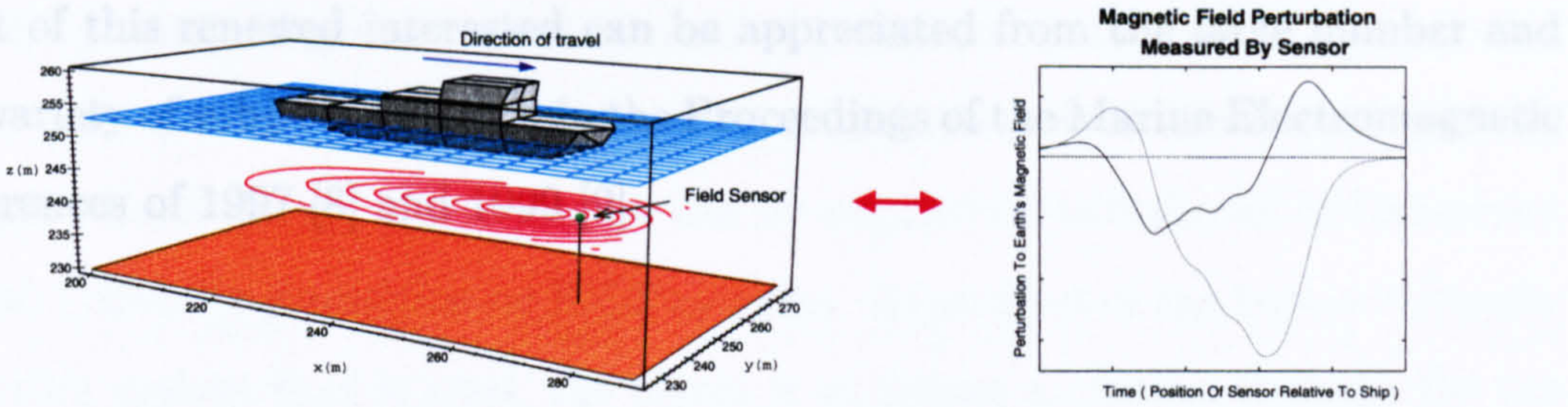

Figure 1.1: Schematic showing the change in the earth's magnetic field recorded by a sensor as a ship passes above.

With the development of more precise magnetometers and electric sensors, the detection of vessels from both their static and low frequency electromagnetic fields has become easier. Magnetometers are commercially available that enable disturbances as small as 1 nT to be detected [3]. Today, the application of magnetic signatures for the detection of shipping takes two main forms. Mines, either lying on the sea bed or tethered a fixed distance below the surface of the sea, are designed to detect a passing vessel from its magnetic signature and respond as appropriate. Modern mines not only search for the magnetic signature but assemble a range of signatures such as acoustical and electric potential to form an overall assessment of the source vessel [4]. For the detection of submarines, an aircraft equipped with an onboard magnetometer and airborne over the sea can detect the magnetic anomalies which arise from a submerged vessel. Airborne detection is hindered by the amount of magnetic noise present originating from the aircraft and the natural environment [5] [6].

With more electrically driven onboard equipment and with trends to full electric propulsion and perhaps even to MHD drives [7] the electromagnetic signature of ships is becoming more significant. With better detectors and with ships exhibiting stronger electromagnetic signatures, there has been a recent increase in research devoted to understanding the electromagnetic signature of ships. The

extent of this renewed interested can be appreciated from the large number and wide variety of subjects reported in the Proceedings of the Marine Electromagnetic Conferences of 1997 [8] and 1999 [9].

1.2 Origins of Electromagnetic Fields Generated by Ships

The following mechanisms produce electromagnetic fields around the hull of a ship.

Induced Magnetisation. When a ferromagnetic material is placed in an external magnetic field the material becomes magnetised [10]. Due to the earth's magnetic field and the high permeability of naval construction steels, the fabric of a ship is magnetised. It is the magnetic field resulting from this magnetisation that is known as the induced magnetic signature of the ship. It is to be noted that since the induced magnetisation of a ship depends on the magnitude and direction of the local earth's field the induced magnetic signature of the ship is governed by both the geographical area of operation and orientation of the vessel.

Permanent Magnetisation. When a ship is under construction some induced magnetism is 'hammered in' due to vibration, welding and other construction processes. A ship can also acquire a permanent magnetisation if it is in dock and its orientation in the earth's magnetic field is fixed for a relatively long time.

Corrosion Related Fields. Another source of electromagnetic fields is a result of the corrosion processes of the hull [11] [12] generating currents which in turn give rise to magnetic fields. Sea water is a very corrosive environment and in order to prevent the corrosion of the hull, ships are generally fitted with a

cathodic protection system. One method of protection is to place sacrificial zinc alloy anodes over the hull. The zinc corrodes in preference to the iron of the hull. In larger vessels the use of zinc anodes can be augmented or replaced by Impressed Current Cathodic Protection or ICCP systems. Regardless of the type of cathodic protection system that is used, the result is to induce a current through the sea with a return current within the ship and these currents produce magnetic fields. A schematic of this process is illustrated in figure 1.2.

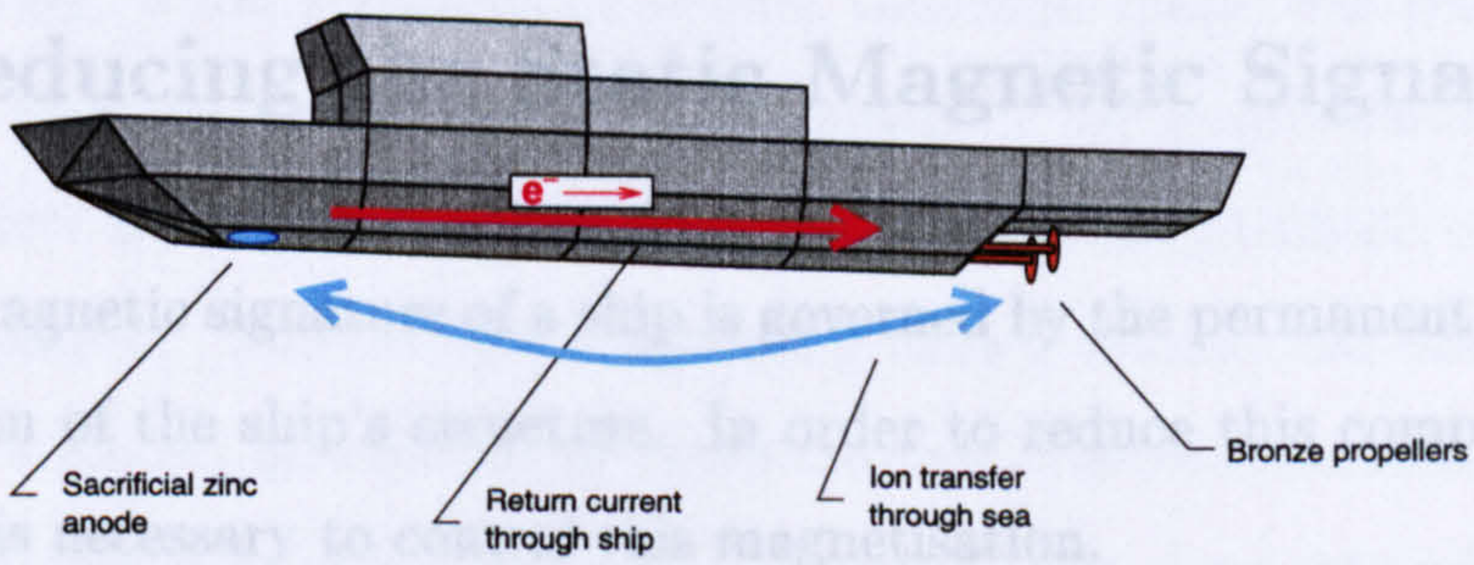

Figure 1.2: Schematic showing the current loops generated by the corrosion process between the ship's propeller and a sacrificial zinc anode.

Some studies into the numerical modelling of these corrosion processes have been undertaken by Jennings [13] using the ANSYS finite element package. It is to be noted that the commercial BEASY boundary element package [14] is available for corrosion related electric and magnetic field modelling.

As well as interest in numerical modelling techniques, work has been published on physical scale modelling of ships to allow the study of corrosion related magnetic fields. It has been reported that the fields generated by the corrosion processes are modulated by the speed of rotation of the propellers of the ship [15].

Machinery. Electric cabling around a ship, radar and telecommunication systems all produce electromagnetic fields. This is of particular importance in naval vessels where high currents are required to drive many of these systems.

Eddy Currents. Eddy Currents are generated in the metal of the hull and decking of the ship due to the roll and pitch of the ship in the earth's magnetic field. Modelling of these eddy currents has been reported [16].

1.3 Reducing the Static Magnetic Signature

The static magnetic signature of a ship is governed by the permanent and induced magnetisation of the ship's structure. In order to reduce this component of the signature it is necessary to control this magnetisation.

One way this is achieved is through the design of the ship. For vessels that require to have an extremely low magnetic signature, for example minesweepers and minehunters, this is accomplished by constructing the hull, decking and superstructure of the ship from non-magnetic materials. Glass Reinforced Plastic or GRP, aluminium and stainless steel are used wherever possible. The HUNT class and SANDOWN class mine countermeasures vessels of the Royal Navy are examples of ships which have been constructed on a non-magnetic basis [17].

The expense of these materials makes this type of non-magnetic construction prohibitive, in all but a few exceptions such as mine countermeasures vessels mentioned above. For ships with a more traditional construction, techniques such as magnetic treatment and degaussing are used for the reduction of the magnetic signature [2].

The term magnetic treatment describes the methods used to attempt to reduce

the underlying permanent magnetisation of a ship by realigning the magnetic domains to give a low average macroscopic magnetisation. Over the years magnetic treatment has taken several forms, but the main feature of these methods is to develop a time varying field around the ship.

An early method, known as wiping, was carried out by encircling the hull of the ship with a single turn of cable. The cable was arranged so that it could be lowered below the waterline and subsequently hauled up in close contact with the hull plating, while a current of several thousand amps was passed through it. This was effective for the vertical components of the magnetisation. A second method, known as deperming, was used against the longitudinal component of the magnetisation. This involved wrapping cables around the hull, to form a longitudinal solenoid, and flashes of direct current of several thousand amps were subsequently passed through the coil. However, the close wrapping of cables around the ship's hull is time consuming and a number of alternatives are currently used. These include 'drive-in' coil structures and systems where the coils are fitted to the sea-bed and the vessel passes across the installation.

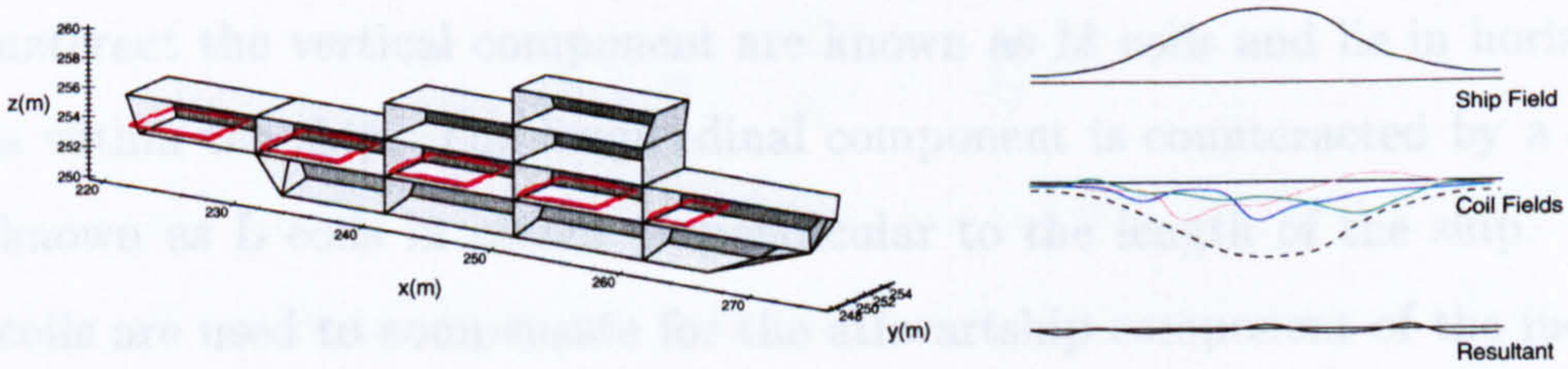

Figure 1.3: Schematic showing the effects of degaussing coils on the magnetic signature of a ship. Degaussing coils fitted within ship structure (left). Effect on static magnetic signature (right).

These magnetic treatment techniques are only effective against the permanent

magnetisation of a ship. To reduce the induced magnetic signature, which varies in use, and to eliminate any permanent magnetisation that remains after treatment, degaussing coil systems are used [18]. Degaussing coils are permanently fitted within a ship and a direct current is driven through them. The aim of these coils is to generate a magnetic field that is equal in magnitude but opposite in direction to the ship's magnetic field and, therefore, in the ideal case the ship's magnetic signature is completely eliminated. The effects of degaussing are summarised in figure 1.3. As previously mentioned the induced magnetic signature is dependent on the ship's position and its orientation and therefore, the currents in the coils require to be constantly updated to account for every change in the ship's heading.

It is to be noted that the degaussing coil system fitted to a ship is only effective against the induce magnetisation of the ship and any permanent magnetisation remaining after magnetic treatment.

The degaussing coils on a ship are usually arranged in three main groups corresponding to the three components of the induced magnetisation with respect to the main axes of the ship, vertical, longitudinal and athwartship. The coils used to counteract the vertical component are known as M coils and lie in horizontal planes within the ship. The longitudinal component is counteracted by a set of coils known as L coils in planes perpendicular to the length of the ship. A set of A coils are used to compensate for the athwartship component of the induced magnetisation and these lie in vertical planes parallel to the length of the ship. In some degaussing coil arrangements one main M coil surrounding the entire ship is used. In this case additional coils are fitted at the bow and stern, these additional coils are known as F and Q coils respectively.

As well as fitting degaussing systems to the entire ship, degaussing can also be applied to individual items of machinery [19]. This type of local degaussing is

common in mine countermeasures vessels in which the non-magnetic hull offers no shielding of internal equipment, and the magnetic effect of a large engine block, for example, becomes more significant.

1.4 Review of Basic Electromagnetics

In this section a brief review of the electromagnetic theory important to this work is presented. Detailed accounts are to be found in references [10] [20] [21].

Maxwell's equations are a set of fundamental equations governing macroscopic electromagnetic phenomena. These equations can be expressed in both differential and integral forms and for general time-varying fields, Maxwell's equations can be written as,

$$\nabla \cdot \mathbf{D} = \rho_f \tag{1.1}$$

$$\nabla \times \mathbf{E} + \frac{\partial \mathbf{B}}{\partial t} = 0 \tag{1.2}$$

$$\nabla \cdot \mathbf{B} = 0 \tag{1.3}$$

$$\nabla \times \mathbf{H} - \frac{\partial \mathbf{D}}{\partial t} = \mathbf{J}_f \tag{1.4}$$

where $\mathbf{D}$ is the electric flux density (coulombs/meter^2) and $\mathbf{E}$ is the electric field strength (volts/meter). $\mathbf{B}$ is the magnetic flux density (webers/meter^2 or tesla) and $\mathbf{H}$ the magnetic field strength (amperes/meter). ρ_f is the free charge density (coulombs/meter^3) and $\mathbf{J}_f$ the free current density (amperes/meter^2).

Another fundamental equation which specifies the conservation of charge can be written as,

$$\nabla \cdot \mathbf{J}_f = -\frac{\partial \rho_f}{\partial t} \tag{1.5}$$

It is to be noted that only three of the equations 1.1 to 1.5 are independent.

In linear materials, the field vectors $\mathbf{D}$ and $\mathbf{E}$ and also $\mathbf{B}$ and $\mathbf{H}$ are related by the properties of the materials at any point in the field region. These are referred to as the constitutive properties of the material and are given by,

$$\mathbf{D} = \epsilon_r \epsilon_0 \mathbf{E} \tag{1.6}$$

$$\mathbf{B} = \mu_r \mu_0 \mathbf{H} \tag{1.7}$$

$$\mathbf{J} = \sigma \mathbf{E} \tag{1.8}$$

where ϵ_r and μ_r are the relative permittivity and permeability respectively, ϵ_0 and μ_0 are the permittivity (farads/meter) and permeability (henrys/meter) of free space and σ is the conductivity (siemens/meter).

When considering electrostatic and magnetostatic fields, where the field quantities do not vary with time, equations 1.2, 1.4 and 1.5 can be written respectively as,

$$\nabla \times \mathbf{E} = 0 \tag{1.9}$$

$$\nabla \times \mathbf{H} = \mathbf{J}_f \tag{1.10}$$

$$\nabla \cdot \mathbf{J}_f = 0 \tag{1.11}$$

but equations 1.1 and 1.3 remain unchanged. It is evident that in the static situation there is no interaction between the electric and magnetic fields, and therefore the electrostatic case, described by equations 1.1 and 1.9 can be considered separately from the magnetostatic case described by equations 1.3 and 1.10. It is to be noted that equation 1.11 is a natural consequence of equation 1.10.

Since this work is focused on magnetostatic problems the magnetostatic case is now considered. To solve the equations corresponding to the magnetostatic case one approach is to convert the first order differential equation, involving two field quantities, into second order differential equations involving only one field quantity.

It it to be noted that equation 1.3 can be satisfied by representing the magnetic flux density $\mathbf{B}$ as,

$$\mathbf{B} = \nabla \times \mathbf{A} \tag{1.12}$$

where $\mathbf{A}$ is called the vector potential. It can be shown that the governing equation is,

$$\nabla \times \left(\frac{1}{\mu}\nabla \times \mathbf{A}\right) = \mathbf{J}_f \tag{1.13}$$

With the specification of the gauge condition $\nabla \cdot \mathbf{A} = 0$, $\mathbf{A}$ can be uniquely determined.

For regions where there are no conductor sources, that is, $\mathbf{J}_f = 0$ the total magnetic field $\mathbf{H}$ can be derived from a scalar potential since, in this case $\nabla \times \mathbf{H} = 0$ and it follows that,

$$\mathbf{H} = -\nabla\phi \tag{1.14}$$

where ϕ is known as the total magnetic scalar potential. Therefore, the governing equation for regions without currents is given by,

$$\nabla \cdot \mu\nabla\phi = 0 \tag{1.15}$$

In regions with current sources an alternative scalar potential can be defined, this potential is known as the reduced magnetic scalar potential and is derived by partitioning $\mathbf{H}$ into two separate components. These components correspond to the magnetic field generated by prescribed sources $\mathbf{H}_s$ and the field arising from the induced magnetism in the materials present $\mathbf{H}_m$. Therefore,

$$\mathbf{H} = \mathbf{H}_m + \mathbf{H}_s \tag{1.16}$$

and from equation 1.10, $\nabla \times \mathbf{H}_m = 0$, it follows that,

$$\mathbf{H} = -\nabla\phi_r + \mathbf{H}_s \tag{1.17}$$

where ϕ_r is the reduced scalar potential. By definition for conductor source regions with current density $\mathbf{J}_s$ the source field, $\mathbf{H}_s$, is given by the Biot-Savart law [10]. The governing equation for the reduced magnetic scalar potential is given by,

$$\nabla \cdot \mu \nabla \phi_r = \nabla \cdot \mu \mathbf{H}_s \tag{1.18}$$

Regardless of the potential representation used for a given problem, the correct solution cannot be determined without the specification of a complete set of boundary conditions. For the magnetostatic problem, at the interface between two media, for example medium 1 and medium 2, the boundary conditions can be expressed mathematically as,

$$\hat{\mathbf{n}} \cdot (\mathbf{B}_2 - \mathbf{B}_1) = 0 \tag{1.19}$$

$$\hat{\mathbf{n}} \times (\mathbf{H}_2 - \mathbf{H}_1) = \alpha_s \tag{1.20}$$

where $\mathbf{H}_1$ and $\mathbf{B}_1$ are repectively the magnetic field strength and magnetic flux density in region 1, and $\mathbf{H}_2$ and $\mathbf{B}_2$ are respectively the magnetic field strength and magnetic flux density in region 2. The vector $\hat{\mathbf{n}}$ is the unit normal to the interface directed from medium 1 into medium 2 and α_s is the surface current density at the interface, (amperes/meter).

1.5 Review of Contemporary Finite Element Work on the Magnetic Signature of Ships

Although numerous computer codes are available for the study of electromagnetic fields [22], it would appear that two commercial packages are predominant for the investigation of electromagnetic signatures.

The first package is made available by Vector Fields Limited [23]. The OPERA finite element software, with the TOSCA analysis package, is widely used by international naval organisations. The TOSCA package has been used for the study of the induced magnetic signature of steel hulled ships [24] and in the study of dyads, magnetic influence mine countermeasures [25].

The FLUX2D and FLUX3D finite element packages, developed by CEDRAT [26] have also been applied to the study of magnetic signatures [27]. Work employing the FLUX3D program has been reported on the relevent use of surface elements for the modelling of thin iron regions, such as the hulls of ships [28]. In addition, the use of the FLUX3D program to model the effects of degaussing coils has been reported [29]. This package has been used to study the magnetic signature of the La Fayette frigate [30]. The same package is used by the French CETEB Magnetism Department as a key part of the DATASSIM package for the study of degaussing coil systems [31]. The use of the FLUX3D program has been reported in a study of the magnetic signatures associated with induction motors on minesweepers [32].

1.6 Project Aims and Outline

The main objective of this project is to develop computational models to facilitate the study of the induced magnetic signature of naval vessels.

Three different models are presented in the three main sections of this work. In chapter 2, an analytical model is developed to describe the main gross features of the magnetic field surrounding a ship. In chapters 3, 4 and 5 work is presented for a finite element based model which takes into account the detailed shape of the hull and the internal structure of the vessel. In addition, it can give a quantitative answer to the effectiveness of degaussing coils. In chapter 6 a specific model is developed for the study of the induced magnetic signature of mine countermeasures vessels. The hull of this type of craft being constructed from non-magnetic materials. The emphasis of study is to quanitfy the effects on the induced magnetic siganture of the individual magnetic components onboard this type of vessels.

Chapter 2

Analytical Considerations

2.1 Introduction

In this chapter aspects of the analytical work undertaken as part of this project are described. In section 2.2 a method of determining the magnetic field at any point in space from the effects of a series of shells of permeable material is described. Concentric spherical shells are examined and this work is then extended, in section 2.2.2, to a set of confocal prolate spheroids. The work on prolate spheroids is subsequently used as the basis for an analytical model for the induced magnetisation of a ship and the spheroidal ship model is detailed in section 2.3.2.

In section 2.4.1 some preliminary work, focusing on degaussing, is presented. The section begins with a look at the theoretical basis of degaussing and describes the requirements for the complete degaussing of a given object. The section is concluded with an application of the Biot-Savart law, to enable the efficient calculation of the magnetic field generated by a system of degaussing coils.

2.2 Shell Model

2.2.1 Spherical Geometry

In this section a method of determining the scalar potential and hence the magnetic field at every point in space, due to a set of concentric spherical shells of permeable material in a previously uniform external field is described.

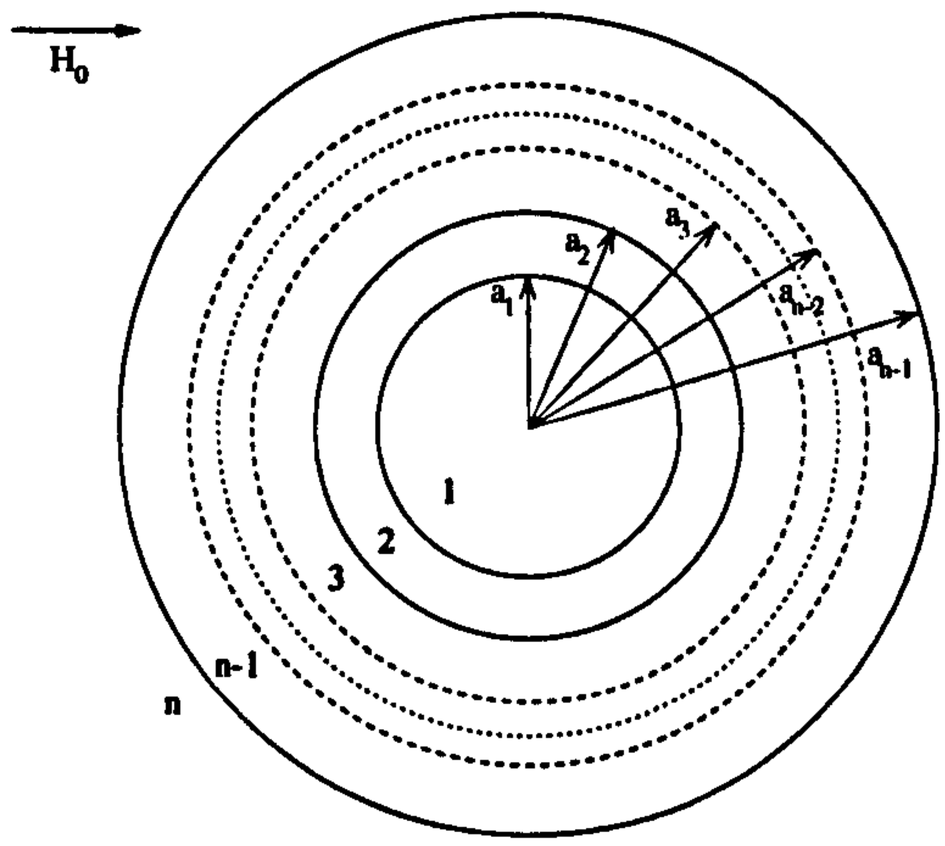

Figure 2.1: A set of $n-1$ concentric spherical shells.

To define a set of concentric shells consider figure 2.1 in which a set of $n-1$ concentric spherical shells is illustrated. Each of these regions $1, 2, .., n$ has a specified permeability $\mu_1, \mu_2, .., \mu_n$ separated by spherical surfaces of radii $a_1, a_2, .., a_{n-1}$.

The problem, which is of particular interest, is the determination of the perturbation to a uniform magnetic field, when this system of shells is placed within its influence. The solution can be found by solving Laplace's equation, equation 1.15, with suitable boundary conditions, thereby determining the scalar potential throughout and hence the magnetic field at any point. The potential can

in general be written as a sum of radial functions times Legendre polynomials. For the problem involving spherical geometries and with a uniform external magnetic field, only the Legendre polynomial $P_1(\cos\theta) = \cos\theta$ survives, and the potential within each region of the problem can be written as,

$$\phi_i = -H_i r\cos\theta + \frac{p_i}{r^2}\cos\theta \tag{2.1}$$

where in region i, H_i is the magnitude of the uniform component of the field and the quantity p_i is related to the dipole moment.

The following boundary conditions apply at the interface between each region [10],

$$\phi_i = \phi_{i+1} \tag{2.2}$$

$$\mu_i \frac{\partial \phi_i}{\partial r} = \mu_{i+1}\frac{\partial \phi_{i+1}}{\partial r} \tag{2.3}$$

where each quantity is evaluated at the interface $r = a_i$ with $i = 1, .., n-1$.

For a problem which contains a number of interfaces between regions or shells of different permeability, as illustrated in figure 2.1, the solution can be obtained by considering the boundary conditions given above at each of the interfaces.

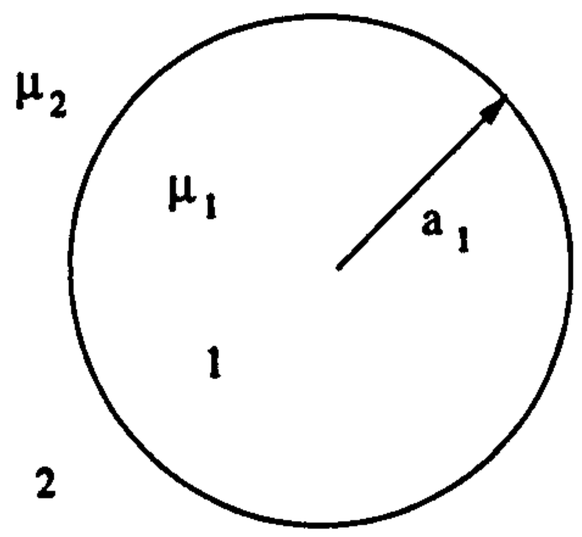

Figure 2.2: Spherical surface of radius a_1 defining two regions 1 and 2 with relative permeabilities μ_1 and μ_2 respectively.

With reference to figure 2.2, for the case of a spherical boundary of radius a_1, with permeability μ_1 on the side $r < a_1$ and μ_2 on the side $r > a_1$, in spherical polar coordinates the solution to the governing equation within each region can be written as,

$$\phi_1 = -H_1 r \cos\theta + \frac{p_1}{r^2}\cos\theta \tag{2.4}$$

$$\phi_2 = -H_2 r \cos\theta + \frac{p_2}{r^2}\cos\theta \tag{2.5}$$

Applying the boundary conditions 2.2 and 2.3 for the potential at the spherical boundary, $r = a$, the following relationships can be derived,

$$H_2 = \frac{1}{3}\left(\frac{\mu_1}{\mu_2} + 2\right)H_1 + \frac{2}{3}\left(\frac{\mu_1}{\mu_2} - 1\right)\frac{p_1}{a^3} \tag{2.6}$$

$$p_2 = \frac{1}{3}\left(\frac{\mu_1}{\mu_2} - 1\right)a^3 H_1 + \frac{1}{3}\left(2\frac{\mu_1}{\mu_2} + 1\right)p_1 \tag{2.7}$$

These equations can be represented as,

$$\begin{bmatrix} H_2 \\ p_2 \end{bmatrix} = T_1 \begin{bmatrix} H_1 \\ p_1 \end{bmatrix} \tag{2.8}$$

where the matrix T_1 is given by equation 2.9, in which the matrix has been rewritten for the general case corresponding to the boundary $r = a_i$.

$$T_i = \frac{1}{3}\begin{bmatrix} \frac{\mu_i}{\mu_{i+1}} + 2 & \frac{2}{a_i^3}\left(\frac{\mu_i}{\mu_{i+1}} - 1\right) \\ a_i^3\left(\frac{\mu_i}{\mu_{i+1}} - 1\right) & 2\frac{\mu_i}{\mu_{i+1}} + 1 \end{bmatrix} \tag{2.9}$$

The matrix T_i relates the quantities H_i and p_i on one side of the boundary, $r < a_i$, to the values H_{i+1} and p_{i+1} for $r > a_i$. It is to be noted that the matrix T_i depends only on the radius of the boundary a_i, and the relative permeabilities on either side of the boundary, μ_i and μ_{i+1}. For a system composed of n regions, as illustrated in figure 2.1, with permeabilities $\mu_1, \mu_2, .., \mu_n$ separated by spherical surfaces of radii $a_1, a_2, .., a_{n-1}$, a set of these transfer matrices can be generated corresponding to

each boundary. The values outside the set can be related to the values within the centre of the system, that is,

$$\begin{bmatrix} H_n \\ p_n \end{bmatrix} = T_{n-1}...T_2T_1 \begin{bmatrix} H_1 \\ p_1 \end{bmatrix} \tag{2.10}$$

It is often necessary to solve for H_1, p_1 from H_n and p_n and the inverse of the matrix T_i is,

$$T_i^{-1} = \frac{1}{3} \begin{bmatrix} \frac{\mu_{i+1}}{\mu_i} + 2 & \frac{2}{a_i^3}\left(\frac{\mu_{i+1}}{\mu_i} - 1\right) \\ a_i^3\left(\frac{\mu_{i+1}}{\mu_i} - 1\right) & 2\frac{\mu_{i+1}}{\mu_i} + 1 \end{bmatrix} \tag{2.11}$$

The determinant of the matrix T_i is μ_i/μ_{i+1}.

By the following example cases, the approach to determine the magnetic field around a set of concentric spherical shells is demonstrated.

Case 1 - Solid Sphere of Permeable Material in a Previously Uniform Field

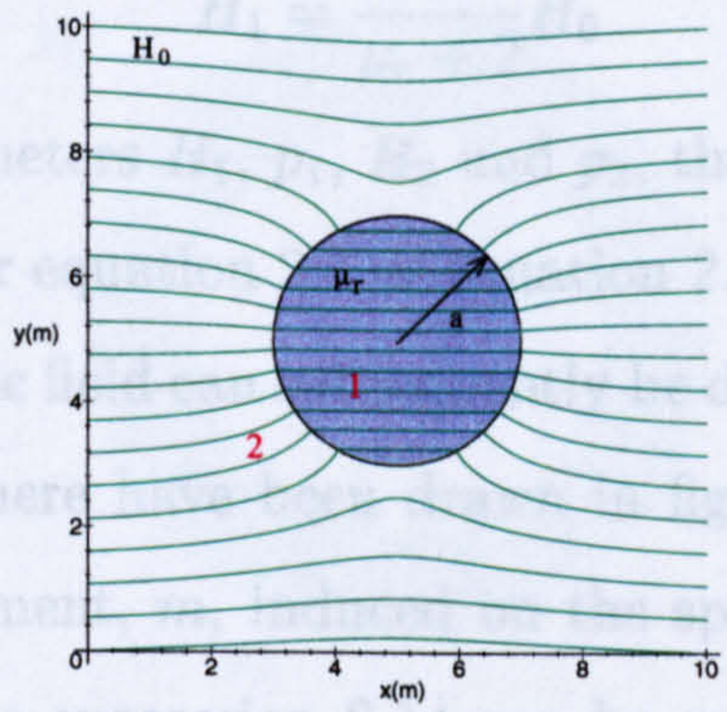

Figure 2.3: Solid sphere of relative permeability μ_r and radius a in a previously uniform field. Magnetic field lines are illustrated.

Consider the example containing just one interface, corresponding to the case of a solid sphere of permeable material placed in a previously uniform field. The geometry of this problem is illustrated in figure 2.3.

In region 1 the solution can be expressed in terms of H_1 and p_1 and in region 2 by H_2 and p_2 corresponding to equations 2.4 and 2.5 considered earlier. The transfer matrix relating these quantities on either side of the boundary can be written as,

$$\begin{bmatrix} H_2 \\ p_2 \end{bmatrix} = \frac{1}{3} \begin{bmatrix} \mu_r + 2 & \frac{2}{a^3}(\mu_r - 1) \\ a^3(\mu_r - 1) & 2\mu_r + 1 \end{bmatrix} \begin{bmatrix} H_1 \\ p_1 \end{bmatrix} \tag{2.12}$$

The quantity H_2 is the uniform field therefore $H_2 = H_0$, and since the potential cannot be infinite at $r = 0$, within region 1, $p_1 = 0$. The two remaining unknowns,

p_2 and H_1, can subsequently be determined from the equations given by 2.12.

$$p_2 = \frac{\mu_r - 1}{\mu_r + 2} a^3 H_0 \tag{2.13}$$

$$H_1 = \frac{3}{\mu_r + 2} H_0 \tag{2.14}$$

Having defined the parameters H_1, p_1, H_2 and p_2, the potential at any point can be determined from either equation 2.4 or equation 2.5 depending on the position of the point. The magnetic field can subsequently be determined and the magnetic field lines around the sphere have been drawn in figure 2.3. The quantity p_2 is related to the dipole moment, m, induced on the sphere. Since the field within the sphere is uniform, the expression 2.14 can be used to calculate the induced dipole moment on the sphere,

$$m = MV = (\mu_r - 1) H_1 V \tag{2.15}$$

where M is the magnetisation per unit volume and V is the volume of the shape. From equation 2.15 the dipole moment on the sphere can then be written as,

$$m = 4\pi \frac{\mu_r - 1}{\mu_r + 2} a^3 H_0 \tag{2.16}$$

and by relating this expression to the quantity p_2 of equation 2.13, it can be noted that the dipole moment is related to p_2 by the constant 4π,

$$m = 4\pi p_2 \tag{2.17}$$

Case 2 - Spherical Shell of Permeable Material in a Previously Uniform Field

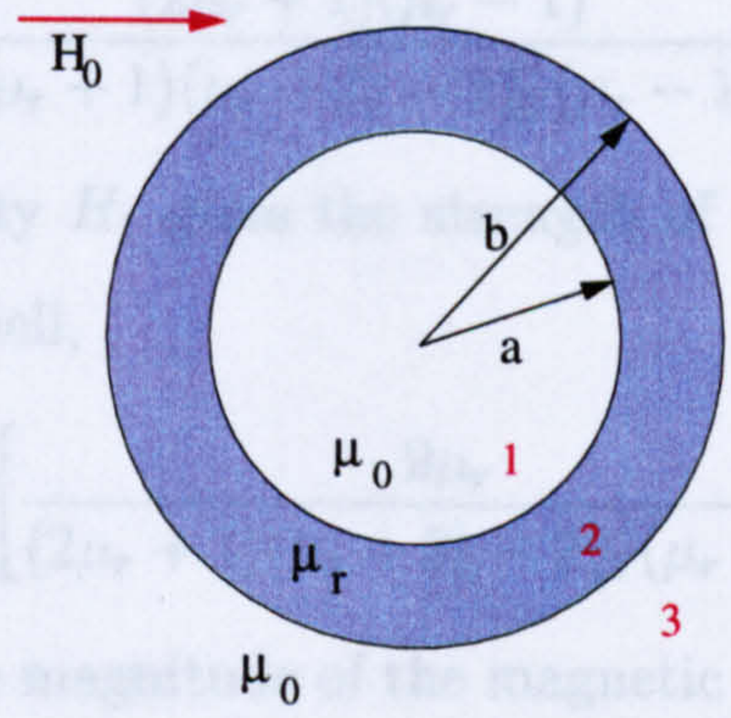

Figure 2.4: Geometry of a spherical shell of relative permeability μ_r, inner radius a, outer radius b in a previously uniform magnetic field $\mathbf{H}_0$.

In case 1 one boundary is involved, but this can be extended to the case of a spherical shell of permeable material with two spherical boundaries. The geometry of this problem is illustrated in figure 2.4 where a spherical shell of permeable material μ_r is defined by an inner spherical surface of radius a and an outer spherical surface of radius b. This shell is situated in free space.

In each of the three regions, 1, 2 and 3, the solution can be defined in terms of the two constants H_i and p_i and, two transfer matrices can be identified to relate these quantities between regions 1 and 2 and between regions 2 and 3. Since p_1 must be zero and H_3 is the external field, the potential can be determined within each region.

Two useful expression can be obtained from this example case. From the quantity p_3 the dipole moment of the shell in the region outside the shell can be determined,

$$m = 4\pi \left[\frac{(2\mu_r + 1)(\mu_r - 1)}{(2\mu_r + 1)(\mu_r + 2) - 2\frac{a^3}{b^3}(\mu_r - 1)^2} \right] (b^3 - a^3) H_0 \qquad (2.18)$$

Furthermore, the quantity H_1 gives the strength of the uniform field within the cavity of the spherical shell,

$$H_1 = \left[\frac{9\mu_r}{(2\mu_r + 1)(\mu_r + 2) - 2\frac{a^3}{b^3}(\mu_r - 1)^2} \right] H_0 \qquad (2.19)$$

Equation 2.19 relates the magnitude of the magnetic field within the cavity of the shell H_1, to the magnitude of the external magnetic field H_0. Consequently the expression can be used to study the magnetic shielding effects of spherical shells of permeable material.

Magnetic Shielding

From equation 2.19 it can be seen that the field within the central region of the shell is proportional to the external field, $H_1 = SH_0$, where the quantity S is given by,

$$S = \frac{9\mu_r}{(2\mu_r + 1)(\mu_r + 2) - 2\frac{a^3}{b^3}(\mu_r - 1)^2} \qquad (2.20)$$

In figure 2.5 the quantity S has been plotted against relative permeability μ_r, for different shell thicknesses t, t=0.01 m, t=0.02 m, and t=0.04 m. In each case a spherical shell of radius 2 m, was considered. For each shell thickness the inner and outer radii, a and b respectively, were determined from the expressions, $a = r - t/2$, $b = r + t/2$.

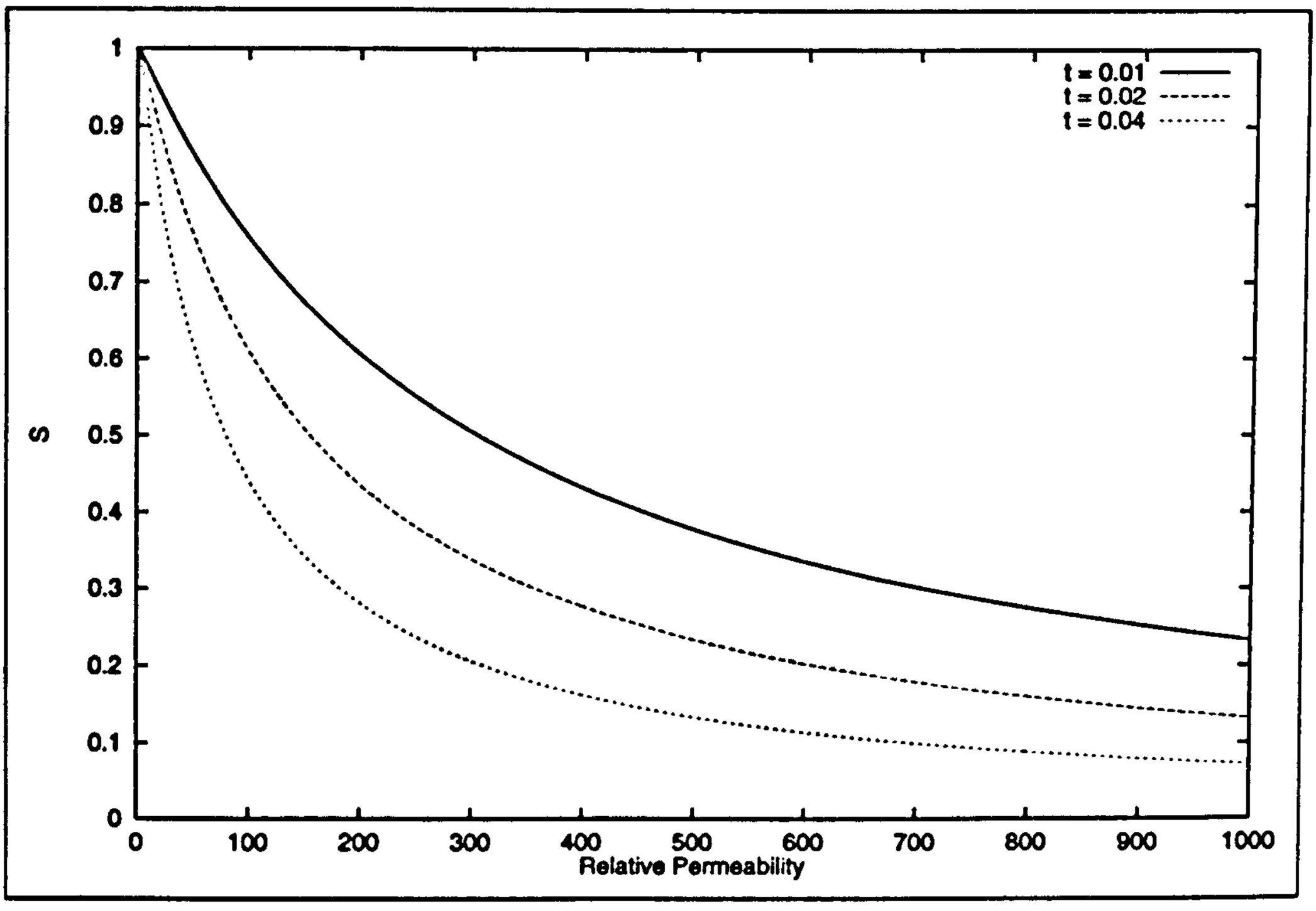

Figure 2.5: S as defined in equation 2.20 plotted against relative permeability for three different shell thicknesses, t. t=0.01 m (a=1.995 m,b=2.005 m), t=0.02 m (a=1.99 m,b=2.01 m) and t=0.04 m (a=1.98 m,b=2.02 m).

From figure 2.5 it is to be noted that as the relative permeability of the material forming the shell increases, the quantity S decreases indicating a reduction in the magnetic field within the shell and consequently an increase in the effectiveness of the magnetic shielding of the shell. This is illustrated in figure 2.6, where for a defined spherical shell of inner radius 1.6 m and outer radius 2.4 m, the magnetic field lines have been plotted around the shell. Three plots are illustrated corresponding to an increasing relative permeability with μ_r=5 in case 1, μ_r=50 in case 2 and μ_r=500 in case 3. It is evident that the field lines tend to pass through the permeable material and as the relative permeability increases more field lines pass through the material. The effect of this is to decrease the magnetic

field within the shell.

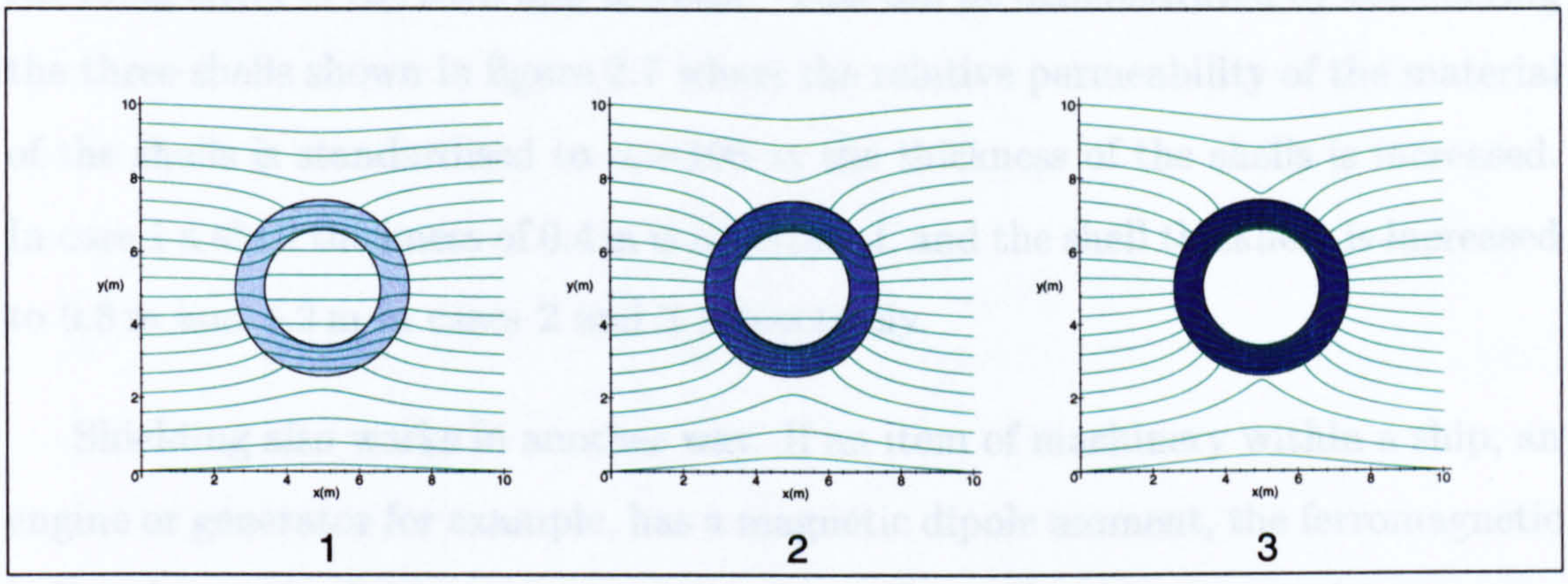

Figure 2.6: Magnetic field lines around a spherical shell of permeable material in a previously uniform field. In each case a=1.6 m b= 2.4 m. Case 1 μ_r=5, case 2 μ_r=50 and case 3 μ_r=500.

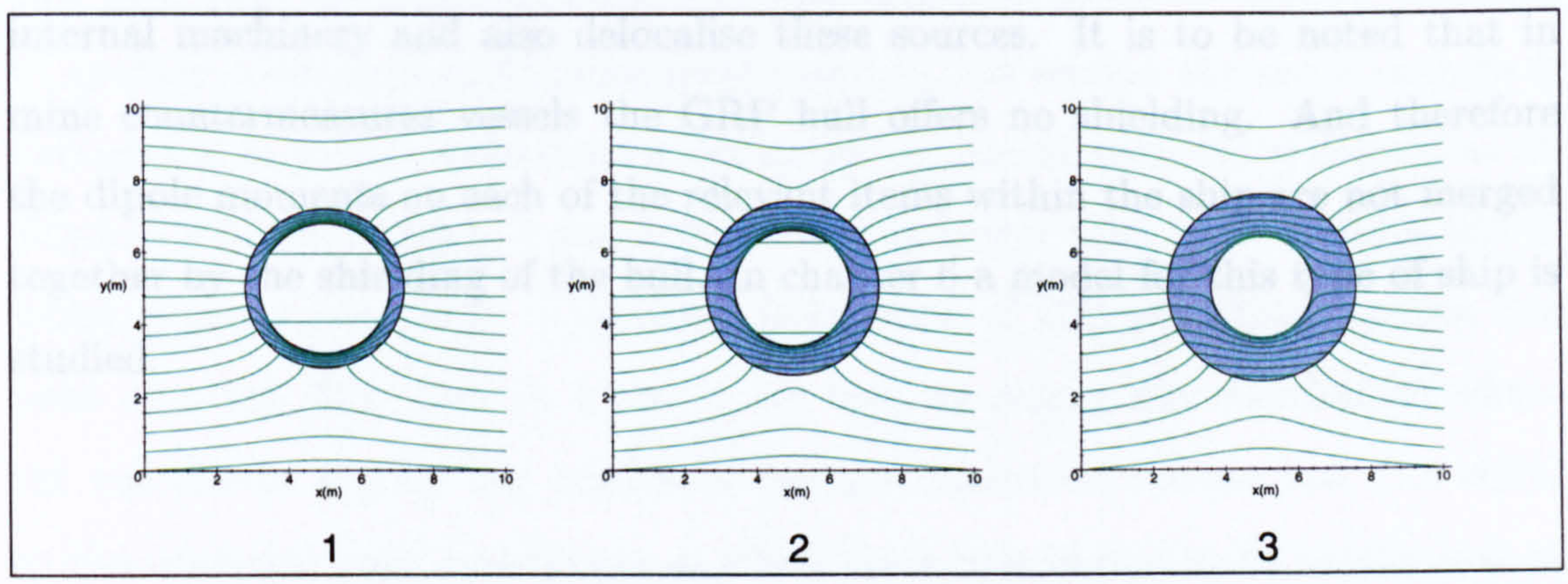

Figure 2.7: Magnetic field lines around a spherical shell of permeable material in a previously uniform magnetic field. In each case μ_r=100. Case 1 t=0.4 m (a=1.8 m,b=2.2 m), case 2 t=0.8 m (a=1.6 m,b=2.4 m) and case 3 t=1.2 m (a=1.4 m,b=2.6 m).

It is also evident from figure 2.5 that as the thickness of the shell increases, the shielding effect of the shell also increase. This can be demonstrated by considering the three shells shown in figure 2.7 where the relative permeability of the material of the shells is standardised to μ_r=100 as the thickness of the shells is increased. In case 1 a shell thickness of 0.4 m is illustrated, and the shell thickness is increased to 0.8 m and 1.2 m in cases 2 and 3 respectively.

Shielding also works in another way. If an item of machinery within a ship, an engine or generator for example, has a magnetic dipole moment, the ferromagnetic hull reduces the field external to the ship. To study this case p_1 is non zero, but $H_3 = 0$ and the dipole moment term p_3 giving the external field, can be calculated. It can be shown that p_3 is proportional to p_1 but reduced by the same shielding factor S, defined in equation 2.20. If several shells are present each shell contributes to and enhances the shielding of internal components. Thus the hull, decking and bulkheads all contribute to the magnetic signature from internal machinery and also delocalise these sources. It is to be noted that in mine countermeasures vessels the GRP hull offers no shielding. And therefore the dipole moments on each of the relevant items within the ship are not merged together by the shielding of the hull. In chapter 6 a model for this type of ship is studied.

2.2.2 Prolate Spheroidal Geometry

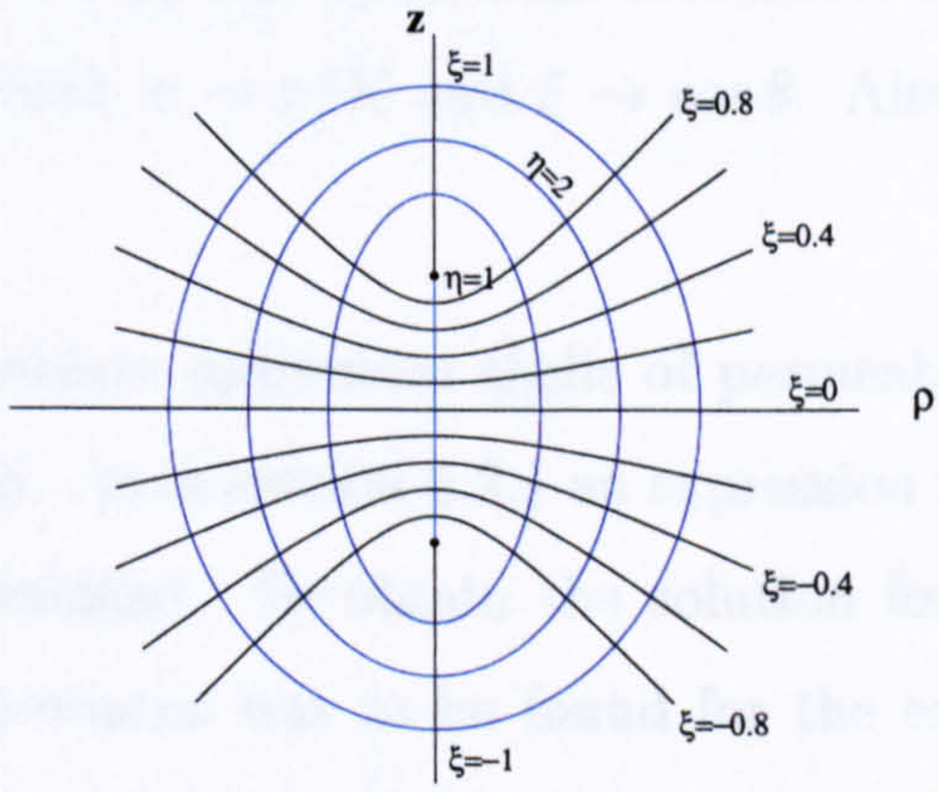

Figure 2.8: Prolate spheroidal coordinates.

To identify a more objective analytical model for the induced magnetic signature of a ship, the previous work involving spherical geometry can be extended to another curvilinear coordinate system and in this section the same analysis is undertaken in prolate spheroidal coordinates. A prolate spheroid is defined as an ellipsoid with semiaxes a, b and c in which c is longer than both a and b and in which a and b are equal. A detailed description of this coordinate system has been reported [33]. Here ξ, η and ζ are used to denote the coordinates where the coordinate η gives one particular prolate spheroidal surface and ζ is equal to the spherical polar coordinate ϕ, when the z axis is chosen to be the axis of symmetry of the spheroid. The coordinate system is diagrammatically illustrated in figure 2.8. It is to be noted that each prolate spheroidal surface is defined by a specific value of the coordinate η and all such surfaces are related by a constant K. For a particular spheroidal surface with semiaxes b_0 and c_0 the value of K is given by the equation $K^2 = c_0^2 - b_0^2$ and the particular value of η for this surface is given by $\eta_0 = c_0/K$. This defines the confocal nature of the prolate spheroidal

surfaces. Surfaces of constant ξ are hyperboloids orthogonal to all the spheroids. In the limit as $K \to 0$, the prolate spheroidal coordinate system reverts to spherical polar coordinates with $\eta \to r/K$ and $\xi \to \cos\theta$. Also as $\eta \to \infty$, $\eta \to r/K$ and $\xi \to \cos\theta$.

Consider a set of prolate spheroidal shells of permeable material placed in a previously uniform field. As in section 2.2.1 an expression for the potential within each region can be identified. To obtain the solution for an arbitrary external field orientation, the potential has to be found for the external field parallel to and perpendicular to the long axis of the prolate spheroid.

For the component of the external field parallel to the long axis, the potential within each region can be written as a product of functions of η and of ξ. As in equation 2.1, for a field uniform at infinity, only one combination survives, giving,

$$\phi_i = [A_i P_1(\eta) + B_i Q_1(\eta)]\,\xi \tag{2.21}$$

Here $P_1(x)$ is the Legendre polynomial defined as,

$$P_1(x) = x \tag{2.22}$$

and $Q_1(x)$ is the Legendre function of the second kind defined by,

$$Q_1(x) = \frac{1}{2}\ln\left(\frac{x+1}{x-1}\right) \tag{2.23}$$

with A_i and B_i being constants which correspond to each region within the problem.

Considering one spheroidal boundary and applying the corresponding boundary conditions at the interface defined by $\eta = \eta_i$ between two adjacent regions i and $i+1$,

$$\phi_i = \phi_{i+1} \tag{2.24}$$

$$\mu_i \frac{\partial \phi_i}{\partial \eta} = \mu_{i+1} \frac{\partial \phi_{i+1}}{\partial \eta} \tag{2.25}$$

A transfer matrix can be defined, in a similar way to the spherical case, relating the constants A_i and B_i within region i to the constants within the adjacent region $i+1$,

$$\begin{bmatrix} A_{i+1} \\ B_{i+1} \end{bmatrix} = T_i^{\parallel} \begin{bmatrix} A_i \\ B_i \end{bmatrix} \tag{2.26}$$

where the matrix $T_i^{\parallel}$ is defined by,

$$T_i^{\parallel} = \left(\frac{\mu_i}{\mu_{i+1}} - 1 \right) \begin{bmatrix} a & b \\ c & d \end{bmatrix} \tag{2.27}$$

$$a = x\eta_i^3 - \eta_i^2 - x\eta_i + \frac{\mu_i}{\mu_i - \mu_{i+1}} \tag{2.28}$$

$$b = x^2\eta_i^3 - 2x\eta_i^2 + \left(1 - x^2\right)\eta_i + x \tag{2.29}$$

$$c = \eta_i - \eta_i^3 \tag{2.30}$$

$$d = -x\eta_i^3 + \eta_i^2 + x\eta_i + \frac{\mu_{i+1}}{\mu_i - \mu_{i+1}} \tag{2.31}$$

$$x = \frac{1}{2} \ln \left(\frac{\eta_i + 1}{\eta_i - 1} \right) \tag{2.32}$$

When the external field is normal to the long axis of the prolate spheroid the potential can be shown to be equal to,

$$\phi_i = \left[C_i P_1^1(\eta) + D_i Q_1^1(\eta) \right] \left(1 - \xi^2\right)^{1/2} \cos\zeta \tag{2.33}$$

where, $P_1^1(x)$ and $Q_1^1(x)$ are the associated Legendre functions of the first and second kind respectively. These are define by,

$$P_1^1(x) = \left(x^2 - 1\right)^{1/2} \tag{2.34}$$

$$Q_1^1(x) = \left(x^2 - 1\right)^{1/2} \left[\frac{1}{2} \ln \left(\frac{x+1}{x-1} \right) - \frac{x}{x^2 - 1} \right] \tag{2.35}$$

The constants C_i and D_i have different values corresponding to the different regions within the problem. In exactly the same way as above, by applying the

boundary conditions 2.24 and 2.25 at the interface, defined by the prolate surface $\eta = \eta_i$, a transfer matrix can be established relating the constants C_i and D_i in the region i to the values of the corresponding quantities in the region $i+1$,

$$\begin{bmatrix} C_{i+1} \\ D_{i+1} \end{bmatrix} = T_i^{\perp} \begin{bmatrix} C_i \\ D_i \end{bmatrix} \tag{2.36}$$

Here the transfer matrix, $T_i^{\perp}$, is defined by,

$$T_i^{\perp} = \frac{1}{2}\left(\frac{\mu_i}{\mu_{i+1}} - 1\right) \begin{bmatrix} a' & b' \\ c' & d' \end{bmatrix} \tag{2.37}$$

$$a' = -x\eta_i^3 + \eta_i^2 + x\eta_i + \frac{2\mu_{i+1}}{\mu_i - \mu_{i+1}} \tag{2.38}$$

$$b' = \frac{1}{(1-\eta_i^2)}\left(x\eta_i^2 - \eta_i - x\right)\left(x\eta_i^3 - \eta_i^2 - x\eta_i + 2\right) \tag{2.39}$$

$$c' = \eta_i^3 - \eta_i \tag{2.40}$$

$$d' = x\eta_i^3 - \eta_i^2 - x\eta_i + \frac{2\mu_i}{\mu_i - \mu_{i+1}} \tag{2.41}$$

$$x = \frac{1}{2}\ln\left(\frac{\eta_i + 1}{\eta_i - 1}\right) \tag{2.42}$$

For each configuration, for a problem with n regions $n-1$ transfer matrices can be generated and the constants within the central region of the system of confocal shells can be related to the constants out with the set of shells. It is to be noted that Legendre functions of the second kind are not defined at the origin, therefore in each configuration the constants B_1 and D_1 within the centre region must be zero unless there is a dipole at the origin. By considering the case as η tends to infinity [33], it can be shown that the constants A_n and C_n are related to the magnitude of the external field strength, parallel to the long axis and normal to the long axis respectively, by,

$$A_n = KH_0^{\parallel} \tag{2.43}$$

$$C_n = KH_0^{\perp} \tag{2.44}$$

where K is the constant defined for the particular set of spheroids.

Once the potential has been determined the field at any point can be calculated from $\mathbf{H} = -\nabla\phi$ which can be expressed in spheroidal prolate coordinates [33].

By the following example cases, the approach to determine the magnetic field around a set of confocal prolate spheroid shells is demonstrated.

Case 1 - Solid Prolate Spheroid of Permeable Material in a Previously Uniform Field

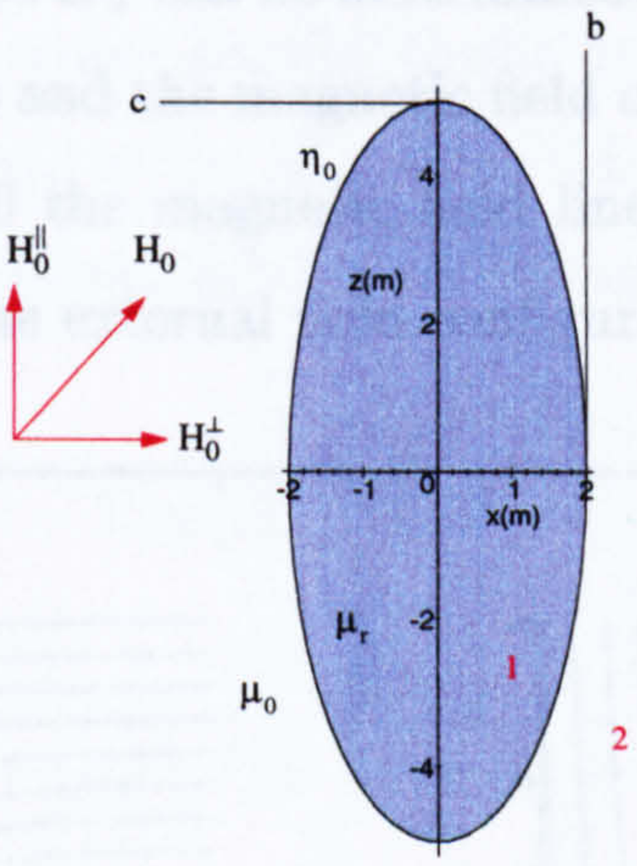

Figure 2.9: Geometry of a solid spheroid of relative permeability μ_r.

In section 2.2.1 case 1 a solid sphere of permeable material in a uniform external field was studied. In prolate spheroidal coordinates the corresponding case is illustrated in figure 2.9. In this diagram a prolate spheroid of relative permeability

μ_r is defined by the prolate surface η_0. In terms of the dimensions of the spheroid, η_0 is given by,

$$\eta_0 = \frac{c}{\sqrt{c^2 - b^2}} \tag{2.45}$$

The spheroid is situated in free space with an external field $\mathbf{H}_0$. The component of the external field parallel to the long axis is $H_0^{\parallel}$ and the component normal to the long axis is $H_0^{\perp}$.

For the interface η_0 the transfer matrices can be generated corresponding to the two external field components. As stated the quantities, B_1 and D_1 within the interior of the spheroid, require to be set to zero and by setting A_2 and C_2 to the values determined from equations 2.43 and 2.44 respectively, the remaining constants, A_1, C_1, B_2 and D_2 can be determined. The potential is now completely determined at all points and the magnetic field can then be obtained at any point in space. In figure 2.10 the magnetic field lines around a prolate spheroid are illustrated for each of the external field configurations.

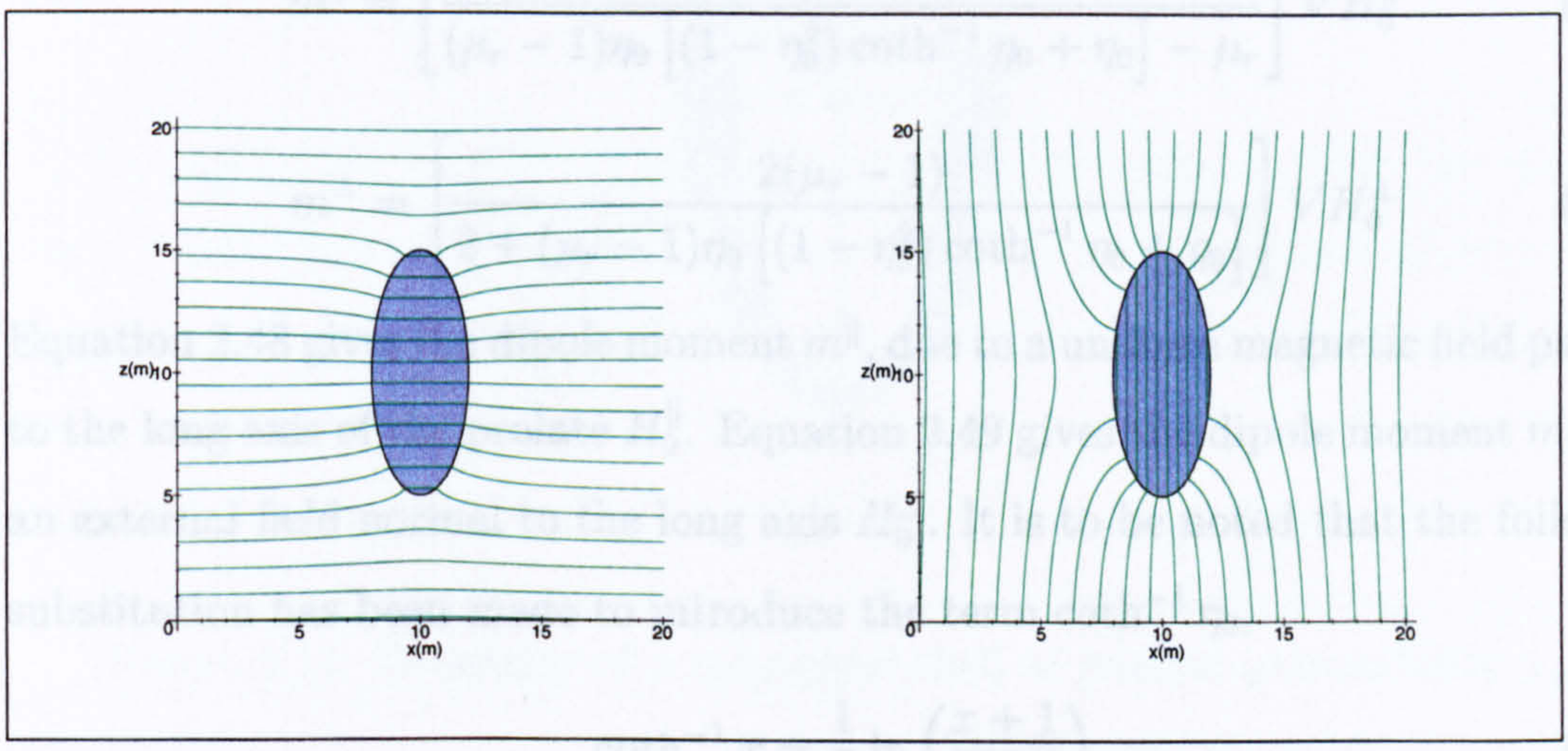

Figure 2.10: Magnetic field lines around a prolate spheroid of permeable material situated in a previously uniform magnetic field perpendicular to the long axis of the prolate (left) and parallel to the long axis (right).

As in the spherical cases, since the magnetic field is uniform within the spheroid, the dipole moment induced on the spheroid can be determine from the volume of the spheroid and the magnetisation as given by equation 2.15. By equating these expressions for the dipole moment to the quantities B_2 and D_2 in the region outside the spheroid, it can be shown that the dipole moment induced on the spheroid is related to B_2 and D_2 by,

$$m^{\parallel} = -\frac{4}{3}\pi K^2 B_2 \tag{2.46}$$

$$m^{\perp} = \frac{8}{3}\pi K^2 D_2 \tag{2.47}$$

Here $m^{\parallel}$ is the dipole moment parallel to the long axis of the spheroid and $m^{\perp}$ is the dipole moment normal to the long axis. Using these expressions the following results for the dipole moment induced on the spheroid can be deduced,

$$m^{\parallel} = \left[\frac{-(\mu_r - 1)}{(\mu_r - 1)\eta_0\left[(1-\eta_0^2)\coth^{-1}\eta_0 + \eta_0\right] - \mu_r}\right] V H_0^{\parallel} \tag{2.48}$$

$$m^{\perp} = \left[\frac{2(\mu_r - 1)}{2 + (\mu_r - 1)\eta_0\left[(1-\eta_0^2)\coth^{-1}\eta_0 + \eta_0\right]}\right] V H_0^{\perp} \tag{2.49}$$

Equation 2.48 gives the dipole moment $m^{\parallel}$, due to a uniform magnetic field parallel to the long axis of the prolate $H_0^{\parallel}$. Equation 2.49 gives the dipole moment $m^{\perp}$, for an external field normal to the long axis $H_0^{\perp}$. It is to be noted that the following substitution has been made to introduce the term $\coth^{-1}\eta_0$,

$$\coth^{-1} x = \frac{1}{2}\ln\left(\frac{x+1}{x-1}\right) \tag{2.50}$$

Case 2 - Prolate Spheroidal Shell of Permeable Material in a Previously Uniform Field

In this case, and with reference to the spherical case with two boundaries, the example of a prolate shell of permeable material, relative permeability μ_r and situated in free space placed in a previously uniform field is studied. The shell, illustrated in figure 2.11, is defined by two confocal prolate spheroids. The outer surface is defined by the semi-axes c_0 and b_0 and the inner surface is defined by c_1 and b_1. It should be stressed that these four quantities are not independent since the spheroids must be confocal, that is $c_0^2 - b_0^2 = K^2 = c_1^2 - b_1^2$. The following terms are also defined, $\eta_0 = c_0/K$ and $\eta_1 = c_1/K$.

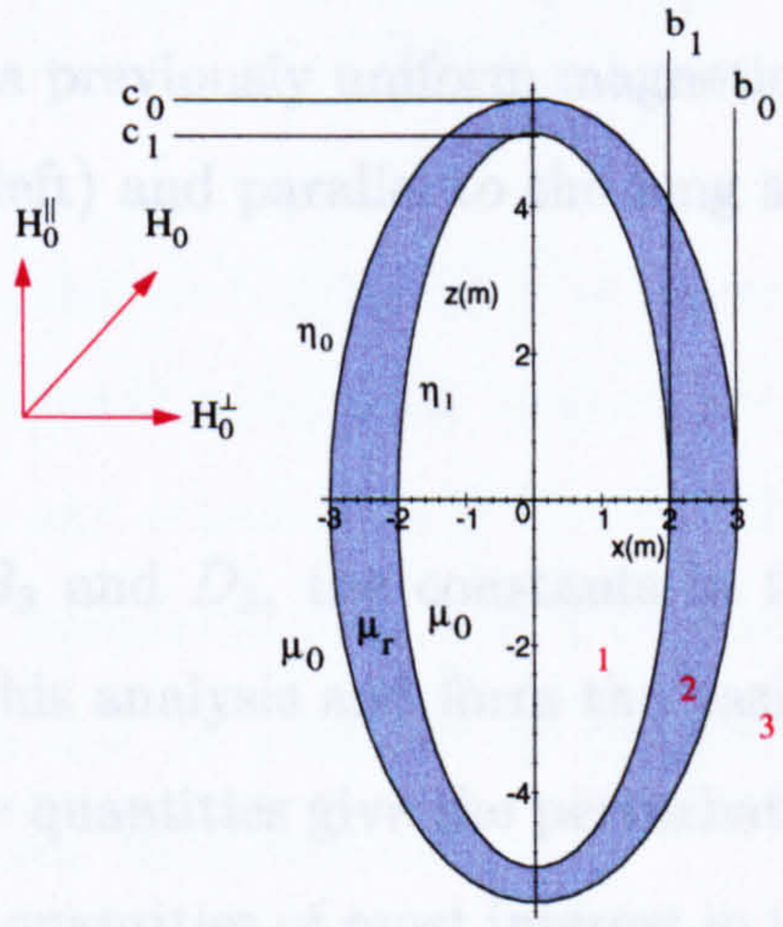

Figure 2.11: Geometry of a spheroidal shell of relative permeability μ_r.

As in case 1 the transfer matrices can be generated, and from these the constants within each region of the problem can be determined. Consequently, the

field can be determined at every point. In figure 2.12 the field lines have been plotted for two orientations of the uniform external field.

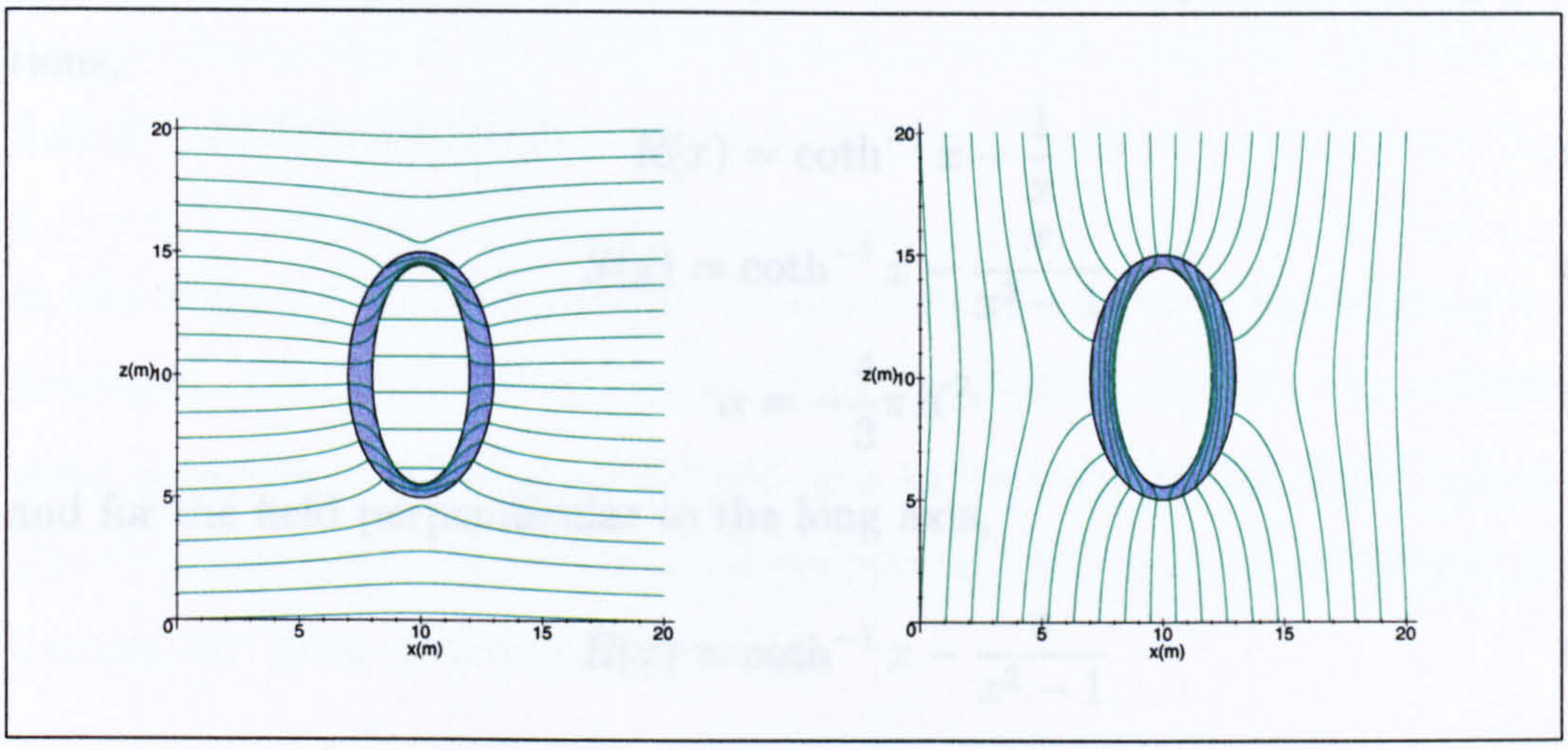

Figure 2.12: Magnetic field lines around a prolate spheroid shell of permeable material situated in a previously uniform magnetic field perpendicular to the long axis of the prolate (left) and parallel to the long axis (right).

The quantities B_3 and D_3, the constants in the region outside the shell are useful results from this analysis and form the basis for the spheroidal ship model in section 2.3. These quantities give the perturbation to the applied uniform field and as such, are the quantities of most interest in terms of calculating the induced magnetic signature of a ship. The following expression gives the dipole moment induced on the shell, with the corresponding substitutions for the particular component of the external field being considered.

$$m^{(\parallel,\perp)} = \frac{\alpha K(\mu_r - 1)\left[\mu_r(S_1 - S_0) - (R_1 - R_0)\right] H_0^{(\parallel,\perp)}}{\mu_r^2 R_0(S_0 - S_1) + \mu_r(R_0R_1 + S_0S_1 - 2R_0S_0) + S_0(R_0 - R_1)} \tag{2.51}$$

For conciseness $R_0 = R(\eta_0)$ and $R_1 = R(\eta_1)$ and similarly $S_0 = S(\eta_0)$ and $S_1 = S(\eta_1)$. The expressions R and S are defined differently, depending on the

component of the dipole moment being calculated. For the component of the external field parallel to the long axis, the corresponding component of the dipole moment can be determined from equation 2.51 by using the following substitutions,

$$R(x) = \coth^{-1} x - \frac{1}{x} \tag{2.52}$$

$$S(x) = \coth^{-1} x - \frac{x}{x^2 - 1} \tag{2.53}$$

$$\alpha = -\frac{4}{3}\pi K^2 \tag{2.54}$$

and for the field perpendicular to the long axis,

$$R(x) = \coth^{-1} x - \frac{x}{x^2 - 1} \tag{2.55}$$

$$S(x) = \coth^{-1} x - \frac{x}{x^2 - 1} + \frac{2}{x(x^2 - 1)} \tag{2.56}$$

$$\alpha = \frac{8}{3}\pi K^2 \tag{2.57}$$

Using the above expressions for R and S in equation 2.51 the dipole moment induced on a shell of permeable material, bounded by two confocal prolate spheroids, can be determine for any orientation of the external field. The quantity α in each case corresponds to equations 2.46 and 2.47 respectively and the values of the constants B_3 and D_3 can be obtained by eliminating the constant α in 2.51 and making the appropriate substitutions.

2.3 A Model for the Induced Magnetic Signature of a Ship

2.3.1 Introduction

In this section a simplified model for the induced magnetic signature of a ship is presented. With reference to section 2.2.2, a model to describe the induced magnetic signature of a ship, represented as a prolate spheroidal shell, is developed. The dimensions are set by the total volume and the mass of permeable material forming the gross structure of the ship.

2.3.2 Spheroidal Ship Model

The outer dimensions of the shell, defined by the prolate spheroidal coordinate η_0 is established by the overall size of the ship. If the ship is enclosed by a cuboid of side lengths $L \times W \times W$ with $L > W$, the dimensions of the spheroid with semiaxes $a(= b)$, b and $c(> a)$, are chosen in the ratio,

$$\frac{c}{b} = \frac{L}{W} \tag{2.58}$$

The volume of a spheroid with semiaxes a, b, c is $\frac{4\pi}{3}abc$. In order that both shapes enclose the same total volume,

$$\frac{4\pi}{3}b^2c = LW^2 \tag{2.59}$$

From these equations the parameters b and c can be determined and from this the outer surface of the spheroid, η_0, obtained,

$$K^2 = c^2 - b^2 \tag{2.60}$$

$$\eta_0 = c/K \tag{2.61}$$

In terms of K and η_0, the volume is $\frac{4\pi}{3}K^3\eta_0(\eta_0^2 - 1)$.

The inner dimensions of the shell, defined by the spheroidal coordinate η_1, is determined by equating the volume of the shell to the total volume of material forming the ship V_s, of relative permeability μ_r, as expressed below,

$$\frac{4\pi}{3}K^3\left[\eta_0\left(\eta_0^2 - 1\right) - \eta_1\left(\eta_1^2 - 1\right)\right] = V_s \tag{2.62}$$

This equation can be solved to give the value of η_1, but in practical cases where $c \gg b$ and η_0 is close to 1, it can be simplified by defining the small quantities, δ_0 and δ_1, by,

$$\delta_0 = \eta_0 - 1 \tag{2.63}$$

$$\delta_1 = \eta_1 - 1 \tag{2.64}$$

and by setting x as the ratio of the total volume of material to the volume contained by the outer shell of the spheroid, as given below,

$$x = V_s / \left[\frac{4\pi}{3}K^3\eta_0\left(\eta_0^2 - 1\right)\right] \tag{2.65}$$

then to a good approximation η_1, defined through δ_1, is given by,

$$\delta_1 = (1 - x)\,\delta_0 \tag{2.66}$$

With the dimensions of the prolate spheroidal shell established the magnetic field can be determined at any position from the work present in section 2.2.2.

2.3.3 Results and Discussion

To give an example of the application of the spheroidal ship model, a ship with a length of 50 m and a beam of 10 m is considered, these values define the parameters L and W respectively in equations 2.58 and 2.59. The volume of the material, V_s, is taken as 24.8 m^3 and the relative permeability of the material is taken to be 500. These same values are used in the finite element case study of the ship structure described in section 5.7.

With these parameters the corresponding spheroidal representation of the ship has,

$$\eta_0 = 1.020621 \tag{2.67}$$

$$\eta_1 = 1.020518 \tag{2.68}$$

From the above values for η_0 and η_1 and from equation 2.51, with the appropriate substitutions, the plots shown in figure 2.13 were determined. In both plots the direction of the external field θ, relative to the spheroid, is varied from $\theta = 0$, corresponding to the field direction normal to the long axis, to $\theta = \pi/2$ corresponding the field directed along the long axis. The magnitude of the external field is held constant at 20000 nT. In the upper plot of figure 2.13 the magnitude of the dipole moment induced on the spheroid is plotted against θ. In the lower plot the angle α, as defined in figure 2.13, indicate the direction of the induced dipole moment and is plotted against θ.

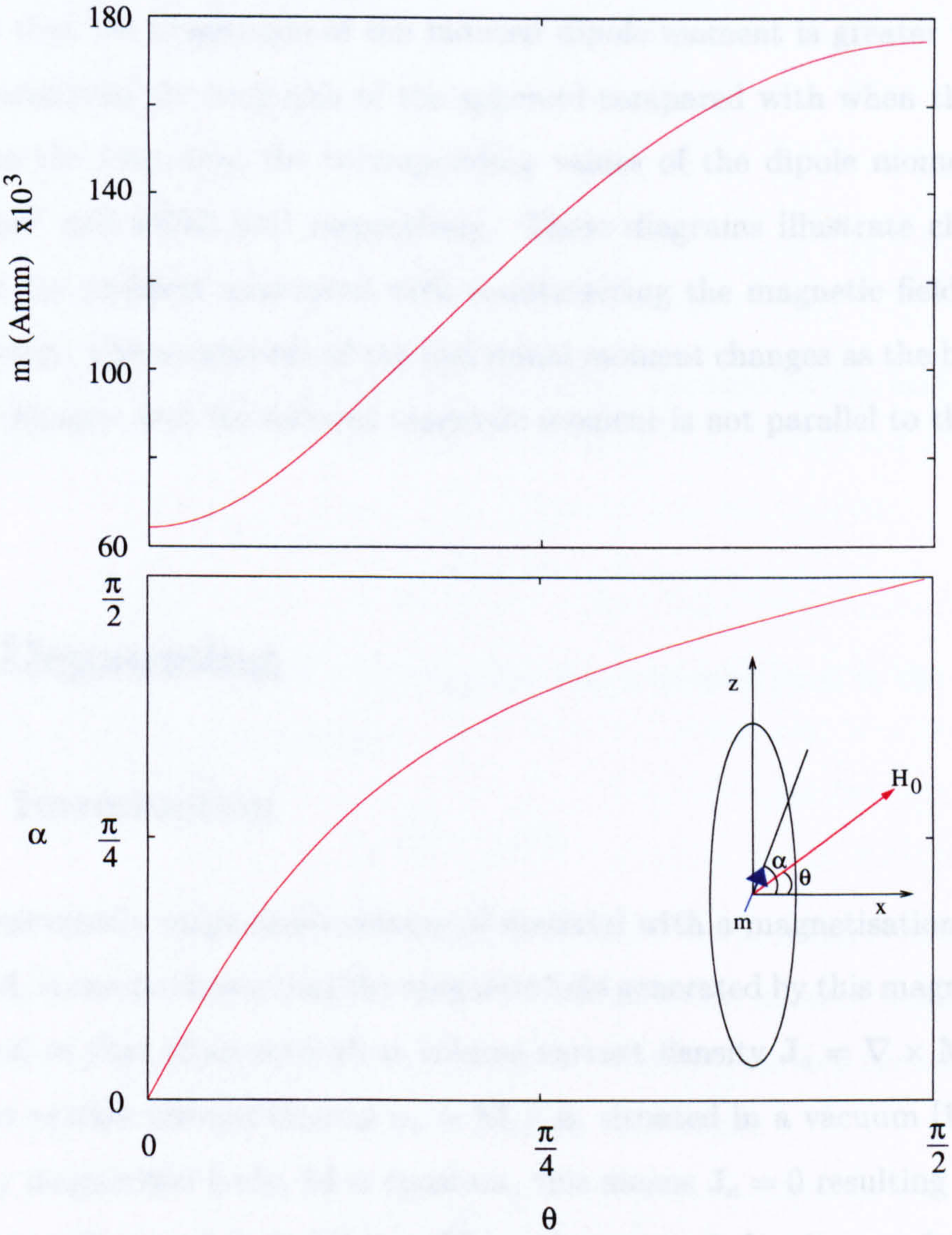

Figure 2.13: Results obtained from the application of the spheroidal ship model. m plotted against θ (upper). α plotted against θ (lower).

From figure 2.13 it can be seen that there is a pronounced dependence of both the magnitude and direction of the induced dipole moment on the direction of the external field. With reference to the upper plot of figure 2.13, it is to be noted that the magnitude of the induced dipole moment is greater when the field is parallel to the long axis of the spheroid compared with when the field is normal to the long axis, the corresponding values of the dipole moment being 174600 Am^2 and 64300 Am^2 respectively. These diagrams illustrate clearly the nature of the problem associated with counteracting the magnetic field induced in a real ship. The magnitude of the individual moment changes as the bearing of the ship changes, and the induced magnetic moment is not parallel to the earth's field.

2.4 Degaussing

2.4.1 Introduction

For a permanently magnetised volume of material with a magnetisation per unit volume M, it can be shown that the magnetic field generated by this magnetisation is identical to that of an equivalent volume current density $\mathbf{J}_e = \nabla \times \mathbf{M}$ and an equivalent surface current density $\alpha_e = \mathbf{M} \times \hat{\mathbf{n}}$, situated in a vacuum [10]. For a uniformly magnetised body, M is constant, this means $\mathbf{J}_e = 0$ resulting in only a equivalent surface current density α_e. If a surface current density equal to α_e, but in the opposite sense, is applied to the surface of the body there will be a complete cancellation of the fields. This means for an object with a uniform permanent magnetisation, by applying a suitable current over the surface of the body it is possible to eliminate entirely the magnetic field generated by the magnetisation. If there are cavities inside the material, the surface of the cavity must also have

an applied current density.

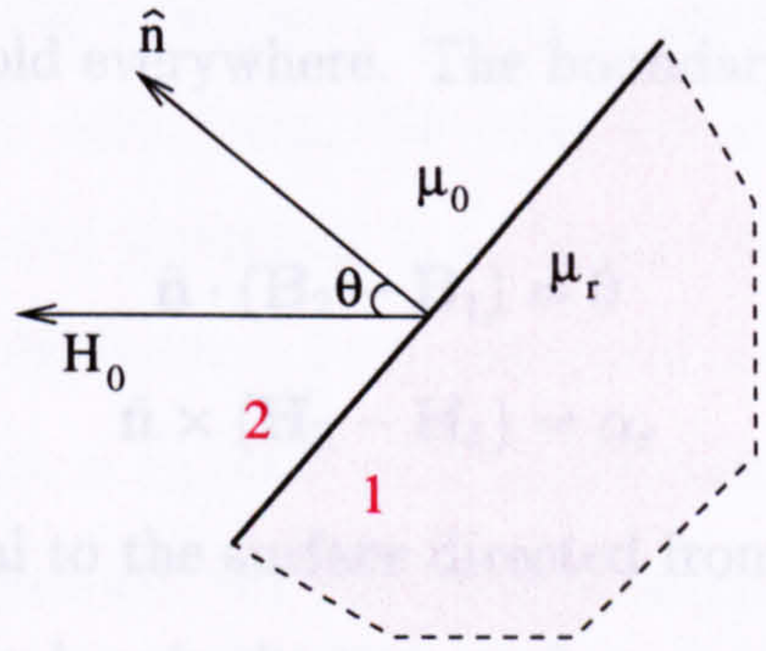

Figure 2.14: Interface between region 1, of relative permeability μ_r and region 2, free space.

For soft magnetic material, the magnetisation is proportional to the magnetic field strength within the material,

$$\mathbf{M} = \chi_m \mathbf{H} \tag{2.69}$$

where $\chi_m = \mu_r - 1$ is the magnetic susceptibility. Here the problem is to cancel any perturbation to the external field that is created due to the induced magnetisation of the material. In this case it can be demonstrated that a surface current density, of the form given in equation 2.70, will produce this result.

$$\alpha = \hat{\mathbf{n}} \times \mathbf{H_0} \left(1 - \frac{1}{\mu_r}\right) \tag{2.70}$$

Where, as illustrated in figure 2.14, $\hat{\mathbf{n}}$ is the unit vector normal to the surface of the body, $\mathbf{H_0}$ is the external field strength and μ_r is the relative permeability of the material. This result can be verified by considering the boundary conditions at the surface of the material, and by noting that for the complete degaussing of the body the magnetic field at any point must be equal to the magnetic field that

would be experienced at that point in the absence of the body. This means that the magnetic field must be equal to the external magnetic field at every point, that is $\mathbf{B} = \mu_0 \mathbf{H}_0$ must hold everywhere. The boundary conditions that apply to $\mathbf{B}$ and $\mathbf{H}$ are,

$$\hat{\mathbf{n}} \cdot (\mathbf{B}_2 - \mathbf{B}_1) = 0 \tag{2.71}$$

$$\hat{\mathbf{n}} \times (\mathbf{H}_2 - \mathbf{H}_1) = \alpha_s \tag{2.72}$$

where $\hat{\mathbf{n}}$ is the unit normal to the surface directed from region 1 into region 2, as illustrated in figure 2.14 and α_s is the true surface current at the interface. For a constant $\mathbf{B}$ throughout, condition 2.71 is satisfied. In region 1 $\mathbf{H}_1 = \mathbf{H}_0/\mu_r$ and in region 2 $\mathbf{H}_2 = \mathbf{H}_0$ and condition 2.72, therefore, is only satisfied if a surface current density as given by equation 2.70 is specified at the interface.

In principle, therefore, it is possible to remove completely the magnetic signature arising from the induced magnetisation. In real terms, however, it is not practical to cover all the surfaces of a ship with the appropriate windings to give the surface currents descibed by equation 2.70. Typical degaussing systems consist only of a small number of coils distributed throughout a ship, but they should approximate to the theoretical optimal distribution.

2.4.2 Modelling Degaussing Coil Systems

An important aspect of studying degaussing coils is to determine the magnetic field at any position from an arbitrary shaped coil. A method to achieve this, based on previously reported work [20], is described in this section.

The magnetic field at a point P, in the neighbourhood of an electric circuit, C, carrying a steady current I is given by the Biot-Savart law [10],

$$\mathbf{B} = \frac{\mu_0 I}{4\pi} \oint_C \frac{\mathbf{dl}' \times \hat{\mathbf{r}}}{r^2} \tag{2.73}$$

where the element $\mathbf{dl}'$ of circuit C is at P' and the vector $\hat{\mathbf{r}}$ points from P' to P.

Using this expression the magnetic field of a system of degaussing coils can be determined. Instead of performing the integration explicitly to calculate the magnetic field, a more useful approach is to break the coil down into a number of straight line segments. In figure 2.15 a section of a coil is illustrated. The coil has been broken down into a number of straight line segements, L_1L_2, L_2L_3,.., L_iL_{i+1},.., L_nL_1. An expression for the magnetic field generated by each line segment can be determined.

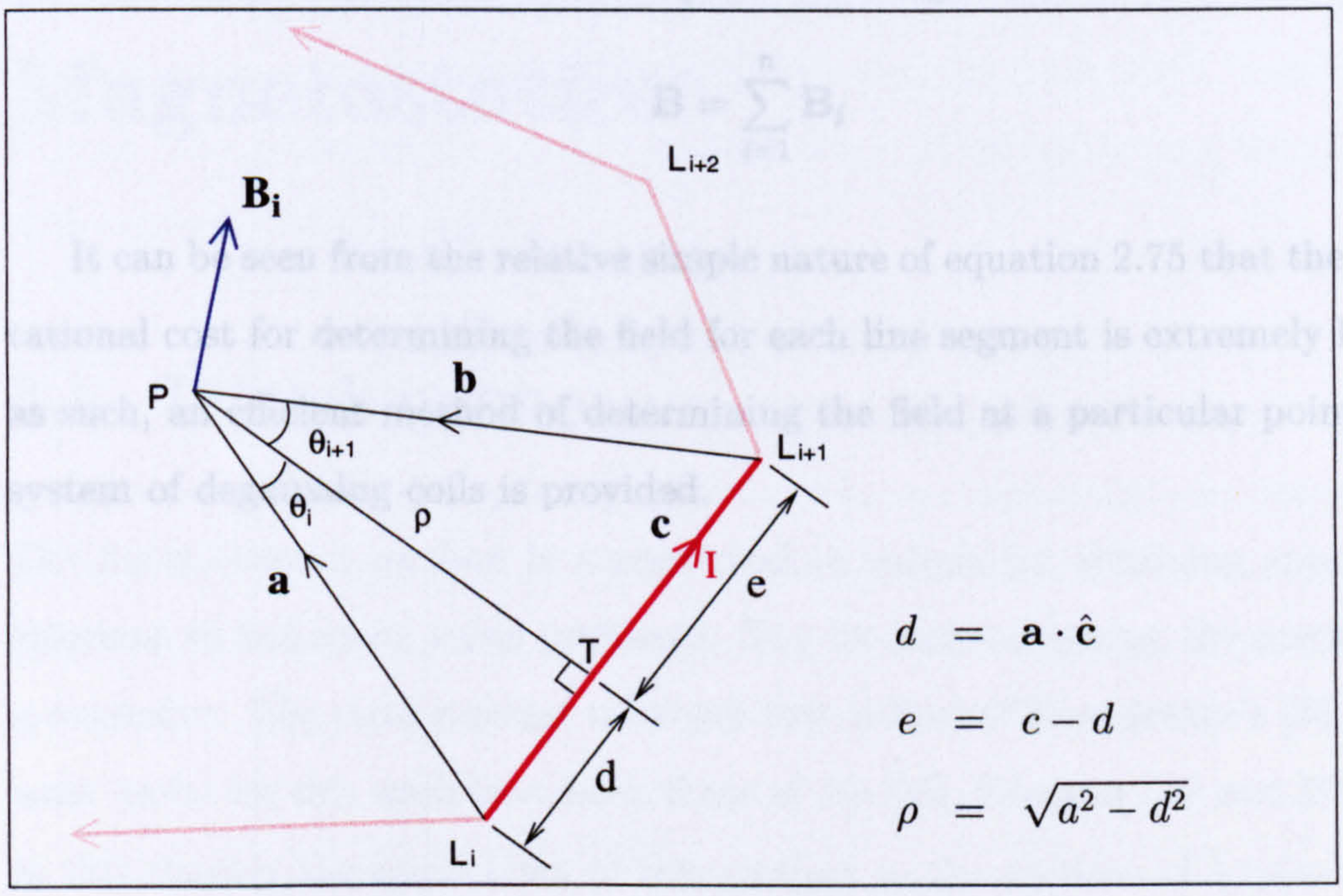

Figure 2.15: Current filament L_iL_{i+1} carrying a current I.

The magnetic flux density $\mathbf{B}_i$, for the straight line segment L_iL_{i+1}, carrying a current I can be calculated at the point P from integrating equation 2.73 over

the length of the line segment. The results is,

$$|\mathbf{B_i}| = \frac{\mu_0 I}{4\pi\rho}(\sin\theta_i + \sin\theta_{i+1}) \tag{2.74}$$

$$= \frac{\mu_0 I}{4\pi\rho}\left(\frac{d}{a} + \frac{e}{b}\right) \tag{2.75}$$

where the direction of $\mathbf{B_i}$ is normal to the plane PL_iL_{i+1}, and is given by,

$$\mathbf{B_i} = |\mathbf{B_i}|\,\hat{\mathbf{a}} \times \hat{\mathbf{b}} \tag{2.76}$$

The magnetic field from the complete coil can then be determined by summing the contributions from each of the separate line segments.

$$\mathbf{B} = \sum_{i=1}^{n} \mathbf{B_i} \tag{2.77}$$

It can be seen from the relative simple nature of equation 2.75 that the computational cost for determining the field for each line segment is extremely low, and as such, an efficient method of determining the field at a particular point from a system of degaussing coils is provided.

Chapter 3

Finite Elements in Magnetostatics

3.1 Introduction

The finite element method is a numerical technique for obtaining approximate solutions to boundary value problems. The literature covering the methodology is extensive. The most popular reference text is that of Zienkiewicz's [34] but the most useful for this work have been those of Jin [35], Silvester [36] and Binns [20]. In this chapter the application of this method to the solution of Laplace's equation, with suitable boundary conditions, to determine the total scalar potential is presented in two dimensions. The extension of this to the three dimensional case is subsequently discussed.

With the aim of applying this technique to the study of the induced magnetic signature of ships, the criteria for modelling the thin iron regions of the hull is presented in section 3.3 and an approach of including the effects of large

current circuits, appropriate for the modelling of degaussing coils, is described in section 3.4.

3.2 The Finite Element Method

The finite element method can be formulated from two different approaches, the Ritz finite element method and Galerkin's method. The Ritz finite element method is a variational method in which the boundary value problem is formulated in terms of a variational expression, or energy functional, whose minimum corresponds to the governing differential equation under the given boundary conditions. The approximate solution is then obtained by minimising the functional with respect to its variables.

The second method, Galerkin's method, belonging to the family of weighted residual methods, is considered to be the corner stone of the finite element method, as this approach can be applied to problems where a variational expression cannot be obtained. In magnetostatics, where a variational expression can be found, both methods lead to exactly the same numerical model. In this work the variational approach is used.

Firstly the boundary value problem for which a solution requires to be obtained is defined. In two dimensional magnetostatic problems the governing equation is,

$$\frac{\partial}{\partial x}\left(\mu_r \frac{\partial \phi}{\partial x}\right) + \frac{\partial}{\partial y}\left(\mu_r \frac{\partial \phi}{\partial y}\right) = 0 \qquad (x, y) \in \Omega \tag{3.1}$$

where ϕ is the total scalar potential and μ_r is the relative permeability of any material present. The boundary conditions to be considered are given by,

$$\phi = p \quad \text{on} \quad \Gamma_1 \tag{3.2}$$

$$\left(\frac{\partial \phi}{\partial x}\hat{\mathbf{x}} + \frac{\partial \phi}{\partial y}\hat{\mathbf{y}}\right) \cdot \hat{\mathbf{n}} = 0 \quad \text{on} \quad \Gamma_2 \tag{3.3}$$

where Γ ($= \Gamma_1 + \Gamma_2$) denotes the contour or boundary enclosing the problem area Ω, $\hat{\mathbf{n}}$ is its outward normal unit vector and p is the known potential on Γ_2. Equation 3.2 is known as the Dirichlet boundary condition and equation 3.3 is known as the homogeneous Neumann condition.

If there are discontinuites in μ_r within the domain Ω, then ϕ must satisfy the continuity conditions,

$$\phi^+ = \phi^- \quad \text{on} \quad \Gamma_d \tag{3.4}$$

and,

$$\mu_r^+ \left(\frac{\partial \phi^+}{\partial x}\hat{\mathbf{x}} + \frac{\partial \phi^+}{\partial y}\hat{\mathbf{y}}\right) \cdot \hat{\mathbf{n}} = \mu_r^- \left(\frac{\partial \phi^-}{\partial x}\hat{\mathbf{x}} + \frac{\partial \phi^-}{\partial y}\hat{\mathbf{y}}\right) \cdot \hat{\mathbf{n}} \quad \text{on} \quad \Gamma_d \tag{3.5}$$

where Γ_d denotes the discontinuity interface, the superscript "+" (or "-") indicates that its associated quantities are on the "+" (or "-") side of Γ_d, and $\hat{\mathbf{n}}$ denotes the unit normal vector to Γ_d.

The variational problem equivalent to this boundary value problem is given by,

$$\begin{cases} \delta F(\phi) = 0 & \\ \phi = p & \text{on } \Gamma_1 \end{cases} \tag{3.6}$$

where the functional $F(\phi)$ is given by,

$$F(\phi) = \frac{1}{2}\int_\Omega \mu_r \left[\left(\frac{\partial \phi}{\partial x}\right)^2 + \left(\frac{\partial \phi}{\partial y}\right)^2\right] d\Omega \tag{3.7}$$

By considering the first variation of $F(\phi)$ with respect to ϕ, it can be shown that 3.6 is the variational expression corresponding to equation 3.1 and the associated boundary conditions, 3.2 and 3.3, and the continuity condition 3.5 [35]. The condition 3.4 should be included in 3.6, however condition 3.4 is satisfied a priori by the finite expansion of ϕ and no measure is required to enforce it.

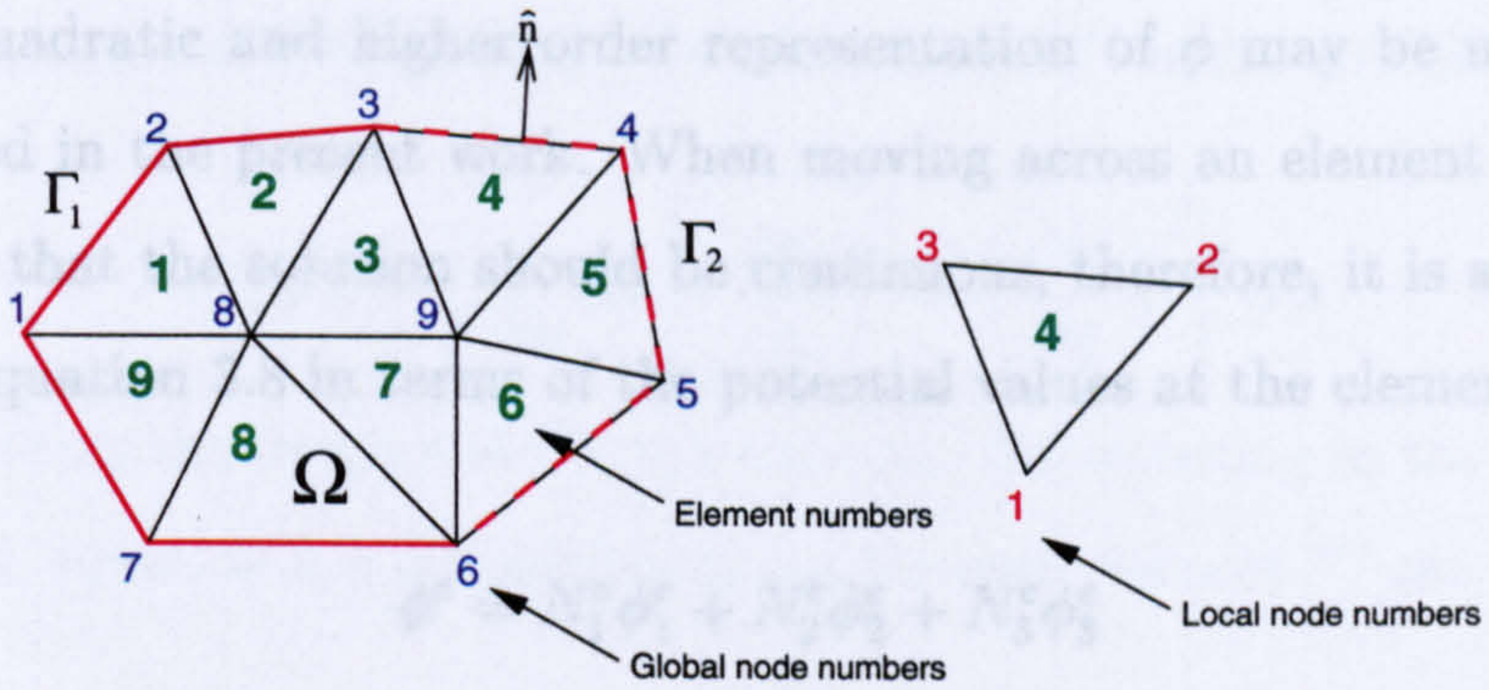

Figure 3.1: Finite element problem space, Ω, discretised into triangular finite elements.

The initial step in any finite element process is to divide the entire problem space Ω, into small subdomains. The subdomains form the required finite elements, with the entire set of the elements forming the finite element mesh. In figure 3.1 the entire domain of a problem space Ω is discretised into triangular finite elements. A vertex of an element is known as a mesh node and each node within the mesh is given a unique number or global node number. As a result each element is defined in terms of three of these global node numbers. For each element a local node numbering scheme is also defined as shown for element 4 in figure 3.1. The procedures used to generate this discretisation are discussed in chapter 4.

The next stage of the analysis is to assume that the potential ϕ obeys a simple relationship within each element. For linear triangular elements, ϕ within each element is approximated by the linear form,

$$\phi^e = a^e + b^e x + c^e y \tag{3.8}$$

where a^e, b^e and c^e are constant coefficients to be determined and e is the element

number. Quadratic and higher order representation of ϕ may be used, but are not employed in the present work. When moving across an element boundary it is necessary that the solution should be continuous, therefore, it is advantageous to express equation 3.8 in terms of the potential values at the element nodes, ϕ_1^e, ϕ_2^e and ϕ_3^e,

$$\phi^e = N_1^e\phi_1^e + N_2^e\phi_2^e + N_3^e\phi_3^e \tag{3.9}$$

where N_j^e are the interpolation or shape functions given by,

$$N_j^e(x,y) = \frac{1}{2\triangle^e}(a_j^e + b_j^e x + c_j^e y) \qquad j = 1,2,3 \tag{3.10}$$

in which the area of the triangle is denoted by $\triangle^e$. Here a_j^e, b_j^e and c_j^e are constants depending only on the node coordinates of the element,

$$\begin{aligned} a_1^e &= x_2^e y_3^e - y_2^e x_3^e \quad & b_1^e &= y_2^e - y_3^e \quad & c_1^e &= x_3^e - x_2^e \\ a_2^e &= x_3^e y_1^e - y_3^e x_1^e \quad & b_2^e &= y_3^e - y_1^e \quad & c_2^e &= x_1^e - x_3^e \\ a_3^e &= x_1^e y_2^e - y_1^e x_2^e \quad & b_3^e &= y_1^e - y_2^e \quad & c_3^e &= x_2^e - x_1^e \end{aligned} \tag{3.11}$$

The potential at node 1, ϕ_1^e is normally thought of as being the same in all the elements sharing node 1. However, for reasons that will emerge later, we wish to reserve the possibility that the same node may have an element defined discontinuity associated with it. In the magnetostatic context, the functional $F(\phi)$ defined in equation 3.7 corresponds to the static magnetic energy in the domain Ω. The aim now is to find the values of the potentials ϕ_i^e which minimise this energy.

Once the problem domain has been discretised and having defined how the potential should vary over each of the individual elements, the system of equations can be formulated. This is achieved by considering the minimisation of the functional, with respect to each element. The functional F can be written as,

$$F = \sum_{e=1}^{M} F^e(\phi^e) \tag{3.12}$$

where M denotes the total number of elements and F^e is the subfunctional given by,

$$F^e(\phi^e) = \frac{1}{2}\int_{\Omega^e} \mu_r \left[\left(\frac{\partial \phi^e}{\partial x}\right)^2 + \left(\frac{\partial \phi^e}{\partial y}\right)^2\right] d\Omega \tag{3.13}$$

with Ω^e denoting the domain of the eth element. Substituting in the equation for the potential, equation 3.9, the subfunctional for each element F^e can be expressed as,

$$F^e = \frac{1}{2}\int_{\Omega^e} \mu_r \left[\left(\sum_{i=1}^{3} \frac{\partial N_i^e}{\partial x}\phi_i^e\right)^2 + \left(\sum_{i=1}^{3} \frac{\partial N_i^e}{\partial y}\phi_i^e\right)^2\right] d\Omega \tag{3.14}$$

Differentiating equation 3.14 with respect to the node potential ϕ_i^e, gives,

$$\frac{\partial F^e}{\partial \phi_i^e} = \sum_{j=1}^{3} \phi_j^e \int_{\Omega^e} \mu_r \left[\frac{\partial N_i^e}{\partial x}\frac{\partial N_j^e}{\partial x} + \frac{\partial N_i^e}{\partial y}\frac{\partial N_j^e}{\partial y}\right] d\Omega \qquad i = 1,2,3 \tag{3.15}$$

For each element, therefore, local contributions can be obtained,

$$\left\{\frac{\partial F^e}{\partial \phi_i^e}\right\} = \mathbf{K}^e \{\phi_i^e\} \qquad i = 1,2,3 \tag{3.16}$$

where the entries in the local element matrix $\mathbf{K}^e$ are given by,

$$K_{ij}^e = \int_{\Omega^e} \mu_r \left[\frac{\partial N_i^e}{\partial x}\frac{\partial N_j^e}{\partial x} + \frac{\partial N_i^e}{\partial y}\frac{\partial N_j^e}{\partial y}\right] d\Omega \qquad i,j = 1,2,3 \tag{3.17}$$

Assuming that μ_r is constant within each element and equal to μ_r^e, this integral can be evaluated analytically to give,

$$K_{ij}^e = \frac{\mu_r^e}{4\triangle^e}\left(b_i^e b_j^e + c_i^e c_j^e\right) \qquad i,j = 1,2,3 \tag{3.18}$$

Using the global node numbering system to merge the local contributions for elements with shared nodes, and equating to zero, the finite element system of equations is formed,

$$\mathbf{K}'\Phi' = \mathbf{0} \tag{3.19}$$

The global matrix $\mathbf{K}'$ is generated from all the individual local matrices $\mathbf{K}^e$.

Finally the boundary conditions are imposed to obtain the final form of the system of equations. Of the boundary conditions considered, the homogeneous Neumann condition 3.3 and the continuity condition 3.5 are satisfied implicitly [35]. These are referred to as natural conditions. The Dirichlet boundary condition 3.2 and the condition 3.4, however, must be imposed explicitly on to the system of equations. These are referred to as essential conditions. Condition 3.4 is satisfied inherently by the finite element formulation but the Dirichlet condition must be enforced [35]. One of the outcomes of this process is to generate a non zero vector on the right hand side of the system of equations, to give,

$$\mathbf{K}\Phi = \mathbf{b} \tag{3.20}$$

The system of equations, described by equation 3.20, can be solved for the potential at each of the node points. The technique used to obtain the solution is discussed in section 3.6.

The three dimensional problem can be approached in a similar way. Here, tetrahedral elements are used and the potential approximated over the volume of each element by,

$$\phi^e = a^e + b^e x + c^e y + d^e z \tag{3.21}$$

The same variational argument remains and the local matrix obtained. Apart from the obvious increase in complexity arising from the increase in the number of dimensions, essentially no new problems arise.

In this section the finite element method has been formulated in terms of the total scalar potential. The finite element method, however, could be equally well developed using either the reduced scalar potential or the vector potential. The vector potential, however, is not commonly used for magnetostatic problems because the three vector components require to be considered at each of the mesh nodes, resulting in a problem effectively three times as large as an equivalent

problem formulated using a scalar potential. Although the reduced scalar potential permits the specification of currents within the problem domain, the total scalar potential has been used in this work, with current circuit represented by the potential discontinuity method outlined in section 3.4. This approach has the advantage that numerical problems arising from the use of the reduced scalar potential in regions of high permeability are eliminated [37]. It is to be noted that finite element problems can be formulated in terms of both the reduced and total scalar problems. This approach means section of the domain containing currents can be described using the reduced scalar potential with regions of the domain containing material with a high permeability described by the total scalar potential. This two potential approach is described in references [20] [36].

3.3 Modelling Thin Regions of High Permeability

A main aim of this work is to study the magnetisation effects in ships. However, two length scales present: The length of the vessel and the thickness of the hull. The overall size of a ship requires the use of a mesh with specification that extends several hundred meters from the ship. The implication of this is that mesh elements, with side lengths of several meters are required. However, typical hull thicknesses are in the range of about one to two centimeters and if the same basic tetrahedral elements were used to model hull thicknesses, elements with a side length in the order of millimeters would be required. Appropriate to this work, the large difference in length scales can be overcome by introducing surface elements to represent the properties of the thin regions, thereby eliminating the need to generate specific mesh elements within these volumes. The development

of these surface elements follows the work presented in reference [28].

The normal component of the magnetic field within the thin regions is very small and it is this property that allows the use of surface elements. From the continuity condition on the normal component of **B** at the surface of a metal plate, it follows that the normal component of **H** inside the metal is $1/\mu_r$ times the normal component of **H** immediately outside the plate. Therefore, the gradient of ϕ across the plate is very small, consequently ϕ is essentially the same at points just through the plate and directly across from each other. For tangential components, the continuity condition for **H** applies, so that the gradient of ϕ immediately inside the plate is the same as the gradient just outside the plate. If it is assumed that the normal component of the magnetic field within a thin region is zero, it can be stated that the potential on the opposite sides of the thin region will be equal. This allows the properties of this volume to be expressed as a surface which can be modelled by triangular surface elements.

It was demonstrated in section 3.2 how each element generates a local matrix, to be combined with all the other local matrices to give a global set of equations. In this section the local matrix that is generated by the surface elements described above is now considered.

The triangular surface elements used in this work are defined by the following quantities: The geometry of the element defined by 3 nodes; a thickness parameter t to describe the thickness of the iron plate, which the element is representing; a relative permeability value. These surface elements have an arbitrary orientation within the finite element mesh, and it is useful to work with a local coordinate system, $\hat{\mathbf{x}}'$,$\hat{\mathbf{y}}'$, $\hat{\mathbf{z}}'$, as illustrated in figure 3.2, where $\hat{\mathbf{x}}'$ and $\hat{\mathbf{y}}'$ lie in the plane defined by the element and $\hat{\mathbf{z}}'$ is a normal to the element.

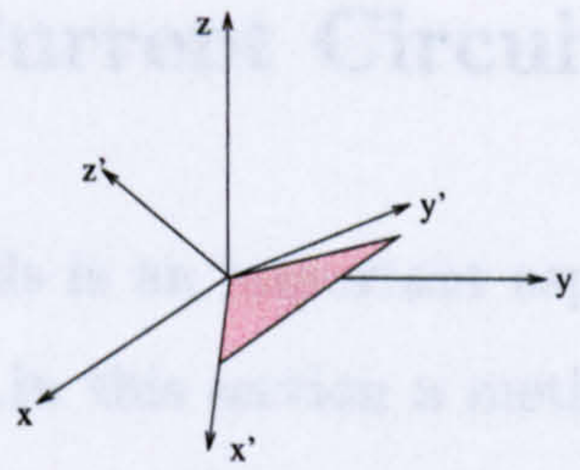

Figure 3.2: Local coordinate system,$\hat{\mathbf{x}}'$,$\hat{\mathbf{y}}'$ and $\hat{\mathbf{z}}'$ of a triangular surface element.

Using this local coordinate system the potential over these elements is defined by the function,

$$\phi_e = a^e + b^e x' + c^e y' \tag{3.22}$$

This is equivalent to the two dimensional triangular element in section 3.2 and the same analysis can be performed. In this case, however, the functional of the element is given by,

$$F^e = \frac{1}{2}\int_{\Omega^e} \mu_r \left[\left(\sum_{i=1}^{3} \frac{\partial N_i^e}{\partial x'} \phi_i^e \right)^2 + \left(\sum_{i=1}^{3} \frac{\partial N_i^e}{\partial y'} \phi_i^e \right)^2 \right] t \, dA \tag{3.23}$$

where the thickness parameter t has now been included. The entries in the local matrix corresponding to a triangular surface element are given by,

$$K_{ij}^e = \frac{\mu_r^e t}{4\triangle^e} \left(b_i^e b_j^e + c_i^e c_j^e \right) \qquad i,j = 1,2,3 \tag{3.24}$$

where b_i^e and c_i^e are defined as in equations 3.11 but calculated using the local coordinate system. By comparing the local number scheme, to the global number scheme the entries of this local matrix are entered into the global matrix in the same way as the normal space filling tetrahedral elements.

3.4 Modelling Current Circuits

The effects of degaussing coils is an important aspect in modelling the induced magnetic signature of a ship.In this section a method of including the magnetic properties of these coils, within the finite element analysis, is described.

Any current circuit, carrying a current I, of arbitrary size and configuration can be resolved into a system of elementary currents as illustrated in figure 3.3, where S is a surface spanning the current contour C. The surface S can be divided into a mesh of small elementary current loops each carrying current I. The field due to this network of elementary currents is identical to that of the single current loop C. As the mesh of current loops becomes finer, the field of each of the elementary current loops approaches that of a dipole whose axis is orientated in the direction of the positive normal to the loop $\hat{\mathbf{n}}$. In the limit, the current I around the contour C is numerically equal to the dipole density on the surface S.

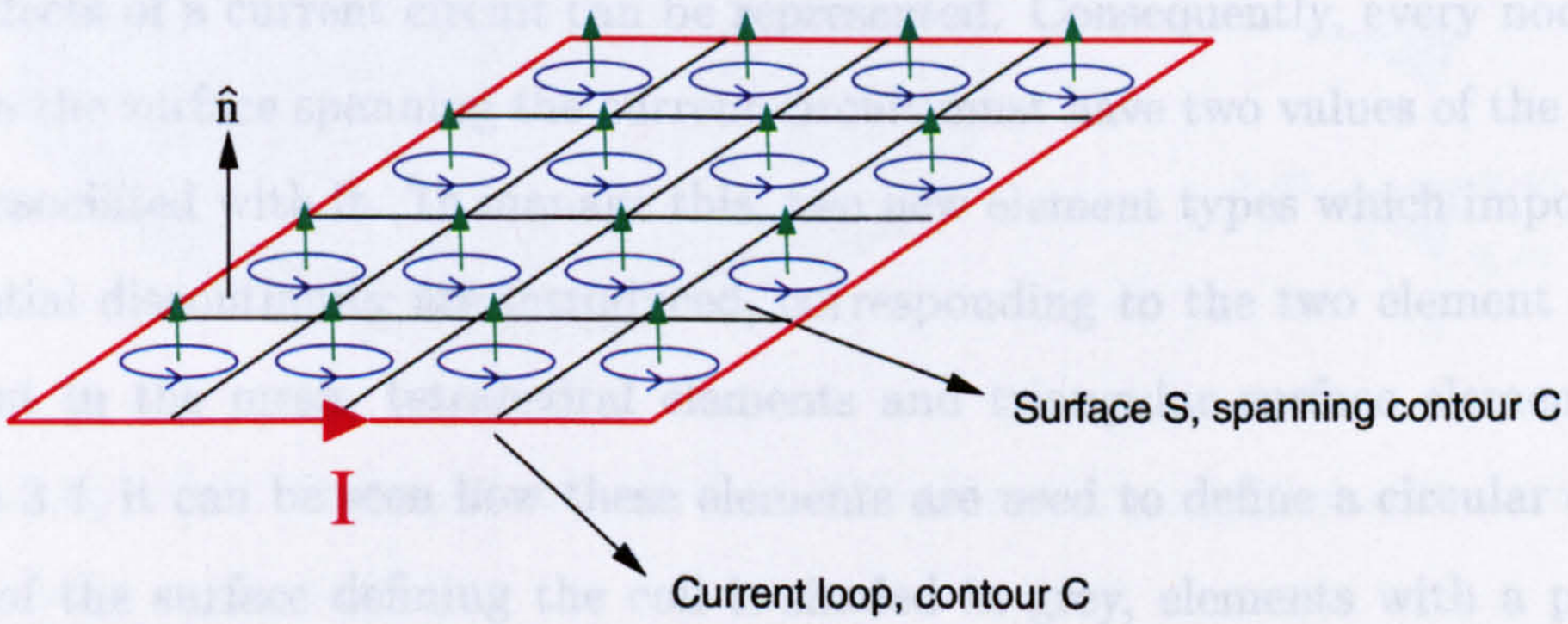

Figure 3.3: A current circuit, defined by contour C, divided into a mesh of elementary current loops over a surface S.

It can be shown [21] that the total scalar potential of such a dipole layer is given by,

$$\phi(x, y, z) = -I\Omega \tag{3.25}$$

where Ω is the solid angle from (x, y, z) subtended by the surface S. Moreover, it can be shown that this potential is multivalued with a discontinuity in ϕ on crossing S equal to the current I,

$$\phi_+ - \phi_- = I \tag{3.26}$$

where ϕ_+ and ϕ_- are the scalar potential on each side of the surface.

It is to be noted that this is relevant for any continuous surface bounded by C. Different surfaces will have the discontinuity in ϕ at different places in space. However, for any two different surfaces at any point the gradient of ϕ, that is the magnetic field, will be the same. Consequently it is permissible to choose the position of the surface S in the mesh, constrained only by the contour C.

By forcing the potential discontinuity, given by equation 3.26, within the mesh, the effects of a current circuit can be represented. Consequently, every node that lies on the surface spanning the current circuit must have two values of the potential associated with it. To manage this, two new element types which impose this potential discontinuity are introduced, corresponding to the two element shapes present in the mesh, tetrahedral elements and triangular surface elements. In figure 3.4, it can be seen how these elements are used to define a circular coil. A part of the surface defining the coil is shaded in grey, elements with a positive offset are shaded green and elements with a negative offset are shaded blue.

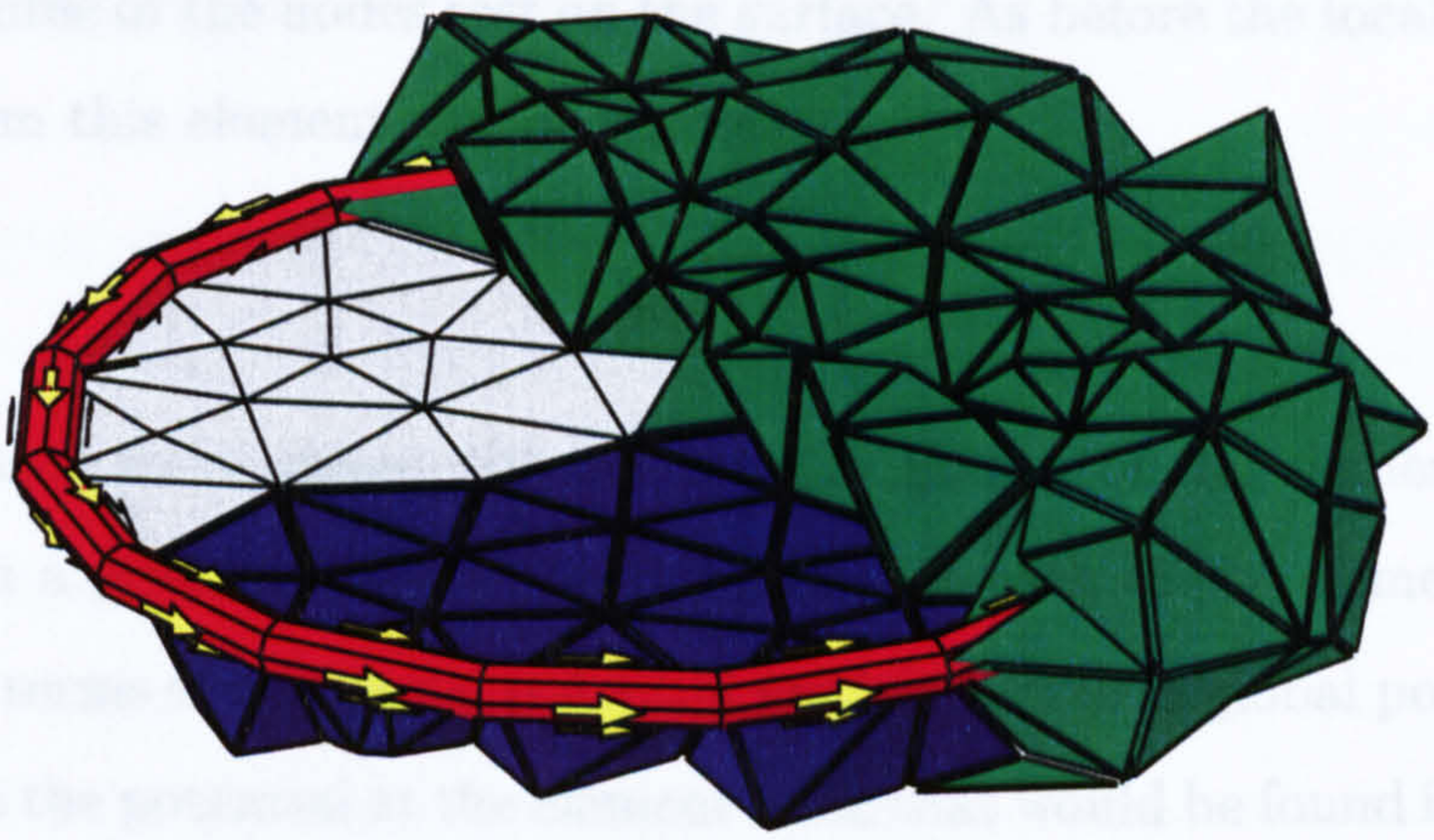

Figure 3.4: Finite element mesh of tetrahedral elements generated around a circular coil. Section of surface defining coil (grey). Elements with a positive offset (green). Elements with a negative offset (blue). Arrows indicate the direction of current flow (yellow).

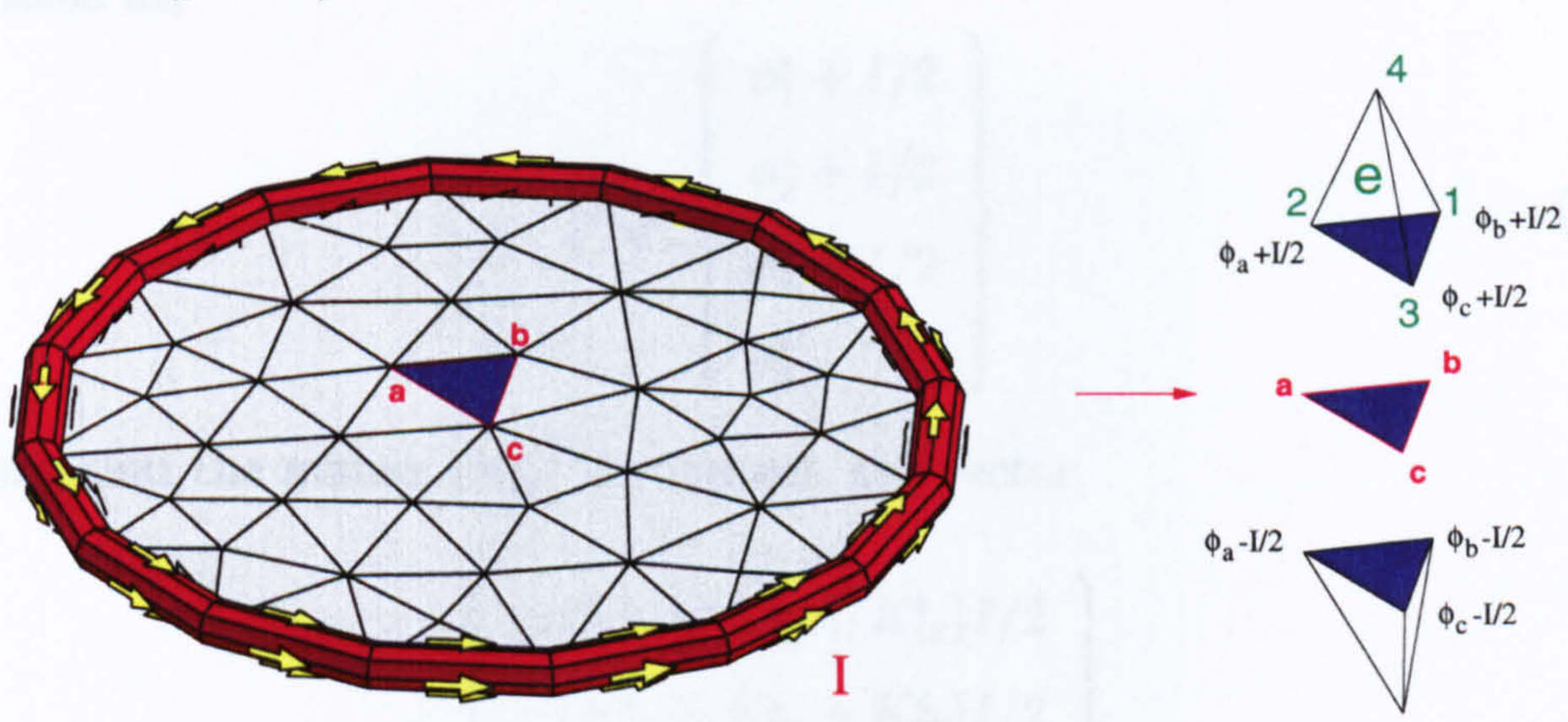

Figure 3.5: Coil with spanning surface. Element e highlighted with nodes a, b and c lying on the surface.

The effects of offsetting the potential at the nodes lying on the current surfaces on the local contributions of the elements, that have a node on these surfaces are now considered. With reference to figure 3.5 and considering element e, four nodes are identified labelled corresponding to the elements local node numbering

scheme and three of the nodes rest on the surface. As before the local contribution generated from this element can be written as,

$$\left[K_{ij}^{e}\right]\left\{\tilde{\phi}_{i}^{e}\right\} \tag{3.27}$$

where $\tilde{\phi}_{i}^{e}$ is used to represent the potential at node i of the element. For these elements with a potential offset, the potentials at each of the element nodes can be written in terms of the global potential values ϕ_{i}^{e}. These global potential values correspond to the potential at the element node that would be found in the absence of the coil. For example, for element e, for the nodes which lie on the surface, that is $i = 1, 2, 3$, the potential at the nodes can be written as, $\tilde{\phi}_{i}^{e} = \phi_{i}^{e} + I/2$ and for the node that does not lie on the surface, in this case $i = 4$, the potential can be written as $\tilde{\phi}_{i}^{e} = \phi_{i}^{e}$. The global matrix contribution, expression 3.27, can now be written as,

$$\left[K_{ij}^{e}\right]\left\{\begin{array}{l}\phi_{1}^{e}+I/2\\ \phi_{2}^{e}+I/2\\ \phi_{3}^{e}+I/2\\ \phi_{4}^{e}\end{array}\right\} \tag{3.28}$$

recalling that the matrix $\left[K_{ij}^{e}\right]$ is constant, the vector,

$$\left\{\begin{array}{l}-(K_{11}^{e}+K_{12}^{e}+K_{13}^{e})I/2\\ -(K_{21}^{e}+K_{22}^{e}+K_{23}^{e})I/2\\ -(K_{31}^{e}+K_{32}^{e}+K_{33}^{e})I/2\\ -(K_{41}^{e}+K_{42}^{e}+K_{43}^{e})I/2\end{array}\right\} \tag{3.29}$$

can be moved to the right side of the global equation, equation 3.20, and the local contribution to the global matrix is $\left[K_{ij}^{e}\right]$ as before. This means that the global matrix is not affected by forcing the potential discontinuity within the mesh, but the constant vector on the right side of the global equation, has to be modified as indicated.

3.5 Defining a Uniform External Field

For the majority of problems considered in this work, interest lies in finding the perturbation to a uniform external field. For the finite element studies conducted in chapter 5, a uniform external field was introduced by applying the appropriate Dirichlet boundary conditions on the external surface of the mesh. This was achieved by setting the potential at each of the nodes on the external surface of the mesh. With the point x_0 defined as the point of zero potential, the external field $\mathbf{H}_0$ was imposed by setting the potential at each of the surface nodes to,

$$\phi = -\mathbf{H}_0 \cdot \mathbf{r} \tag{3.30}$$

where $\mathbf{r}$ is the vector form the point x_0 to the position of the surface node.

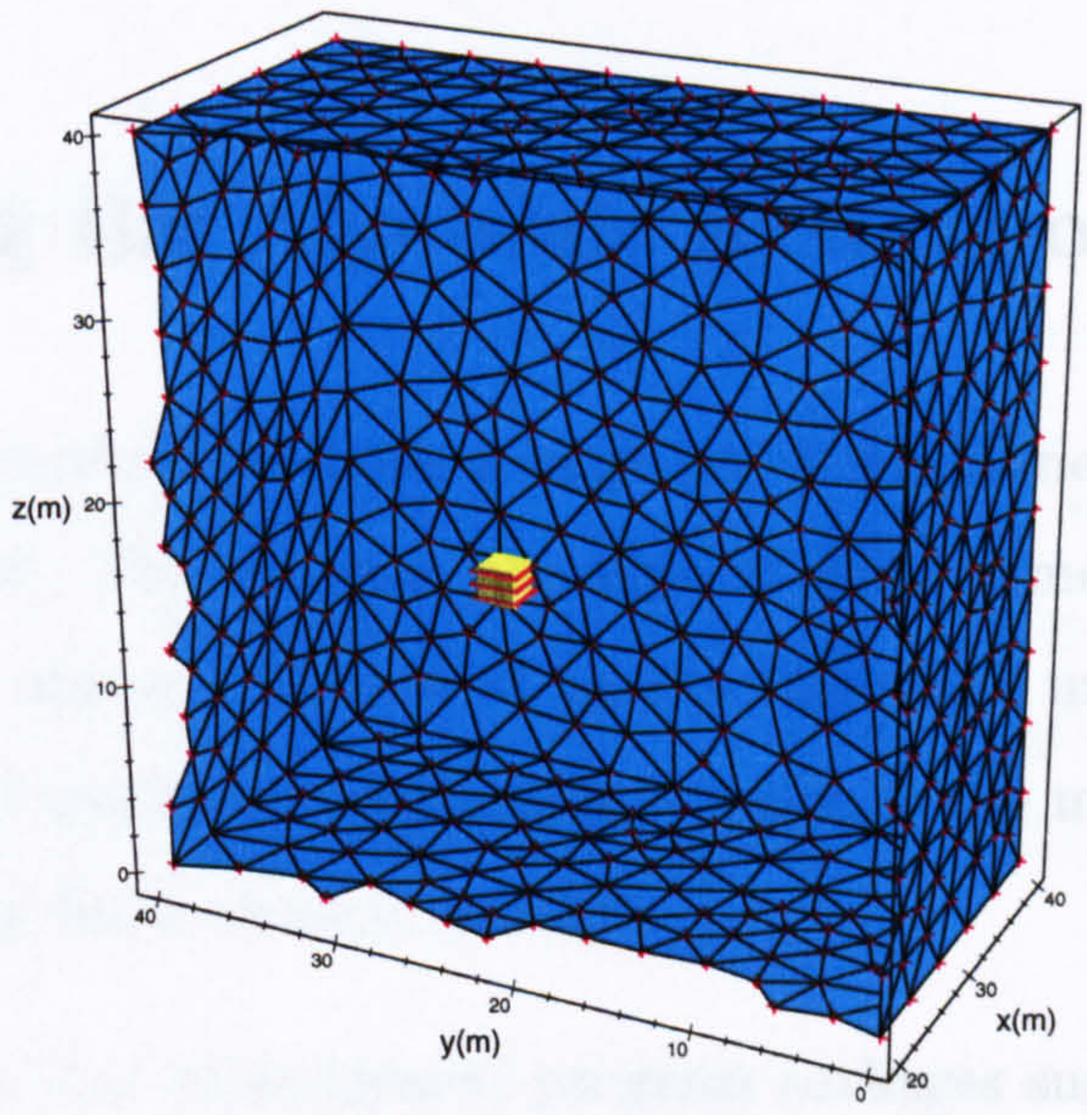

Figure 3.6: A cube of material surrounded by three degaussing coils. Half of the external surfaces of the mesh are shown (blue) and nodes with a fixed potential are indicated (red) on the external surfaces.

As an example consider the problem that is studied in section 5.4 where a cube of permeable material with three degaussing coils is placed in a uniform external field as illustrated in figure 3.6. In this figure half the external surfaces of the mesh and the nodes with a fixed potential lying on these surfaces are illustrated.

A disadvantage of this method is that the external boundaries of the mesh require to be sufficiently distant from the structure under study so that the perturbation field generated by the coils and the magnetisation of the material within the mesh is negligible at the boundaries of the mesh. The resulting large mesh volume of the example being considered is evident from figure 3.6. It is to be noted, however, that with the use of variable element sizing, achieved by the mesh generation techniques described in chapter 4, this disadvantage is not excessively limiting.

3.6 Solving the Algebraic System of Equations

The finite element method produces a large set of simultaneous equations which require to be solved. For example, the type of three dimensional problem reported in chapter 5 may contain several hundred thousand unknowns. Because of the large number of unknowns, finding the solution is the most computationally intensive step in any finite element problem.

It is to be noted that sophisticated program packages such as LINPACK and the Yale Sparse Matrix Package are available which have been designed particularly for large linear systems. However, as an alternative to working with these black box algorithms, the work described in sections 3.6.1 to 3.6.3 was undertaken for this project.

3.6.1 Conjugate Gradient Method

The conjugate gradient method was developed by E. Stiefel and M. R. Hestenes [38] and a good account of the method can be found in [39]. Nevertheless, the method is outlined because of its appropriateness to the solving process required for this work.

Consider the nonsingular matrix equation,

$$\mathbf{Ax} = \mathbf{b} \tag{3.31}$$

where $\mathbf{A}$ denotes a $n \times n$ symmetric positive definite matrix, $\mathbf{x}$ is the unknown vector and $\mathbf{b}$ is the given matrix. The conjugate gradient method is based on the principle of minimising the function,

$$f(\mathbf{x}) = \frac{1}{2}\mathbf{x} \cdot \mathbf{Ax} - \mathbf{b} \cdot \mathbf{x} \tag{3.32}$$

The function is minimised when its gradient,

$$\nabla f = \mathbf{Ax} - \mathbf{b} \tag{3.33}$$

is zero which is equivalent to equation 3.31. In other words it is the vector $\mathbf{x}$ that minimises the equation 3.32, which is the solution to equation 3.31. The conjugate gradient method is an iterative method and attempts to minimise equation 3.32 by progressively improving estimates for the vector $\mathbf{x}$. For each iteration the new vector $\mathbf{x}$ is taken to be,

$$\mathbf{x}_{k+1} = \mathbf{x}_k + \alpha_k \mathbf{p}_k \tag{3.34}$$

where $\mathbf{x}_{k+1}$ is the new estimate of the solution and $\mathbf{p}_k$ is a vector which determines the direction in the n dimensional space in which the algorithm moves to correct the estimate. The parameter α_k is a scalar coefficient which determines how far the algorithm moves in the $\mathbf{p}_k$ direction. Each iteration α_k is the value that minimises $f(\mathbf{x}_k + \alpha_k \mathbf{p}_k)$.

The key to the conjugate gradient method is in the choice of the search directions, $\mathbf{p}$. These vectors are selected so that for each iteration, $\mathbf{p}_k$ is A-conjugate to every previously calculated direction vector. Two vectors are A-conjugate if $\mathbf{p}_i \cdot \mathbf{A}\mathbf{p}_j = 0$ for all $i \neq j$. A consequence of this is that the conjugate gradient method will theoretically converge in at most n steps and as such the method is often referred to as semi-iterative. Due to rounding errors, however, the method is treated as being iterative with termination based upon an iteration maximum, k_{max}, and the norm of the residual vector. The residual vector for the kth iteration is defined by,

$$\mathbf{r}_k = \mathbf{b} - \mathbf{A}\mathbf{x}_k \tag{3.35}$$

and the conjugate gradient method is terminated when the quantity, referred to as the residual error,

$$\frac{||\mathbf{r}_k||}{||\mathbf{b}||} \tag{3.36}$$

falls below a defined value. The norm of the vector is defined by, $||\mathbf{x}|| = (\mathbf{x} \cdot \mathbf{x})^{1/2}$

The implementation of the conjugate gradient method used in this work is summarised in figure 3.7. It is to be noted that the algorithm requires only one matrix vector multiplication per iteration.

An example of the rate of convergence of the conjugate gradient method is illustrated in figure 3.8. In this plot the residual error, as defined by equation 3.36, has been plotted against the iteration number. These results have been obtained for the finite element problem of a spherical shell of permeable material in a uniform external field with a plate thickness of 0.01 m and relative permeability of 500 as studied in section 5.3.

$x = x_0$

$k = 0$

$r = b - Ax_0$

$\rho_0 = |r|^2$

while$(\sqrt{\rho_k} > \epsilon\,||b||)$ **and** $(k < k_{max})$

$k = k + 1$

if $k = 1$

$p = r$

else

$\beta_k = \rho_{k-1}/\rho_{k-2}$

$p = r + \beta_k p$

end

$w = Ap$

$\alpha_k = \rho_{k-1}/(p \cdot w)$

$x = x + \alpha_k p$

$r = r - \alpha_k w$

$\rho_k = ||r||^2$

end

Figure 3.7: Summary of Conjugate Gradient Method [39]. For a given positive definite symmetric real matrix **A**, a vector **b** and an initial guess $\mathbf{x}_0$ then the above algorithm computes the vector **x** such that $\mathbf{Ax} = \mathbf{b}$.

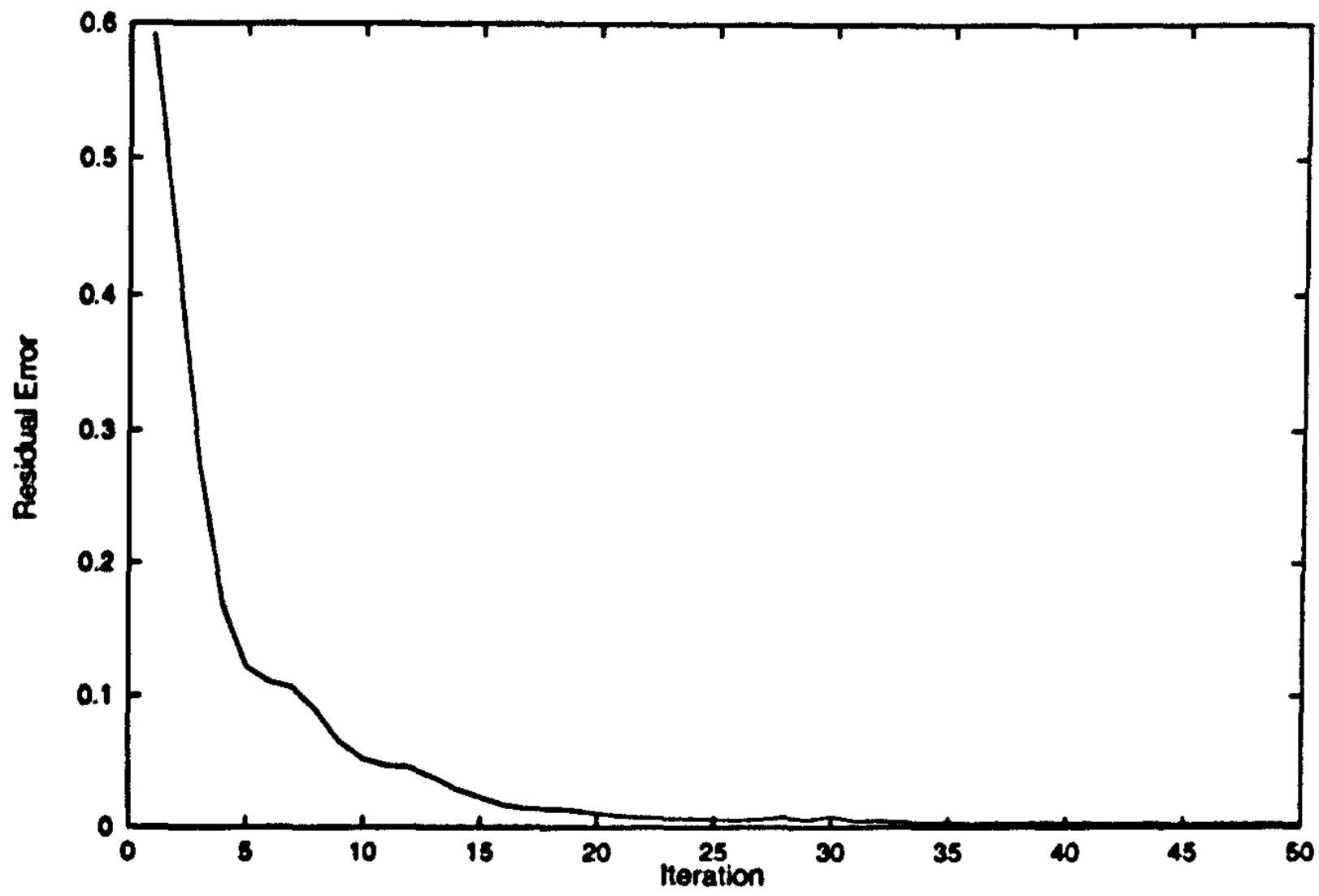

Figure 3.8: Residual error ($\frac{||r_k||}{||b||}$) against iteration (k) for the conjugate gradient method when applied to the finite element problem of a spherical shell in an external magnetic field, section 5.3. Initial 50 iterations are shown.

3.6.2 Matrix-Vector Multiplication

As mentioned in the previous section, an important attraction of the conjugate gradient method for the solution of large systems of equations is that a matrix vector multiplication is the main operation per iteration. For handling large systems, matrix vector multiplication is the rate determining step and therefore the computational efficiency for this is important. Many factors are relevant to the computational cost and one of these factors, the way in which the matrix is stored in memory is outlined in section 3.6.3. In this section, however, it is to be noted that the matrix-vector multiplication can be performed without the need to form explicitly the global matrix K.

Since $\mathbf{K}^e$ has a simple form it can be conveniently calculated when required, with the advantage that the need to generate the global matrix K is completely eliminated. As a consequence, memory requirement is kept to a minimum. There is the disadvantage, however, that the computation of $\mathbf{K}^e$ is required each time the matrix vector product is computed.

Taking this a stage further, since each element in a mesh is considered sequentially, the entire mesh need not be stored in the memory. When a particular section of the mesh is involved in the matrix vector multiplication it can be loaded into memory, thereby removing any limitation on the size of the mesh that can be handled in the finite element analysis. In this situation, however, the speed of the conjugate gradient algorithm is governed not only by the additional computation time required to generate the $\mathbf{K}^e$ matrix each iteration, but also by the time required to retrieve different sections of the mesh from a storage device. With this additional burden and with the large memory of most computers this scheme proved to be impractical and unnecessary.

3.6.3 Matrix Storage

The matrix K generated by the finite element analysis has two main properties: It is a real symmetric matrix and it is sparse. In light of these two factors it is important to consider the method by which the matrix is stored in memory. In this section the dynamic storage method of the global matrix K, which was incorporated into the finite element code written for this work, is described.

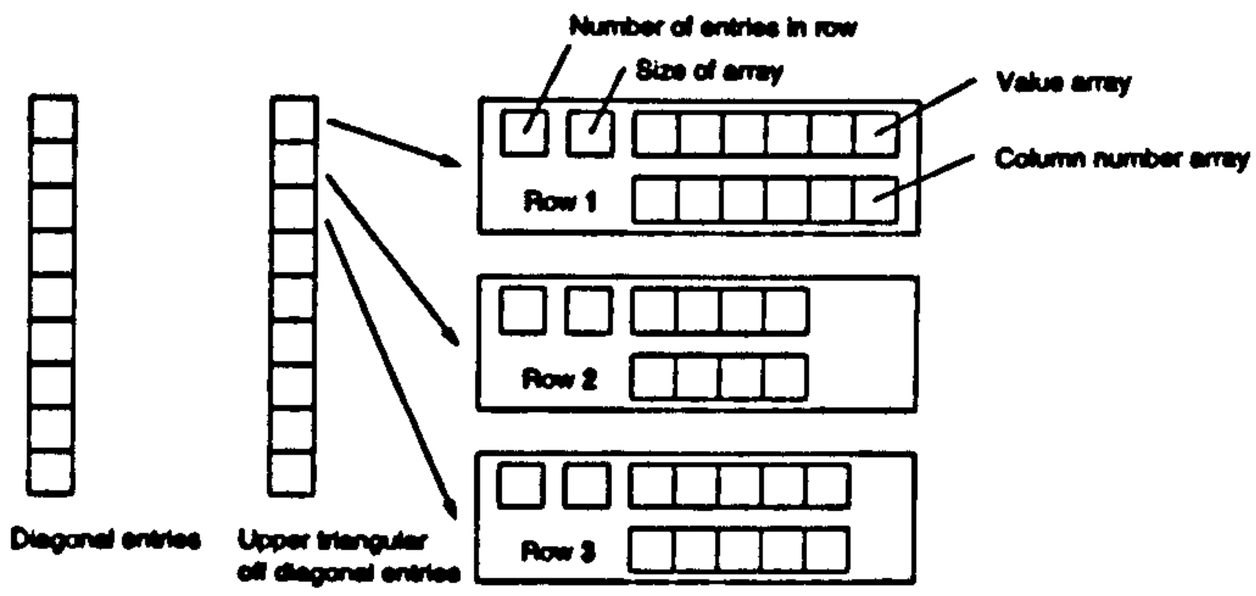

Figure 3.9: Schematic showing storage method of a real symmetric sparse matrix.

A schematic of the matrix storage scheme is illustrated in figure 3.9. Firstly, it is to be noted that the matrix K is symmetric, this means that only the upper triangular half of the matrix needs to be stored without loss of information. The diagonal entries are stored separately and the remaining entries are contained in arrays corresponding to their row. Each row of the matrix is described by two arrays, an array of the entry values and a corresponding array storing the column to which the entry belongs. Two essential pieces of information are also stored for each row, the number of entries in the row and the size of each of the arrays.

When a new off diagonal entry is added to the matrix, the row to which that entry corresponds in the upper triangle is determined, remembering that the

matrix is taken to be symmetric. This defines the set of row arrays to which the matrix element belongs. Any entries already defined in that row are checked and if the additional entry has already been defined the appropriate updates are made. If the additional entry has not been previously defined it is added to the row arrays and the counter tracking of the number of entries belonging to the row is increased. For a particular row, if the number of entries is equal to the size of the arrays more memory is allocated to the row to allow the information to be included. The array size counter is subsequently set to the new array length. Once the matrix has been generate a garbage-collection process is used to remove zero entries and free up memory that is not required.

Using this scheme the matrix stored will contain zero entries only if they exist on the diagonal of the matrix. As such, the storage scheme provides a memory efficient method for storing sparse matrices. The cost of identifying one particular matrix entry is at most a search over all the entries in a given row. It is also to be noted that with the matrix stored in this form, efficient matrix vector multiplication routines can be written.

3.6.4 Solution Finding Strategy

From section 3.2 the system of equations generated from the finite element analysis can be written in terms of a global matrix **K** and a vector **b**. This system of equations is subsequently solved to find the solution vector Φ. The vector **b** can be thought of as a source vector, since the contributions to this vector originate from the Dirichlet boundary conditions used to simulate the external field as discussed in section 3.5 and from the potential offsets used to model the current carrying coils as described in section 3.4. Therefore the vector **b** can be written

as the linear combination,

$$\mathbf{b} = \mathbf{b}_{0x} + \mathbf{b}_{0y} + \mathbf{b}_{0z} + \sum_{i=1}^{m} \mathbf{b}_i \tag{3.37}$$

where $\mathbf{b}_{0x}$ is the source vector generated with an external field of $1\,\mathrm{Am}^{-1}$ along the x axis and with no current passing in the coils. The vectors $\mathbf{b}_{0y}$ and $\mathbf{b}_{0z}$ are similary defined with a unit field along the y and z axes respectively. The vector $\mathbf{b}_i$ corresponds to the source vector generated with no external field and with a current of 1 A in the ith coil. The remaining coils are set to have zero current.

The solution to each of these separate problems can be determined and consequently the solution to an arbitrary problem, involving an external field,

$$\mathbf{H}_0 = H_{0x}\hat{\mathbf{x}} + H_{0y}\hat{\mathbf{y}} + H_{0z}\hat{\mathbf{z}} \tag{3.38}$$

and a given set of current values for each of the m coils, can be obtained from,

$$\phi = H_{0x}\Phi_{0x} + H_{0y}\Phi_{0y} + H_{0z}\Phi_{0z} + \sum_{i=1}^{m} I_i\Phi_i \tag{3.39}$$

where I_i denotes the current in the ith coil. The vector Φ_{0x} is calculated from solving the set of equations defined by $\mathbf{K}\Phi_{0x} = \mathbf{b}_{0x}$ and similary for Φ_{0y} and Φ_{0z}. The vector Φ_i corresponds to the solution vector with unit current in the ith coil and no external field, that is the solution to the set of equation defined by $\mathbf{K}\Phi_i = \mathbf{b}_i$.

By expressing the solution vector as the linear sum in equation 3.39 and once this basis of solution vectors has been calculated, the computational effort required to obtain the solution to a number of different problems is minimal. In view of the aims of this work, this approach proved to be advantageous. For example, and with particular reference to the case study described in section 5.7 for a ship with a given system of degaussing coils, it is often the case that a number of different external magnetic field orientations, corresponding to different headings

of the ship, require to be examined with different current configurations in the degaussing system.

The generation of the $m + 3$ solution vectors, is the most computationally intensive step and the procedure used in this work for the calculation of the set of solution vectors is summarised in figure 3.10.

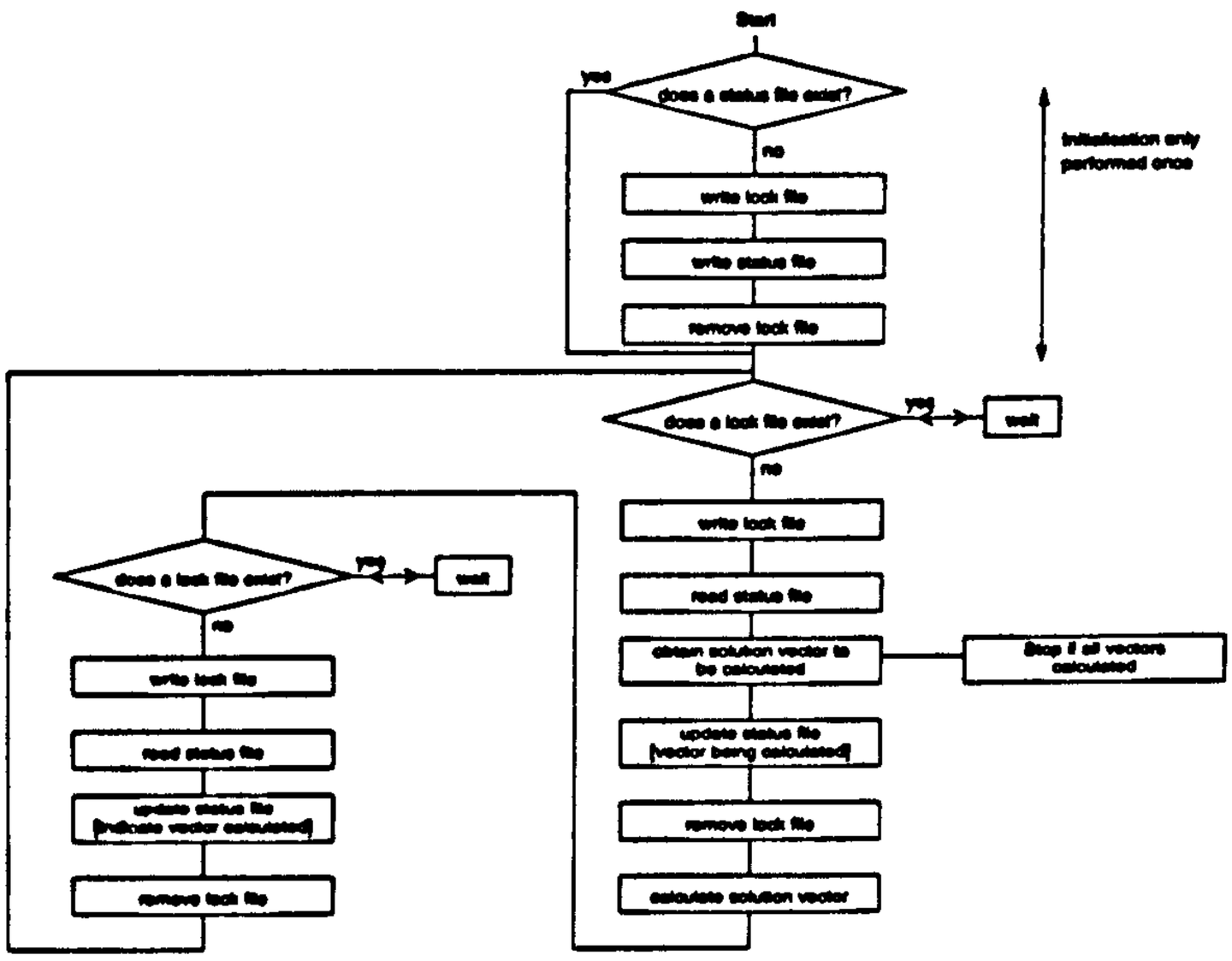

Figure 3.10: Flow diagram outlining the main stages for the computation of the set of solution vectors.

The initialisation step of this process is the creation of a status file. The main task of the status file is to keep track of the solution vectors. Each vector is saved to a separate file and the status file associates the corresponding file names to the particular vectors. The status file is also used to monitor which vectors have been calculated, which vectors are currently being calculated and which vectors require to be calculated. This means that several computers can simultaneously work on

constructing the same set of solution vectors for a particular problem. The use of a lock file, as detailed in figure 3.10, ensures that only one process can access the status file at any particular time and consequently any duplication of work is prevented.

For a problem containing a large number of coils this approach greatly reduces the time required to obtain a set of solution vectors. In section 5.7.3 a large mesh is used to study the degaussing of a ship with 13 degaussing coils. The average time required to obtain a solution for one particular problem was approximatly 1 hour. Running on one computer the generation of the complete set of solution vectors would therefore take approximately 16 hours. Using the scheme designed for this work, as summarised in figure 3.10, the same problem was split over four machines. The calculation of all the solution vectors was favourably completed within approximately 4 hours.

3.7 Post-processing

Once the set of equations generated by the finite element analysis has been solved the potential at each of the mesh points is available. This information can then be used to determined the potential at any point within the mesh by identifying the element which contains the point and subsequently using equation 3.8 in the two dimensional case or equation 3.21 in a three dimesional analysis.

In most cases, however, it is the magnetic field and not the potential which is of particular interest. Since the magnetic field is related to the potential by $\mathbf{H} = -\nabla\phi$, the field associated with each element can be calculated. For the two dimensional case, when linear triangular elements are used, the magnetic field is

given by equation 3.40.

$$\mathbf{H}^e = \frac{-1}{2\Delta^e} \sum_{i=1}^{3} \left(b_i^e \hat{\mathbf{x}} + c_i^e \hat{\mathbf{y}} \right) \phi_i^e \tag{3.40}$$

For tetrahedral elements in three dimensions the corresponding expression can be obtained.

Instead of working with the local node number scheme of the element it is useful to write the equation 3.40 in terms of the global numbering scheme,

$$\mathbf{H}^e = \mathbf{D}^e \Phi \tag{3.41}$$

where Φ is the solution vector containing the potential at each of the mesh nodes defined by equation 3.20. The matrix $\mathbf{D}^e$ has been formed by relating the local node numbering scheme to the global scheme. In some calculations, where the field at a number of different points has to be calculated for a number of different solution vectors, the matrix $\mathbf{D}$ can be generated, such that,

$$\begin{Bmatrix} H_x^1 \\ H_y^1 \\ H_z^1 \\ \vdots \end{Bmatrix} = \mathbf{D}\Phi \tag{3.42}$$

The matrix $\mathbf{D}$ is formed from the individual $\mathbf{D}^e$ matrices associated with the elements from which the field is to be calculated. This means, that once the matrix $\mathbf{D}$ has been generated, the field can be calculated at each point from one matrix vector multiplication.

Since linear elements are used the magnetic field is a constant vector within each element as given by equation 3.40. To introduce variation in the magnetic field within each element, one solution would be to resort to higher order elements, however, working with linear elements a different approach is used in this work.

For ease of explanation consider the two dimensional case, but it is to noted that the extension to three dimensional follows naturally. Working with linear triangular elements, the field at a point P lying in element e can be determined by considering the magnetic field within each of the adjacent elements. It is required that all the elements immediately surrounding e exist and have the same permeability. Taking each node of element e, the elements containing this node are identified and the average field of these elements is determined, giving a field value at each of the element nodes $\mathbf{H}_i^e$. If it is assumed that the field varies linearly over the element, the field at point P can be calculated in a similar way to that which was used to calculate the potential at a given point. The field at P can be written as,

$$\mathbf{H}^e(x,y) = \sum_{i=1}^{3} N_i^e(x,y)\mathbf{H}_i^e \tag{3.43}$$

This averaging process can be used in regions that have a constant permeability and in elements that do not lie at the edge of the mesh.

Therefore, two methods have been described that calculate the field at a point directly from the mesh. The calculations either involve the element containing the point or average over a small number of elements surrounding the point. The field at a particular point in space can also be determined from the individual field sources defined in the problem, by,

$$\mathbf{H}(x,y,z) = \mathbf{H}_0 + \mathbf{H}_{coils}(x,y,z) + \mathbf{H}_{mag}(x,y,z) \tag{3.44}$$

The magnetic field at the point (x,y,z) is the sum of the constant external field $\mathbf{H}_0$, the field due to any current carrying coils $\mathbf{H}_{coils}$ and the field due to the induced magnetisation of the material $\mathbf{H}_{mag}$. For a particular problem, $\mathbf{H}_0$ will be known, and the field due to the coils can be calculated by the method detailed in section 2.4.2. The field from the magnetisation of the material can be calculated

from,

$$\mathbf{H}_{mag}(x,y,z) = \frac{1}{4\pi}\sum_{e=1}^{n}\left(\frac{3(\mathbf{m}^e\cdot\mathbf{r}^e)\mathbf{r}^e}{(r^e)^5} - \frac{\mathbf{m}^e}{(r^e)^3}\right) \tag{3.45}$$

where the sum is over all the material elements defined in the mesh and where $\mathbf{r}^e$ is the vector from the element to the field point and $\mathbf{m}^e$ is the dipole moment of element e calculated from,

$$\mathbf{m}^e = (\mu_r^e - 1)\,\mathbf{H}^e V^e \tag{3.46}$$

In equation 3.46, $\mathbf{H}^e$ is the magnetic field within the element, μ_r^e is the relative permeability and V^e is the volume of the element.

3.8 Degaussing

From section 3.4 the magnetic characteristics of current carrying coils within our problem can be represented. Thereby the solution to a particular problem involving a mass of permeable material, situated in an external field with a given distribution of current circuits, can be determined. In this section the identification of the optimal set of degaussing coil currents for a given distribution of material and fixed degaussing coil system is described. For example, given a ship structure containing a set of degaussing coils and exposed to the earth's magnetic field, this section describes the method for determining the set of coil currents that minimises the perturbation to the earth's field, on a given surface, caused by the ship.

The main objective is to minimise the perturbation to the external field generated by both the magnetisation of the material present in the problem and the currents in the degaussing coils. To achieve this a region of the problem in which the perturbation is to be minimised is defined and a number of sample points

identified within the region. For this work the region is defined by specifying a rectangular plane, as illustrated in figure 3.11 on which a regular grid of sample points are selected. In the example described in figure 3.11 50×50 sample points have been defined.

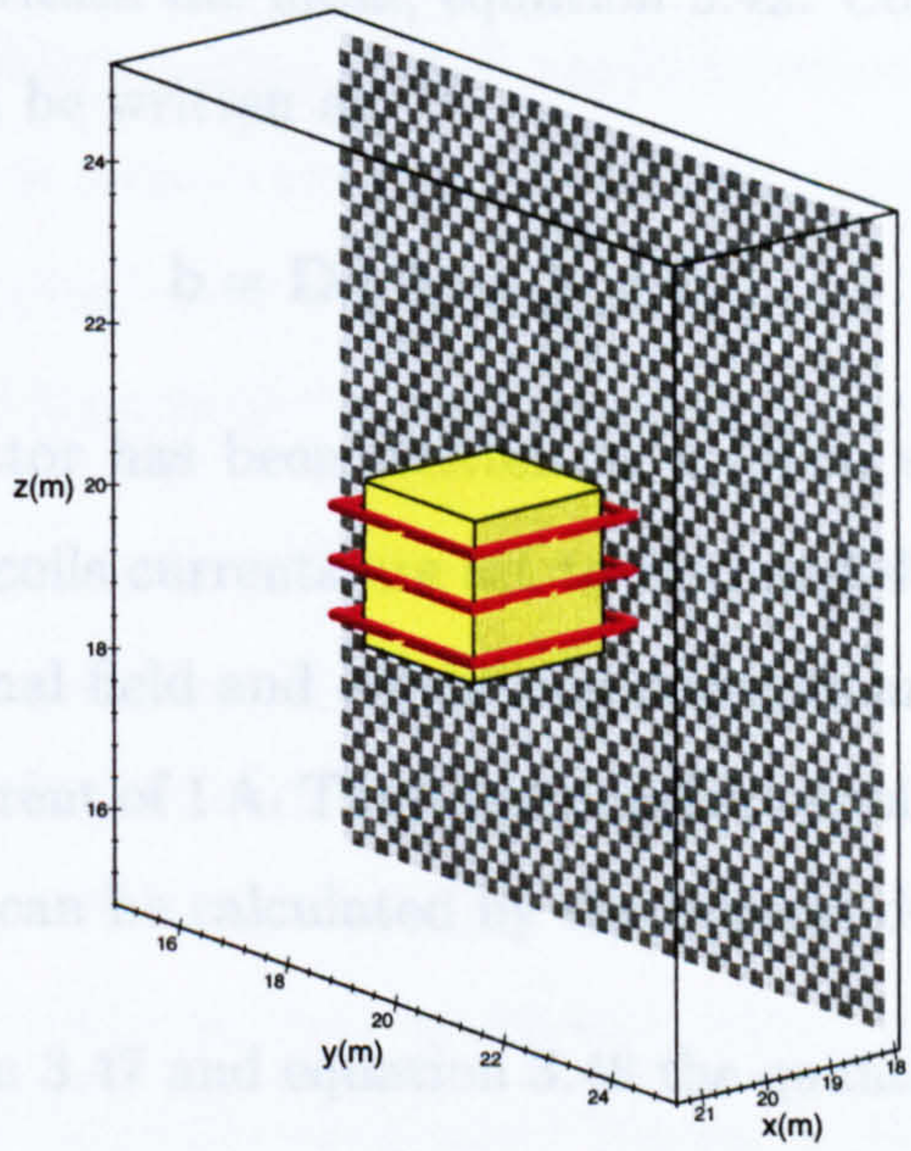

Figure 3.11: Example highlighting the specification of a minimisation plane. The minimisation plane defines 50×50 sample points set 1 m from a cube of permeable material surrounded by three degaussing coils. The corner of each grey square on the chequered minimisation plane corresponds to one sample point.

The first step in progressing the minimisation is to defined the vector δ which is a measure of the magnetic perturbation or, in other words, the magnetic signature over the minimisation plane. The vector δ is defined by,

$$\delta = \mathbf{b} - \mathbf{b}_e \tag{3.47}$$

where $\mathbf{b}$ is a vector containing the magnetic field at each of the sample points and $\mathbf{b}_e$ is the external magnetic field, again at each of the sample points. The quantity to be minimise is δ^2.

From section 3.7 a matrix $\mathbf{D}$ can be constructed that can be used to calculate the field at any point within the mesh, equation 3.42. Consequently the vector $\mathbf{b}$ from equation 3.47 can be written as,

$$\mathbf{b} = \mathbf{D}\left(\Phi_e + \sum_{i=1}^{m} I_i \Phi_i\right) \tag{3.48}$$

where the solution vector has been written as a linear sum of Φ_e, the solution obtained when all the coils currents are set to zero and Φ_i, the solution obtained when there is no external field and all the coil currents are set to zero except the ith coil which has a current of 1 A. The total number of coils is denoted by m. This set of solution vectors can be calculated by the process detailed in section 3.6.4.

Combining equation 3.47 and equation 3.48 the quantity δ^2 can be written as,

$$\delta^2 = (\mathbf{b}_e)^2 - (\mathbf{D}\Phi_e)^2 + 2\sum_{i=1}^{m} I_i \left(\mathbf{D}\Phi_e - \mathbf{b}_e\right) \cdot \mathbf{D}\Phi_i + \sum_{i=1}^{m}\sum_{j=1}^{m} I_i I_j \left(\mathbf{D}\Phi_i \cdot \mathbf{D}\Phi_j\right) \tag{3.49}$$

Differentiating δ^2 with respect to each of the currents I_i and setting this equal to zero, the best set of degaussing currents can be obtained by solving the set of equations defined by,

$$\sum_{j=1}^{m} \left(\mathbf{D}\Phi_i \cdot \mathbf{D}\Phi_j\right) I_j = \left(\mathbf{b}_e - \mathbf{D}\Phi_e\right) \cdot \mathbf{D}\Phi_i \tag{3.50}$$

3.9 Summary and Discussion

In this chapter the finite element and associated techniques used in this work have been described. The work detailed in the chapter was implemented as a two dimensional code using Java. The graphical ability of Java resulted in good visualisation of the problem geometry and resulting solution [40]. The aim of the two dimensional code was to provide a test bed for the three dimensional program. The main three dimensional code was implemented as a C++ program [41], with visualisation performed separately by a different program written in Java [42].

The object orientated nature of C++ enabled the three dimensional code to be written to allow the addition of new elements types within the finite element scheme. For example, higher order elements could be included to improve the computational accuracy. Furthermore, line elements could be included to model the effects of support structures, such as girders, within a ship. The development of these elements could be easily progressed similar to the procedures as used in this work to represent thin iron regions.

Chapter 4

Mesh Generation

4.1 Introduction

Before the finite element method can be applied to a particular problem, the domain in which the solution has to be found requires to be divided into elements. The discretisation of the problem domain is the initial step in any finite element analysis.

In this chapter the mesh generation techniques, used to construct the finite element meshes required for this work, are described. The chapter focuses on mesh generation in two dimensions, before proceeding to describe the three dimensional mesh creation process.

Different schemes have been reported for the generation of unstructured meshes suitable for finite element analysis and two of the most popular are advancing front schemes [43], and those based on Delaunay triangulation [44][45].

A review of unstructured mesh generation has been published [46] and an

overview of mesh generation has been reported [47]. A discussion on the variety of different methods is reported in reference [48]. Due to the wide use of the finite element method, the demand for quality mesh generators is high. This is reflected in the number of software packages currently available [49].

4.2 Requirements of a Finite Element Mesh

Before describing the mesh generation procedure for this work some of the main properties that a finite element mesh should exhibit are outlined.

An essential requirement of the finite element mesh is that there should be no gaps in the mesh and no two elements should overlap. In addition to this, the finite element method is greatly simplified if all the elements are connected via their vertices. This means that the vertex of one element can only be at the vertices of its neighbouring elements. The vertices cannot be at the side of another element. If these conditions are satisfied the mesh is said to be conformal.

The mesh must correctly define the physical properties and the geometry of the problem to be studied. That is to say, if the mesh has to contain elements with a particular set of properties, for example surface elements to describe thin regions of high permeability, then these elements must be present in the mesh with the correct physical parameters and with the correct position and orientation.

The shape of the elements must be sufficiently regular. In two dimensions, where a mesh is generated from a set of triangular elements, triangles with a large obtuse angle are to be avoided. Each triangle in the mesh should be as close as possible to an equilateral triangle. In three dimensions, where the basic element shape is tetrahedral, flat or long narrow elements should not be present in the

final mesh. Although irregular element shapes can be accommodated by the finite element algorithm they tend to increase the error in the solution [50].

In any finite element analysis the number of elements within the mesh is one of the main influences on the accuracy of the final result. The solution obtained from a coarse mesh is less reliable than a solution obtained from a fine mesh of the same element types. It is, therefore, important that the mesh is constructed with enough elements to ensure that the solution can be calculated with suitable accuracy. It is to be noted, however, that for any problem, as the number of elements increases so to does the time required to calculate a solution. Consequently there is a limit to the number of mesh elements that can be efficiently handled. To maintain the accuracy of the solution, but to avoid the specification of too many elements, the mesh should have a variable element density.

4.3 Mesh Generation Strategy

A two stage process, that met all the criteria described in section 4.2, was used to obtain the meshes for this work. By a Delaunay triangulation algorithm the first stage involved the construction of an initial mesh, based only on the geometry of the corresponding problem. In the second stage, to improve the accuracy of the finite element solution, the initial mesh can be refined to increase the number of elements within particular regions of the mesh.

4.4 Delaunay Triangulation

In this section the automatic generation of a two dimensional mesh composed of triangular elements is reported. It is to be noted that the methods described are not particular to the two dimensional case but can be extended to the generation of a mesh of tetrahedra in three dimensions.

Regularity of element shape within a mesh is of significant importance for the accuracy of the finite element solution. With reference to figure 4.1 it can be seen that the same set of points are connected to form two different meshes. Mesh (a) is

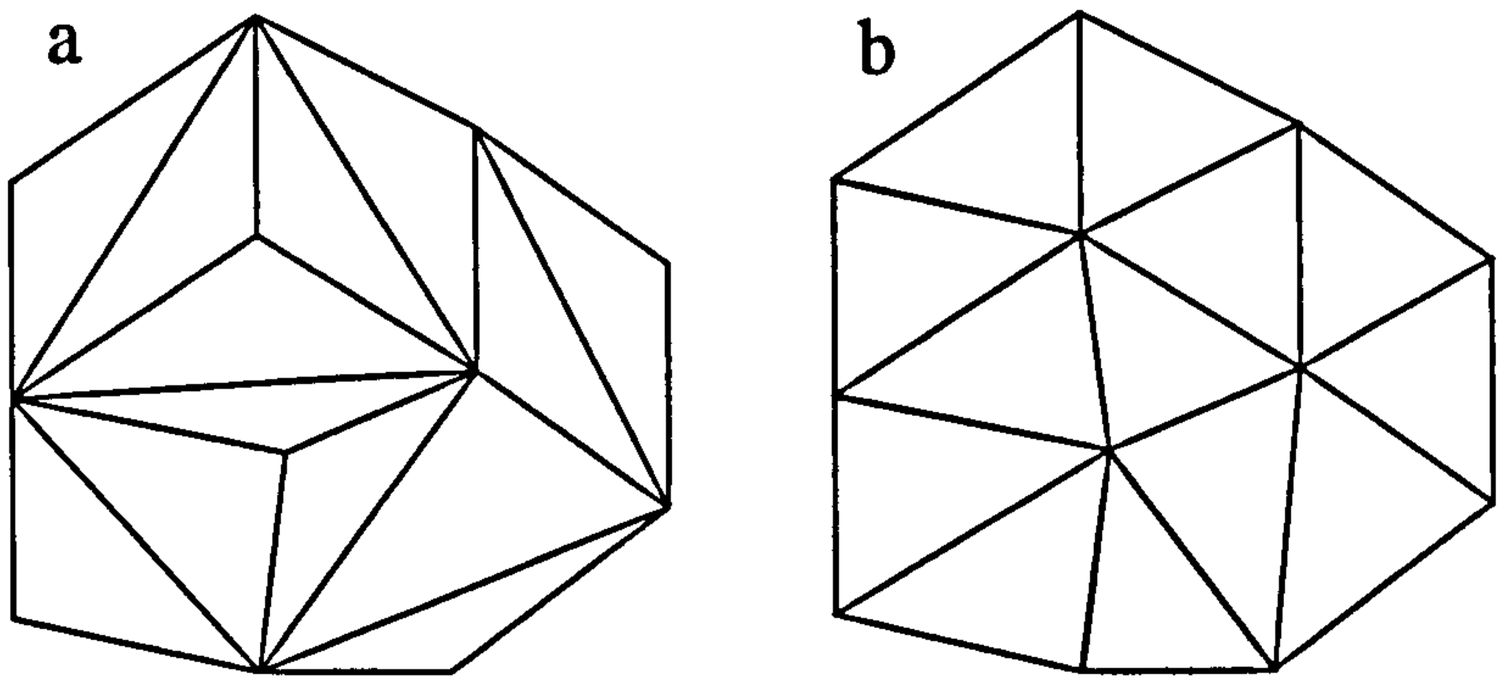

Figure 4.1: (a) Points forming a 'bad' mesh (b) Points forming a 'good' mesh

a 'bad' mesh because it contains triangles with large obtuse angles. Alternatively, mesh (b) is 'good' because the triangles are relatively regular in size and shape. The main goal of any mesh generator algorithm is, therefore, not just to obtain a tessellation of a given set of points but to generate a discretisation that contains elements of an acceptable shape.

The optimal tiling of a domain, using a given set of points, is achieved by constructing a Delaunay triangulation. A Delaunay triangulation is usually defined in terms of an auxiliary graph called the Dirichlet tessellation [51]. For a set of n points in a plane, the Dirichlet tessellation consists of n polygons, V_i, each

centered on point i such that every point within the polygon V_i is nearer to point i than any other point. These polygons are called Voronoi polygons. In general, a vertex of a Voronoi polygon is shared by two other neighbouring polygons and connecting the generating points associated with this vertex forms a triangle. The set of all the triangles is called the Delaunay triangulation. The Dirichlet tessellation and the corresponding Delaunay triangulation are illustrated in figure 4.2.

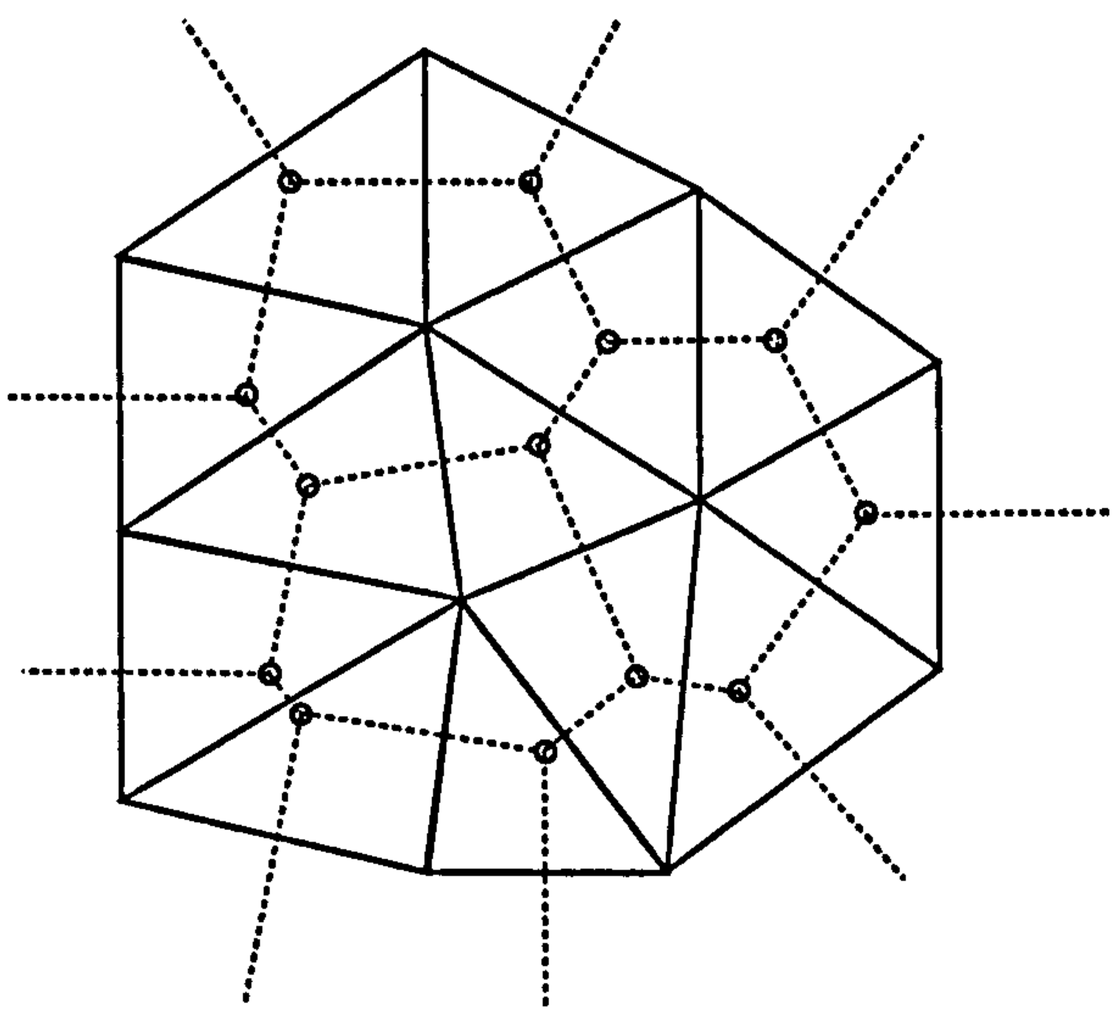

Figure 4.2: Dirichlet tessellation (broken lines), Voronoi polygon vertices (red circles) and Delaunay triangulation (solid lines)

A Delaunay triangulation has several important properties. Provided four or more points are not co-circular the triangulation is unique. The triangulation maximises the sum of the smallest angles in the mesh which is equivalent to achieving a set of triangles that are as near equilateral as possible using the given set of points. This max-min angle property is only true in two dimensions. Furthermore, the circumcircle of a Delaunay triangle cannot contain another vertex.

Despite the fact that the Dirichlet tessellation is closely linked to the Delaunay

triangulation, the generation of the tessellation is not the most computationally efficient approach for obtaining the triangulation. A number of different methods have been described for the generation of the Delaunay triangulation [51]. The most practical algorithms, however, use a node insertion strategy that relies on the fact that in a Delaunay triangulation the circumcircle of any component triangle does not contain another mesh point within its interior [52][53][54].

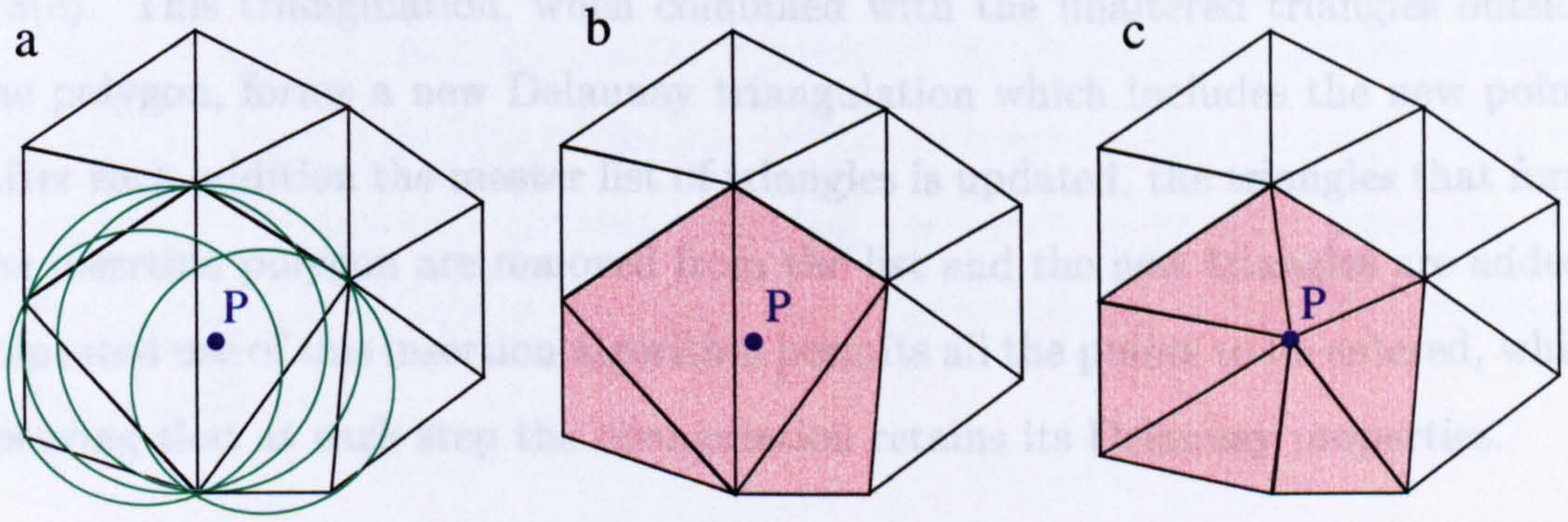

Figure 4.3: Insertion of new point, P, into a Delaunay triangulation using Watson's algorithm. (a) Initial triangulation containing point P (circumcircles containing P shown) (b) Insertion polygon (shaded region) (c) Triangulation after insertion (new triangles shaded).

The method, outlined below, used to generate the meshes for this project has been reported by Watson [53]. In a Delaunay triangulation composed from n points, Watson's algorithm defines the procedure to add the $(n+1)$th point to this mesh. Therefore, the algorithm is initialised by establishing a simple Delaunay triangulation, composed of perhaps one or two triangles, with all the points to be added to the mesh lying within the initial small set of triangles. The algorithm operates by maintaining a master list of triangles which stores all the essential information particular to each triangle, that is the vertices, the coordinates of the circumcentre and the square of the circumradius. To demonstrate the algorithm, consider the insertion of the point P in the mesh illustrated in figure 4.3(a). The

master list is searched for all the triangles whose circumdisks contain the new point, the union of all these triangles is called the insertion polygon, described in figure 4.3(b). It can be shown that no previously inserted point is contained in the interior of this polygon, and that each boundary point of the polygon may be connected to the new point by a straight line lying entirely within the polygon. Thus, a new triangulation of the region enclosed by the polygon is formed, figure 4.3(c). This triangulation, when combined with the unaltered triangles outside the polygon, forms a new Delaunay triangulation which includes the new point. After each addition the master list of triangles is updated, the triangles that form the insertion polygon are removed from the list and the new triangles are added. Repeated use of this insertion algorithm permits all the points to be entered, while ensuring that at each step the triangulation retains its Delaunay properties.

As mentioned previously this construction carries over easily to three dimensions, in which a three dimensional triangulation of tetrahedra is generated using circumspheres and circumballs instead of circumcircles and circumdisks. It is common to use the term triangulation with reference to three dimensions instead of the correct terminology, tetrahedralisation.

4.5 Mesh Generation in 2D

In this section the mesh generation scheme that was used in this work to generate two dimensional meshes around a set of prescribed contours is described. The prescribed contours to be generated within the mesh are defined by two sets of information. One set gives the positions of a set of points on the contour and the other set defines how these points are connected. The contours, therefore, are composed of a series of straight line segments. It is assumed that no two line

segments cross. These prescribed contours are considered to be defined in the mesh if every line segment of a contour is equal to the edge of one of the triangles within the mesh. In fact, if the contour is in the interior of the mesh each defined contour line segment should be the edge of exactly two triangles. A mesh that is required to define a prescribed contour is known as a constrained triangulation.

The mesh generation scheme can be divided up into three main stages: Construction of a set of auxiliary points; creation of the Delaunay triangulation using Watson's method; definition of the prescribed contours within the mesh. A fourth stage, which is optional, involves adjusting the mesh to produce elements of a more regular shape. Each of these four stages is considered in turn with reference to an example case.

4.5.1 Auxiliary Point Initialisation

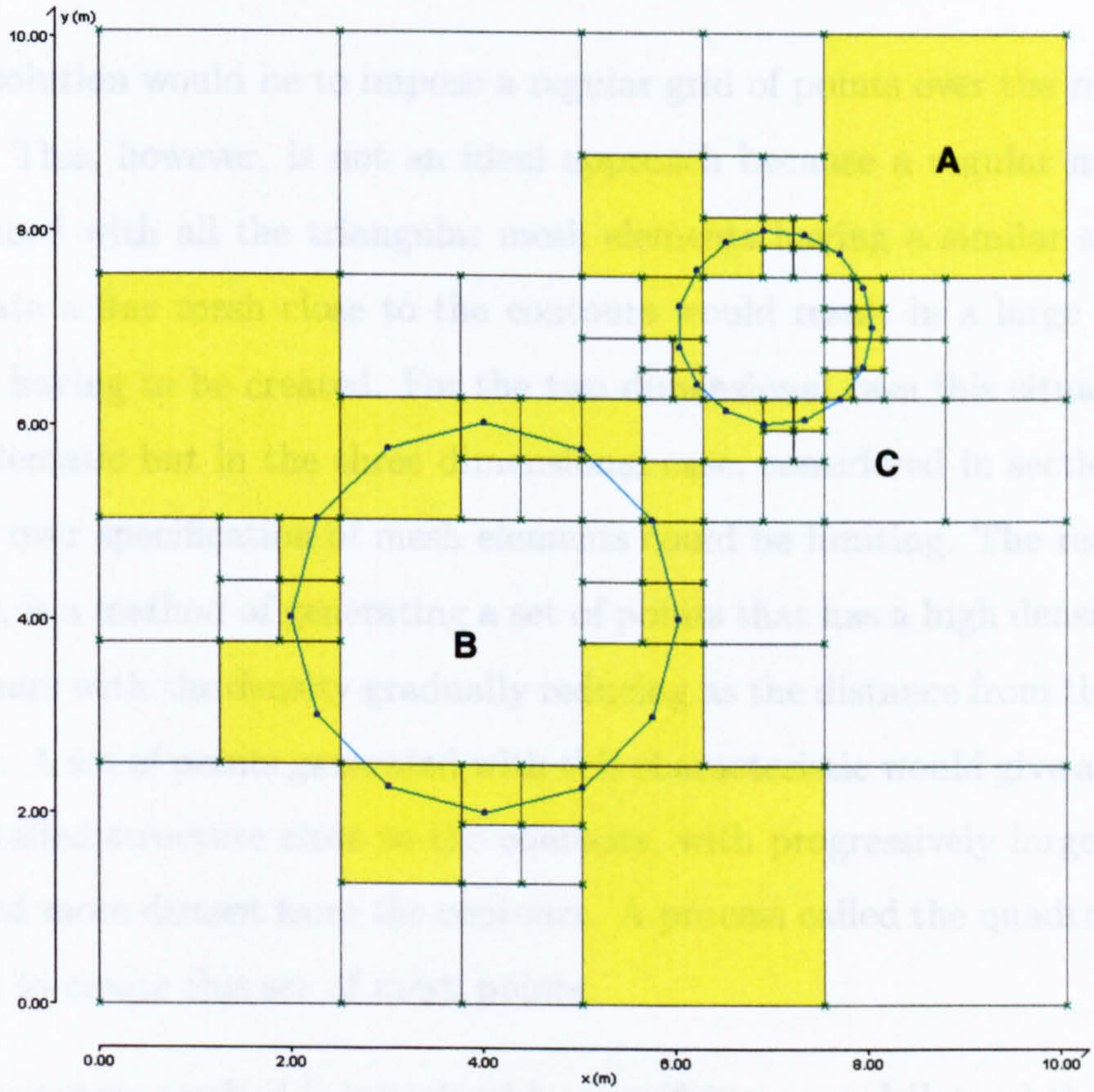

Figure 4.4: Auxiliary point initialisation before balancing. Quadtree squares containing contour points are shaded (yellow). Two prescribed contours to be defined within the final mesh are shown (blue).

In section 4.4 a method for obtaining a Delaunay triangulation from a given set of mesh points was described. A mesh generated from only the contour points would result in a mesh composed of a small set of triangles with irregular shapes and as such would not be suitable as a finite element mesh. The complete set of mesh points should, therefore, not only include the contour points but also a set

of auxiliary points that fill the space between the contours and the boundary of the mesh. The method used to generate the set of auxiliary points is described.

One solution would be to impose a regular grid of points over the region to be meshed. This, however, is not an ideal approach because a regular mesh would be produced with all the triangular mesh elements having a similar area. Thus to generate a fine mesh close to the contours would result in a large number of elements having to be created. For the two dimensional case this situation is not too problematic but in the three dimensional case, considered in section 4.6, the resulting over specification of mesh elements could be limiting. The requirement, therefore, is a method of generating a set of points that has a high density close to the contours with the density gradually reducing as the distance from the contours increases. A set of points generated with this characteristic would give a mesh that has a detailed structure close to the contours, with progressively larger elements being used more distant from the contours. A process called the quadtree method was used to create this set of mesh points.

The quadtree method is initialised by specifying a quadrilateral that contains all the contour points. The size of this quadrilateral, as used in this work, also defines the extent of the final mesh. Then, by a recursive process, each quadrilateral is split into four quadrilaterals. The splitting is repeated until each quadrilateral element contains at most one contour point or until a defined limit on the depth of the recursion has been reached. An example of a quadtree structure is illustrated in figure 4.4. Two circular contours, approximated by straight line segments, are described around which a mesh is to be generated.

The process of splitting results in a tree like structure in which each split quadrilateral can be thought of as the parent of four daughter quadrilaterals. The notion of generations can also be used to indicate the rank of a particular element

in the hierarchy of the splitting process.

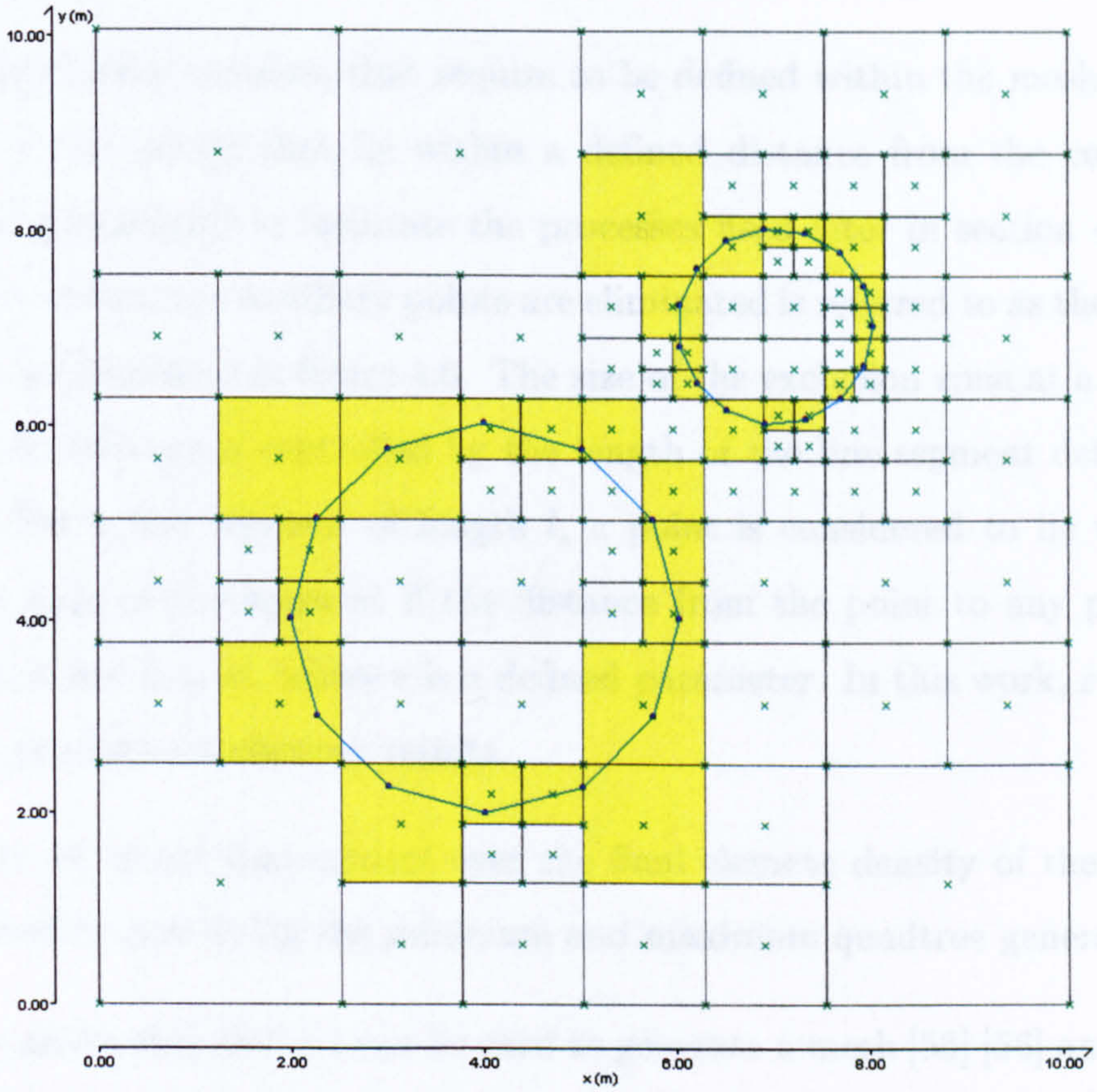

Figure 4.5: Auxiliary point initialisation after balancing. Auxiliary mesh points are shown (green crosses).

The resultant partitioning generated by the quadtree method can be balanced. The splitting is continued until no quadrilateral is adjacent to another quadrilateral which is two or more generations older than itself. This is equivalent to checking that each quadrilateral has no more than one auxiliary point on an edge. A balanced quadtree mesh is illustrated in figure 4.5 and by comparing this to that of the unbalanced case in figure 4.4 it can be noted that the squares A, B

and C, and some other squares, have been quartered. A set of mesh points is generated by taking the corners and the centre point of each quadrilateral.

It is particular contours that require to be defined within the mesh. Removal of some of the points that lie within a defined distance from the contour line segments is beneficial to facilitate the processes used later in section 4.5.3. The region from which the auxiliary points are eliminated is referred to as the exclusion zone and is illustrated in figure 4.6. The size of the exclusion zone at a particular section of a contour is controlled by the length of the line segment defining that section. For a line segment of length l, a point is considered to lie within the exclusion zone of the segment if the distance from the point to any part of the segement is less that ϵl, where ϵ is a defined parameter. In this work, $\epsilon = 0.3$ was found to produce satisfactory results.

It is to be noted that control over the final element density of the mesh can be obtained by specifying the minimum and maximum quadtree generation.

As an aside, this method can be used to generate a mesh [55] [56] and not just, as it has been applied here, to generate a set of auxiliary points. The method involves generating the box grid as described above until each box is occupied by only one boundary point. The boxes that contain a boundary point are then deformed so that the boundary points and contours are included in the mesh. Each quadrilateral is then split into a predefined pattern of triangles corresponding to the number of nodes that lie on its edge.

4.5.2 Delaunay Triangulation in 2D

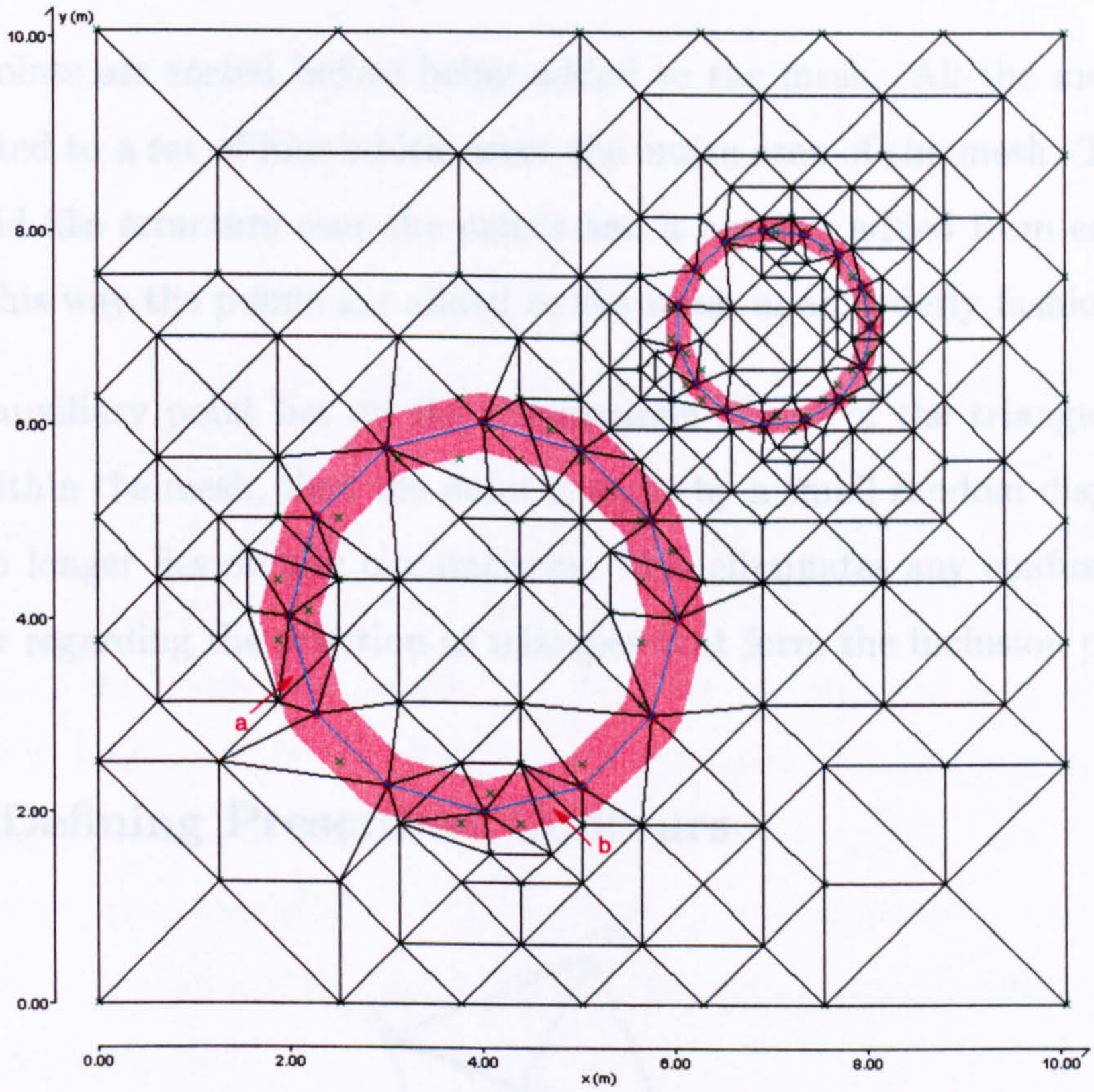

Figure 4.6: Delaunay triangulation. Exclusion zone shown (red).

Having generated a set of auxiliary points an initial Delaunay triangulation is formed by using the vertices of the first generation quadrilateral in the quadtree method to defined an initial mesh of two triangles. Watson's method is then used to add the auxiliary and contour points. The Delaunay triangulation of the example case is illustrated in figure 4.6. In this diagram the exclusion zone has been shaded red and the points lying within this region that have not been included in the triangulation are evident.

There are two noteworthy factors about the way in which the points are added to the triangulation that effect the stability of the algorithm.

The points are sorted before being added to the mesh. All the mesh points are allocated to a set of bins which cover the entire area of the mesh. These bins form a grid like structure over the points and a point is added from each bin in turn. In this way the points are added to the mesh in an orderly fashion.

If an auxiliary point lies on the circumcircle of one of the triangles already present within the mesh, then the point is move by a small random displacement until it no longer lies on any circumcircle. This eliminates any confusion which may occur regarding the selection of triangles that form the inclusion polygon.

4.5.3 Defining Prescribed Contours

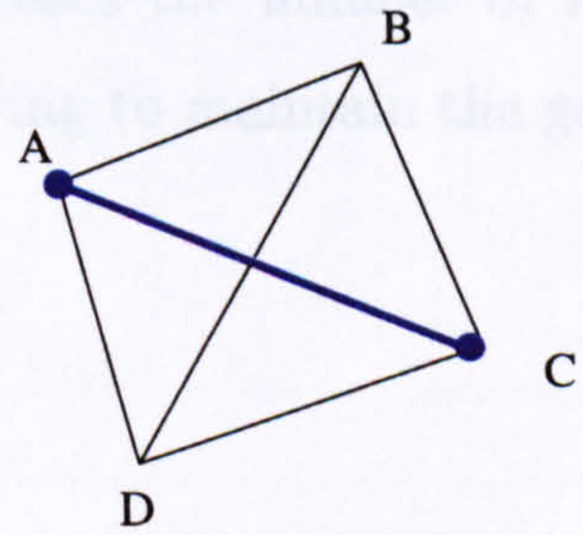

Figure 4.7: Generation of line segment AC by diagonal swapping.

Although a mesh has been generated, it does not necessarily mean that all the contours, required to be present in the mesh, have been correctly defined. For example, consider the triangles ABD and BCD illustrated in figure 4.7, which lie within a mesh and the contour line segment. In this figure the line segment is not the edge of either of the two triangles and is, therefore, not defined in the mesh.

In the example case, as illustrated in figure 4.6, the two contour line segments a and b are not defined by the triangulation.

There are a number of methods that can be used to include a particular line segment within the mesh. Again, with reference to figure 4.7, one method could be to swap the diagonal of the quadrilateral $ABCD$ generated by the two triangles, thereby redefining the triangles ABD to ABC and BCD to ACD, giving the required result. There are, however, disadvantages of this diagonal swapping method. Firstly and most importantly, if the four points are not co-circular, diagonal swapping would result in a mesh that is not of type Delaunay. Also, for the case illustrated in figure 4.7, the line segment is cut by just two triangles and only one rearrangement is required, but the line segment b in the example illustrated in figure 4.6, is cut by three triangles and two rearrangements of the mesh triangles would be required to define the line segment. As the number of intersecting triangles increases the number of rearrangements also increases, presenting the problem of trying to maintain the generation of elements, all with an appropriate shape.

Figure 4.8: Generation of line segment AC by node insertion.

The more reliable solution adopted for this work was to add a new contour point at the midpoint of the undefined line segment, and to use this point to split the

line segment into two new line segments. The new contour point is then added to the mesh using the same method as used in the section 4.5.2. If either or both of the new line segments are still not defined in the mesh the splitting process is repeated. This node insertion process is summarised in figure 4.8.

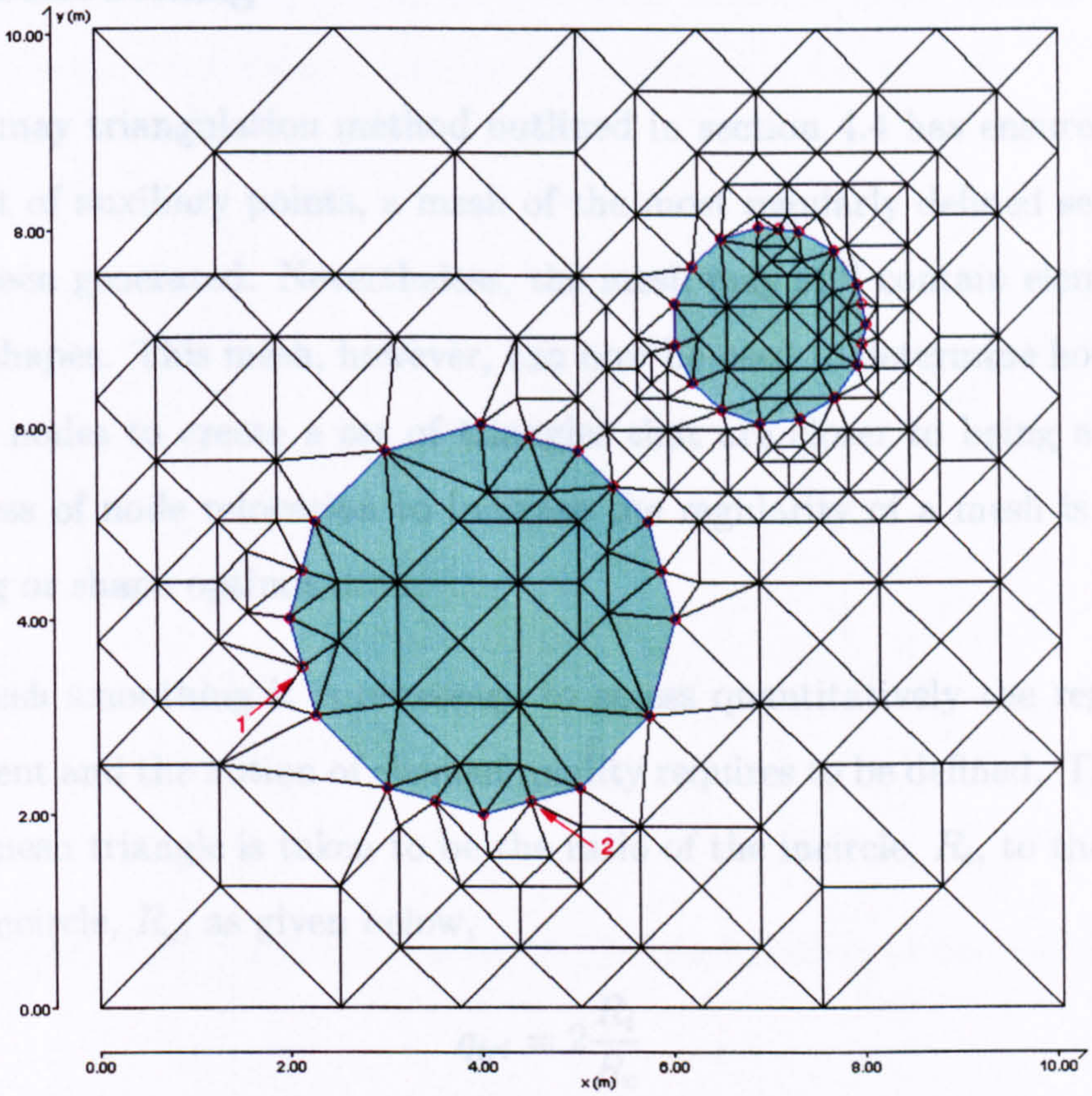

Figure 4.9: Triangulation after application of the node insertion procedure to define prescribed contours.

By checking each contour line segment in turn and by using the above point insertion technique if the segment is not defined within the mesh all the contours can be correctly defined. For the example case involving two contours the final

mesh is illustrated in figure 4.9. In this figure both contours are fully defined. In particular two nodes are identified, 1 and 2, which have been added to define the contour line segments, a and b as defined in figure 4.6.

4.5.4 Smoothing

The Delaunay triangulation method outlined in section 4.4 has ensured that for a given set of auxiliary points, a mesh of the most regularly defined set of triangles has been generated. Nevertheless, the mesh may still contain elements with irregular shapes. This mesh, however, can now be used to determine how to reposition the nodes to create a set of triangles that are closer to being equilateral. The process of node relocation to increase the regularity of a mesh is known as smoothing or shape optimisation.

For mesh smoothing it is necessary to assess quantitatively the regularity of each element and the notion of element quality requires to be defined. The quality, q_{tri}, of a mesh triangle is taken to be the ratio of the incircle, R_i, to the radius of the circumcircle, R_c, as given below,

$$q_{tri} = 2\frac{R_i}{R_c} \tag{4.1}$$

The factor 2 in the above equation gives a value for q_{tri} in the range 0 to 1. A quality value close to 0 would indicate a triangle of poor quality, or in other words a triangle with an acute inner angle. A quality value of 1 would indicate an equilateral triangle. This equation can be rewritten, in terms of the side lengths of the triangle a, b and c as shown in equation 4.2, which can be easily calculated for any triangle,

$$q_{tri} = \frac{8(s-a)(s-b)(s-c)}{abc} \qquad s = \frac{1}{2}(a+b+c) \tag{4.2}$$

Two different smoothing schemes were used in this work; smoothing by the combination of two nodes and smoothing by node repositioning or Laplacian smoothing [57].

Smoothing by the combination of two nodes is based on detecting poorly defined elements, and attempting to remove them from the mesh by combining two nodes. The node combining procedure is illustrated in figure 4.10.

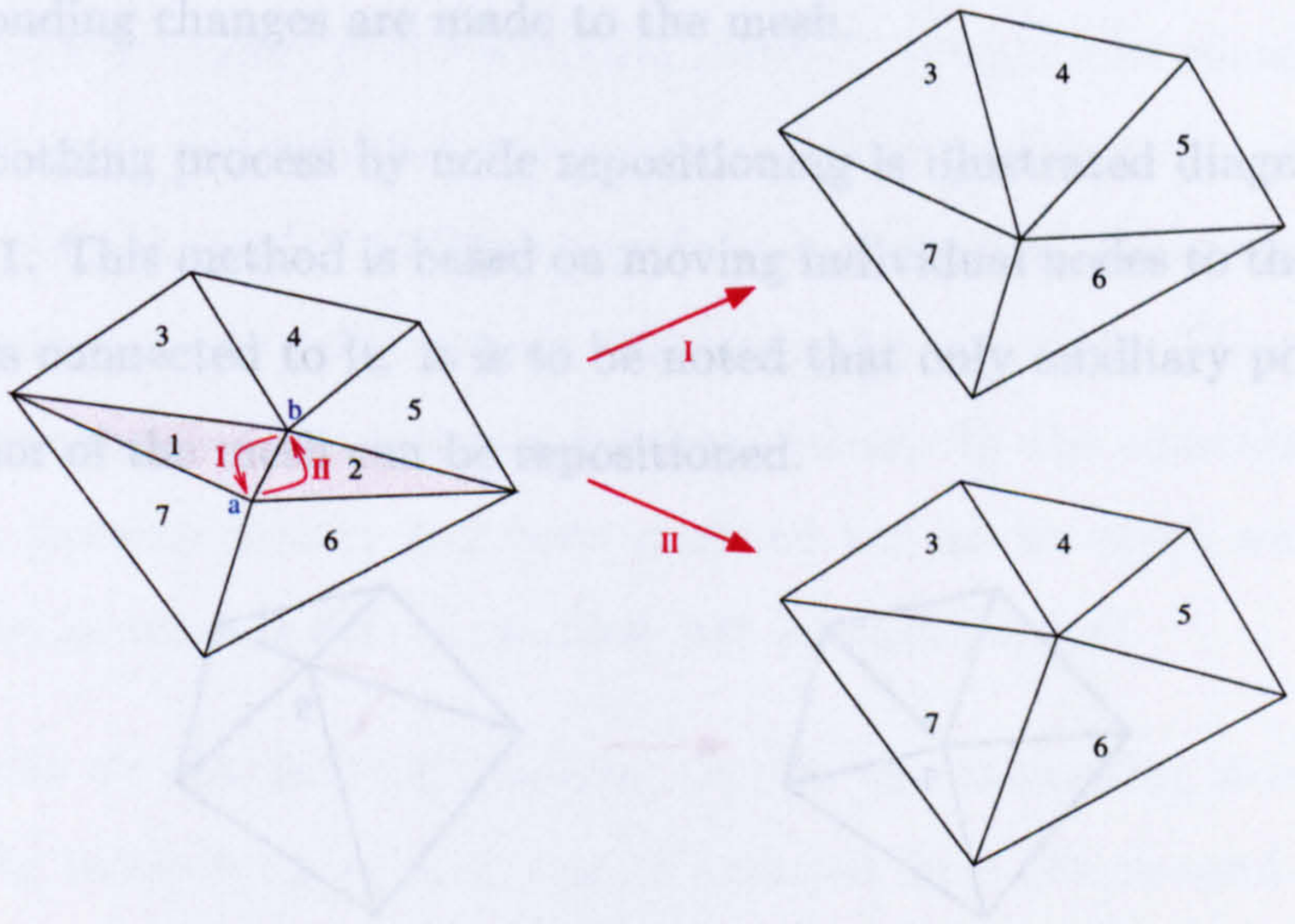

Figure 4.10: Mesh smoothing by the combination of two nodes.

With reference to figure 4.10 element 1 has been identified as having a poor quality. The shortest side of the triangle is chosen, the nodes of this side are denoted a and b, and all the elements that share these edge nodes are selected. The minimum element quality and average quality of this set of triangles is calculated. If node a can be repositioned, then it is set equal to node b. A node can be repositioned if it is in the interior of the mesh and if it is not a contour point. Elements 1 and 2 now have zero area and therefore they are removed from the

set of triangles. The average and minimum quality for this new arrangement is determined. The set of triangles are returned to their original mesh configuration and the process is repeated, this time, however, if node b can be moved it is set equal to node a. If both a and b have a fixed mesh position the smoothing procedure fails and the mesh is left unaltered. The arrangement with the best average quality value, that does not create any elements with a quality poorer than the quality of the worst element in the original set of elements is chosen, and the corresponding changes are made to the mesh.

The smoothing process by node repositioning is illustrated diagrammatically in figure 4.11. This method is based on moving individual nodes to the barycentre of the points connected to it. It is to be noted that only auxiliary points that lie in the interior of the mesh can be repositioned.

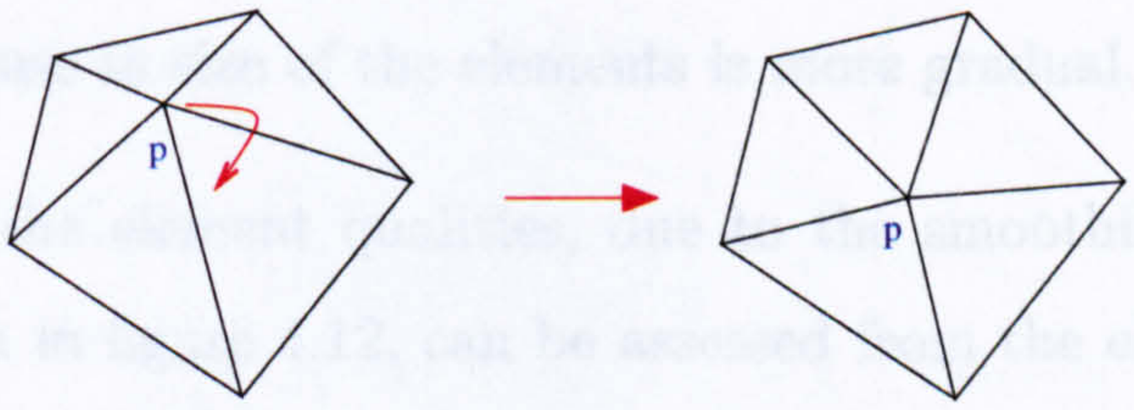

Figure 4.11: Mesh smoothing by node repositioning.

If the polygon created by the neighbouring points is not convex, checks are made to ensure that the new position of the node is valid in that it does not lie outside the polygon. If the new node position is valid, and the average element quality is increased, then the node is repositioned.

Both the smoothing procedures outlined do not depend on the original mesh being of type Delaunay. It is to be noted, however, that neither method guarantees

that when it is applied to a Delaunay mesh that the mesh will remain of type Delaunay. If a Delaunay mesh is required then the mesh can be reconstructed using the new node coordinates.

An example case of smoothing a mesh surrounding a complex contour is illustrated in figure 4.12. These meshes were constructed from approximately 2200 elements and 1100 nodes. In the upper diagram the unsmoothed mesh, generated from the set of auxiliary points created by the quadtree method, is illustrated. The rectangular geometry of the resulting mesh is evident. The smoothed version of the initial mesh is illustrated in the lower diagram. This mesh was generated by first applying the node combining operation, repositioning the movable nodes to their barycentres and subsequently reconstructing the mesh. The repositioning and mesh regeneration process was repeated twice. In the smoothed mesh the variation in element density has been retained but as we move away from the boundary the increase in size of the elements is more gradual.

The effects on the element qualities, due to the smoothing process used to generated the mesh in figure 4.12, can be assessed from the element quality profile plots in figure 4.13. These plots record the number of elements that have a quality in a particular range. The profile of the unsmoothed mesh has a large peak corresponding to the high number of triangles in the unsmoothed mesh that have a right angle and two sides of equal length. Triangles of this type have a quality of 0.828. For the unsmoothed mesh the average element quality is 0.815. The distribution of element qualities after smoothing is greater, but the average element quality has improved to a value of 0.902.

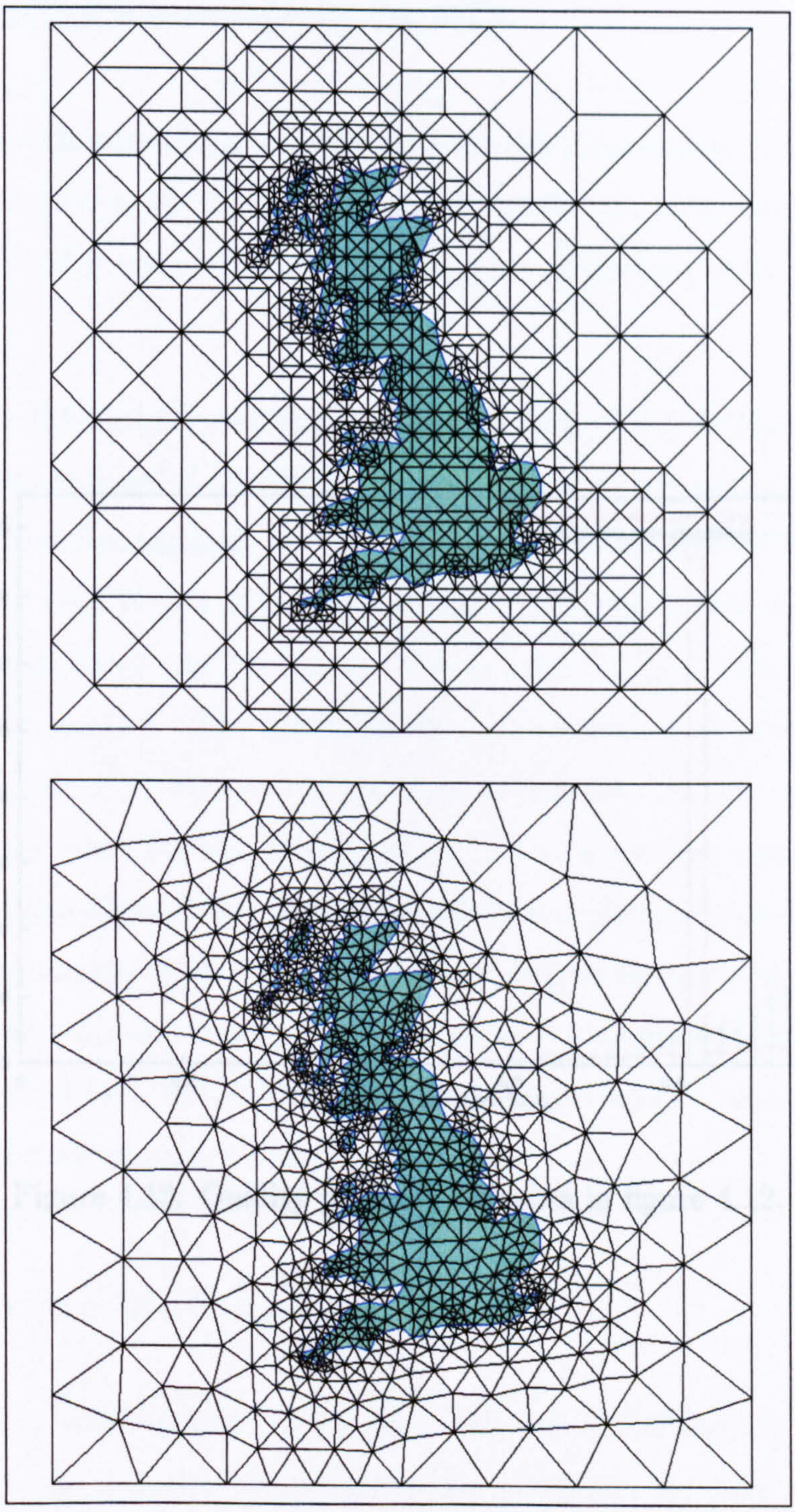

Figure 4.12: Triangular mesh. Before smoothing (upper). After smoothing (lower).

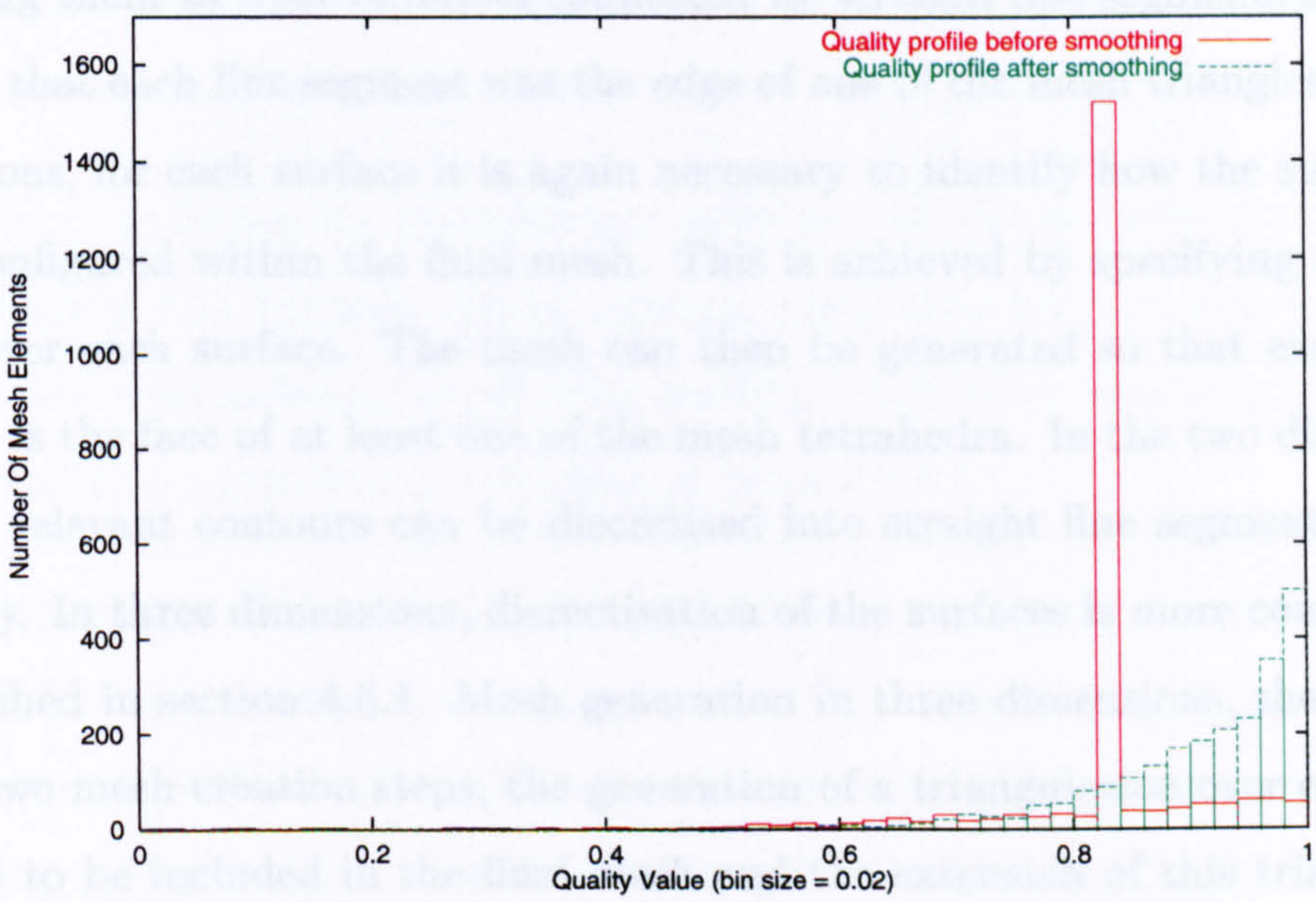

Figure 4.13: Quality profiles of meshes in figure 4.12.

4.6 Mesh Generation in 3D

For this project the concepts and procedures for two dimensional mesh generation, as described in section 4.5 require to be developed for the three dimensional case. The generation of meshes of tetrahedral elements around prescribed surfaces are considered.

In the two dimensional case the contours are defined within the final mesh by specifying them as a set of points connected by straight line segments and it was ensured that each line segment was the edge of one of the mesh triangles. In three dimensions, for each surface it is again necessary to identify how the surfaces are to be configured within the final mesh. This is achieved by specifying a triangulation over each surface. The mesh can then be generated so that each surface triangle is the face of at least one of the mesh tetrahedra. In the two dimensional case all relevant contours can be discretised into straight line segments without difficulty. In three dimensions, disrectisation of the surfaces is more complex, and is described in section 4.6.1. Mesh generation in three dimensions, therefore, involves two mesh creation steps; the generation of a triangulation over each of the surfaces to be included in the final mesh and the extension of this triangulation to a total space filling mesh of tetrahedra.

4.6.1 Surface Mesh Generation

To describe the surfaces over which the mesh has to be formed two standard surface shapes are defined: Triangular surfaces, defined by three vertex points; convex quadrilateral surfaces, defined by four co-planar vertex points. Although any planar quadrilateral can be easily split into a number of triangles it was decided to use quadrilateral surface shapes for this work to attempt to keep the

area of each individual surface as large as possible and to avoid surfaces that have small inner angles. It is assumed that any structure to be modelled can be built up from a number of these surface shapes.

A main problem with generating any surface mesh is to maintain the continuity in the triangulation between two adjoining surfaces. This difficulty can be overcome by setting the following requirements. If two surfaces are connected, both must only share the same vertex or an entire edge and both must define the same number of triangles along that edge. Two correctly connected quadrilateral surfaces are illustrated in figure 4.16.

Before progressing the triangulation processes all the surfaces are checked to ensure that if two surfaces are in contact, then they are correctly connected. Surfaces are automatically subdivided until they are all correctly specified. The surface splitting algorithm is described in section 4.6.2.

To ensure that each surface defines the correct number of triangles along each edge a length parameter, l, is associated to each surface. This length is subsequently used to define a set of points along each edge. Each point is separated by a distance corresponding to the longest length, which is shorter than l, that divides the length of the side. A Delaunay triangulation over the surface is formed using these points. By this process it is ensured that provided two connected surfaces have the same length parameter then continuity in the triangulation is maintained between the two surfaces. To produce a regular triangulation over the surface, extra points are added in the interior of the surface. This is managed by defining a maximum triangle area, $A_{max} = \sqrt{3}/4\, l^2$, based on the length parameter, l, and corresponding to the area of a equilateral triangle with a side length of l. A new point is added to the Delaunay surface triangulation at the centre of gravity of each triangle with an area greater that A_{max}. Points are added until

no triangle with an area greater than A_{max} is present. If required, the surface can be smoothed by repositioning the surface points as outline in section 4.5.4. A summary of the triangulation of a quadrilateral surface is illustrated in figure 4.14.

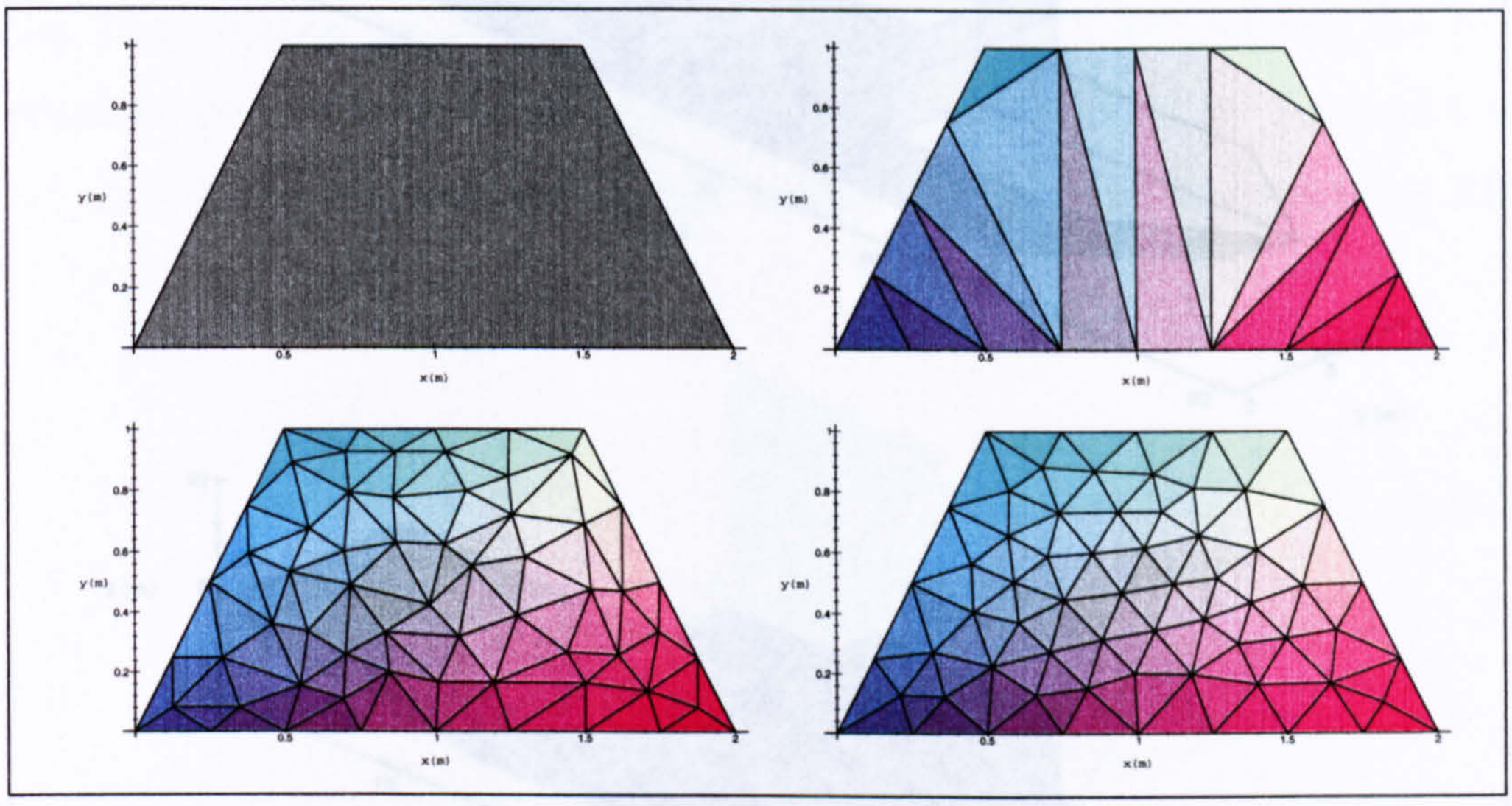

Figure 4.14: Surface mesh generation. Initial planar quadrilateral (upper left). Triangulation of surface with no internal point (upper right). Triangulation of surface with internal points (lower left). Final surface mesh after smoothing (lower right).

To demonstrate the application of the surface mesh generation process to complex structures, derived from a large number of surfaces, the example of a ship with average hull and superstructure as illustrated in figure 4.15 is considered. The surfaces, and their relationships, on to which the mesh is generated is described by the upper diagram. The surface mesh, generated from approximately 9500 triangles, is illustrated in the lower diagram.

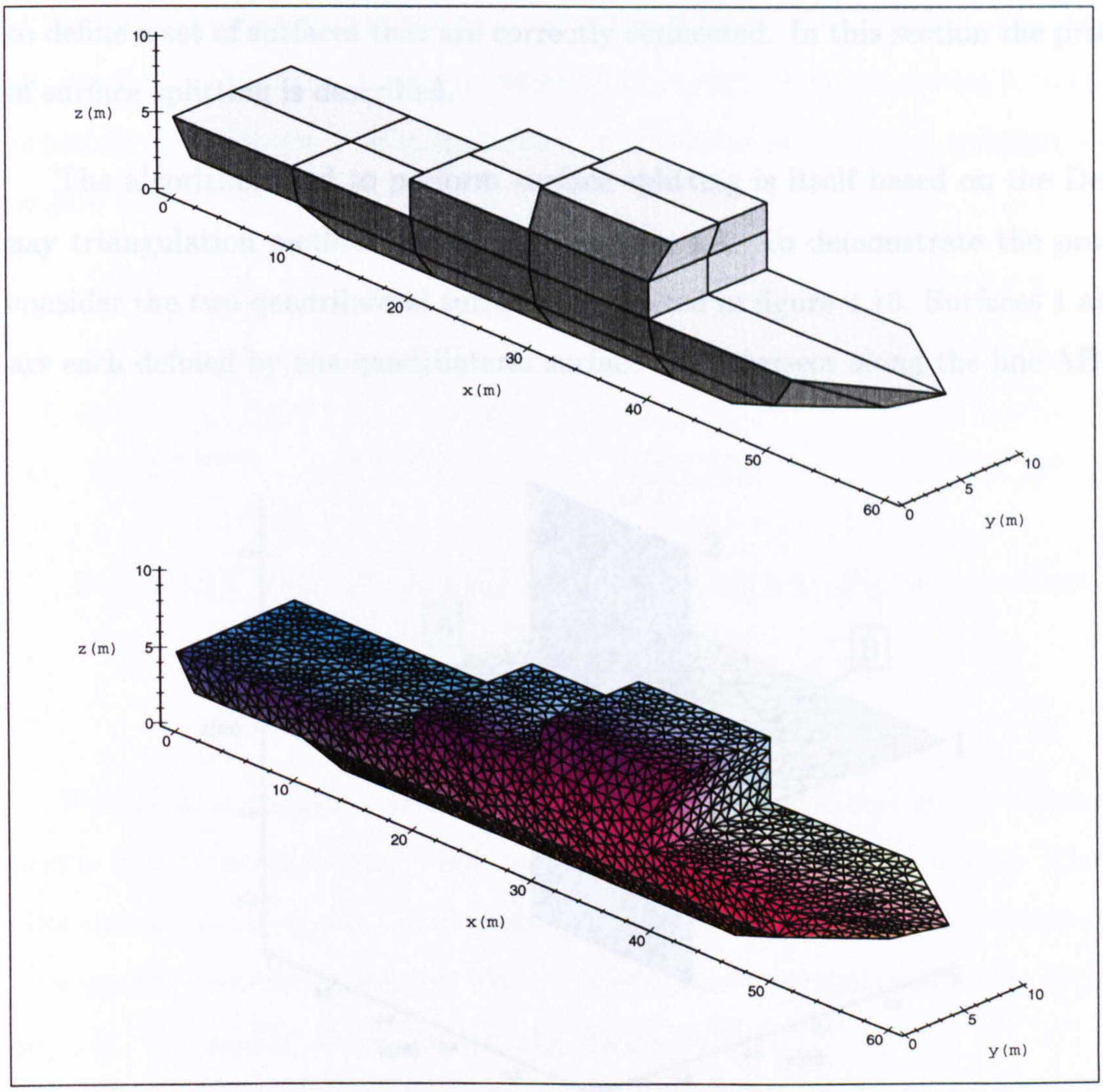

Figure 4.15: Surface mesh generation example. Surfaces defining ship (upper). Surface mesh (lower).

4.6.2 Surface Splitting

From section 4.6.1 the surface mesh generation process relies on the fact that for all the surfaces over which the mesh is to be generated, if two surfaces are in contact they must either only share the same vertex or an entire edge. Two surfaces cannot intersect each other. To ensure that all the surfaces are correctly defined in terms of their connectivity, any surfaces that do intersect are subdivided

to define a set of surfaces that are correctly connected. In this section the process of surface splitting is described.

The algorithm used to perform surface splitting is itself based on the Delaunay triangulation method described in section 4.4. To demonstrate the process consider the two quadrilateral surfaces illustrated in figure 4.16. Surfaces 1 and 2 are each defined by one quadrilateral surface and intersect along the line AB.

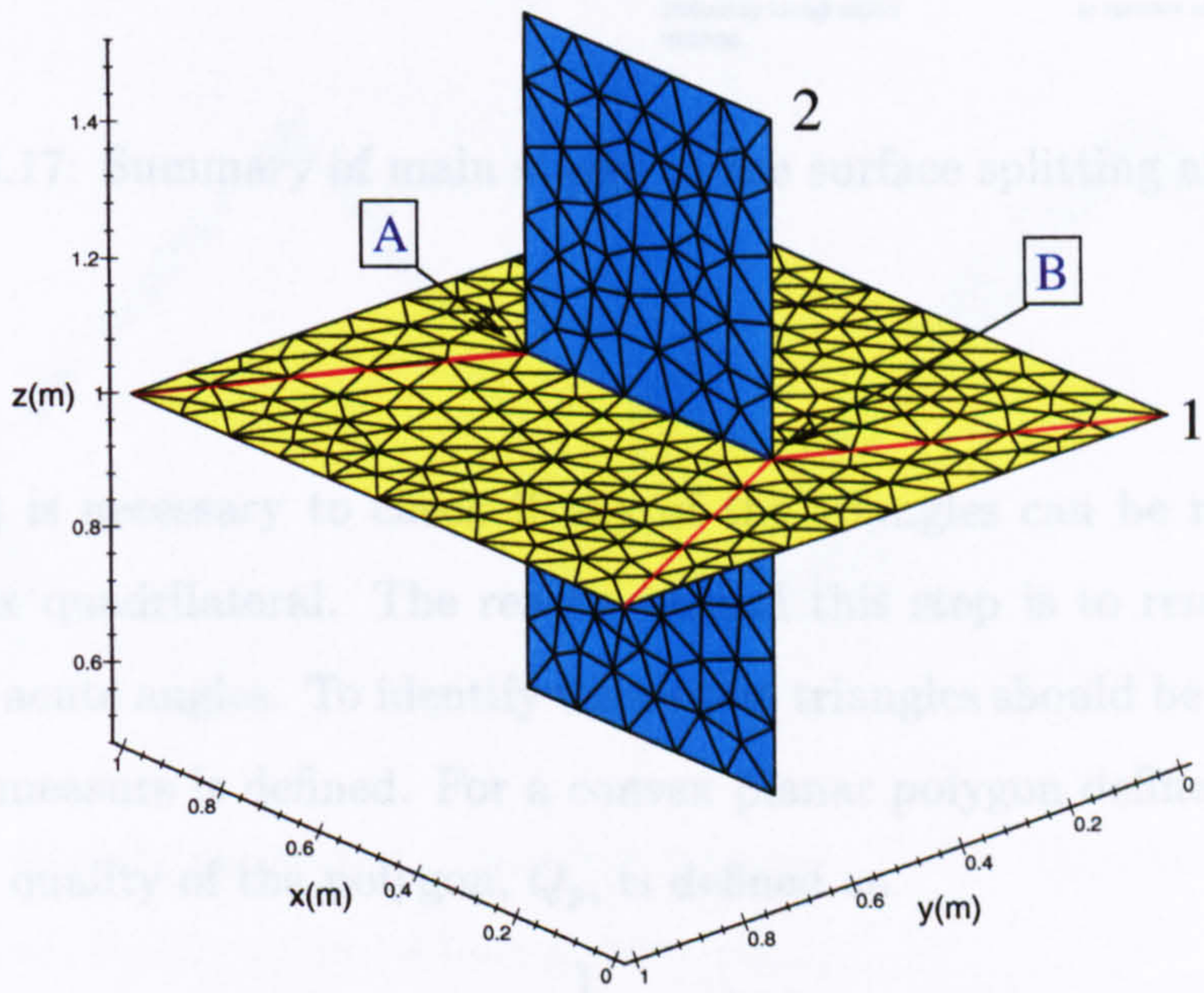

Figure 4.16: Surface mesh generated on two intersecting planar quadrilateral surfaces.

The splitting process applied to surface 1 is summarised in figure 4.17. This surface requires to be split to include the line segment AB. This is achieved by generating an initial triangulation and then incorporating the two points A and B by the Delaunay triangulation method. If the line AB is not defined by the edges

of the triangles, new points are added in a similar way to the method described in section 4.5.3. If the two surfaces intersect at a point then that point is similarly added to the surfaces. A triangulation that provides an adequate splitting of the surface is obtained.

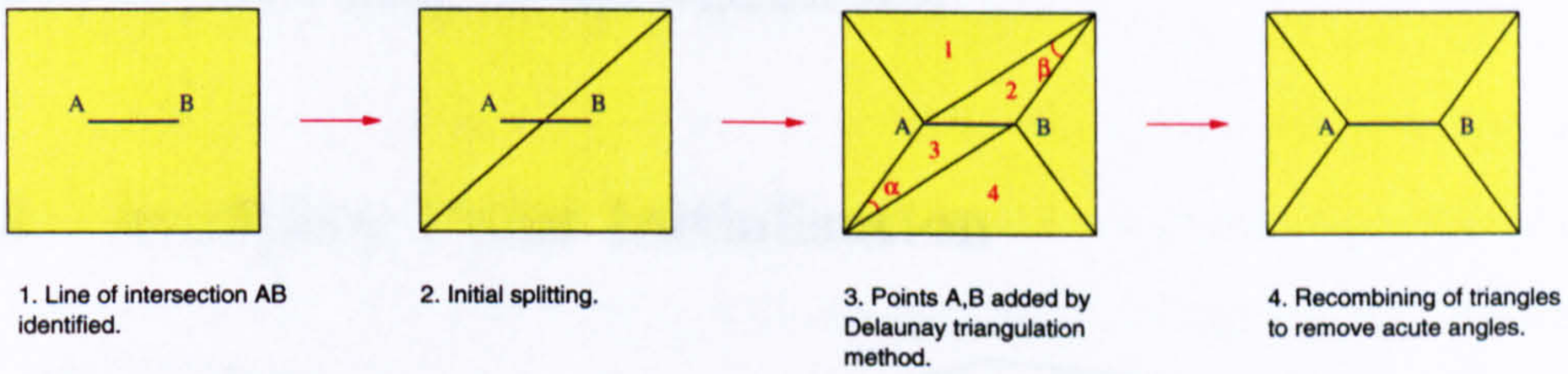

Figure 4.17: Summary of main stages of the surface splitting algorithm.

Finally it is necessary to check if any of the triangles can be recombined to give a convex quadrilateral. The reason behind this step is to remove triangles that contain acute angles. To identify where two triangles should be recombined a new quality measure is defined. For a convex planar polygon defined by n points $p_1, .., p_n$, the quality of the polygon, Q_p, is defined as,

$$Q_p = \frac{1}{2\pi} \min \{\theta_i\} \tag{4.3}$$

where $i = 1, .., n$ and θ_i is the angle between the vectors $v_i = p_{i-1} - p_i$ and $v_{i+1} = p_{i+1} - p_i$. For a given surface, the triangles can be considered sequentially from the lowest Q_p to the greatest. A triangle is combined with a neighbouring triangle if: The two triangles give a convex quadrilateral; the two triangles are not connected by an edge that is required to be defined by the splitting process; improvement in Q_p between the triangle and the quadrilateral formed is the best that can be achieved for that triangle, noting that for a given triangle there is the possibility of three different combinations. With reference to figure 4.17(3),

the two triangles 1 and 2 have been combined to eliminate the small angle β and triangles 3 and 4 have been combined to remove the angle α. After splitting the surface meshes are generated over the resultant set of surfaces. In figure 4.16 the meshes over the surfaces are shown, and it is to be noted that the surface meshes are correctly joined along the line segment AB.

4.6.3 Auxiliary Point Initialisation

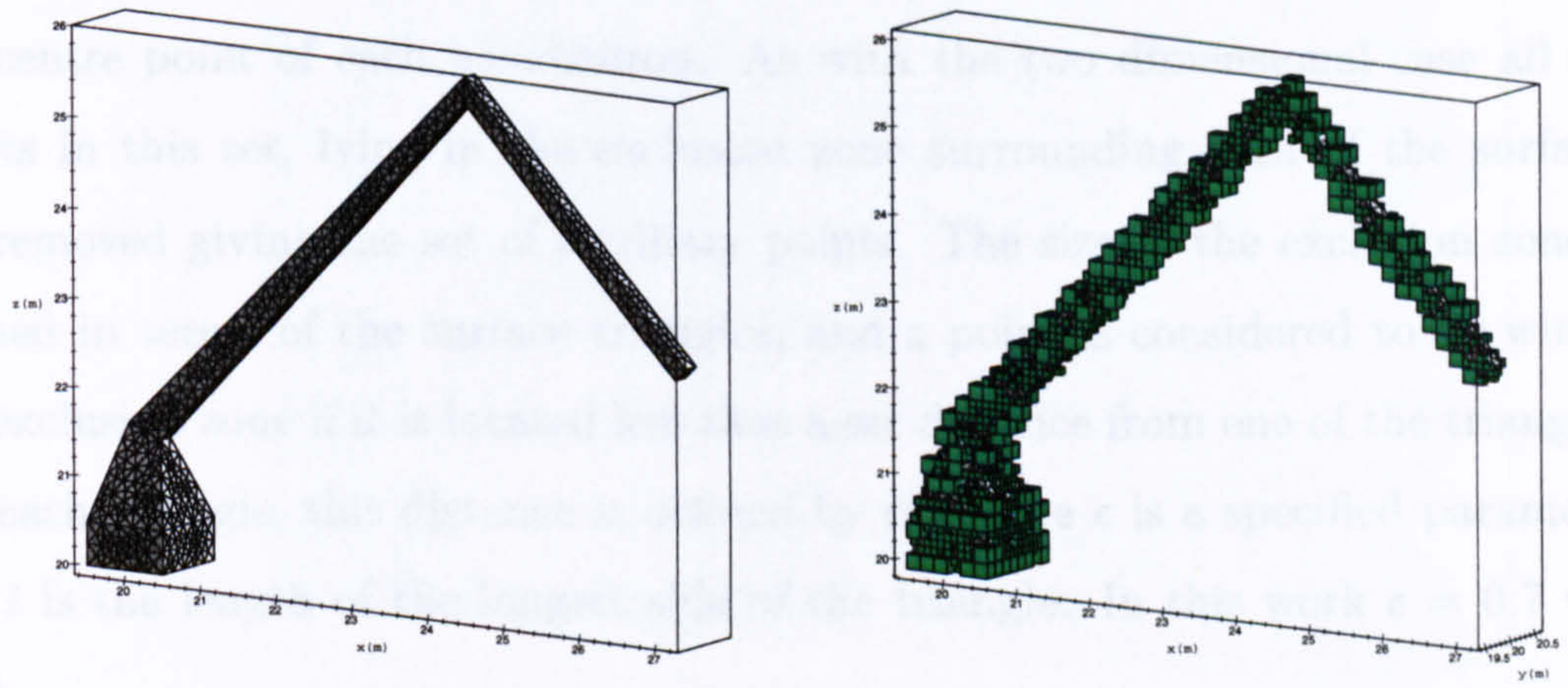

Figure 4.18: Surface mesh of a crane like structure (left). Hexahedra (green) of the octree mesh that contain surface points (right).

The three dimensional equivalent of the quadtree method described in section 4.5.1 is known as the octree method. It is to be noted that grid deformation mesh generation techniques, based on the octree method have been reported [58]. The splitting procedure is effectively identical to that described in the two dimensional case except that it is necessary to specify an initial hexahedron which encompasses all the surface points. As in the two dimensional case the initial

hexahedron defines the outer perimeters of the final mesh. Each hexahedron is split into eight daughters, depending on the number of surface points contained within its volume, and the same balancing procedure is used to ensure that no element is adjacent to another which is more than two generations removed.

In the example of a crane like structure, illustrated in figure 4.18, some of the octree hexahedra, cubes in this case, are shown (right) surrounding the surface mesh defining the crane structure (left). Only the cubes containing a surface point have been included. A set of mesh points is generated by taking the vertices and the centre point of each hexahedron. As with the two dimensional case all the points in this set, lying in the exclusion zone surrounding each of the surfaces are removed giving the set of auxiliary points. The size of the exclusion zone is defined in terms of the surface triangles, and a point is considered to lie within the exclusion zone if it is located less that a set distance from one of the triangles. For each triangle, this distance is defined by ϵl, where ϵ is a specified parameter and l is the length of the longest side of the triangle. In this work $\epsilon = 0.7$ was used.

In addition, the final number of elements within the mesh can be controlled by specifying a limit on the minimum and maximum generation.

4.6.4 Delaunay Triangulation in 3D

The Delaunay triangulation was progressed in much the same way as the two dimensional case. Here, however, the Delaunay triangulation is initialised by subdividing the first generation hexahedron used in the octree method into 6 tetrahedra, with the nodes being added to the mesh in a similar way as for the two dimensional case.

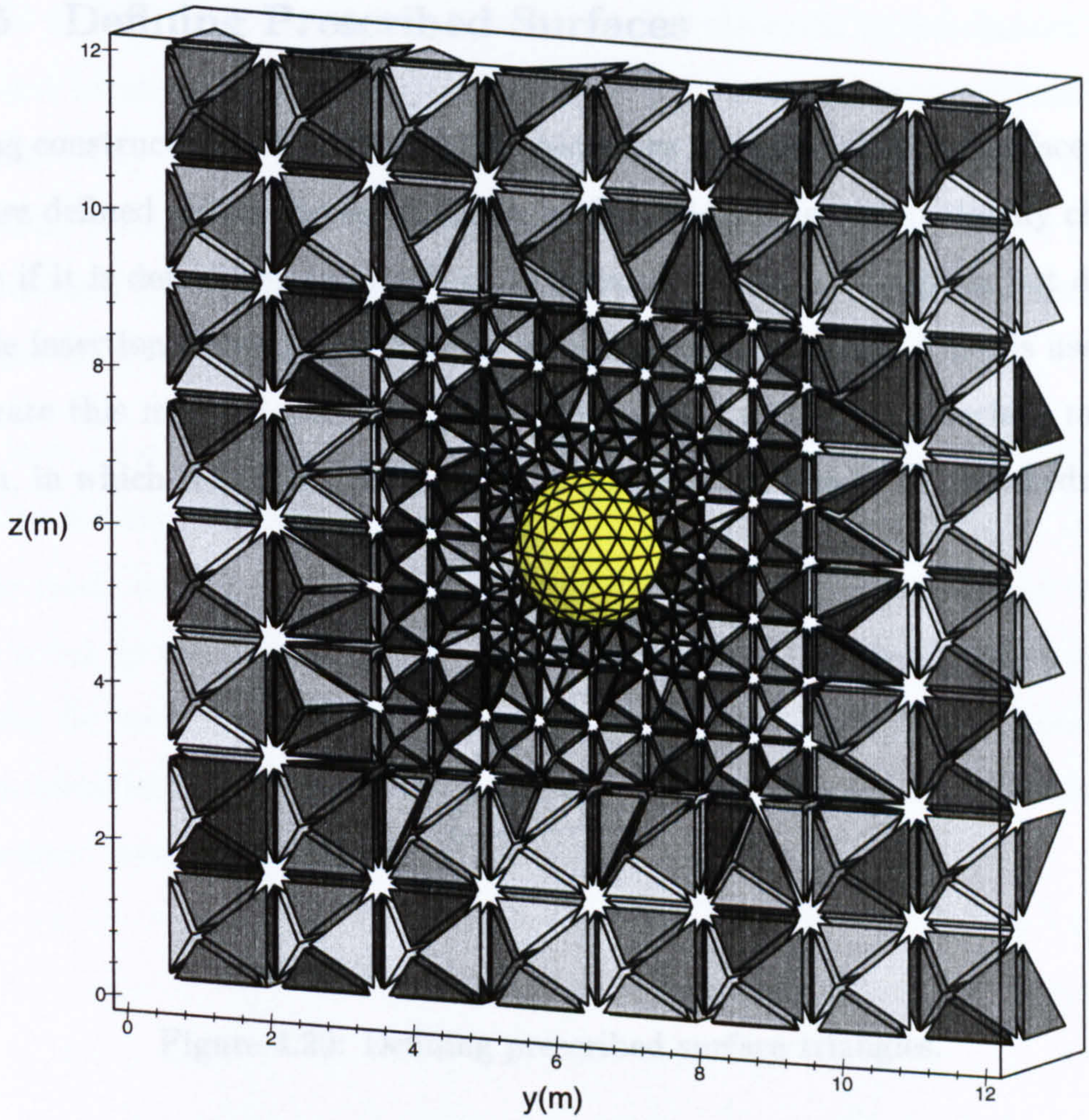

Figure 4.19: Three dimensional Delaunay mesh generated around a sphere.

An example of a section of the three dimensional Delaunay triangulation, generated around a spherical surface of radius 1 m is illustrated in figure 4.19. The complete mesh was generated in a cubical box of side length 12 m and was composed of approximately 20000 tetrahedra. The variation in element size is to be noted with the size of each the elements increasing as the distance from the sphere increases.

4.6.5 Defining Prescribed Surfaces

Having constructed an initial mesh it is necessary to ensure that the surface triangles are defined within the mesh. Each surface triangle is systematically checked to see if it is defined by the mesh of tetrahedra. When a triangle is not defined a node insertion technique, similar to that described in section 4.5.3, is used. To illustrate this method consider figure 4.20 where a section of a surface mesh is shown, in which triangles 1 and 2 are not defined in the mesh by tetrahedra.

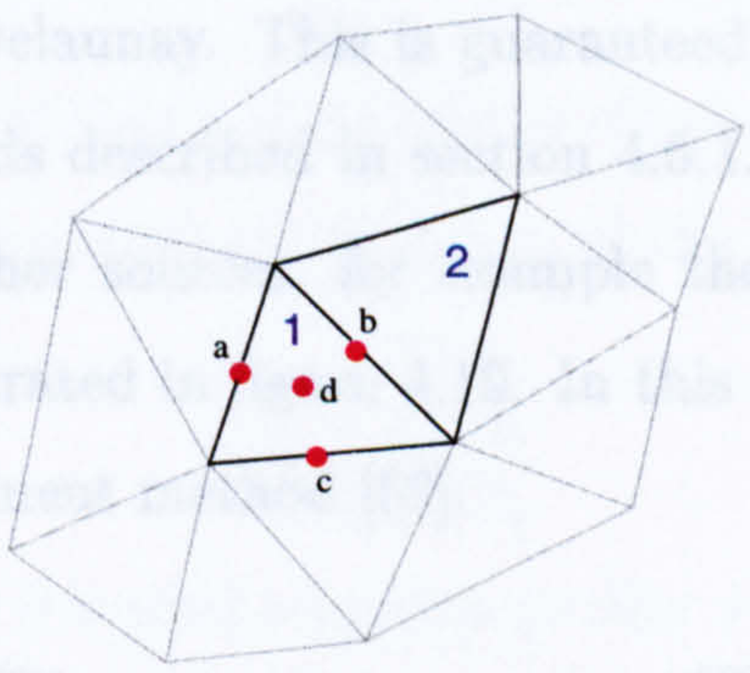

Figure 4.20: Defining prescribed surface triangles.

Working with element 1, four new node positions are tested, a,b and c, corresponding to the midpoint of each of the element edges and d, the centre of gravity of the triangle. For each of these positions, the effect of adding a new node to the mesh and to the surface triangulation at this position is measured. This means that for each case the number of surface triangles defined and the average quality of the submesh of tetrahedra in contact with triangle 1 is determined. A node is then inserted at the position that defines the most surface triangles. If two or more node positions define the same maximum number of surface triangles, the node is inserted at the position that gives the best average quality. Using this

method to find the node position, the quality of the mesh is maintained and a minimum number of additional points are added to the mesh. In this example case the most likely outcome would be the addition of a node at position b, because this would result in defining the surface area of both undefined triangles 1 and 2 and maintain the element quality of the surrounding tetrahedra. This process is repeated until every surface triangle is defined within the mesh.

It is to be noted that since the nodes are added to the surface triangulation, using the two dimensional version of Watson's method, it is a requirement that the surface mesh be of type Delaunay. This is guaranteed when the surface mesh is constructed by the methods described in section 4.6.1. However, surface meshes can also be used from other sources, for example the surface mesh generating the spherical surface illustrated in figure 4.19. In this case the surface mesh was constructed using a refinement method [59].

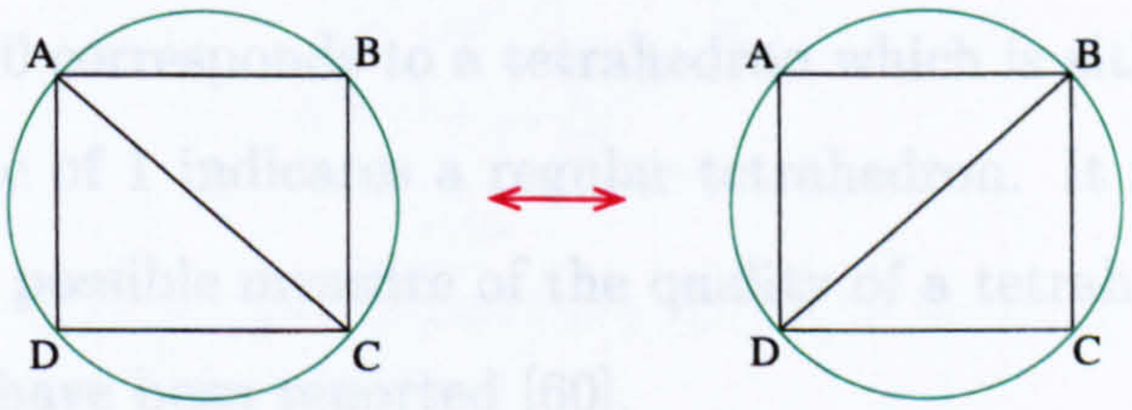

Figure 4.21: Degenerate triangulations of the four co-circular nodes A,B,C and D.

The above procedure is the main process used to define the surface triangles for this work. An additional check, however, is performed on pairs of degenerate triangles within the mesh. When four nodes are co-circular there are two possible triangular splittings of the nodes. With reference to figure 4.21, the four nodes

A,B,C and D can be split into two triangles to give either ABC and ACD or ABD and BCD. Each triangle in both the arrangements has the same circumsphere and circumpoint and, as such, either arrangement would be valid in a Delaunay triangulation. Before using the above node insertion strategy, therefore, a check is made to ensure that pairs of surface triangles, that are not defined in the mesh but have four co-circular nodes, cannot be defined by rearrangement.

4.6.6 Smoothing

As with the two dimensional case a value can be obtained for the quality, q_{tetra}, of a tetrahedron, by taking the ratio of the radius of the insphere, R_i, to the radius of the circumsphere, R_c.

$$q_{tetra} = 3\frac{R_i}{R_c} \tag{4.4}$$

In this equation the factor 3 is used to give a quality value in the range from 0 to 1. A value close to 0 corresponds to a tetrahedron which is either flat or long and narrow, and a value of 1 indicates a regular tetrahedron. It is to be noted that equation 4.4 is one possible measure of the quality of a tetrahedron, a number of different measures have been reported [60].

Smoothing of tetrahedral elements in a three dimensional mesh uses the extension of some of the methods described in section 4.5.4. The elimination of elements with a poor quality, by the combining of two nodes, is used when an element is detected that has one or more edges considerably shorter than the longest edge of the element. In the three dimensional case each edge that is half the length of the longest edge is tested. For each case that is checked, the average quality of the set of neighbouring tetrahedra is determined and the best arrangement, in terms of improved average element quality, is chosen.

Node repositioning to the barycentre of the surrounding polygon is used. It is to be noted that only nodes that do not lie on a surface or on the boundary of the mesh can be moved. As with the two dimensional case the smoothing procedure can be applied locally to a particular element, for example when an element with a poor quality is detected, the quality of the element can usually be improved by repositioning one of its nodes as previously described. Alternatively this procedure can be applied globally, thereby repositioning every movable node within the mesh, regardless of the quality of the surrounding elements. As for the two dimensional case this process can be coupled with a mesh regeneration step which restores the Delaunay properties of the mesh.

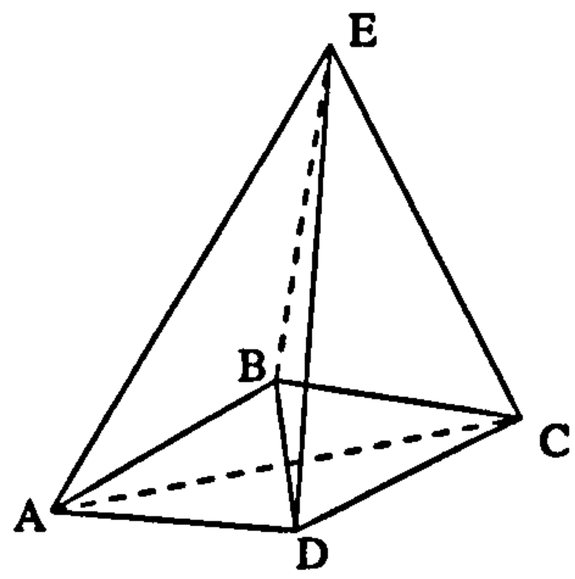

Figure 4.22: Smoothing by sliver removal.

In addition to these smoothing methods which are extensions of the procedures used in the two dimensional case, there is a third method which involves the removal of very thin elements or slivers [44]. Slivers are formed by four points that are not quite co-planar. In figure 4.22 a sliver is demonstrated, formed by the four points $ABCD$. The sliver is removed from the mesh by rearranging the two tetrahedra $ABDE$ and $BCDE$, to $ABCE$ and $ACDE$, and deleting it from the list of mesh elements. This rearrangement of the elements is only possible if

two of the four tetrahedra, that share a face with the sliver, also share a face with each other.

The effects of mesh smoothing in three dimensions is illustrated in figure 4.23. This diagram illustrates the surface mesh of an average ship structure and a set of surrounding elements. In each case the mesh was constructed from approximately 62000 elements and 9700 nodes generated around a surface mesh of 2800 triangles. The elements have been colour coded according to their quality. In the upper diagram of figure 4.23 the mesh generated around the ship structure before smoothing is illustrated and the box structure that is generated by the octree method can be clearly identified. In the lower diagram of figure 4.23 the results of smoothing the mesh by the global smoothing process described earlier in this section is evident. In this particular example both the auxiliary node repositioning and mesh regeneration processes were performed twice. In the smoothed mesh it is to be noted that the change in element size is gradual.

An assement of the change in element quality, due to the smoothing processes applied to the mesh in figure 4.23 (upper), can be made from the element quality profile plots in figure 4.24. Similar to the two dimensional study, the profile for the unsmoothed mesh has individual irregular peaks. These correspond to the regular node positions generated by the octree method. The average quality of the unsmoothed mesh is 0.779. The profile for the smoothed mesh shows a greater variation in the element quality, but the average element quality has improved to a value of 0.812. The large peak at 0.94 in the unsmoothed mesh has, however, diffused towards elements of lower quality.

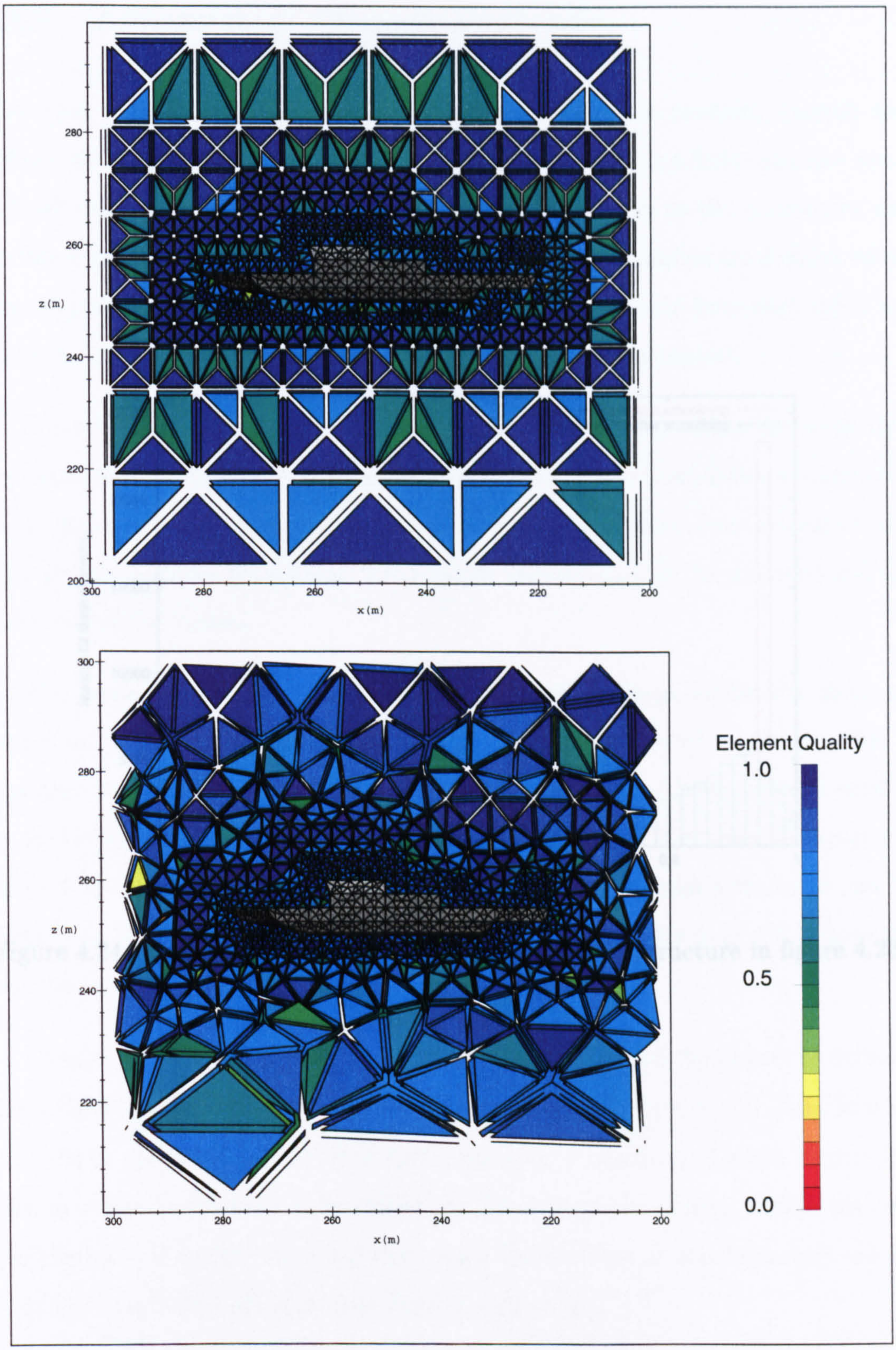

Figure 4.23: Mesh elements close to a ship structure. Before smoothing (upper). After smoothing (lower). The colour of each element corresponds to its quality.

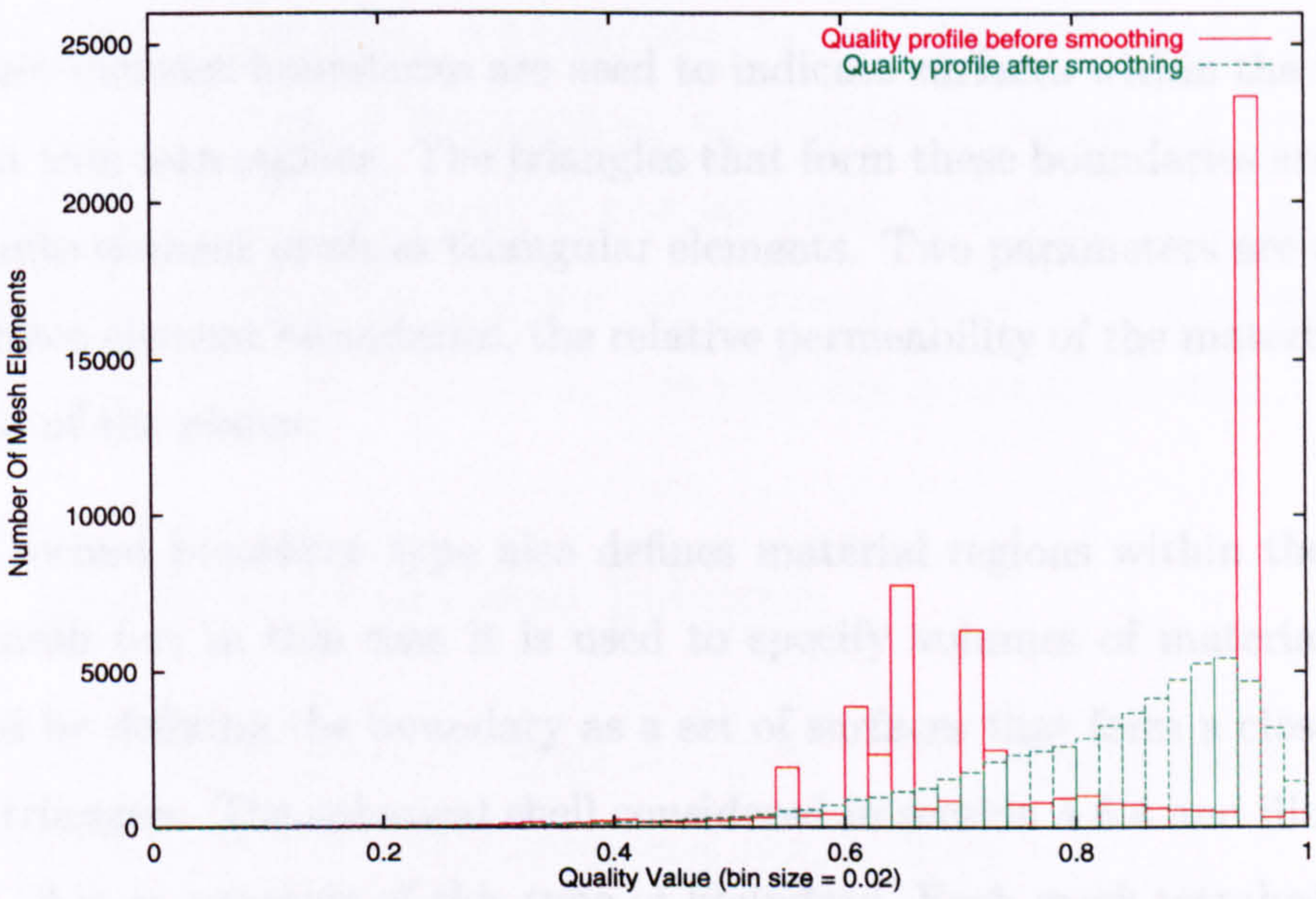

Figure 4.24: Quality profiles of meshes around the ship structure in figure 4.23.

4.6.7 Allocation of Element Properties

Now that a mesh has been generated that fills the entire problem domain and defines all the prescribed surfaces, the last stage of creating a finite element mesh is to allocate the appropriate element types and properties to the tetrahedra and surface triangles of the mesh. To achieve this a set of boundaries are defined which impart particular properties to the mesh surfaces. Four main boundary types are defined: Surface element; material volume; coil; defined potential.

Surface element boundaries are used to indicate surfaces within the mesh that represent thin iron regions. The triangles that form these boundaries are included in the finite element mesh as triangular elements. Two parameters are associated with surface element boundaries, the relative permeability of the material and the thickness of the plates.

The second boundary type also defines material regions within the finite element mesh but in this case it is used to specify volumes of material. This is managed by defining the boundary as a set of surfaces that form a closed shell of surface triangles. The spherical shell considered in section 4.6.4 and illustrated in figure 4.19 is an example of this type of boundary. Each mesh tetrahedra can be checked to identify if it lies within the interior of this boundary and if it does the relative permeability of the element can be set as required.

To specify current carrying coils within the mesh a coil boundary is defined. Here, three parameters are required: The current in the coil; a coil identification number, to allow the current in a particular coil to be changed when required; a normal vector to the surface, to define the direction of the current within the coil. Tetrahedra and surface elements that touch the surfaces of this boundary are set to define a potential offset as described in section 3.4.

The final boundary type is used to define nodes with a fixed potential in the mesh. The most important use of this boundary type is to include the effects of a uniform external field as described in section 3.5.

4.7 Mesh Refinement

There are several different approaches to mesh refinement. These approaches may be classified as either h or p methods. In the h method, the accuracy of the solution of the problem is increased by a reduction in the size of the elements. This is achieved by the addition of new elements. The p method, on the other hand, leaves the element size constant but increases the order of the approximating shape functions over the element. In this work the h method is used.

4.7.1 Mesh Modification Scheme

The creation of new elements within the mesh is achievd by a bisection process. This is illustrated for the two dimensional case in figure 4.25.

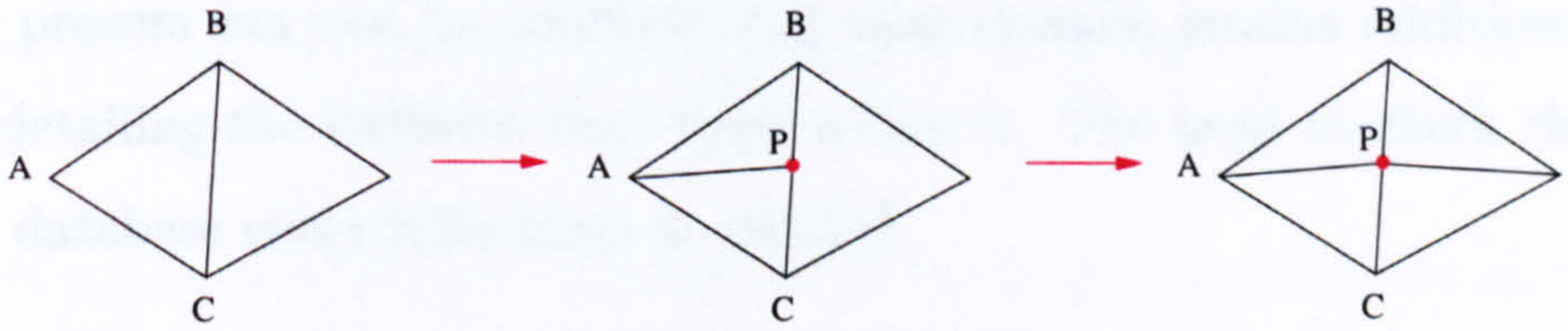

Figure 4.25: Mesh refinement scheme in two dimensions.

In this diagram element ABC is refined. The longest side of this element, BC, is determined and a new node is then inserted into the mesh at the midpoint of

this edge, point P. The element is subsequently split to give two new elements ABP and ACP. All remaining mesh elements are checked to see if they share the edge BC and if so they are split in a similar fashion using the new node P. The overall application of this modification scheme is summarised in figure 4.26, where an initial mesh containing 9 elements is refined to a mesh of approximately 1000 elements. This figure also demonstrates an extension to the refinement scheme illustrated in figure 4.25. If the side BC of the element to be refined has a specified geometry to represented, for example the circular contour in figure 4.26, then the point P can be positioned on this contour instead of the midpoint of the edge. This extension ensures that the geometry of defined contours is maintained within the mesh. Figure 4.26 also demonstrates how different element shapes can be defined, here rectangular element have been specified with the finite element scheme. These elements can be refined by splitting to two triangular elements. In addition, suitable pairs of triangular elements can be recombined to form rectagular elements.

In three dimensions the same procedure is performed, with a node being generated at the midpoint of the longest edge of the element. Here, however, the number of elements that share a particular edge within the mesh is not known and the process can can be accelerated if each element retains additional information detailing the elements that share a face it. The need to check the entire element database every refinement is avoided.

An alternative refinement scheme could be the addition of new nodes using the Delaunay triangulation method. At the onset of this project, however, the bisection splitting method was preferred because of its computational speed. Our work involves a set of mesh elements that is required to possess defined properties dependent on positioning within the mesh. Therefore, not only has the refinement

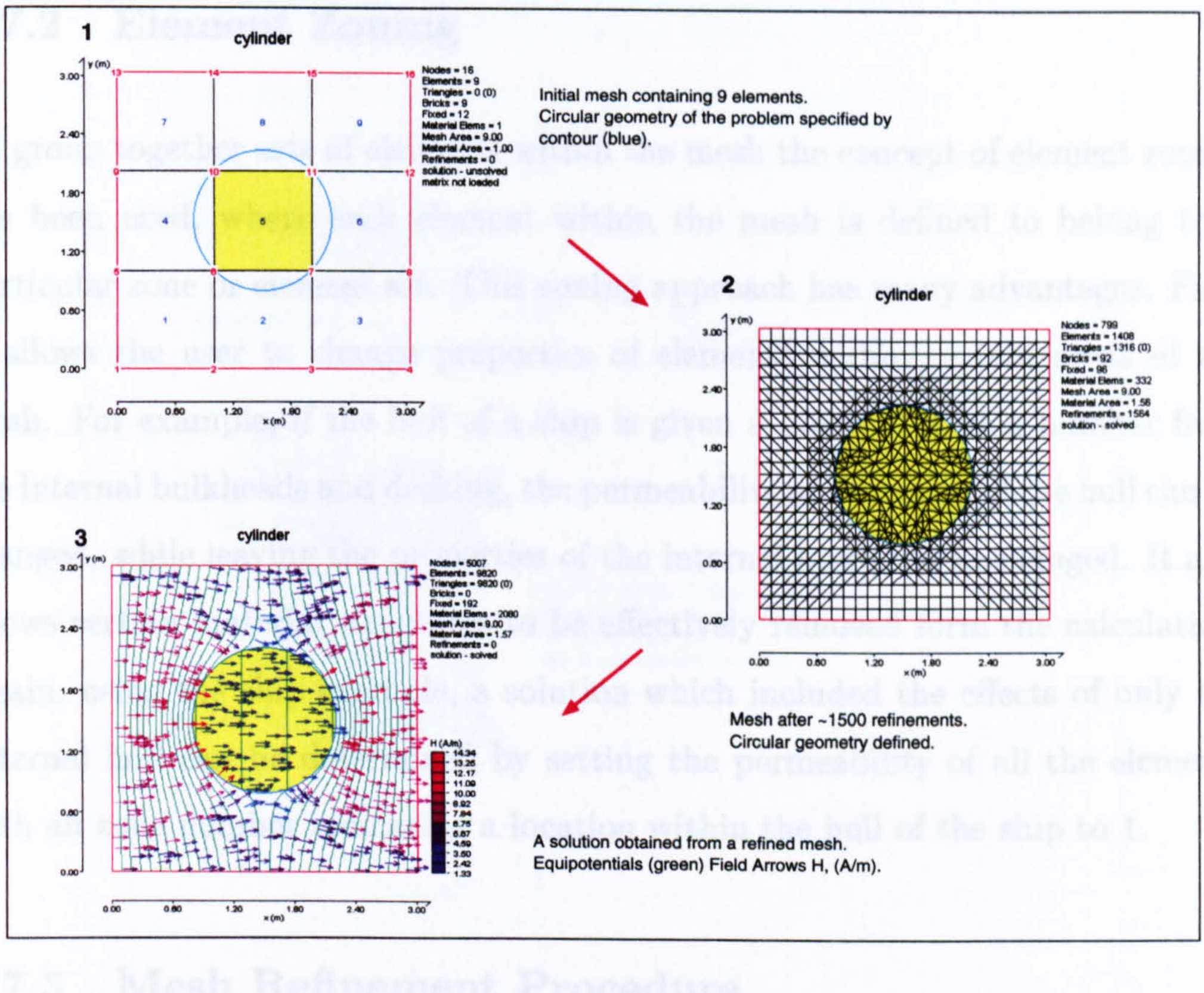

Figure 4.26: Finite element mesh refinement in two dimensions. Inset 1 - Initial mesh specified by only 9 rectangular elements with a required circular contour (blue). Inset 2 - After approximately 1500 refinements a much finer mesh is achieved which more precisely defines the circular contour. Inset 3 - Results of finite element analysis (equipotentials are shown in green).

process to generate additional elements but there is also the requirement to retain the element properties within the mesh. With the bisection method, the properties of the new elements can be derived directly from their parent elements. However, with the Delaunay triangulation method, new elements that are created by node insertion require additional checking to assign the appropriate element properties to each new element.

4.7.2 Element Zoning

To group together sets of elements within the mesh the concept of element zoning has been used, where each element within the mesh is defined to belong to a particular zone or element set. This zoning approach has many advantages. First it allows the user to change properties of elements within certain areas of the mesh. For example, if the hull of a ship is given a different zoning number from the internal bulkheads and decking, the permeability or thickness of the hull can be changed, while leaving the properties of the internal structure unchanged. It also allows certain material structures to be effectively removed form the calculation. Again, using the ship example, a solution which included the effects of only the external hull can be determined by setting the permeability of all the elements with an zone number indicating a location within the hull of the ship to 1.

4.7.3 Mesh Refinement Procedure

The refinement process used in this work allows the maximum element volume within certain zones of the mesh to be specified. The mesh elements within this zone are subsequently refined by the scheme outlined in section 4.7.1 until no elements present in the zone have a volume greater than the specified maximum volume.

4.8 Summary and Discussion

In this chapter the mesh generation process used in this project has been described. The two dimensional mesh generation process, described in section 4.5,was implemented as a Java code. The three dimensional work reported in section 4.6, which

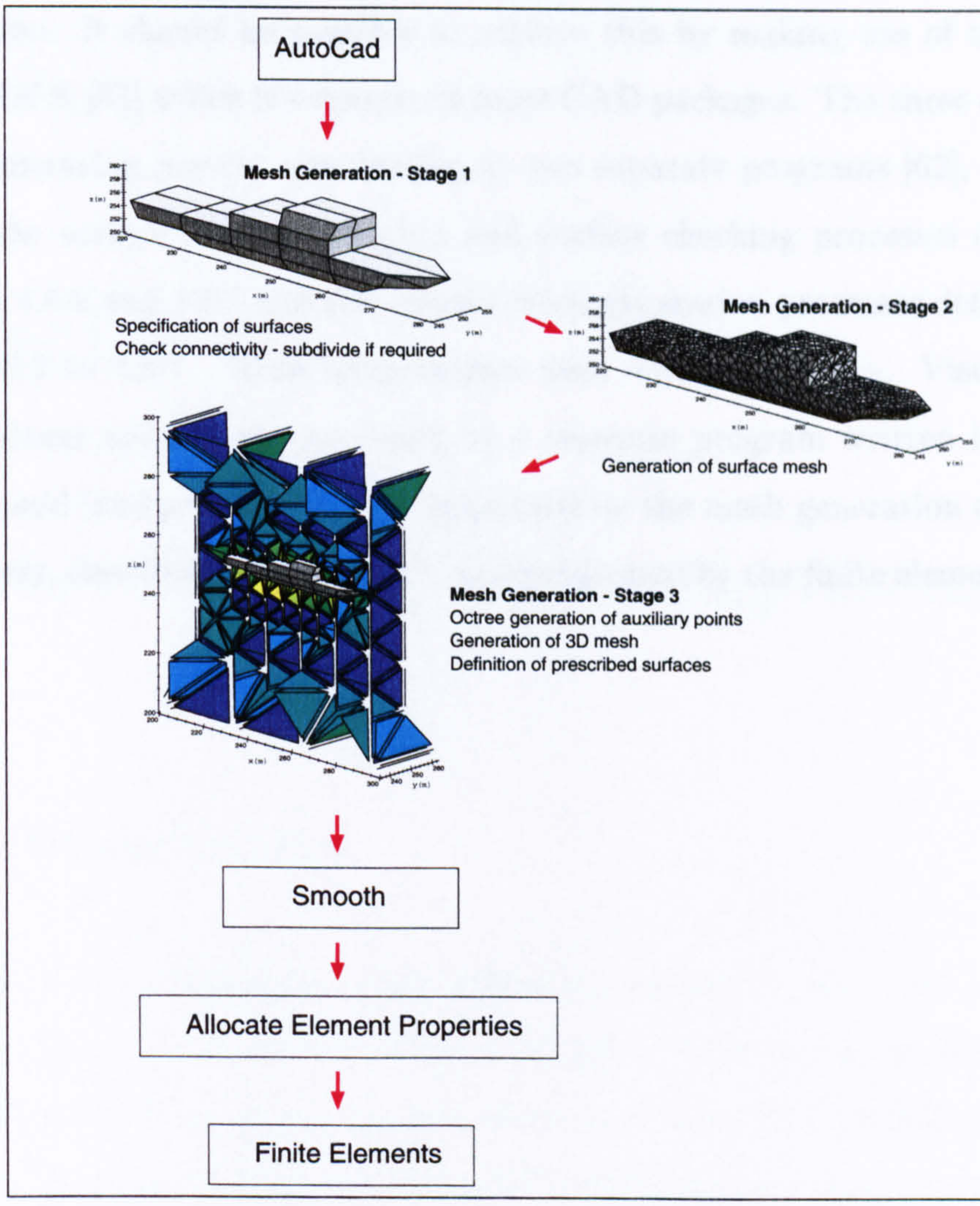

Figure 4.27: Scheme of main mesh generation stages.

is used throughout chapter 5 to construct the finite element meshes, is summarised in figure 4.27. The insets summarise the three main mesh generation stages: Specification of the surfaces to be defined within the final mesh, including the surface connectivity checking; generation of the surface mesh; extrapolation to the three dimensional mesh. At present the initial files used to define the geometry of the surfaces defining the object require to be manually specified. It is to be noted, however, that the specification of the initial files, by an AutoCAD package, is a

future aim. It should be possible to achieve this by making use of the open file format DFX [61] which is common in most CAD packages. The three dimensional mesh generation process was written as two separate programs [62], corresponding to the surface mesh generation and surface checking processes described in sections 4.6.2 and 4.6.1 and the volume mesh generation processes detailed in sections 4.6.3 to 4.6.7. These programmes were written in C++. Visualisation of the resultant meshes was managed by a separate program written in Java [42], which could interpret display files generated by the mesh generation codes. Mesh refinement, described in section 4.7, was progressed by the finite element program.

Chapter 5

Finite Element Investigations

5.1 Introduction

From the finite element and mesh generation procedures described in chapters 3 and 4 a series of linked evaluations is reported. The use of the potential jump method described in section 3.4 is assessed as a method of modeling current circuits and more specifically degaussing coils. Spherical shells of permeable material are subsequently examined, to provide a test case for assessing the suitability of using surface elements, as described in section 3.3, to model thin iron regions. In both of these studies comparisons are made between the results obtained from finite element analysis and the corresponding analytical solutions.

By finite element analysis, degaussing coils are evaluated and the reliability of the degaussing procedure described in section 3.8 is tested. The contribution of the internal structure of a ship relevant to the induced magnetic signature of the ship is assessed, and finally the finite element method is applied to two case studies: The contribution to the induced magnetic signature from the crane of a

mine countermeasures vessel; the induced magnetic signature of an average ship structure without and with degaussing.

5.2 Circular Hoop - Modelling Current Circuits

5.2.1 Introduction

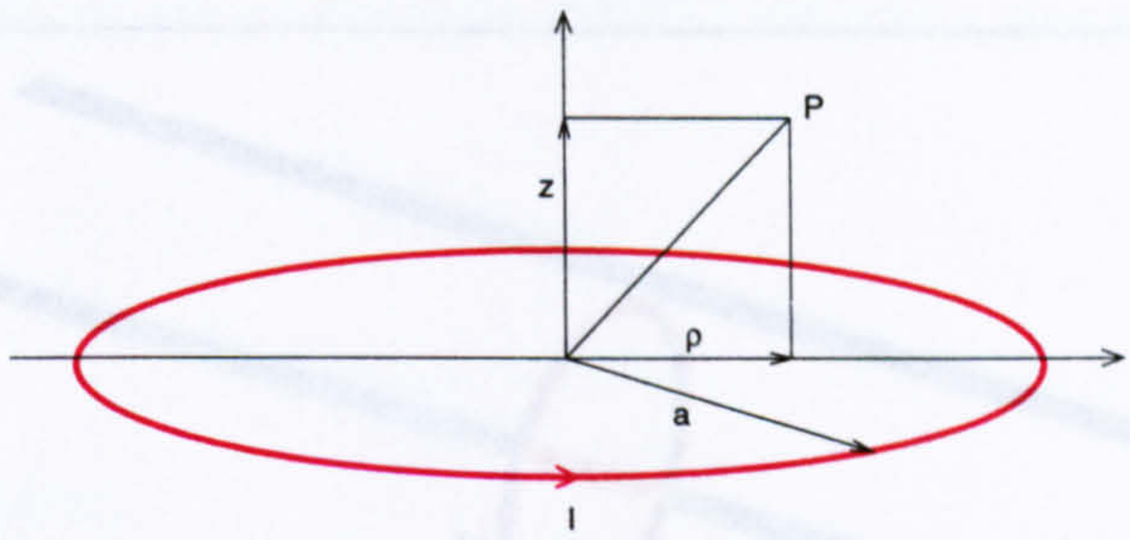

Figure 5.1: Circular coil of radius a carrying current I.

To examine the accuracy of modelling current circuits by the finite element scheme described in chapter 3 the simple geometry of a circular hoop of radius a and carrying a current I, as illustrated in figure 5.1, is studied. Expressions for the magnetic field produced by this circular current loop at an arbitrary point can be obtained [63]. In cylindrical coordinates these expressions are,

$$B_\rho = \frac{\mu_0 I}{4\pi} \frac{2z}{\rho\sqrt{(a+\rho)^2+z^2}} \left[-K(k) + \frac{a^2+\rho^2+z^2}{(a-\rho)^2+z^2} E(k)\right] \tag{5.1}$$

$$B_z = \frac{\mu_0 I}{4\pi} \frac{2}{\sqrt{(a+\rho)^2+z^2}} \left[K(k) + \frac{a^2-\rho^2-z^2}{(a-\rho)^2+z^2} E(k)\right] \tag{5.2}$$

$$k = 2\sqrt{\frac{a\rho}{(a+\rho)^2+z^2}} \tag{5.3}$$

where K and E are complete elliptic integrals of the first and second kind. On the principle axis, with $\rho = 0$, the above expressions simplify to,

$$B_\rho = 0 \tag{5.4}$$

$$B_z = \frac{\mu_0 I a^2}{2(a^2 + z^2)^{3/2}} \tag{5.5}$$

5.2.2 Specification and Results

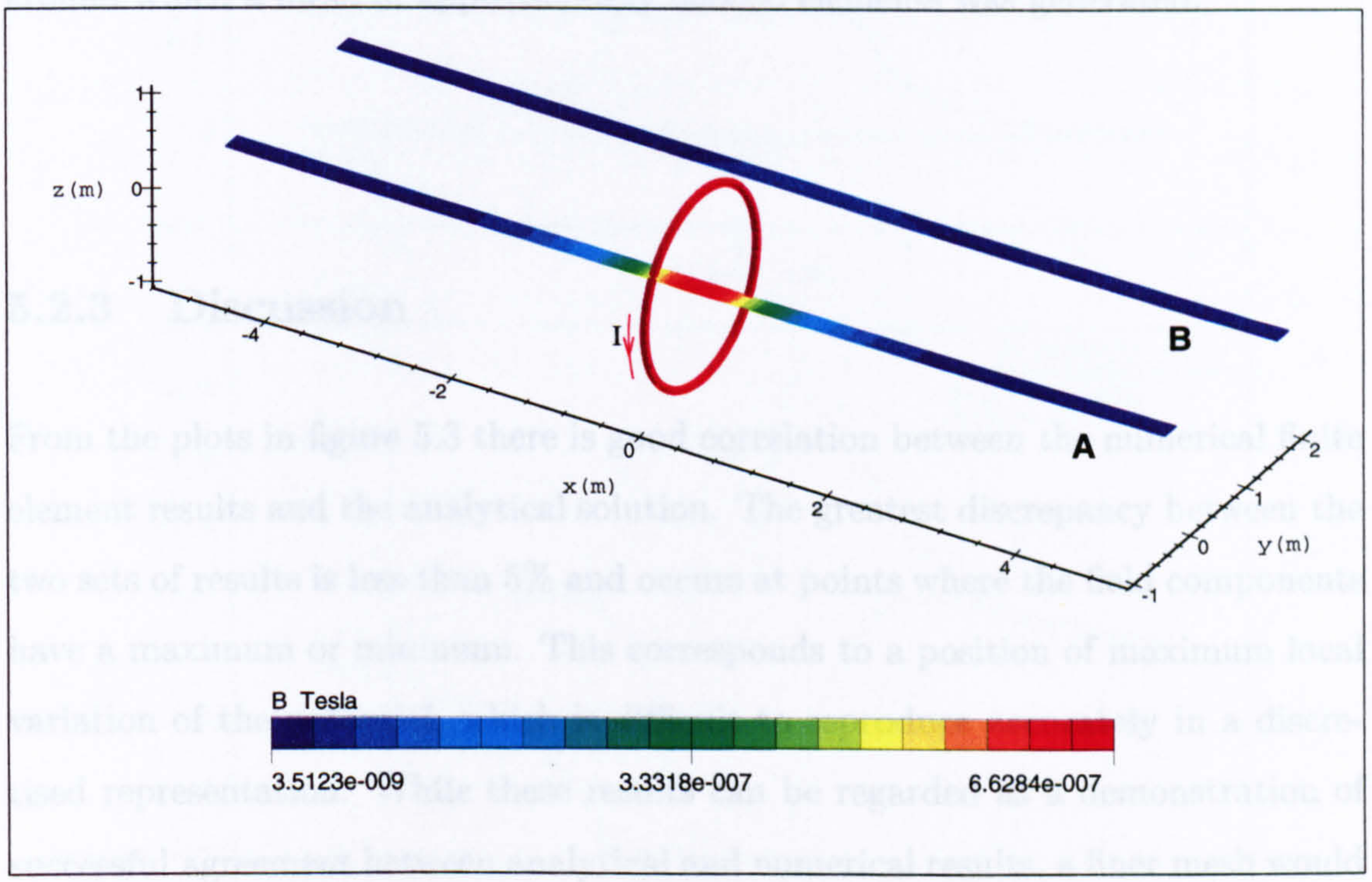

Figure 5.2: Circular coil of radius 1 m and current of 1 A. Data lines A and B are shown.

With reference to figure 5.2, a hoop with its centre positioned at the origin, of radius 1 m, lying in the yz plane and with a current of 1 A with a direction as shown, was considered. In this diagram two data lines are shown. Data lines A

and B have z=0 m with x ranging from x=-6 m to x=6 m. Data line A has y=0 m and data line B has y=2 m. The field values at points along these lines are plotted in figure 5.3. In both the plots the z component has not been included since it is zero at every point on the data lines.

The finite element mesh was contained within a cube of side length 20 m. The dipole layer, introduced to represent the coil, was defined by a circular disc lying in the yz plane with x=0 m. This surface was defined by 15000 tetrahedral elements around which a mesh of approximately 300000 elements was generated.

5.2.3 Discussion

From the plots in figure 5.3 there is good correlation between the numerical finite element results and the analytical solution. The greatest discrepancy between the two sets of results is less than 5% and occurs at points where the field components have a maximum or minimum. This corresponds to a position of maximum local variation of the potential, which is difficult to reproduce accurately in a discretised representation. While these results can be regarded as a demonstration of successful agreement between analytical and numerical results, a finer mesh would give even closer agreement.

Furthermore, it can be seen that the discontinuity in the potential on the dipole layer x=0 m in the yz plane, that has been introduced into the mesh to represent the coil, is not evident in figure 5.3 confirming that the gradient is the same on both sides of the layer.

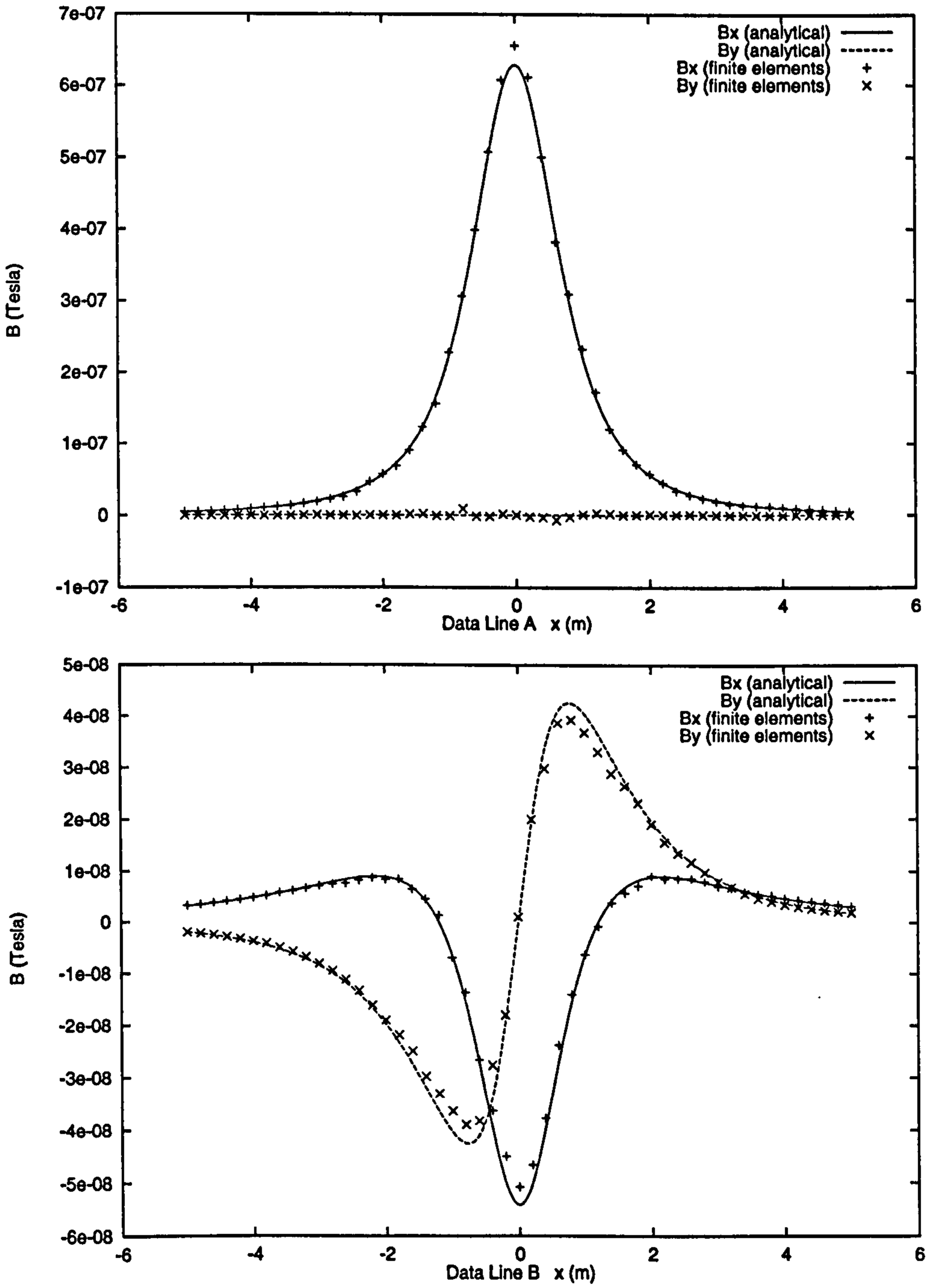

Figure 5.3: Magnetic field plotted along data lines A (upper) and B (lower) defined in figure 5.2. Coil of radius 1 m with current of 1 A. Points correspond to values obtained from finite element analysis and lines represent the analytical results.

5.3 Spherical Shell - Modelling Thin Iron Regions

5.3.1 Introduction

In this section the effectiveness of using surface elements to describe thin regions of material with a high permeability is examined. To achieve this, comparisons are made between analytical expressions and the finite element analysis for the case of a spherical shell in a uniform external field. In particular thin spherical shells are considered, for which the analytic expression for the field inside a spherical shell is known. In section 2.2.1, equation 2.19, it was shown that for a spherical shell with inner radius a, outer radius b, relative permeability μ_r and situated in a uniform external field, $\mathbf{B_0}$, the field within the central cavity of the shell is uniform and parallel to $\mathbf{B_0}$ with a magnitude, B, given by,

$$B = \left[\frac{9\mu_r}{(2\mu_r+1)(\mu_r+2) - 2\frac{a^3}{b^3}(\mu_r-1)^2}\right] B_0 \tag{5.6}$$

5.3.2 Specification and Results

The results reported have been obtained for a spherical shell of radius 1 m. The surface mesh used to defined the finite element mesh is illustrated in figure 5.4 and was generated by a refinement procedure [59]. The spherical shell is composed of 1280 triangular surface elements which lie in a overall mesh of approximately 100000 elements. The entire mesh was defined to lie within a cube of side length 20 m. The centre of the shell is at the point x=10 m, y=10 m and z=10 m.

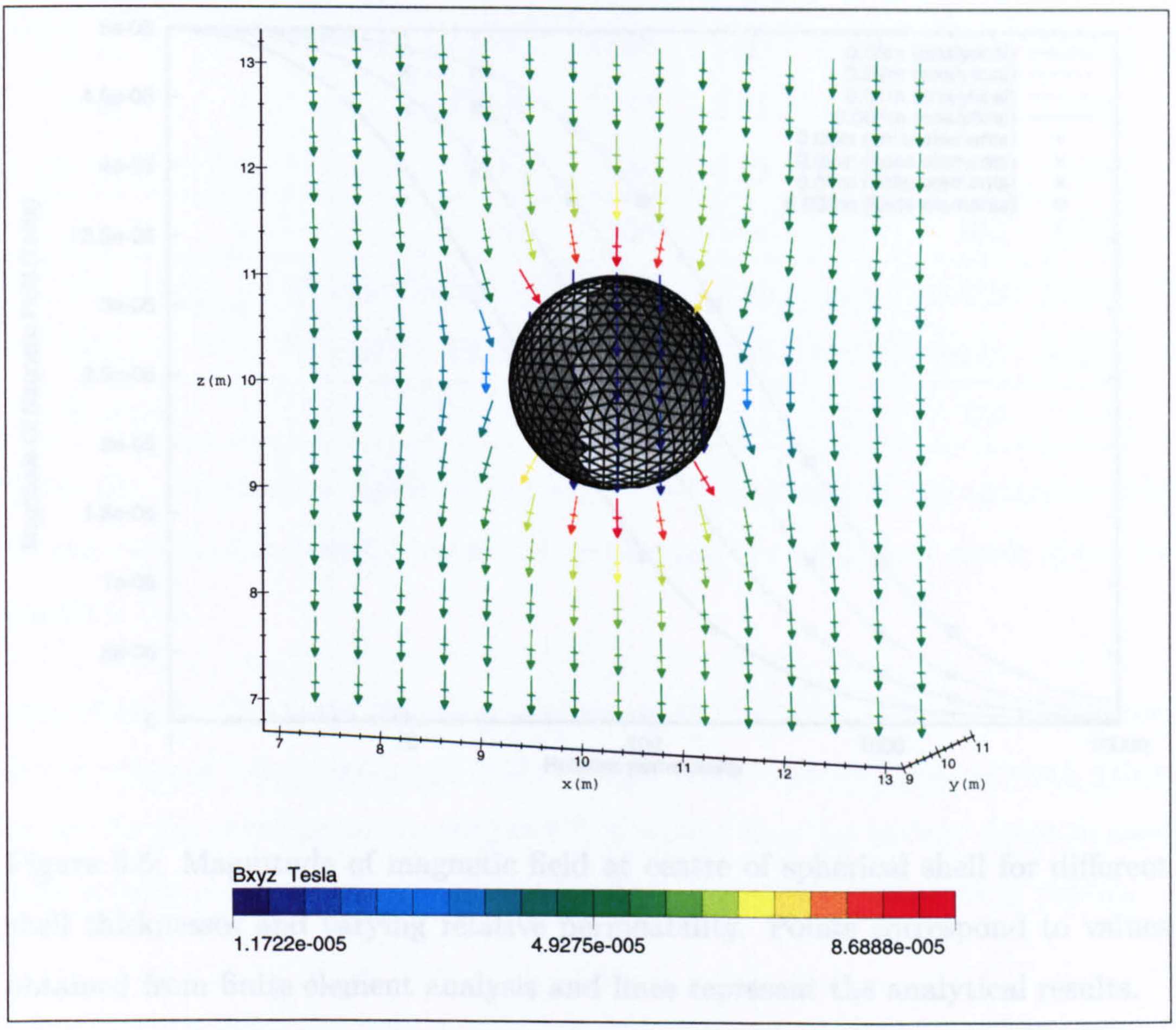

Figure 5.4: Geometry of the spherical shell (3/4 shown). Field arrows plotted for a relative permeability of 500 and shell thickness of 0.01 m.

From the mesh, the results are plotted in figure 5.5. Four shells of thicknesses 0.05 m, 0.02 m, 0.01 m and 0.005 m were considered and for each shell thickness the magnetic field at the centre of the respective shell has been plotted for a range of permeabilities. Selected points from the plots in figure 5.5 are given in table 5.1. The external field in every calculation is -50000 nT, directed along the z axis.

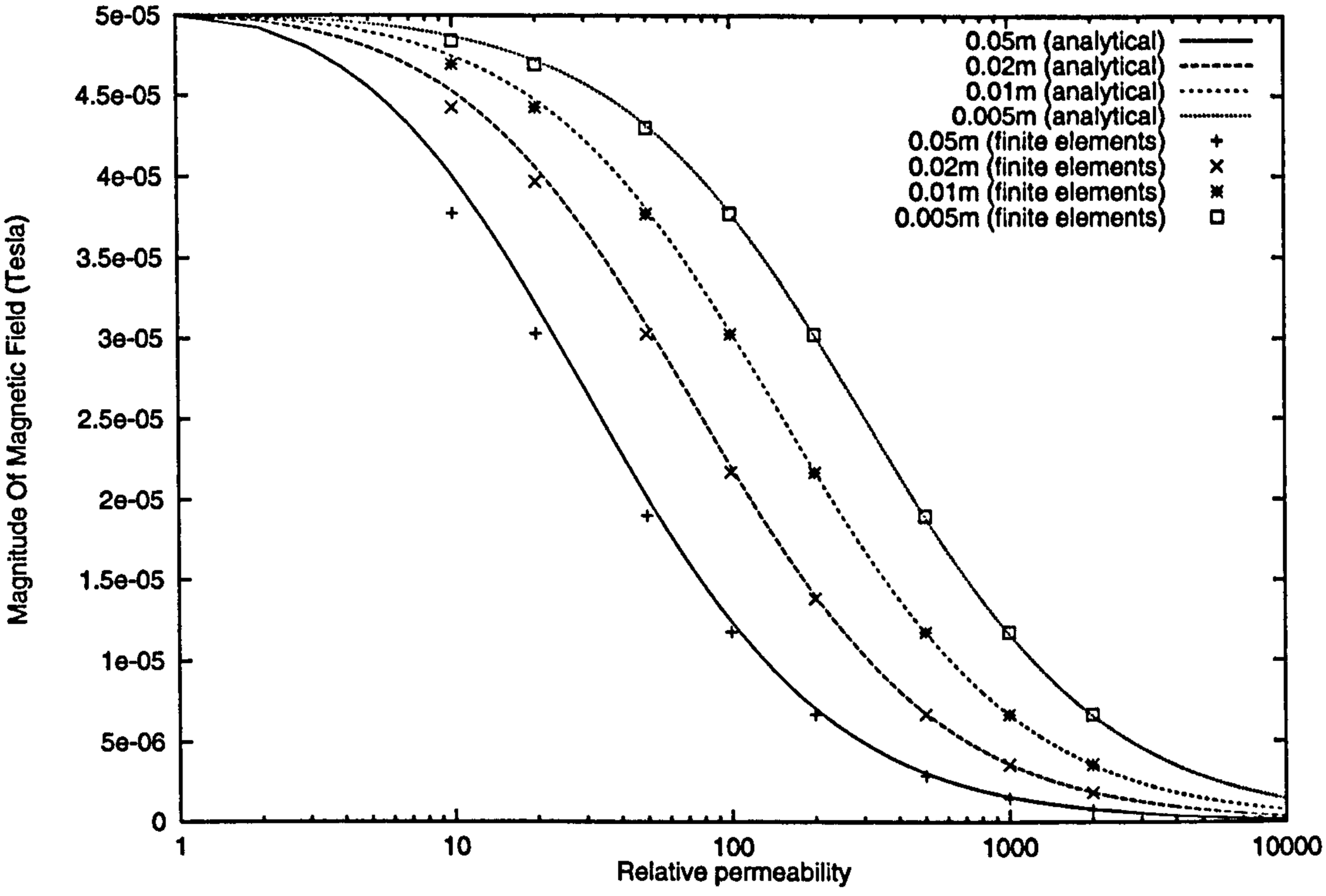

Figure 5.5: Magnitude of magnetic field at centre of spherical shell for different shell thicknesses and varying relative permeability. Points correspond to values obtained from finite element analysis and lines represent the analytical results.

5.3.3 Discussion

The results indicate that for high permeability and small thicknesses there is good agreement between the finite element results and the analytical solution. As the permeability is reduced or as the thickness of the surface elements increases, it is to be noted that the discrepancy between the finite element result and the analytical solution increases. This is as anticipated since the assumption, that the normal component of the magnetic field within the surface elements is zero, no longer applies at these limits.

The main purpose of the surface elements was to provide a means of accurately

a m		0.9975	0.995	0.99	0.95	0.995	0.995
b m		1.0025	1.005	1.01	1.05	1.005	1.005
t m		0.005	0.01	0.02	0.05	0.01	0.01
μ_r		500	500	500	500	100	1000
$\lvert B\rvert_{\text{analytical}}$	T $\times 10^{-6}$	18.884	11.708	6.716	3.045	30.419	6.618
$\lvert B\rvert_{\text{fe}}$	T $\times 10^{-6}$	18.991	11.721	6.639	2.885	30.245	6.639
% error		0.5	0.1	1.1	5.2	0.6	0.3

Table 5.1: Comparison between the computed magnitude of the magnetic field at the centre of a range of spherical shells and the analytical result given by equation 5.6.

modelling the thin plate regions of the structure of a ship. With hull thicknesses in the range of 1 cm to 2 cm and with the high relative permeability of steel, taken as 500 for the investigation in section 5.7, it is clear that the surface elements used here provide a successful and efficient method of modelling these plate regions.

5.4 Degaussing

5.4.1 Introduction

In this section the degaussing scheme described in section 3.8 is evaluated as an effective approach to calculate the optimal degaussing currents for a defined structure and a given set of degaussing coils.

5.4.2 Specification and Results

Three test cases with different degaussing coil configurations are examined. In each case the object to be degaussed was standardised as a cube of side length 2 m and a relative permeability of 100. The three coil configurations are illustrated in figure 5.6. In each case the coils were defined to lie in the xy plane and the corresponding z coordinate of each coil is given in table 5.2. The x and y limits of each coil are illustrated in figure 5.7 and it is to be noted that the separation between the coils and the cube is 0.25 m. In figures 5.6 and 5.7 arrows indicate the direction of current flow. An external field of -50000 nT, equivalent to -39.78 Am^{-1}, directed along the z axis was defined.

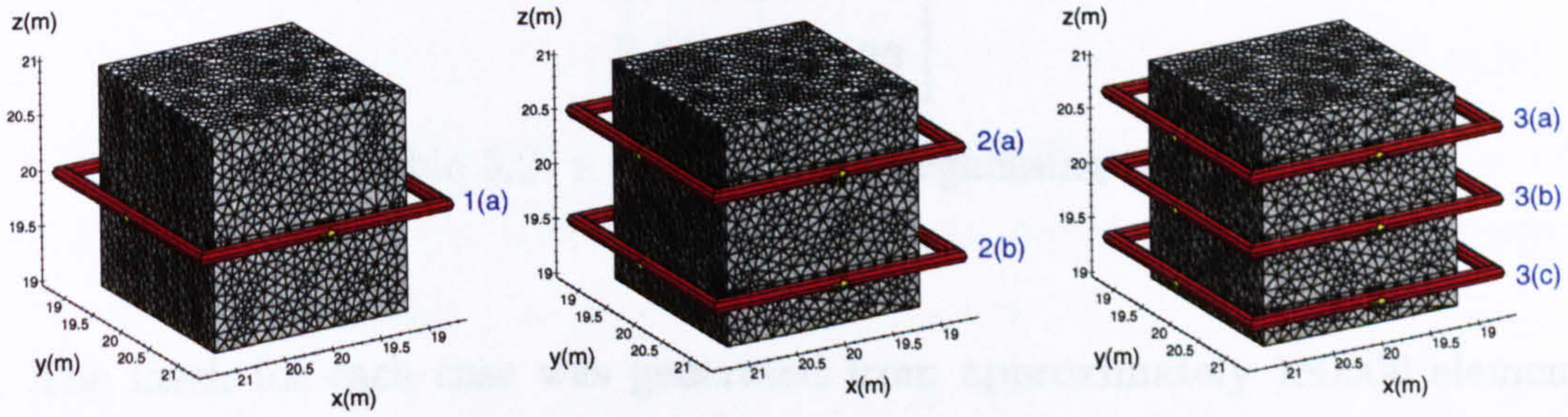

Figure 5.6: Degaussing coil configurations around a cube of permeable material.

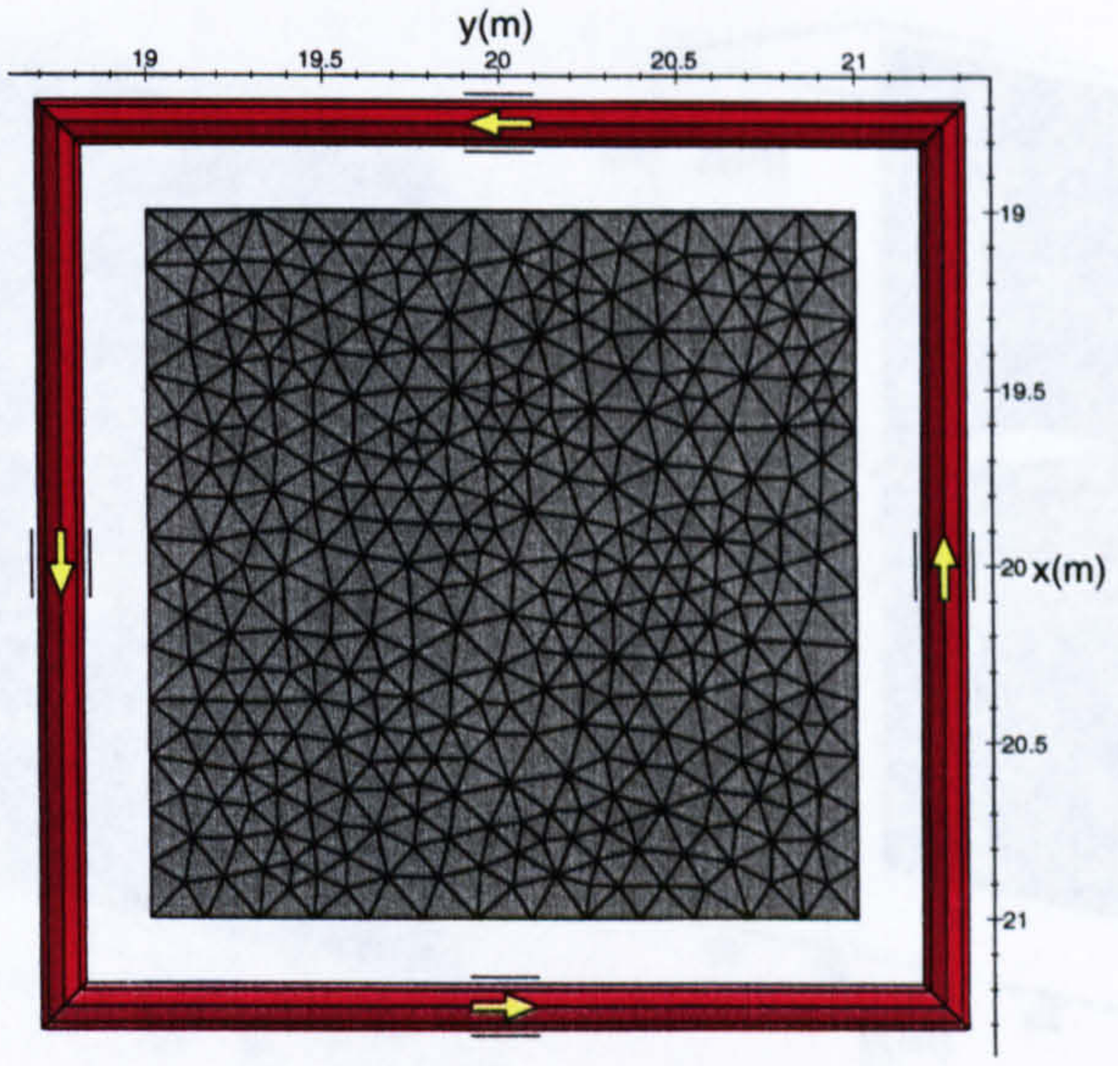

Figure 5.7: Plan view of cube and degaussing coil.

Coil	z (m)
1(a)	20.00
2(a)	20.50
2(b)	19.50
3(a)	20.66
3(b)	20.00
3(c)	19.33

Table 5.2: z plane of each degaussing coil.

The mesh for each case was generated from approximately 180000 elements of which 30000 elements defined the material of the cube. The entire mesh was defined within a cube of side length 40 m with the centre of the cube at the point x=20 m, y=20 m and z=20 m.

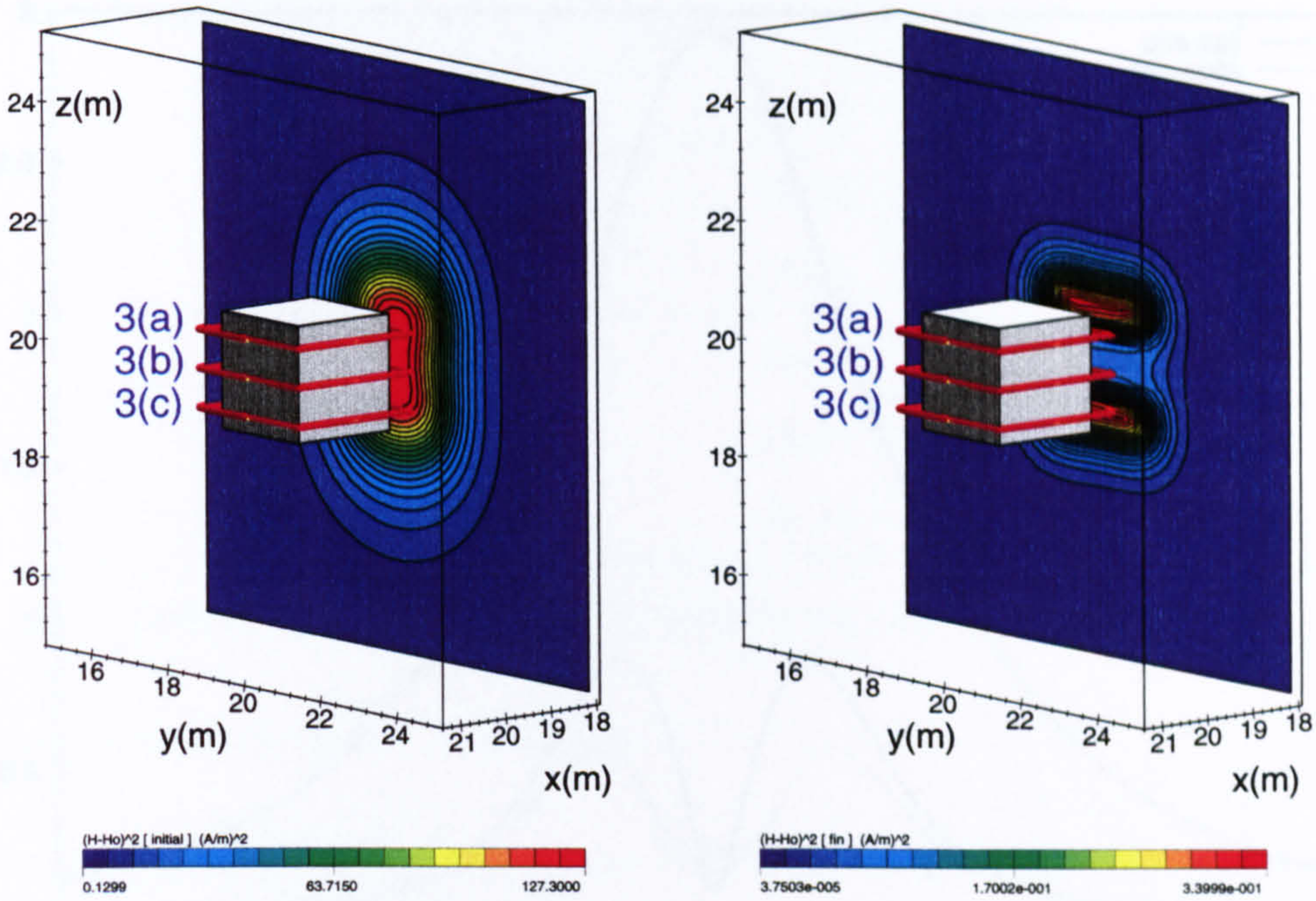

Figure 5.8: Degaussing of cube, side length 2 m, relative permeability of 100, with three coils. Without degaussing, coil currents set to zero (left). With degaussing, coil currents given in table 5.3 (right).

The magnetic perturbation squared, $(\mathbf{H} - \mathbf{H}_0)^2$, before and after degaussing was determined and the results are plotted on the plane x=18 m in figure 5.8. Before degaussing, with no current in the coils, the peak pertubation value is $127.30\,\mathrm{A^2m^{-2}}$. After degaussing the maximum plotted value is $0.34\,\mathrm{A^2m^{-2}}$. The plot planes illustrated in figure 5.8 also define the minimisation plane on which 50×50 sample points were defined. The quantity $(\mathbf{H} - \mathbf{H}_0)^2$ is plotted because it is this quantity that is minimised over the minimisation plane. For each of the cases the calculated degaussing currents are given in table 5.3.

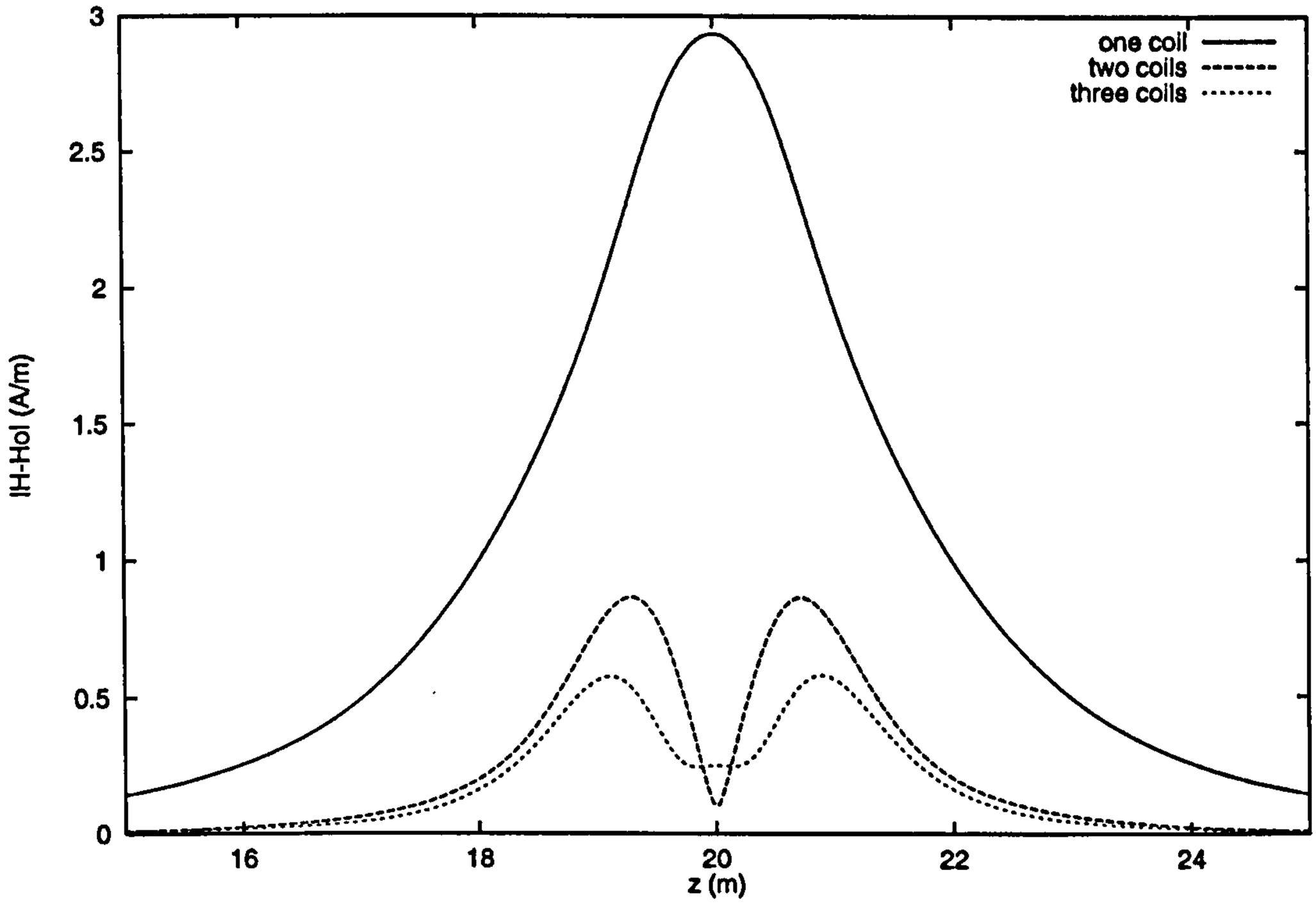

Figure 5.9: Comparison of degaussing cases. The maximum perturbation of the cube without degaussing is $11.28\,\mathrm{Am}^{-1}$.

To compare the effectiveness of the degaussed cube for each of the coil arrangements the perturbation to the external field, $|\mathbf{H} - \mathbf{H}_0|$, has been plotted along the line with x=18 m, y=20 m and z ranging from z=15 m to z=25 m and these results are illustrated in figure 5.9.

5.4.3 Discussion

For the three coil case illustrated in figure 5.8 it can be seen that the use of degaussing coils greatly reduces the perturbation to the external field on the study plane. When no degaussing is used the greatest perturbation on this plane is $11.28\,\mathrm{Am}^{-1}$ compared to $0.58\,\mathrm{Am}^{-1}$ when the coil currents are set to the calculated

Coil	Current (A)
1(a)	60.40
2(a)	36.30
2(b)	36.34
3(a)	25.51
3(b)	23.91
3(c)	25.49

Table 5.3: Degaussing coil currents for test configurations.

degaussing currents given in table 5.3.

It is also to be noted from the plots illustrated in figure 5.9 that as the number of coils increases the perturbation to the external field becomes smaller. This is due to the fact that as the number of coils is increased a closer approximation to the surface current that would result in complete magnetic silencing is reached. By referring to the results presented in section 2.4.1, the required surface current density for complete degaussing of the structure in this study, a cube with side length 2 m and relative permeability of 100 in an external magnetic field of -39.78 Am^{-1}, is given by, equation 2.70,

$$\alpha = \hat{n} \times H_0 \left(1 - \frac{1}{\mu_r}\right) \tag{5.7}$$

Using this expression the surface current distribution required to give no external perturbation is 39.39 Am^{-1}. This corresponds to a total current of 78.78 A uniformly distributed over the faces of the cube parallel to the z axis. The total optimal current in one coil is 60.40 A, in two coils it is 72.64 A and in three it is 74.91 A. It is clear from these results that as the number of coils is increased the approximation to the total surface current required for complete degaussing improves. These results suggest that increasing the number of coils would improve

the degaussing even further.

5.5 Internal Structure

5.5.1 Introduction

Before evaluating the induced magnetic signature of a ship it is necessary to identify the level of detail to which the ship needs to be represented within the model. In this section a simplified structure is considered to assess whether the internal decking and bulkheads of a ship are important structures which require to be included within a ship model.

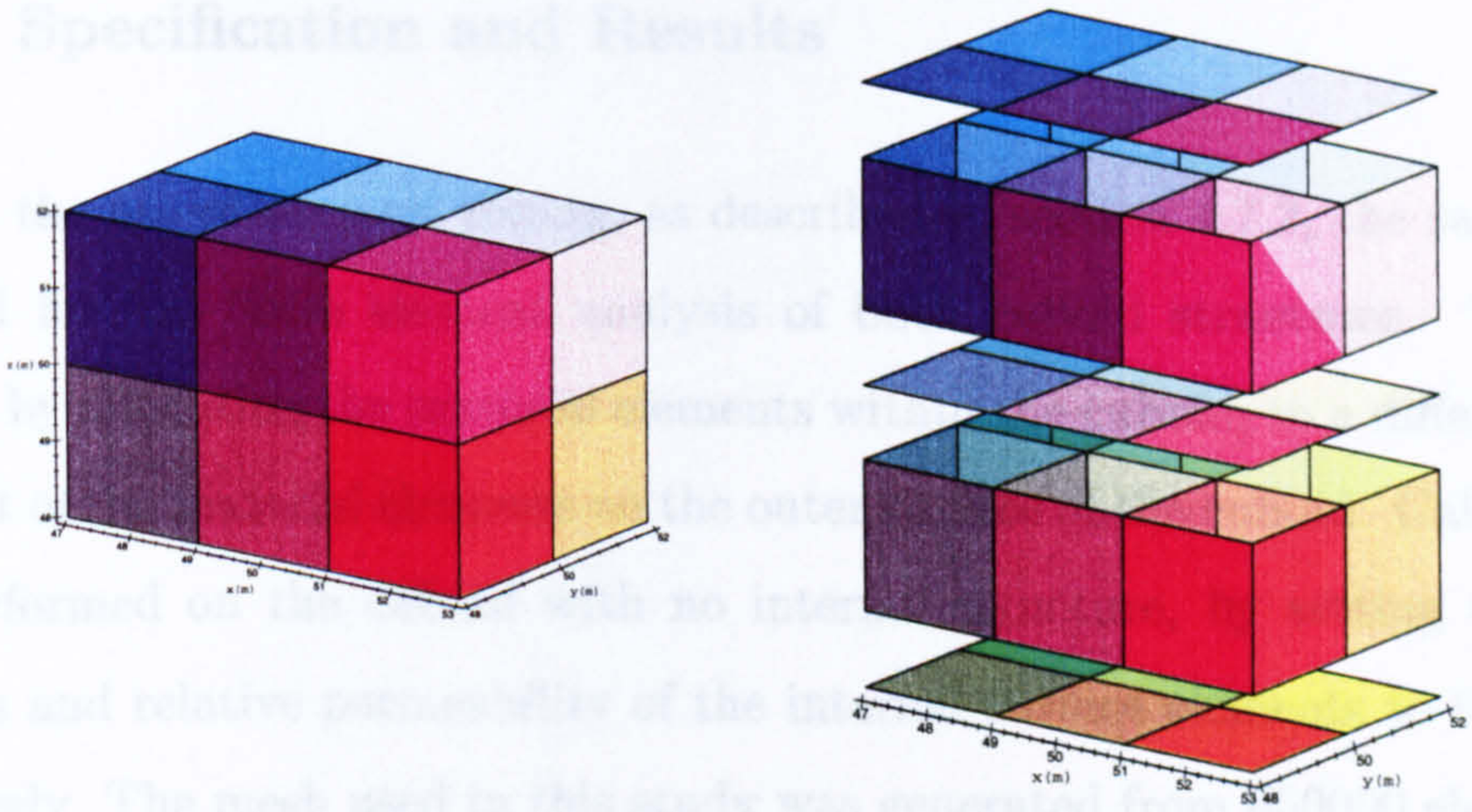

Figure 5.10: External dimensions of cuboid (left). Break down of structure showing internal partitioning (right).

To evaluate the significance of internal structures in relation to the induced magnetic signature, the dipole moments of two different cuboidal structures are

compared.

Although the external dimensions of each cuboid are the same with length 6 m, and a height and width of 4 m, one cuboid consists of a shell with no material within it, the other is partitioned, as illustrated in figure 5.10. The internal partitions can be considered as dividing the inside of the cuboid into 12 cubical rooms of side length 2 m.

To make comparisons between the two structures the dipole moment of each shape is calculated. Although each case will have higher moments, the dipole moment provides a good measure of perturbation to the external field because its contribution is largest and falls off least rapidly with distance.

5.5.2 Specification and Results

Through the use of element zoning, as described in section 4.7.2, the same mesh was used for the finite element analysis of both cuboid structures. This was achieved by allocating the material elements within the cuboid, to a different zone from that of the material elements on the outer surface of the cuboid. Calculations were performed on the cuboid with no internal structure, by setting the plate thickness and relative permeability of the internal surface elements to 0 m and 1 respectively. The mesh used in this study was generated from 650000 elements of which 38000 correspond to surface elements representing the material. The entire mesh was contained within a cube of side length 100 m with the centre of the cuboid at the point x=50 m, y=50 m and z=50 m. It is useful to note that the structure is defined by 52 square surfaces, 32 forming the external surface of the cuboid and 20 defining the internal partitions.

The x component of the dipole moment for a range of plate thicknesses and

relative permeabilities for the cuboid with no internal partitions is given in table 5.4. For the cuboid with internal partitioning the x components of the dipole moment for the same range of plate thicknesses, t, and relative permabilities are given in table 5.5. An external field of 50000 nT along the x axis was used in all the calculations.

For a relative permeability of 500 and a plate thickness of 0.01 m the magnetisation of the surface elements for the cuboid with no internal partitions is illustrated in figure 5.11 and for the case of the cuboid with internal structure the magnetisation of the material is illustrated in figure 5.12.

		t(m)			
		0.005	0.01	0.02	0.05
μ_r	10	169.37	334.20	652.01	1527.1
	100	1685.4	3079.4	5286.6	9353.1
	500	6236.3	9447.4	12757	16174
	1000	9459.2	12774	15504	17793

Table 5.4: Dipole moments (x component) (Am^2) for cuboid with no internal structure. External field 50000 nT along x axis.

		t(m)			
		0.005	0.01	0.02	0.05
μ_r	10	252.95	497.04	962.12	2206.3
	100	2426.9	4291.5	7006.5	11363
	500	8094.0	11455	14482	17228
	1000	11466	14496	16716	18412

Table 5.5: Dipole moments (x component) (Am^2) for cuboid with partitions. External field 50000 nT along x axis.

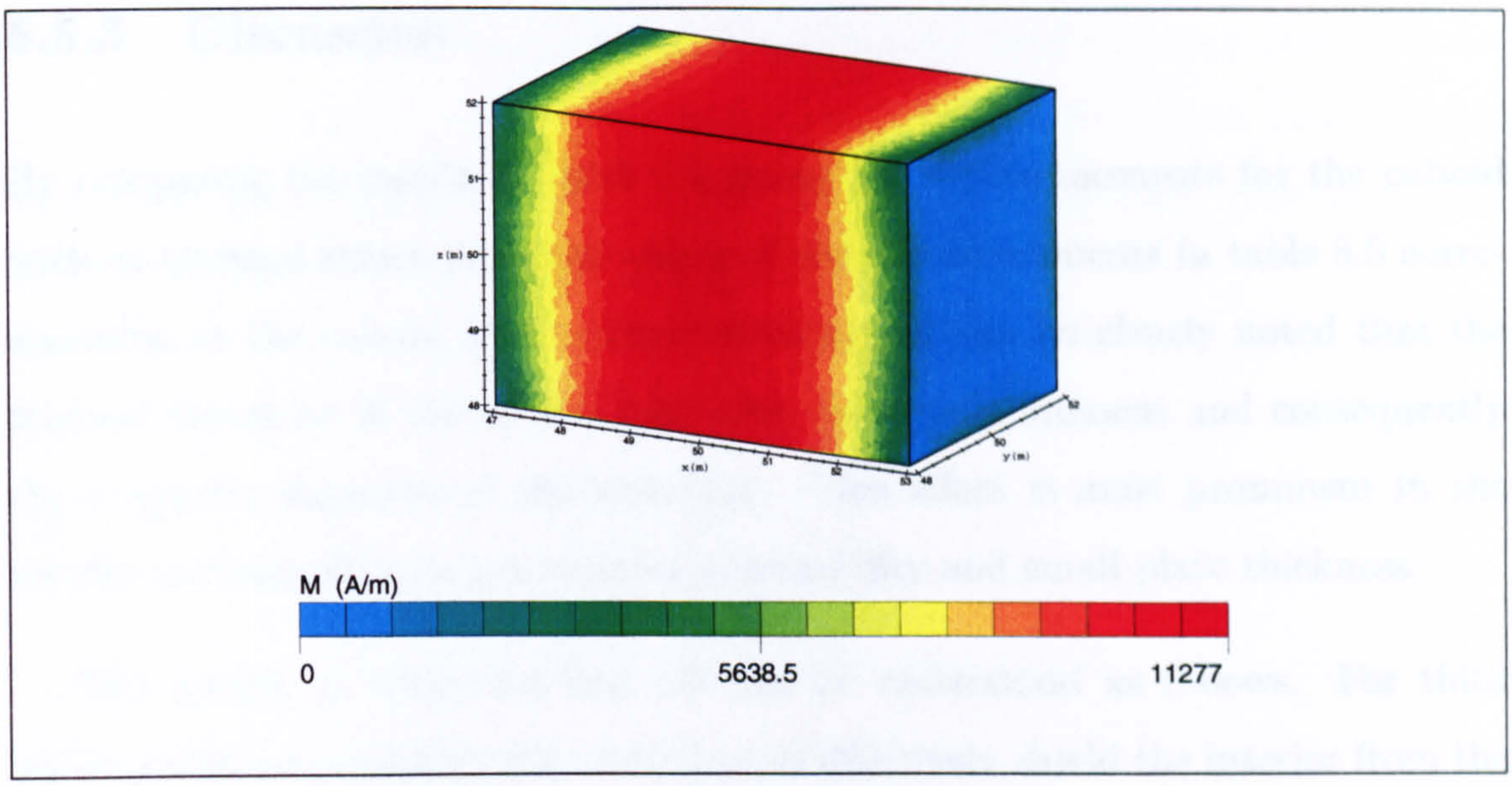

Figure 5.11: Plate magnetisation of cuboid with no internal structure. Plate thickness 0.01 m relative permeability 500. External field 50000 nT along x axis.

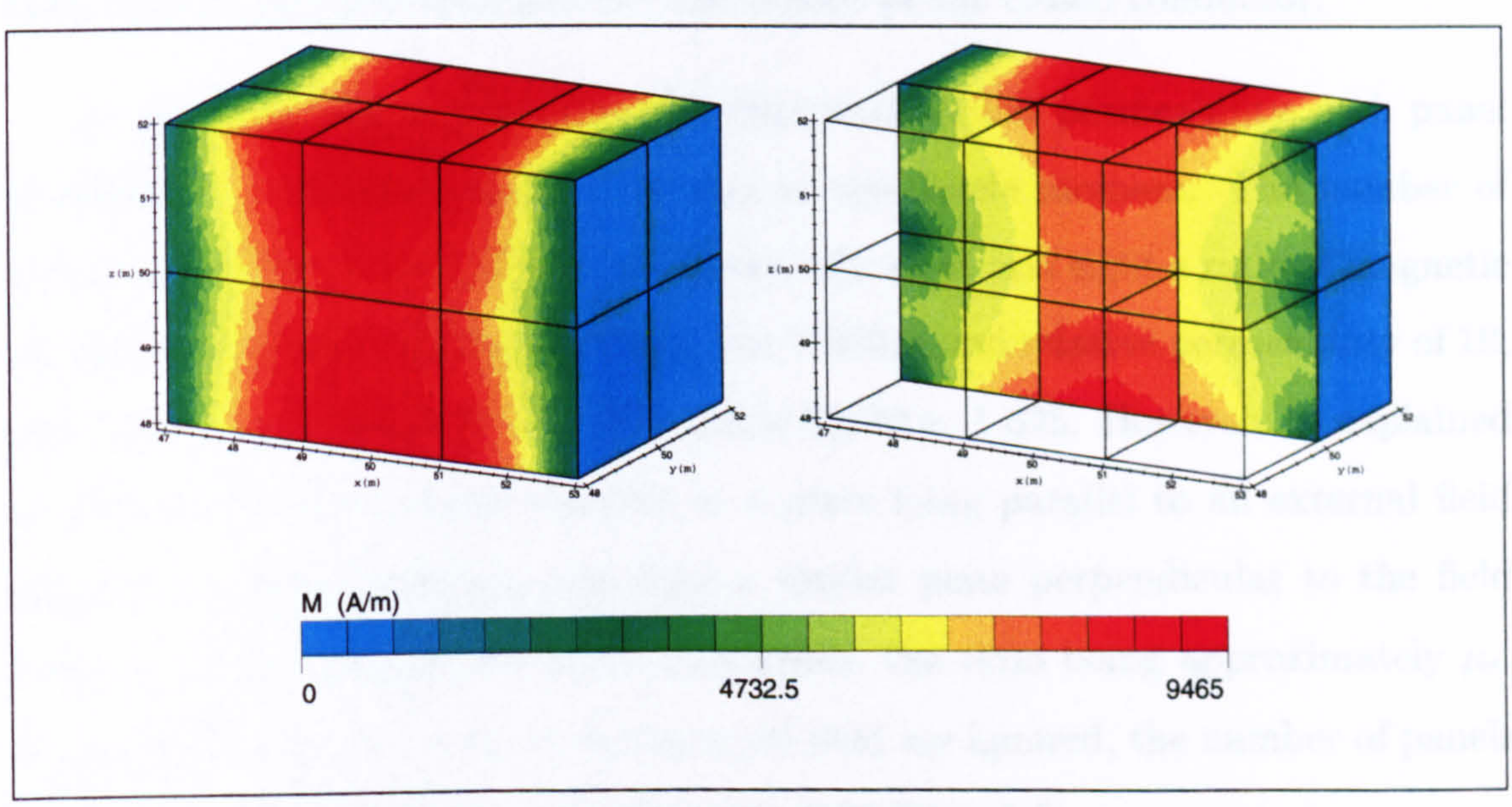

Figure 5.12: Plate magnetisation of cuboid with internal structure. Plate thickness 0.01 m relative permeability 500. External field 50000 nT along x axis.

5.5.3 Discussion

By comparing the results in table 5.4 giving the dipole moments for the cuboid with no internal structure to the values of the dipole moments in table 5.5 corresponding to the cuboid with internal structure, it can be clearly noted that the internal structure of the cuboid does alter the dipole moment and consequently the magnetic signature of the structure. This effect is most prominent in the results corresponding to low relative permeability and small plate thickness.

The results in tables 5.4 and 5.5 can be understood as follows. For thick walls of high permeability, the outer panels effectively shield the interior from the influence of the external field and they contribute little to the magnetic moment. The results are 17793 Am^2 and 18412 Am^2 for a thickness of 0.05 m and relative permeability of 1000. The electrostatic analogy is a Faraday cage in which the field lines do not penetrate beyond the surface of the closed conductor.

At the other end of the scale, with thin walls of low permeability, each panel is effectively unshielded and contributes to the dipole moment. The number of panels in the two cases is 52 and 32 respectively, so at first sight a ratio of magnetic moments of 52/32 would be expected. For 0.005 m and relative permeability of 10, the ratio is 252.95/169.37 = 1.4935, while 52/32 = 1.625. However, as explained in section 3.3, the induced moment in a plate lying parallel to an external field acquires a much larger moment than a similar plate perpendicular to the field because of the different boundary conditions, the ratio being approximately μ_r. If the panels perpendicular to the external field are ignored, the number of panels are 36 and 24 respectively, giving a ratio of 36/24 = 1.5.

Noting that the average thickness of the material of the hull is approximately 0.01 m the results of this study indicate that the internal decking and bulkhead

structure do contribute significantly to the induced magnetic signature. The results of calculations for our model structure give a 20% contribution. In a real ship with longitudinal, transverse and vertical partitions and decking, these structures will all contribute to the magnetic signature.

5.6 Study 1 - Minesweeper Crane

5.6.1 Introduction

The reduction of the magnetic signatures of mine countermeasures vessels is of great importance and where possible non-magnetic materials are used in their construction. A principle example of this material choice is the use of GRP for hull construction, as an alternative to steel. The use of non-magnetic materials in the construction of these vessels shifts the emphasis of modelling the induced magnetic signature from the gross structure of the craft to the study of the individual components within the ship, of which drive components and deck cranes are two examples.

In this section the contribution of a crane to the induced magnetic signature of a minesweeper is studied. Two different geometries of the crane are examined corresponding to a general operational position and a stowed position when the crane is not in use. Both these geometries are illustrated in figure 5.13. The geometry of the model is simplified and each arm of the crane is approximated by surfaces. The first section of the jib is 6 m in length and the load arm is 4 m in length.

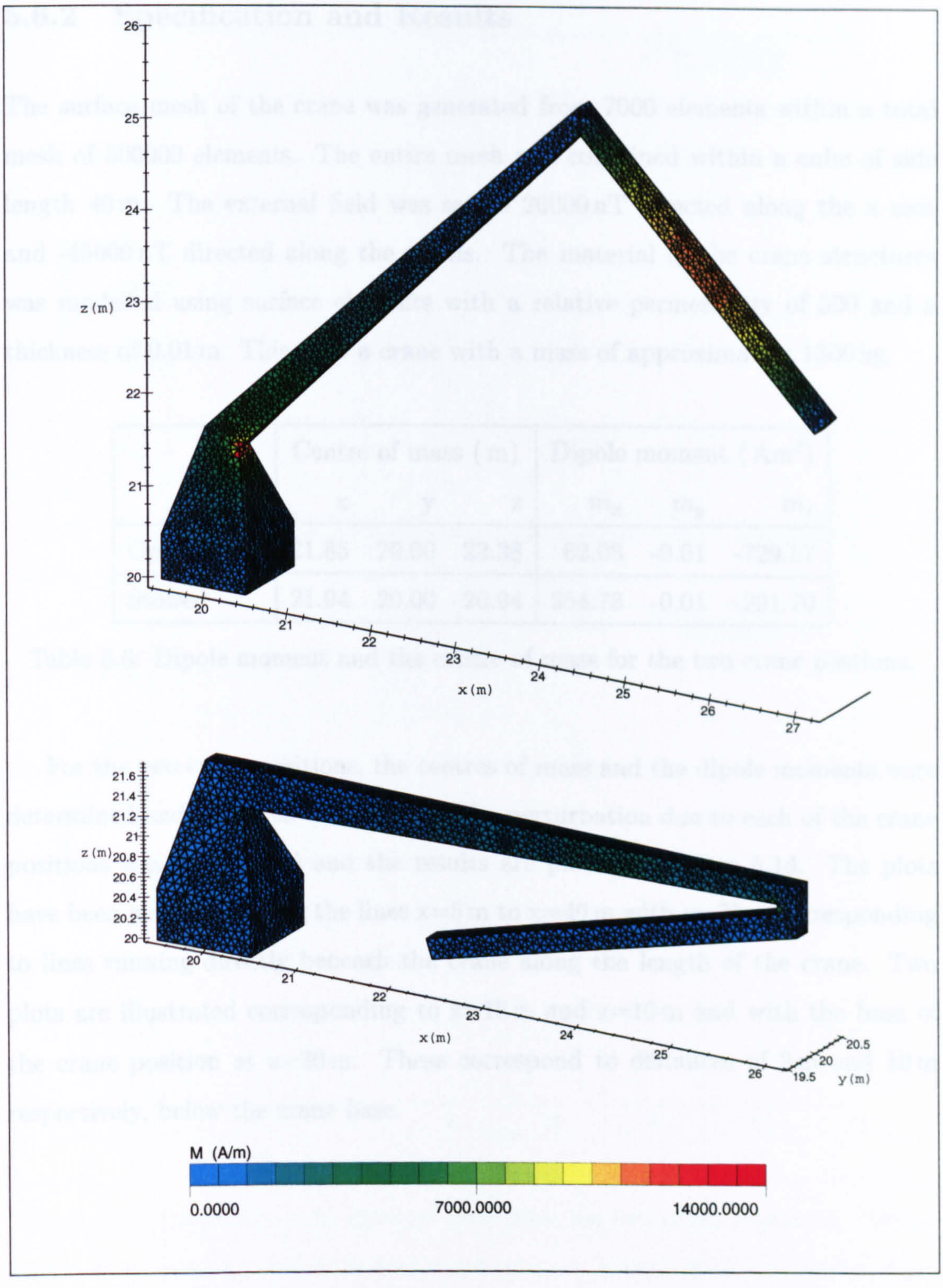

Figure 5.13: Geometry of crane. Crane in an operational position (upper). Crane in stowed position (lower). The two surface meshes are shaded to show the magnetisation of the surface elements. In the upper diagram the load arm has a high magnetisation because it is roughly aligned to the external field.

5.6.2 Specification and Results

The surface mesh of the crane was generated from 7000 elements within a total mesh of 500000 elements. The entire mesh was contained within a cube of side length 40 m. The external field was set to 20000 nT directed along the x axis and -45000 nT directed along the z axis. The material of the crane structures was modelled using surface elements with a relative permeability of 500 and a thickness of 0.01 m. This gave a crane with a mass of approximately 1300 kg.

	Centre of mass (m)			Dipole moment (Am^2)		
	x	y	z	m_x	m_y	m_z
Operational	21.85	20.00	22.38	62.08	-0.01	-729.57
Stowed	21.94	20.00	20.94	354.78	-0.01	-221.70

Table 5.6: Dipole moment and the centre of mass for the two crane postions.

For the two crane positions, the centres of mass and the dipole moments were determined and are given in table 5.6. The perturbation due to each of the crane positions was determined and the results are plotted in figure 5.14. The plots have been generated along the lines x=5 m to x=40 m with y=20 m corresponding to lines running directly beneath the crane along the length of the crane. Two plots are illustrated corresponding to z=18 m and z=10 m and with the base of the crane position at z=20 m. These correspond to distances of 2 m and 10 m respectively, below the crane base.

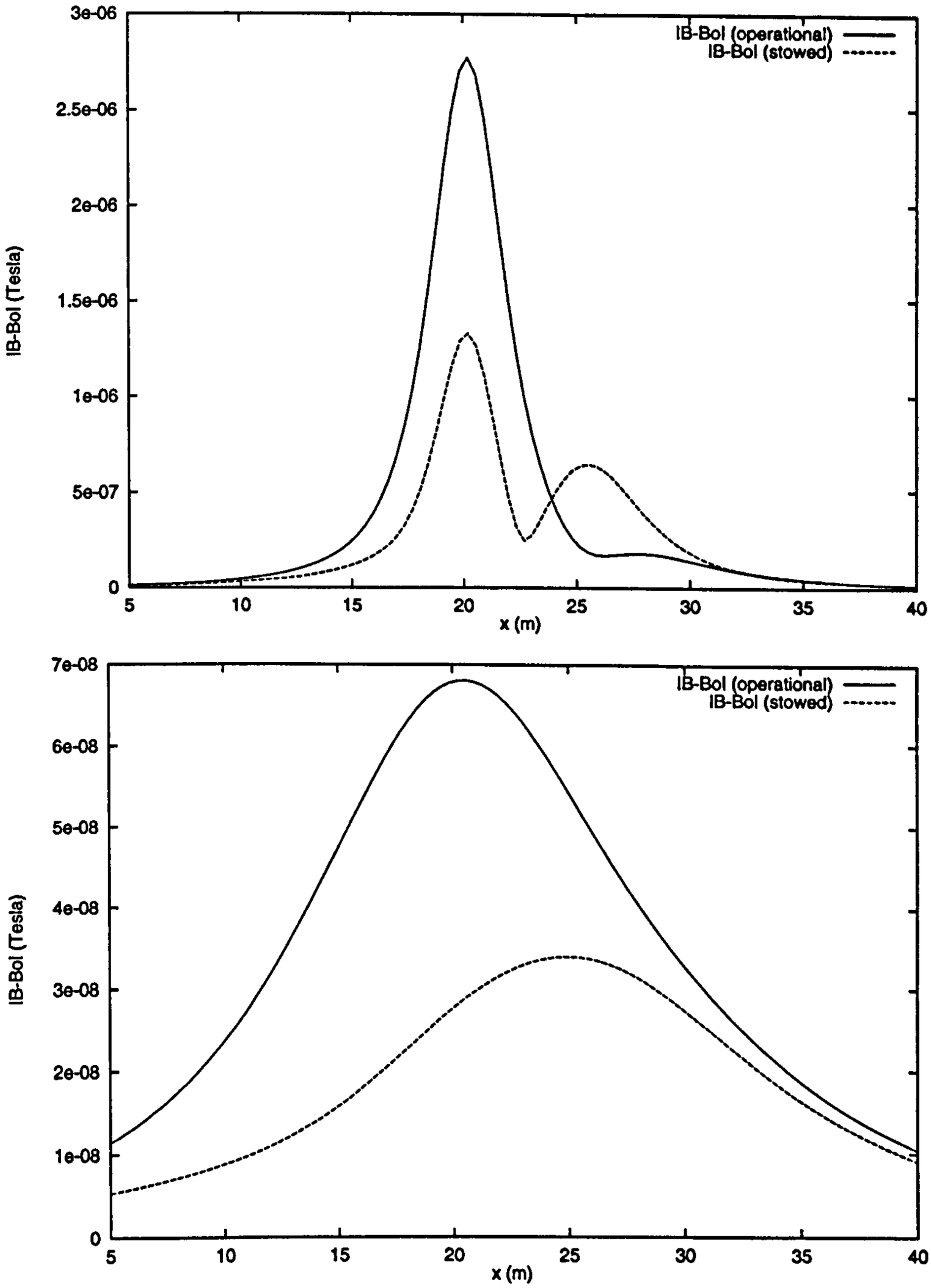

Figure 5.14: Perturbation to external field from the two crane positions. Perturbation at z=18 m, 2 m below base of crane (upper). Perturbation at z=10 m, 10 m below base of crane (lower).

5.6.3 Discussion

From the results presented it is evident that the crane has quite different induced magnetic signatures depending on its position. When the crane is in the operational position, the magnetic perturbation is approximately twice that of the crane in the stowed position. The most important signature is that of the crane when it is stowed because it is in this position when the minesweeper is working and consequently the magnetic signature must be small.

From the second plot in figure 5.14, showing the magnetic perturbation at a depth of 10 m below the crane base, it can be seen that for the operational position the peak magnetic perturbation is 68 nT, but when the crane is in the stowed position the peak magnetic perturbation is 34 nT. At the design stage it is often the case that a limit is placed on the maximum magnetic perturbation at a given depth beneath the ship. For example typical values for this limit may be 500 nT at a depth of 6 m below the keel. If the results presented in this plot correspond to a distance of 6 m under the ship, it is to be noted that the crane accounts for a significant fraction of the maximum allowed perturbation. In present day minesweepers the contribution to the induced magnetic signature from a steel crane is unacceptable and because of this the crane is constructed from non-magnetic GRP.

As a general principle, the magnetic signature of the crane could be minimised by arranging the arms to be fully extended and positioned at right angles to the earth's magnetic field. A dynamic control system could be envisaged which maintained this position while the minesweeper is working. However, associated practical considerations probably make this approach unacceptable.

5.7 Study 2 - Induced Magnetic Signature of a Ship in the Earth's Magnetic Field

5.7.1 Introduction

In this section the induced magnetic signature of a hypothetical ship in the earth's magnetic field is examined. The signature of the ship, when no attempt at degaussing is made, is presented in section 5.7.2. In section 5.7.3 a number of degaussing coils are introduced and using the procedure detailed in section 3.8 the optimal set of degaussing currents is determined. The new degaussed signature for the vessel is presented.

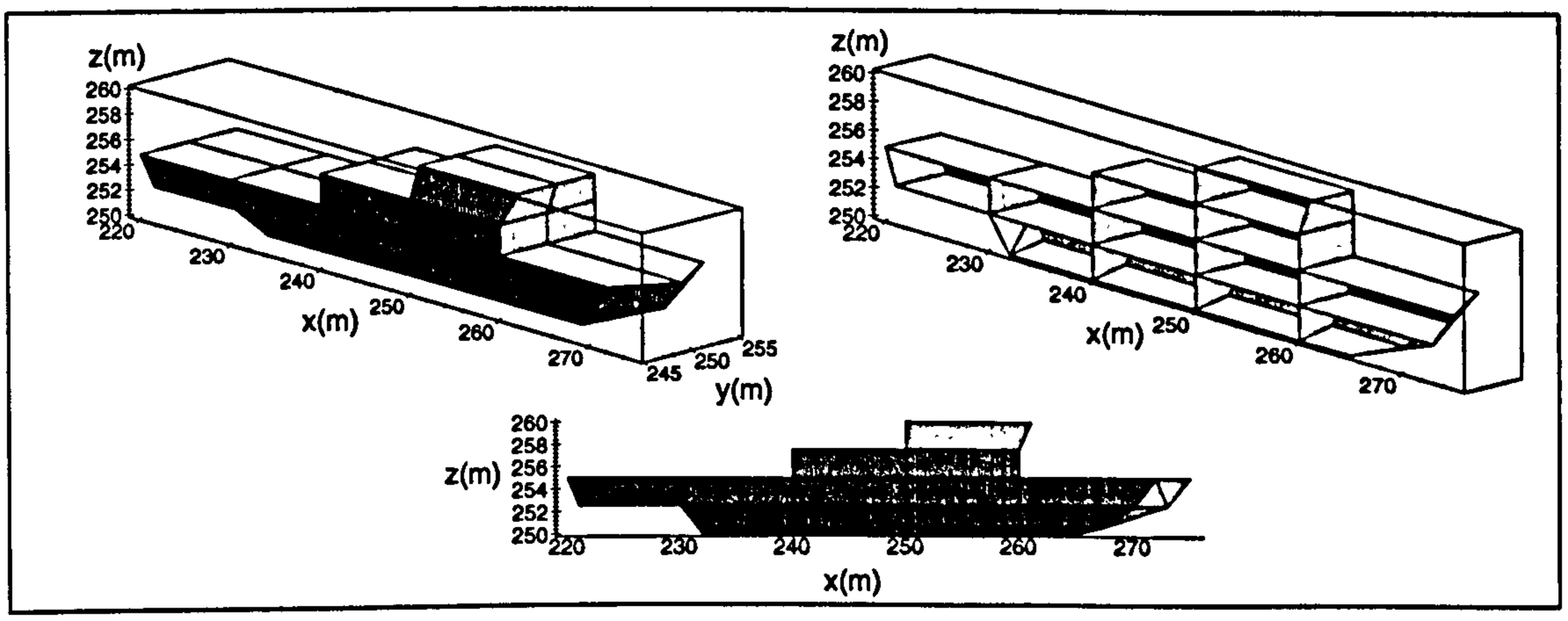

Figure 5.15: Ship geometry. Full structure (left). Internal bulkheads and decking (right). Side view (lower).

The aim of the work presented in this section is to demonstrate how the finite element methods detailed in chapter 3 and the mesh generation techniques presented in chapter 4 can be applied to study the magnetic characteristics of ship

geometries. It is to be emphasised that the structure examined in this section is not based on a particular vessel.

The structure of the ship studied is illustrated in figure 5.15. From bow to stern the ship is 55 m in length, with a beam of 10 m and a height of 10 m. The internal decking and bulkhead structure of the ship is to be noted. The relative permeability of the hull material is taken as 500 with the average hull thickness set at 0.01 m, giving the volume of material forming the ship structure to be 24.8 m^3.

For the two models, without and with degaussing, two orientations of the ship in the earth's magnetic field are assessed. The two orientations correspond to two different headings of the ship. It is to be noted that the same finite element mesh is used for both headings and it is the orientation of the earth's magnetic field that is changed. For a location in the northern hemisphere the two headings correspond to the ship sailing magnetic north and magnetic east. The external fields for both headings are defined in table 5.7 and subsequently are referred to as northward and eastward. For both headings the vertical component of the earth's magnetic field was set at -45000 nT. This component is not effected by the ship's orientation.

Ship Heading	External Field B_0 (nT)		
	$\hat{x}$	$\hat{y}$	$\hat{z}$
Northward	20000	0	-45000
Eastward	0	20000	-45000

Table 5.7: External fields for ship headings.

5.7.2 Induced Magnetic Signature

The results presented in this section have been obtained from a mesh of 500000 elements, 30000 of which correspond to surface elements representing the material structure of the ship. These surface elements have been specified with a relative permeability of 500 and a thickness of 0.01 m. No degaussing coils have been defined within the mesh. The outer surface of the entire finite element mesh forms a cube with one vertex at the origin with side length 500 m. The location of the ship within the mesh is defined in figure 5.15.

In figure 5.16 the magnetic perturbation has been plotted around the ship. In this figure the lower plane of the plot corresponds to a distance of 5 m below the keel line. At this same level beneath the ship the different field components are give in figure 5.17 along the line y=250 m, z=245 m and x ranging from 200 m to 300 m. The centre of mass of the ship is x=248.5 m, y=250.0 m, z=254.1 m. The calculated values for the dipole moments are given in table 5.8.

Ship Heading	Dipole moment $\mathbf{m}$ (Am^2)		
	$\hat{\mathbf{x}}$	$\hat{\mathbf{y}}$	$\hat{\mathbf{z}}$
Northward	139000	5.6	-80900
Eastward	-3295	68780	-82360

Table 5.8: Dipole moments of ship structure in two different external field orientations.

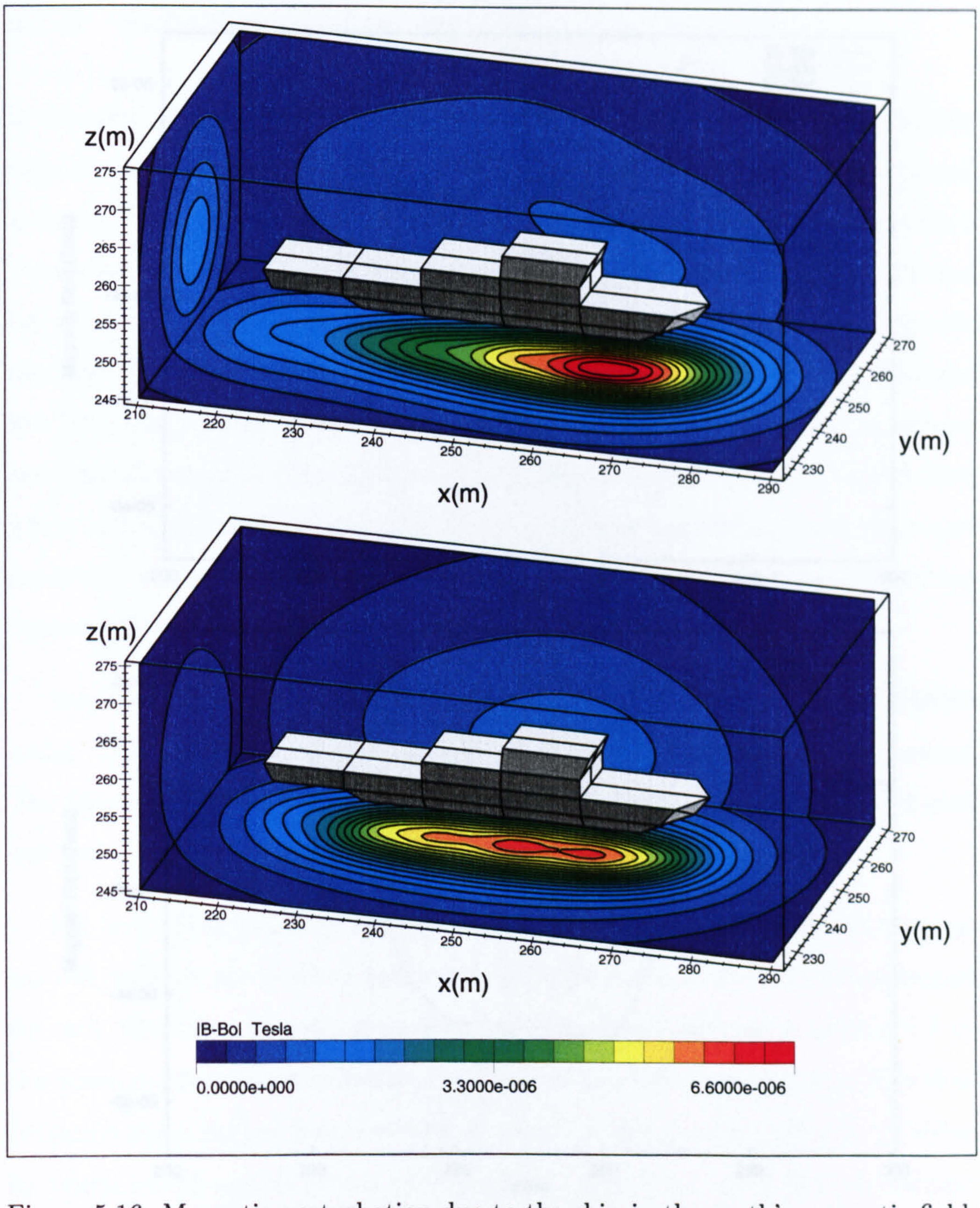

Figure 5.16: Magnetic perturbation due to the ship in the earth's magnetic field. Northward (upper). Eastward (lower).

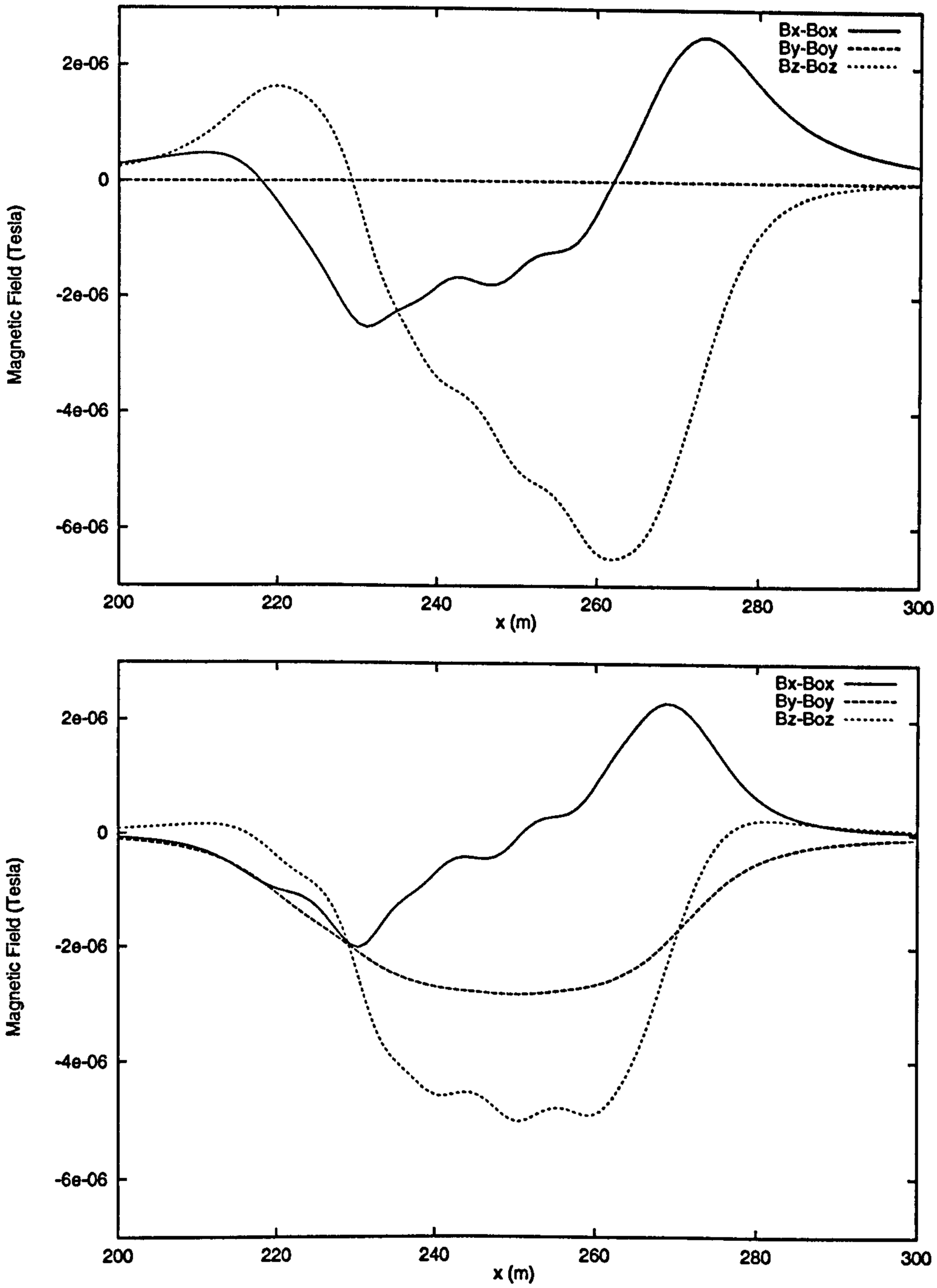

Figure 5.17: Components of the perturbation to the earth's magnetic field without degaussing, 5 m below keel. Stern x=220 m. Bow x=275 m. Northward (upper). Eastward (lower).

5.7.3 Ship Degaussing

In this section the geometry for the ship structure is unaltered but 13 degaussing coils are introduced into the model. The arrangement of the coils is illustrated in figure 5.18. It is to be noted that the coils are grouped in three sets with a convention for current flow as follows. The first set includes coils L1, L2, L3 and L4, which are parallel to the yz plane, and positive currents give rise to magnetic moments in the positive x direction. The second set includes coils M1, M2 and M3, which lie parallel to the xy plane, and positive currents give rise to upward and vertical moments. The third set of coils are grouped in pairs A1(a) and A1(b), A2(a) and A2(b), A3(a) and A3(b). These A coils lie parallel to the xz plane and positive currents give moments in the positive y direction. The dimensions of the degaussing coils can be determined from figure 5.18.

The mesh used in this study was composed of 1500000 elements and 240000 nodes. The material of the ship was defined by 65000 triangular surface elements. The degaussing coils were defined by specifying a dipole layer in the plane of each coil and a total of 93000 elements were used to define all the coils.

For each of the headings, northward and eastward, the optimal set of degaussing coil currents are given in tables 5.9 and 5.10 respectively. The minimisation for each direction was performed using the procedures outlined in section 3.8 on the plane z=245 m, corresponding to a depth of 5 m below the keel line. The minimisation plane ranged from x=200 m to x=300 m and from y=220 m to y=290 m on which 50×50 sample points were specified. It is to be noted that the current values in table 5.9 and table 5.10 correspond to the current that would be required if the coil was composed of just one turn. In other words the current values in these table correspond to the ampere-turns required in each coil.

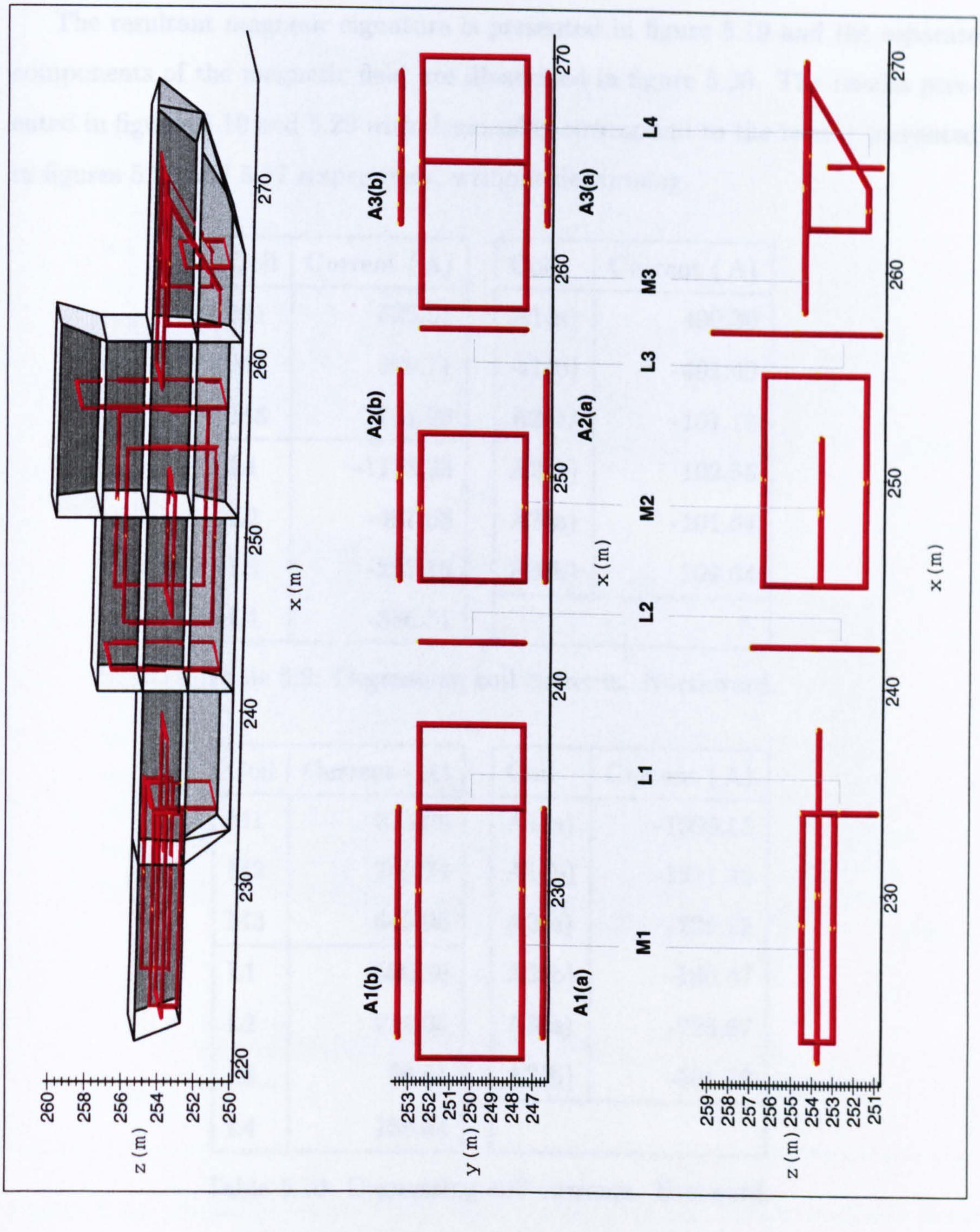

Figure 5.18: Degaussing coil arrangement.

The resultant magnetic signature is presented in figure 5.19 and the separate components of the magnetic field are illustrated in figure 5.20. The results prosented in figures 5.19 and 5.20 with degaussing correspond to the results presented in figures 5.16 and 5.17 respectively, without degaussing.

Coil	Current (A)
M1	525.91
M2	409.74
M3	761.29
L1	-1173.38
L2	-497.68
L3	-203.15
L4	-356.51

Coil	Current (A)
A1(a)	490.30
A1(b)	-491.49
A2(a)	-101.18
A2(b)	102.55
A3(a)	-101.64
A3(b)	109.64

Table 5.9: Degaussing coil currents. Northward.

Coil	Current (A)
M1	375.08
M2	789.74
M3	643.90
L1	-550.86
L2	214.05
L3	58.51
L4	158.54

Coil	Current (A)
A1(a)	-1099.53
A1(b)	-1211.40
A2(a)	-228.79
A2(b)	-180.47
A3(a)	-723.67
A3(b)	-561.12

Table 5.10: Degaussing coil currents. Eastward.

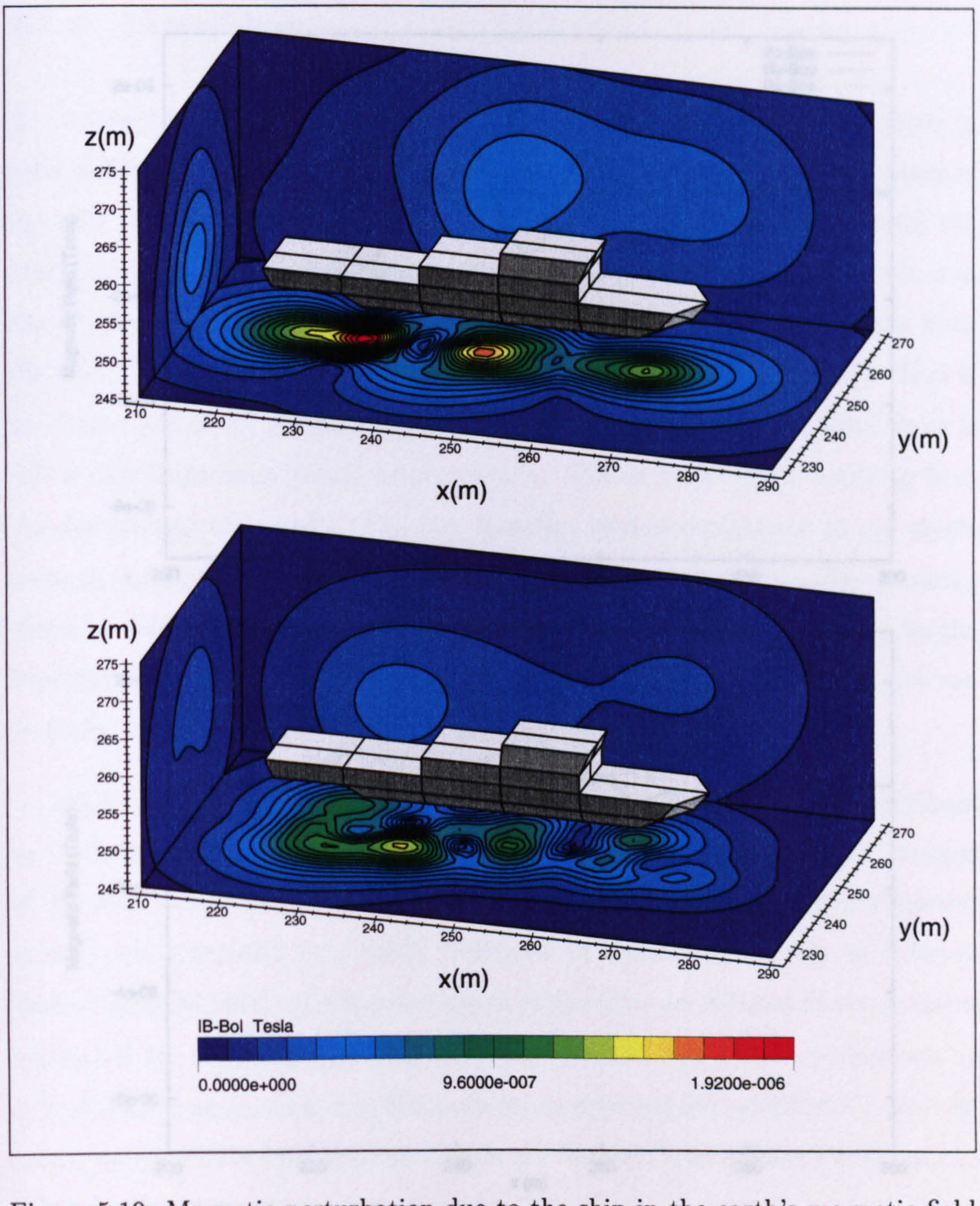

Figure 5.19: Magnetic perturbation due to the ship in the earth's magnetic field with degaussing. Northward (upper). Eastward (lower).

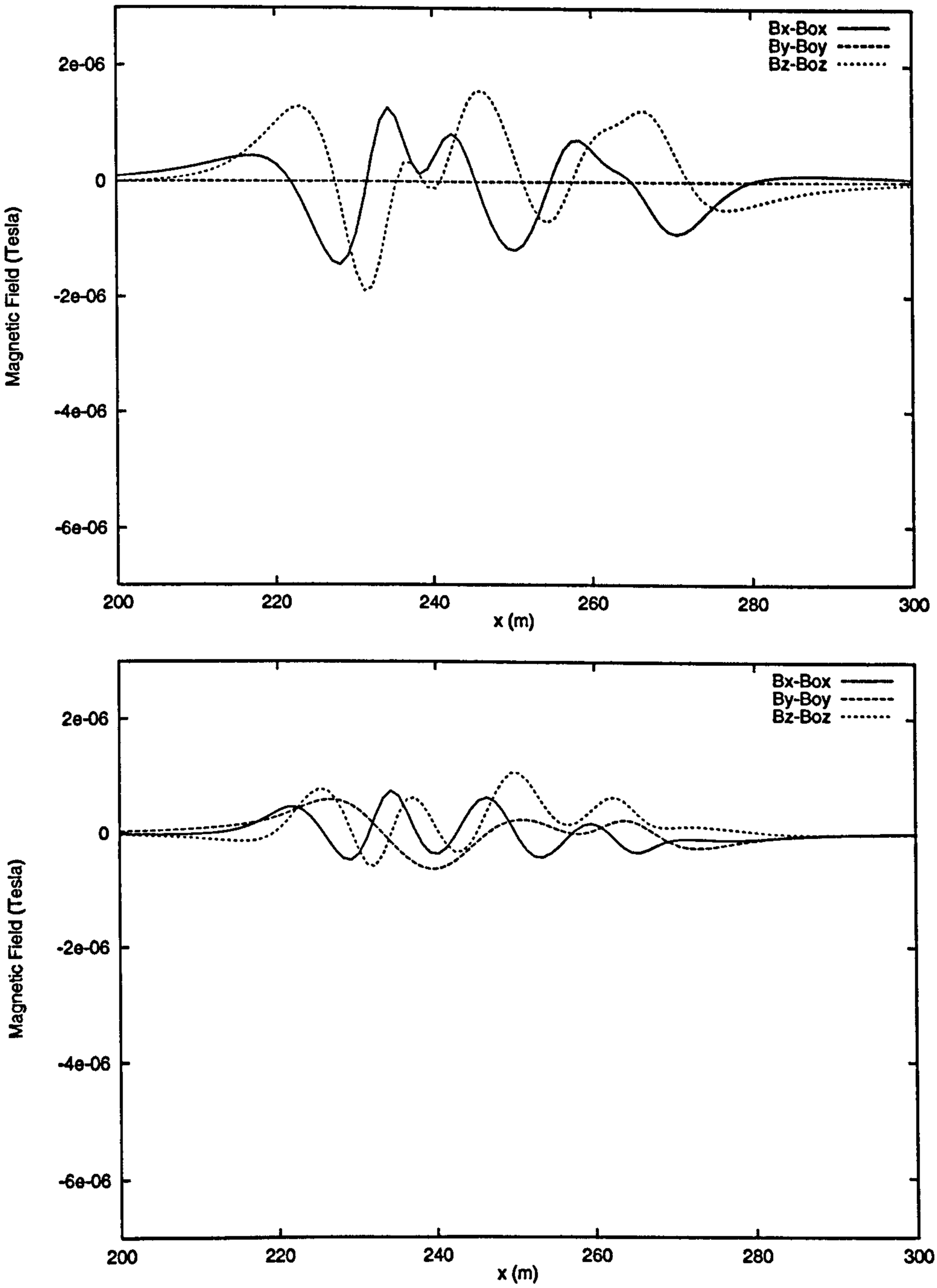

Figure 5.20: Components of the perturbation to the earth's magnetic field with degaussing, 5 m below keel. Stern x=220 m. Bow x=275 m. Northward (upper). Eastward (lower).

5.7.4 Discussion

By considering the dipole moments for the two headings of the ship given in table 5.8 it is evident that the magnetic signature depends on the orientation of the ship in the earth's magnetic field. When the ship is sailing northward the athwartship component of the earth's magnetic field is zero and this is reflected in the y component of the dipole moment, which is considerably smaller than both the x and z components. In contrast, for the eastward heading, although there is no component of the earth's magnetic field along the length of the ship, there is still a significant longitudinal magnetisation. This is a real effect resulting from the distribution of material. The fact that the vertical component of the dipole moment are approximately the same for both orientations of the ship confirms that the vertical induced magnetisation of the ship is relatively uneffected by the heading of the ship. The different characteristics in the magnetic signature can be noted from figures 5.16 and 5.17.

Assuming that the vertical component of the external field does not contribute to the longitudinal or arthwartship components of the induce magnetic moment of the ship, comparisons can be drawn between the finite element study present here to the spheroidal ship model described in section 2.3.3. For an external field of 20000 nT directed along the length of the ship the induced dipole moment calculated by the spheroidal ship model was 174600 Am^2, this corresponds to 139000 Am^2 given in table 5.8. Similarly for an external field of 20000 nT directed athwartships, 64300 Am^2 calculated from the spheroidal ship model compares to 68780 Am^2 from the finite element model.

By comparing the results for the undegaussed case presented in figure 5.17 with the corresponding results for the degaussed ship, presented in figure 5.20, the effectiveness of the degaussing coils can be noted. The greatest redution in the

induced magnetic signature is from $B_z - B_{0x}$ of -6.5 μT to -2 μT for the northward case and this improvement is typical of other components. Fluctuations in the field components with degaussing coils in use are much increased, because there are effectively more dipoles in different directions attempting to cancel each other out.

The general arrangement of currents in the coils can be understood. Both north and east headings are associated with a large downward induced component of moment, which the M coils try to neutralise. In both cases, the M coils carry large currents in the same direction.

The x component of induced moment is large and positive when heading north and significant and negative when heading east. The L coils act together in the first case to give a cancelling negative moment, but in the second case the currents are not all in the same direction indicating a more complicated interaction.

The y component is large when heading east and is balanced by large negative currents in the A coils. When heading north, the y component is small and arises from computing error. In this case it can be seen that the A1 coils have quite large but competing currents: A1(a) is 490.30 A and A1(b) is -491.49 A. The net effect is roughly a current of -1.19 A in one coil. The same conclusions hold for pairs A2 and A3. These results correspond to the calculation where the coils in these pairs can act as an individual coil in the minimisation. Further minimisation calculations could be performed when the same current is passed through both coils in each pair.

Chapter 6

Minesweeper Model

6.1 Introduction

The rationale of restricting, where possible, the use of magnetic materials for the construction of mine countermeasures vessels has already been emphasised in section 1.3. There is, however, a range of different items of equipment on these ships which requires the use of magnetic materials. Consequnetly modelling the induced magnetic signature of a minesweeper craft requires each item of equipment on the vessel, constructed from magnetic material, to be considered. Reference is made to both the design and the construction stages of this type of ship.

In this chapter, a method of setting degaussing coil currents to minimise the resultant induced magnetic signature is described and one application is evaluated.

6.2 Modelling Theory

The magnetic field **B**, from a point dipole **m**, can be determined at any point distant from the dipole by using the expression,

$$\mathbf{B} = \frac{\mu_0}{4\pi}\left(\frac{3\,(\mathbf{r}\cdot\mathbf{m})\,\mathbf{r}}{r^5} - \frac{\mathbf{m}}{r^3}\right) \tag{6.1}$$

where **r** is the vector from the dipole to the field point. This expression can be rewritten as,

$$\mathbf{B} = \mathbf{K}\mathbf{m} \tag{6.2}$$

where **K** is a symmetric 3×3 matrix defined by,

$$\mathbf{K} = \frac{\mu_0}{4\pi}\begin{bmatrix} \frac{3r_x^2}{r^5} - \frac{1}{r^3} & \frac{3r_x r_y}{r^5} & \frac{3r_x r_z}{r^5} \\ \frac{3r_y r_x}{r^5} & \frac{3r_y^2}{r^5} - \frac{1}{r^3} & \frac{3r_y r_z}{r^5} \\ \frac{3r_z r_x}{r^5} & \frac{3r_z r_y}{r^5} & \frac{3r_z^2}{r^5} - \frac{1}{r^3} \end{bmatrix} \tag{6.3}$$

and where r_x, r_y and r_z are the x, y and z components of the vector **r** respectively. Therefore, for a fixed position relative to the dipole, the matrix **K** can be evaluated and consequently the field at this point can be determined for any dipole moment **m**.

For all the items of equipment on the ship that have to be included in the model, it is assumed that the induced dipole moment **m** of each can be represented as,

$$\mathbf{m} = \mathbf{N}\mathbf{B} \tag{6.4}$$

where **B**, in this equation, is the external magnetic flux at the point of the dipole and **N** is a 3×3 matrix relating **B** to **m**. For example and with reference to equation 2.16, for a sphere of volume V and permeability μ_r, the induced dipole

moment can be expressed as,

$$\mathbf{m} = \frac{3V}{\mu_0}\frac{(\mu_r - 1)}{(\mu_r + 2)}\begin{bmatrix} 1 & 0 & 0 \\ 0 & 1 & 0 \\ 0 & 0 & 1 \end{bmatrix}\mathbf{B} \tag{6.5}$$

It is necessary to obtain the corresponding matrix N for each item that has to be included within the model and methods for determining each matrix N are discussed in section 6.3.

When a number of different items are to be included in the model, the magnetic field experienced by each item and hence the induced dipole moment on the item depends on three factors: A uniform external magnetic field, that is the earth's magnetic field $\mathbf{B}_0$; the field due to the degaussing coils $\mathbf{B}_{Ii}$, at the position of $\mathbf{m}_i$; the field due to the surrounding dipoles $\mathbf{B}_{ij}$. The dipole moment on the ith item can then be written as,

$$\mathbf{m}_i = \mathbf{N}_i\left[\mathbf{B}_{Ii} + \mathbf{B}_0 + \sum_{j=1, j\neq i}^{n}\mathbf{B}_{ij}\right] \tag{6.6}$$

where n is the total number of items within the model and $\mathbf{B}_{ij}$ is the magnetic field due to the jth dipole at the position of the ith dipole. This means that each $\mathbf{m}_i$ depends on the surrounding dipoles, resulting in a system of $3n$ linear equations for all the components of all the dipoles.

For illustration the example of a model required to include two items of equipment is considered. Each of the items has an induced magnetic moment governed by the matrix $\mathbf{N}_i$ and by the magnetic field at the item, as defined by equation 6.6. For each item,

$$\mathbf{m}_1 = \mathbf{N}_1\left[\mathbf{B}_{I1} + \mathbf{B}_0 + \mathbf{B}_{12}\right] \tag{6.7}$$

$$\mathbf{m}_2 = \mathbf{N}_2\left[\mathbf{B}_{I2} + \mathbf{B}_0 + \mathbf{B}_{21}\right] \tag{6.8}$$

Since the relative positions of the dipoles are fixed, the above equations can be written in terms of the appropriate matrix **K** as defined by equation 6.2,

$$\mathbf{m}_1 = \mathbf{N}_1 [\mathbf{B}_{I1} + \mathbf{B}_0 + \mathbf{K}_{12}\mathbf{m}_2] \tag{6.9}$$

$$\mathbf{m}_2 = \mathbf{N}_2 [\mathbf{B}_{I2} + \mathbf{B}_0 + \mathbf{K}_{21}\mathbf{m}_1] \tag{6.10}$$

where the matrices $\mathbf{K}_{12}$ and $\mathbf{K}_{21}$ correspond to equation 6.3. It is to be noted that $\mathbf{K}_{12} = \mathbf{K}_{21}$. These equations when combined give,

$$\begin{bmatrix} I & -\mathbf{N}_1\mathbf{K}_{12} \\ -\mathbf{N}_2\mathbf{K}_{21} & I \end{bmatrix} \begin{bmatrix} \mathbf{m}_1 \\ \mathbf{m}_2 \end{bmatrix} = \begin{bmatrix} \mathbf{N}_1 (\mathbf{B}_0 + \mathbf{B}_{I1}) \\ \mathbf{N}_2 (\mathbf{B}_0 + \mathbf{B}_{I2}) \end{bmatrix} \tag{6.11}$$

where I is the 3×3 identity matrix and the submatrix, defined by $-\mathbf{N}_1\mathbf{K}_{12}$, represents the influence of item 2 on item 1 and vice versa for $-\mathbf{N}_2\mathbf{K}_{21}$. Since $\mathbf{N}_1$ may not be equal to $\mathbf{N}_2$, the resultant matrix on the left side of equation 6.11 may not be symmetric. This set of 6 equations can be solved for the values of $\mathbf{m}_1$ and $\mathbf{m}_2$ and hence the magnetic field at any point determined. This analysis can be extended to any number of items of equipment, the matrix can be formed and the set of equations solved to determine the induced dipole moment for each item within the ship.

The degaussing coils are modelled by a closed loop of straight line segments and the magnetic field at any point calculated from the method outlined in section 2.4.2.

6.3 Representation of Onboard Items

One of the key aspects of this model is the representation of each of the items as a point dipole. It is, therefore, important to be able to obtain the matrix N for each item of equipment which is to be included in the model. The matrix N is

required to relate the magnetic flux and the position of the item to its induced dipole moment. In this section the different methods available to determine this matrix are described.

This type of modelling has potential for use at both the design and the construction stages of a naval vessel. It has to be recognised that the available technical information pertaining to each item of onboard equipment increases during the development of the vessel. Nevertheless, at the initial design stage of the vessel the matrix N can be estimated for each component of equipment.

During the design stage, the matrix can be estimated from a number of methods. Some equipment, for example the marine engines, are specific for minesweepers and the information on the relevant magnetic signatures are given with the engine specifications. This data can normally be used to derive the values of the matrix N .

For larger items of equipment, finite element analysis can be used. This would be applicable to the finite element study of the crane structure examined in section 5.6 and illustrated in the stowed position in figure 5.13. This example case is developed below. For a known orientation of the crane relative to the ship, from the finite element analysis that was undertaken in section 5.6, the dipole moments were calculated for an external field of $1\,\mathrm{Am}^{-1}$ along the direction of each axis. The results are given in table 6.1. The material of the crane was represented by surface elements with a relative permeability of 500 and a thickness of 0.01 m.

These values define the matrix **N** and the following equation can be written,

$$\mathbf{m} = \frac{1}{\mu_0} \begin{bmatrix} 31.727 & 0.0 & 4.193 \\ 0.0 & 3.805 & 0.0 \\ 4.193 & 0.0 & 8.055 \end{bmatrix} \mathbf{B} \tag{6.12}$$

H_0 (Am^{-1})			Dipole moment m (Am^2)		
$\hat{x}$	$\hat{y}$	$\hat{z}$	$\hat{x}$	$\hat{y}$	$\hat{z}$
1	0	0	31.727	0.0	4.193
0	1	0	0.0	3.805	0.0
0	0	1	4.193	0.0	8.055

Table 6.1: Dipole moments of minesweeper crane in the stowed position, as illustrated in figure 5.13, for different external field orientations.

However, for the majority of items of equipment to be fitted to the ship, analytical expressions are required to determine the matrix **N**. This method relies on approximating the shape of each item to a prolate spheroid or to a sphere of known dimensions and relative permeability. It is to be noted that each item of equipment should be subdivided into a number of appropriate components and each component regarded as a single item in the model. For example, a relatively compact solid item of equipment, with a known volume and permeability, can be regarded as a sphere allowing equation 6.5 to be used to determine the approximate **N**. In mathematical terms the expression for a sphere can be used because all the higher multipole contributions to the field are insignificant, when compared with the dipole contribution.

During the construction stage, all items of equipment are available for the determination of their magnetic signatures and if appropriate these values can be used to improve the accuracy of the respective matrices.

In addition, at the construction stage, the effects of any permanent magnetisation can be included and worked into a revised model. This involves rewriting equation 6.6 as,

$$\mathbf{m}_i = \mathbf{N}_i \left[\mathbf{B}_{Ii} + \mathbf{B}_0 + \sum_{j=1, j\neq i}^{n} \mathbf{B}_{Pij} + \sum_{j=1, j\neq i}^{n} \mathbf{B}_{ij} \right] \tag{6.13}$$

where the term $\mathbf{B}_{Pij}$ describes the influence of the permanent magnetisation of item j on item i. Apart from adding extra terms to the source vector on the right side of equation 6.11, the complexity of the system of equations is not increased.

6.4 Degaussing

From sections 6.2 and 6.3 the magnetic signature of a minesweeper, for a given distribution of material and a specified degaussing coil system operating with a known set of coil currents, has been determined. In this section a method is described for determining the optimum set of degaussing coil currents to produce the smallest magnetic signature for a given region.

First, it is necessary to define the region where the magnetic signature is to be reduced. As in the finite elements section 3.8, the method adopted is to specify a plane close to the ship on which a number of sample points are selected.

From equation 6.11 it can be noted that the system of equations that is solved to determine the induced dipole moment on each item within the model can be represented as,

$$\mathbf{Gm} = \mathbf{b} \tag{6.14}$$

where $\mathbf{G}$ is a non symmetric matrix and the vector $\mathbf{m}$ contains the induced dipole moments. The vector $\mathbf{b}$ can be thought of as a source vector containing information about the field at the position of each dipole. This source vector $\mathbf{b}$ can rewritten as,

$$\mathbf{b} = \mathbf{b}_0 + \sum_{i=1}^{n} I_i \mathbf{b}_i \tag{6.15}$$

where $\mathbf{b}_0$ is the component from both the earth's magnetic field and any permanent magnetisation and $\mathbf{b}_i$ is the vector that gives the contribution to the field, at the

location of each dipole from the ith degaussing coil when carrying unit current. The total number of degaussing coils is n.

The dipole moment vector $\mathbf{m}$ can also be expanded as a linear combination,

$$\mathbf{m} = \mathbf{m}_0 + \sum_{i=1}^{n} I_i \mathbf{m}_i \tag{6.16}$$

where,

$$\mathbf{m}_0 = \mathbf{G}^{-1}\mathbf{b}_0 \tag{6.17}$$

and for $I_i = 1$,

$$\mathbf{m}_i = \mathbf{G}^{-1}\mathbf{b}_i \tag{6.18}$$

The inverse of the matrix $\mathbf{G}$ is determined using Gauss-Jordan elimination. The algorithm used for this procedure is detailed in reference [64].

At this stage it is to be noted that a matrix $\mathbf{D}$ can be constructed, so that the vector $\mathbf{P}$ defined by,

$$\mathbf{P} = \mathbf{D}\mathbf{m} \tag{6.19}$$

contains the magnetic field, resulting from all the induced dipole moments, at each of the sample points on the minimisation plane. The entries in the matrix $\mathbf{D}$ are derived from equation 6.3. Substituting the expression 6.16 for $\mathbf{m}$ into equation 6.19, $\mathbf{P}$ can be written as,

$$\begin{aligned} \mathbf{P} &= \mathbf{D}\mathbf{m}_0 + \sum_{i=1}^{n} I_i \mathbf{D}\mathbf{m}_i \\ &= \mathbf{p}_0 + \sum_{i=1}^{n} I_i \mathbf{p}_i \end{aligned} \tag{6.20}$$

which defines the vectors $\mathbf{p}_0$ and $\mathbf{p}_i$. A set of vectors $\mathbf{q}_i$ can be defined such that the vector $\mathbf{Q}$ in the expression,

$$\mathbf{Q} = \sum_{i=1}^{n} I_i \mathbf{q}_i \tag{6.21}$$

gives the magnetic field at each of the sample points on the minimisation plane from each of the n degaussing coils specified in the model. The entries in the vectors $\mathbf{q}_i$ can be derived from the equations 2.75 and 2.76. The magnetic signature δ on the minimisation plane is then,

$$\delta = \mathbf{P} + \mathbf{Q} \tag{6.22}$$

$$= \mathbf{p}_0 + \sum_{i=1}^{n} I_i(\mathbf{p}_i + \mathbf{q}_i) \tag{6.23}$$

The quantity to be minimised is δ^2,

$$\delta^2 = \mathbf{p}_0^2 + \sum_{i=1}^{n}\sum_{j=1}^{n} I_i I_j(\mathbf{p}_i + \mathbf{q}_i)\cdot(\mathbf{p}_j + \mathbf{q}_j) + 2\sum_{i=1}^{n} I_i \mathbf{p}_0 \cdot (\mathbf{p}_i + \mathbf{q}_i) \tag{6.24}$$

Differentiating δ^2 with respect to each of the coil currents I_i,

$$\frac{\partial \delta^2}{\partial I_i} = 2\sum_{j=1}^{n} I_j(\mathbf{p}_i + \mathbf{q}_i)\cdot(\mathbf{p}_j + \mathbf{q}_j) + 2\mathbf{p}_0 \cdot (\mathbf{p}_i + \mathbf{q}_i) \tag{6.25}$$

and by setting the resulting expression to zero, a set of n linear equations is obtained. These can be solved to determine the set of degaussing currents which minimises the magnetic signature on the minimisation plane for a particular $\mathbf{B}_0$, degaussing coil arrangement and distribution of material. The set of equations to be solved is,

$$\sum_{j=1}^{n} I_j(\mathbf{p}_i + \mathbf{q}_i)\cdot(\mathbf{p}_j + \mathbf{q}_j) = -\mathbf{p}_0 \cdot (\mathbf{p}_i + \mathbf{q}_i) \tag{6.26}$$

6.5 Specification and Results

To demonstrate the application of the procedure for modelling the induced magnetic signature of a minesweeper and to assess the reduction of the signature by degaussing, a hypothetical minesweeper was considered as illustrated in figure 6.1. 19 degaussing coils are illustrated including 9 A coils, arranged in 4 set of pairs

with a single coil at the bow, and 5 L coils and 5 M coils. Items of equipment, constructed from magnetic material onboard the ship, are described by circles. The size of each circle is proportional to the size of the item of equipment that it represents. These items range in mass from the smallest at 5 kg to the largest at 3000 kg. The total mass of material is approximately 42000 kg.

The magnitudes of the magnetic fields resulting from only the dipoles for different depths z beneath the ship is illustrated in the left column of figure 6.2. The keel defines the plane z=0 m and the planes correspond to depths of z=-2 m, z=-4 m and z=-6 m. These results correspond to the inherent magnetic signature of the ship with no attempt to reduce the signature. For the same planes beneath the ship the magnetic field magnitude with the degaussing coils set to their optimal current values are illustrated in the right hand column of figure 6.2. The currents were obtained by minimising δ^2, as detailed in section 6.4, over the plane z=-4 m. This plane is illustrated in the middle two plots of figure 6.2 with a total of 30×30 sample points.

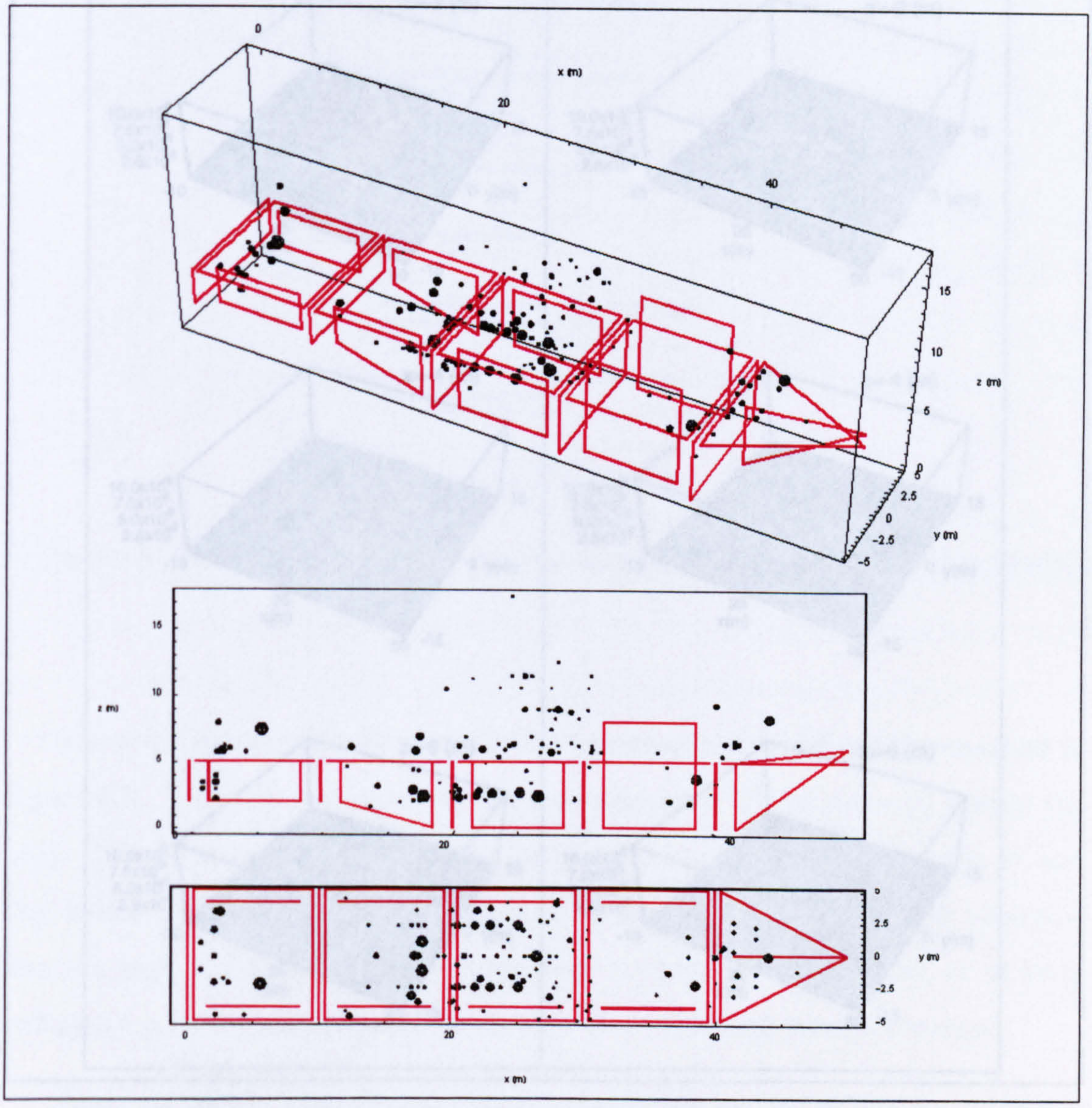

Figure 6.1: Geometry of minesweeper. Items of equipment (circles) and location of degaussing coils (red).

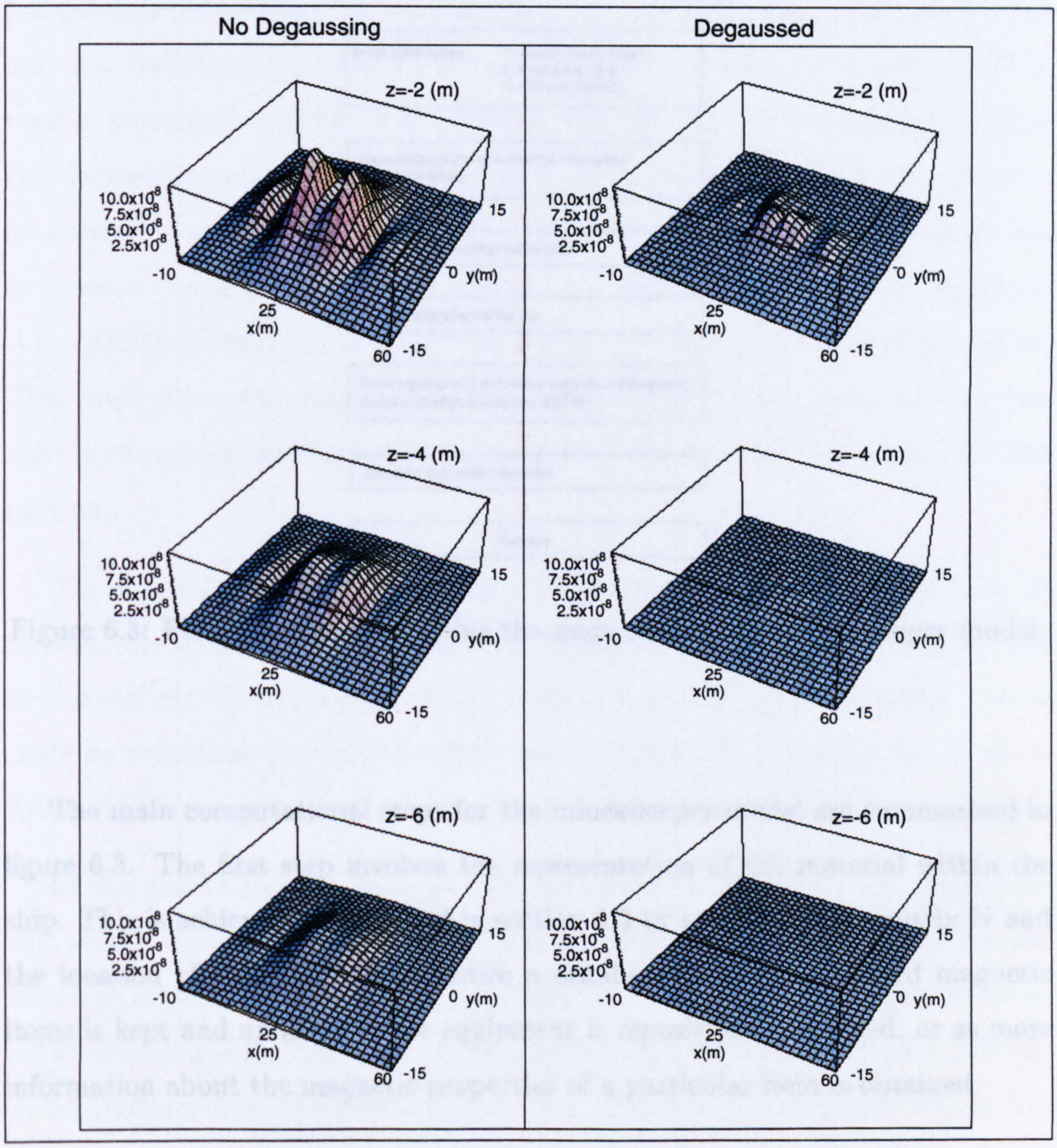

Figure 6.2: Left column : $|\mathbf{B}|$ (T) without degaussing. Right column : $|\mathbf{B}|$ (T) with degaussing, coils set to minimise the field on the plane z=-4 m. From upper to lower, plots are calculated on the planes z=-2 m, z=-4 m, z=-6 m. The earth's magnetic field was set to 50000 nT $\hat{\mathbf{x}}$.

6.6 Discussion

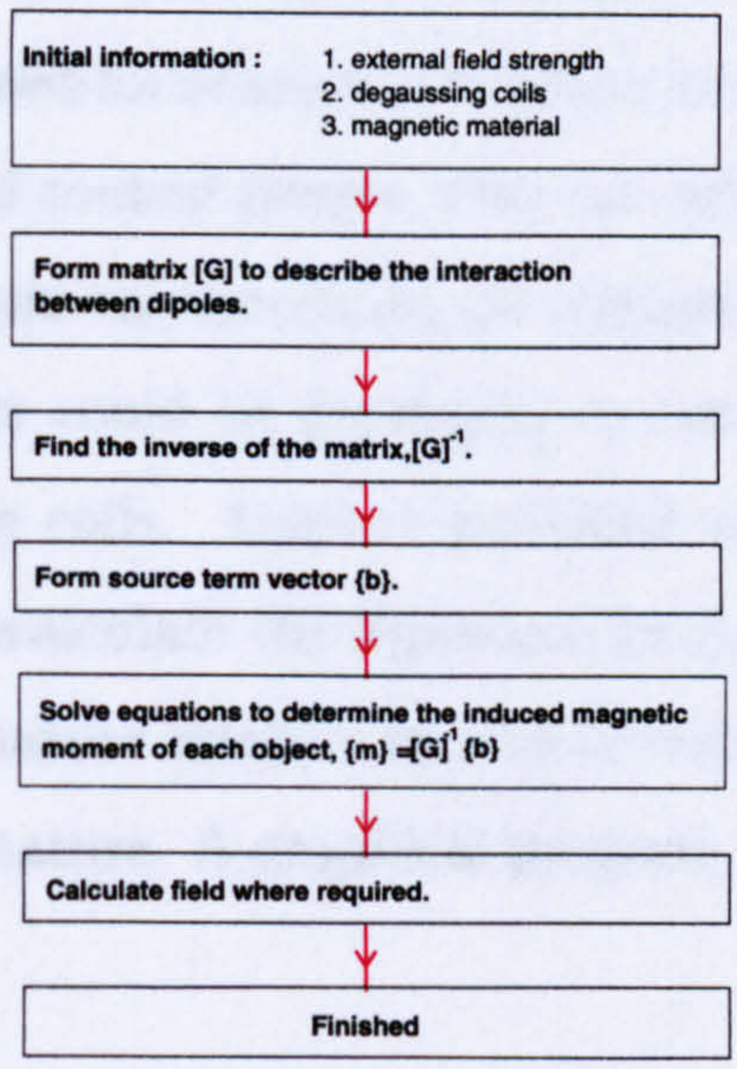

Figure 6.3: Flow diagram illustrating the main steps of the minesweeper model.

The main computational steps for the minesweeper model are summarised in figure 6.3. The first step involves the representation of the material within the ship. This is achieved as described in section 6.3 by specifying the matrix **N** and the location of each item. In practice a database of all the onboard magnetic items is kept and updated as the equipment is repositioned, changed, or as more information about the magnetic properties of a particular item is obtained.

Once the distribution of material is defined, the matrix **G** can be generated and its inverse determined. The inverse is found as opposed to solving the set of equations by, for example, the conjugate gradient method. Both methods are equally valid but the inverse can be used repeatedly to obtain results for different source vectors **b**, arising from different external fields or from different degaussing coil arrangements. Calculation of the inverse is time consuming, but once

obtained, results are instantaneously available. Therefore, forming the inverse has potential advantages. With minimal computation the optimal degaussing coil currents could be determined for changes in a ship's heading. The model could be used as part of an onboard control system with the ability to continuously adjust the degaussing coil currents corresponding to changes in heading. In addition, an onboard control system could be developed to compensate for failure in one or more of the degaussing coils. Another potential advantage of this approach is the ability to quickly recalculate the signature for different coil configurations. This could allow the signature analyst to add or reposition coils and evaluate quickly changes in the signature. A graphical program could be envisaged for this purpose.

The magnetic signature arises from localised and discrete sources and, at present, the degaussing countermeasure is obtained from large coils orientated to line the interior of the craft's hull . From this model future comparative work could be progressed to study the effectiveness of individual degaussing coils set to items of equipment that possess significant induced dipole moments.

In this model only the induced dipole moment on each item was considered, and higher order moments ignored. This simplification is appropriate for the following reason. Compared with the higher order moments, the dipole moment is the more important in terms of the rate at which its field component falls off, as the distance from the dipole, r, increases. The field of a magnetic dipole falls off as r^3, whereas, the higher order moments fall off more rapidly as r^5, r^7, etc. and it is, therefore, not unreasonable to ignore the higher order contributions at large distances from the ship. Also at the design stage simplifications are made to obtain the dipole moment of each item. It could be argued that it would be too costly to model each item, by using finite elements for example, in order to

obtain details on the higher moments.

Chapter 7

Summary and Conclusions

The aim of this work was to study the induced magnetic signature of marine vessels through the development of computational models. Three models have been developed in this work.

In chapter 2 an analytical model is proposed, which is based on representing a ship as a prolate spheroidal shell of permeable material. The dimensions of the ship and the volume of material forming the gross structure of the ship are used to set the dimensions of the shell. This model was used to demonstrate how the orientation of the ship in the earth's magnetic field has a significant influence on the induced magnetic signature of the ship. The main features of the magnetic properties of the ship are represented in this model and it is unlikely that a more realistic analytical model could be usefully developed.

The second model is based on the finite element method and this work is presented in chapters 3, 4 and 5.

In chapter 3 the basic finite element method was formulated in terms of the

total scalar potential, and two extensions of the method for the modelling of thin iron regions and current carrying coils are subsequently reported. Surface elements were developed to model the thin regions of high permeability, which correspond to the hull and decking of a ship. The use of this element type was validated in the finite element scheme by considering a spherical shell of permeable material. Without this technique, it would not be possible to model a realistic ship made of large thin metallic plates. To include the effects of current carrying coils, or more specifically degaussing coils, within the finite element formalism, current circuits were replaced by dipole sheets. This method was validated by studying a current carrying circular loop and by comparing the analytical solution with the corresponding finite element analysis.

Also outlined in chapter 3 are a number of important features that have been incorporated into the finite element code. The use of the conjugate gradient method and the formation of a basis set of solution vectors is described, allowing the larger scale problems of this work to be efficiently undertaken. In the final section of this chapter, a method used to quantify the optimal set of degaussing coils required for the reduction of the magnetic signature of a given ship is reported.

In chapter 5, applications of the finite element method are studied. The degaussing strategy, for identifying the optimal set of degaussing coil currents, was verified by considering a cube of permeable material in an external field with three different arrangements of degaussing coils. As the number of coils were increased, the degaussing currents approached the anticipated value required for complete degaussing. Also examined in this chapter are the contributions to the induced magnetic signature from decking and bulkhead structures within the interior of a ship. From this investigation it was concluded that the external structure of the ship provided only limited magnetic shielding of the internal gross structure

and consequently the internal structure is an important feature to be considered within the finite element model.

In the final sections of chapter 5 two case studies are reported. In the first case study, the magnetic signature associated with a crane, constructed from metal with a high permeability onboard a minesweeper, is considered. This work demonstrated that the induced magnetic signature of the crane significantly contributed to the overall magnetic signature of the vessel. The orientation of the arms of the crane was also found to alter significantly the magnetic signature. Consequently it would be very difficult indeed to degauss actively a crane made of magnetic material. In the second case study the application of the finite element method to a steel hulled ship is considered. In terms of the number of elements this was the largest model undertaken in this work. Both the finite element and mesh generation processes proved to be sufficiently robust and computationally efficient. The induced magnetic signature was determined for two different orientations of the vessel in the earth's magnetic field. For each orientation, the induced magnetic signature was determined without and with degaussing. From this investigation, a favourable reduction in the induced magnetic signature was demonstrated. Furthermore, the results demonstrated that for different orientations of the ship in the earth's magnetic field, different currents in the degaussing coils are required for efficient degaussing. The technique implemented here could be used to investigate possible improvements in degaussing arising from varying the position of the coils, and changing their number and size. It was also shown that once the magnetic properties of the ship and the magnetic effects of individual coils have been calculated, the optimum current settings needed for optimum degaussing in a given external field can be easily calculated. This implies that limited onboard computing is required for degaussing control systems, since all the time consuming computation has been concluded during commissioning of the vessel.

The development of the third model, specific for studying the induced magnetic signature of mine countermeasures vessels is detailed in chapter 6. In the previous models, modelling of the magnetic signatures was based on the gross structure of the ship, including hull, decking and bulkheads. In mine countermeasures vessels, reduction in the magnetic signature is of paramount importance, and the choice of material for their construction reflects this, with material of low relative permeability being used where possible. The use of GRP is the primary example of this. The model developed in this chapter is derived from the resultant of the individual magnetic dipole moments induced on all onboard items of equipment constructed from magnetic material. The effects of degaussing coils was also considered as part of this model and a method was developed for obtaining the optimal set of degaussing coil currents for a given degaussing coil system. A hypothetical ship is taken as a case study in this chapter and results are presented for the magnetic signature without and with degaussing.

In this work three models have been described for assessing the induced magnetic signature of a ship. Both the design of the ship, GRP versus steel hull, and the required accuracy for quantifying the magnetic signature have to be considered in choosing the modelling method suitable for a particular application. The analytical model provides a convenient approach suitable for preliminary studies. The finite element method permits a more detailed geometry to be followed and consequently has the potential for application to more accurate studies of the induced magnetic signatures of vessels in service or under development. Furthermore, there is a requirement to validate the modelling methods against the magnetic signatures of appropriate naval vessels currently in use. For this comparative investigation, however, the required magnetic signature data from these ships is not currently available for a public domain study.

Bibliography

[1] Swansea History Web. The mine war in the Bristol Channel 1934-41. www.swanseahistoryweb.org.uk/history/bristolc/uboats.htm.

[2] B. Gordon. Degaussing: The demagnetisation of ships. *Electronics and Power*, 30(6):473–476, 1984.

[3] *Bartington Instruments Limited.* 10 Thorney Leys Business Park, Witney, Oxford, England. OX8 7GE. www.bartington.com/mag566.htm.

[4] C. S. Buck, G. A. Steel. A mobile range for measurement of undewater magnetic and electric fields. *Proceedings, Marelec Conference 1997*, 1997.

[5] L. C. Bobb, J. P. Davis, S. R. Swyers. Airborne magnetic noise reduction. *Proceedings, Marelec Conference 1997*, 1997.

[6] A. D. Ash. Noise and noise reduction techniques for airborne magnetic measurements at sea. *Proceedings, Marelec Conference 1997*, 1997.

[7] Y. Sasakawa, K. Imaichi, E. Tada, S. Takezawa. Japanese experimental ship with the superconducting electro-magnetic thruster. *International Symposium on New Developments in Applied Superconductivity*, pages 686–691, 1988.

[8] Proceedings, International Conference on Marine Electromagnetics, June 1997. Marelec 1997.

[9] Proceedings - 2nd International Conference on Marine Electromagnetics, July 1999. Marelec 1999.

[10] P. Lorrain, D. R. Corson, F. Lorrain. *Electromagnetic Fields and Waves.* W. H. Freeman and Company, 1988.

[11] D. L. Piron. *The Electrochemistry of Corrosion.* NACE International, 1991.

[12] T. H. Rogers. *Marine Corrosion.* Newnes, 1968.

[13] A. J. Jennings. *Underwater Electromagnetic Field Modelling.* BAeSEMA, 1997. Confidential.

[14] *BEASY.* Ashurst Lodge, Ashurst, Southampton, Hampshire, England. SO40 7AA. www.beasy.com.

[15] P. Khambhaita, J. N. McGrath, K. H. D. Slack, D. J. Tigne. Physical scale modelling of the modulation of ship ICCP current output by propeller shaft rotation. *Proceedings, Marelec Conference 1999*, pages 269–279, 1999.

[16] Pei Yuan Hang. An analysis of eddy current magnetic field of moving permeable conductive shell. *Proceedings, Marelec Conference 1999*, pages 425–434, 1999.

[17] Richard Sharpe, editor. *Jane's Fighting Ships.* Jane's Data Division, Coulsen, Surrey, 1992-93.

[18] United States Navy. Naval Ships' Technical Manual: Chapter 475 Magnetic Silencing, 1989. www.fas.org/man/dod-101/sys/ship/nstm.

[19] R. A. Wingo, J. J. Holmes, M. H. Lackey. Test of a closed loop degaussing algorithm on a minesweeper engine. *Naval Engineers Journal*, 104(3):219–227, 1992.

[20] K. J. Binns, P. J. Lawrenson, C. W. Trowbridge. *The Analytical and Numerical Solution of Electric and Magnetic Fields.* Wiley, 1992.

[21] J. A. Stratton. *Electromagnetic Theory.* McGraw-Hill, 1941.

[22] G. Molinari. *Classification of Software Available and Criteria of Approach in Industrial application of Electromagnetic Computer Codes.* Kluwer Academic, London, 1990.

[23] *Vector Fields Limited.* 24 Bankside, Kidlington, Oxford, England. OX5 1JE. www.vector-fields.co.uk.

[24] John Whitney. Vector Fields Limited: Software for electromagnetic design. Private communication.

[25] A. S. Christopoulos. Finite element analysis and the magnetic characteristics of bouyant vehicle dyads. *Proceedings, Marelec Conference 1999*, pages 473–478, 1999.

[26] *CEDRAT.* 10, Chemin de Pré Carré - Zirst, 38246 MEYLAN Cedex, France. www.cedrat-grenoble.fr.

[27] X. Brunotte, G. Meunier, J .P. Bongiraud. Ship magnetizations modelling by the finite element method. *IEEE Transactions on Magnetics*, 29:1970–1965, 1993.

[28] G. Meunier X. Brunotte. Line element for efficient computation of the magnetic field created by thin iron plates. *IEEE Transactions on Magnetics*, 26:613–616, 1990.

[29] F. Le Dorze, J. P. Bongiraud, J. L. Coulomb, P. Labie, X. Brunotte. Modeling of degaussing coils effects in ships by the method of reduced scalar potential jump. *IEEE Transactions on Magnetics*, 34:2477–2480, 1998.

[30] F. Le Dorze, J. P. Bongiraud, J. L. Coulomb, P. Labie, X. Brunotte. Ship magnetization modelling by finite element method. *Electromagnetic Silencing Symposium - Bergen*, 1995.

[31] J. P. Dallet. Presentation of a magnetic degaussing systems software study for ship. *Proceedings, Marelec Conference 1997*, 1997.

[32] G. Le Coat, et al. Electromagnetic stray fields of a propulsion induction machine. *Proceedings, Marelec Conference 1997*, 1997.

[33] W. R. Smythe. *Static and Dynamic Electricity.* McGraw-Hill, 1939.

[34] O. C. Zienkiewicz, R. L. Taylor. *The Finite Element Method Volume 1: Basic Formulation and Linear Problems.* McGraw-Hill, New York, 4th edition, 1989.

[35] Jianming Jin. *The Finite Element Method In Electromagnetics.* Wiley, New York, 1993.

[36] P. P. Silvester, R. L. Ferrari. *Finite Elements for Electrical Engineers.* Cambridge University Press, Cambridge, second edition, 1990.

[37] J. Simkin, C. W. Trowbridge. On the use of the total scalar potential in the numerical solution of field problems in electromagnetics. *International Journal for Numerical Methods in Engineering*, 14:423–440, 1979.

[38] M. R. Hestenes, E. Stiefel. Methods of conjugate gradients for solving linear systems. *Journal of Research of the National Bureau of Standards*, 49(6):409–436, Dec 1952.

[39] G. H. Golub, C. F. Van Loan. *Matrix Computations.* Johns Hopkins University Press, third edition, 1996.

[40] G. J. C. Aird. Magnetostatic Finite Elements In 2D : Demonstration Applets. www.physics.gla.ac.uk/~gordona.

[41] G. J. C. Aird. *FEM3D v1R6 User's Guide.* Department of Physics and Astronomy, University of Glasgow, 1999.

[42] G. J. C. Aird. *Display3D - A Visualisation Tool : User's Guide.* Department of Physics and Astronomy, University of Glasgow, 1999.

[43] P. Moller, P. Hansbo. On advancing front mesh generation in 3 dimensions. *International Journal for Numerical Methods in Engineering*, 38:3551–3569, 1995.

[44] C. D. Cavendish, D. A. Field, W. H. Fery. An approach to automatic three dimensional finite element mesh generation. *International Journal for Numerical Methods in Engineering*, 21:329–347, 1985.

[45] D. N. Shenton, Z. J. Cendes. *Three-dimensional finite element mesh* generation using delaunay tesselation. *IEEE Transactions on Magnetics*, 21(6):2535–2538, 1985.

[46] P. L. George. *Automatic Mesh Generation: Application to Finite Element Methods.* Wiley, 1991.

[47] M. Filipiak. Technology watch report on mesh generation. EPCC Edinburgh, 1996. www.epcc.ed.ac.uk/epcc-tec/documents/tw-meshgen.

[48] K. Ho-Le. Finite element mesh generation methods: a review and classification. *Computer Aided Design*, 20:27–38, 1988.

[49] S. J. Owen. A survey of unstructures mesh generation technology. *Proceedings, 7th International Meshing Roundtable*, 1998. www.andrew.cmu.edu/user/sowen/index.html.

[50] I. Babuska, A. K. Aziz. On the angle condition in the finite element method. *SIAM Journal On Numerical Analysis*, 13:214–226, 1976.

[51] J. O'Rourke. *Computational Geometry in C.* Cambridge University Press, 1993.

[52] A. Bowyer. Computing Dirichlet tessellations. *The Computer Journal*, 24:162–166, 1981.

[53] D. F. Watson. Computing the n-dimensional Delaunay tesselation with application to Voronoi ploytopes. *The Computer Journal*, 24:167–172, 1981.

[54] C. L. Lawson. Software for C1 surface interpolation. *Mathematical Software III (Ed. R. Rice)*, pages 161–193, 1977.

[55] P. L. Baehmann, et al. Robust, geometrically based, automatic two dimensional mesh generation. *International Journal for Numerical Methods in Engineering*, 24:1043–1048, 1987.

[56] M. A. Yerry, M. S. Shephard. A modified quadtree approach to finite element mesh generation. *IEEE Computer Graphics and Applications*, pages 36–46, 1983.

[57] D. A. Field. Laplacian smoothing and delaunay triangulations. *Communications In Applied Numerical Methods*, 4:709–712, 1988.

[58] M. A. Yerry, M. S. Shephard. Automatic three dimensional mesh generation by the modified-octree technique. *International Journal for Numerical Methods in Engineering*, 20:1965–1990, 1984.

[59] L. Ammeraal. *Computer Graphics for Java Programmers.* John Wiley and Sons, 1998.

[60] S. H. Lo. Optimization of tetrahedral meshes based on element shape measures. *Computers and Structures*, 63(5):951–961, 1997.

[61] K. Rule. *3D graphics file formats: A programmer's reference.* Addison Wesley Longman, 1996.

[62] G. J. C. Aird. *MESH3D v1R5 User's Guide.* Department of Physics and Astronomy, University of Glasgow, 1999.

[63] J. Van Bladel. *Electromagnetic Fields.* McGraw-Hill, 1964.

[64] W. H. Press et al. *Numerical Recipes in C.* Cambridge University Press, second edition, 1988.